The Effect of Sequential Oxidation and Composition on the Structural and Electronic Properties of Gas-Phase Transition-Lanthanide Bimetallic Clusters

Alexander Gentleman

B.Sc. (Hons), MRACI CChem

A thesis submitted in total fulfilment of the requirements for the degree of Doctor of Philosophy

May, 2014

School of Chemistry and Physics

Department of Chemistry

The University of Adelaide

Statement of Originality

I certify that this work contains no material which has been accepted for the award of any other degree or diploma in any university or other tertiary institution and, to the best of my knowledge and belief, contains no material previously published or written by another person, except where due reference has been made in the text. In addition, I certify that no part of this work will, in the future, be used in a submission for any other degree or diploma in any university or other tertiary institution without the prior approval of the University of Adelaide and where applicable, any partner institution responsible for the joint-award of this degree.

I give consent to this copy of my thesis when deposited in the University Library, being made available for loan and photocopying, subject to the provisions of the Copyright Act 1968. The author acknowledges that copyright of published works contained within this thesis resides with the copyright holder(s) of those works.

I also give permission for the digital version of my thesis to be made available on the web, via the University's digital research repository, the Library catalogue, and also through web search engines, unless permission has been granted by the University to restrict access for a period of time.

Alexander S. Gentleman

May, 2014.

Abstract

This thesis presents experimental and theoretical work performed on various rhodium-holmium (Rh-Ho) and gold-praseodymium (Au-Pr) bimetallic clusters and their oxide counterparts. More specifically, structural and/or electronic properties for these clusters are ascertained from investigating how their adiabatic ionisation energies (IEs) are affected by: (a) the sequential addition of oxygen atoms onto the base bimetallic cluster within each series, or (b) the composition of the bimetallic clusters i.e. the transition:lanthanide metal atom ratio within each cluster.

The clusters were experimentally generated via dual laser ablation and detected using time-of-flight mass spectrometry (TOF-MS) coupled with threshold laser ionisation. Upon successful formation and detection, the experimental adiabatic IEs of these clusters were determined using Photoionisation Efficiency (PIE) spectroscopy. In regards to aspect (a) of this thesis listed above, it was observed that the sequential addition of individual oxygen atoms onto bare Rh-Ho and Au-Pr clusters either caused: (i) a significant change in or (ii) had little-to-no effect on the experimental adiabatic IE. For clusters that displayed the former behaviour, the addition of the first oxygen atom was observed to significantly decrease the adiabatic IE relative to that of the bare bimetallic cluster within that series. The addition of a second oxygen atom onto the monoxide counterpart was observed to significantly increase the adiabatic IE back to a value similar to that of the bare bimetallic cluster. In regards to aspect (b) of this thesis listed above, it was observed that: (i) the substitution of a transition metal atom for a lanthanide metal atom generally lowers the experimental adiabatic IE of each cluster, and (ii) the sequential addition of transition metal atoms onto a cluster generally increases the experimental adiabatic IE of each cluster.

In order to gain more insight into the nature of the observed experimental adiabatic IE trends mentioned above, Density Functional Theory (DFT) Investigations were performed on the neutral and cationic species for the $RhHo_2O_n$ (n = 0-2), $Rh_2Ho_2O_m$ (m = 0-2) and the $Au_{3-k}Pr_k$ (k = 0-3) clusters. From these, the lowest energy

neutral and cationic geometries (in addition to other properties such as atomic charges and normal modes of vibration) were determined and subsequently, the theoretical adiabatic IEs of each cluster were calculated. When compared within each series, the experimental and theoretical adiabatic IE trends as a function of: (i) sequential addition of oxygen atoms in the $RhHo_2O_n$ (n = 0-2) and $Rh_2Ho_2O_m$ (m = 0-2) cluster series, and (ii) substitution of a gold atom for a praseodymium atom in the $Au_{3-k}Pr_k$ (k = 0-3) cluster series, both displayed similar behaviour. From this, specific ionisation transitions between neutral and cationic structures were able to be assigned and thus, structural and electronic information about each cluster was able to be inferred.

In addition to the DFT investigations, Franck-Condon Factor (FCF) calculations were performed in order to simulate the Zero Electron Kinetic Energy (ZEKE) and PIE spectra for each cluster in the $RhHo_2O_n$ (n = 0-2), $Rh_2Ho_2O_m$ (m = 0-2) and $Au_{3-k}Pr_k$ (k = 0-3) series. The purposes of these additional calculations were to: (i) identify the most likely transition from two or more competing candidates that occurs upon ionisation for each cluster, and (ii) apply slight corrections to the experimental adiabatic IEs obtained from the PIE spectra in order to account for thermal tailing resulting from vibrational hot band transitions at 300 K.

Acknowledgments

First and foremost, I would like to thank my supervisor and mentor Assoc. Prof. Greg Metha for his enthusiasm, encouragement, guidance and unyielding patience over the years. His intimate knowledge of molecular spectroscopy, passion for all things science-related, and eagerness to discuss new ideas and work through issues (even at the most inconvenient of times!) have always been invaluable and greatly appreciated.

I would also like to thank my co-supervisor Prof. Mark Buntine for encouraging and guiding me through my scientific life ever since I told him in my first year of undergraduate studies that I wanted to be a physical chemist/chemical physicist. Our many passionate discussions (both science and non-science related) and longer-than-scheduled Skype chats have always been entertaining and truly inspiring.

Thanks must also go to Dr. Jason Gascooke, Dr. Vik Dryza and Dr. Matt Addicoat for their invaluable help with all things experimental and/or computational. If it were not for them, I would most definitely have been lost on many occasions!

A big "Ευχαριστώ" goes to Peter Apoefis for his priceless expertise in building the parts to the cluster source and maintaining the equipment required for this project. Without him, PhD life would have been infinitely more difficult!

To all of the other Honours students, PhD students and Postdocs that I have had the immense pleasure of sharing the lab with over the years – Cheers! Special thanks go to (Soon-to-be) Dr. Sam Wallace, Dr. Chris Colyer and Dr. Mark Stevenson for showing me that lab life should consist of more than just science in order to keep your sanity.

Lastly, I would like to thank my friends and family for their continual love and support over the many years. I am most privileged to have such fantastic people in my life. I would especially like to thank my Mum for always encouraging me to follow my passions in life and supporting me throughout my entire PhD tenure, and my partner Krystal, whose love, support and belief in me during these past few years has pushed me through my darkest days and kept the light burning at the end of the PhD tunnel.

Publications

The following publication contains some of the work presented in this thesis:

Photoionisation Efficiency Spectroscopy and Density Functional Theory Investigations of $RhHo_2O_n$ (n = 0-2) Clusters.
A. S. Gentleman; M.A. Addicoat; V. Dryza; J. R. Gascooke; M. A. Buntine; G.F. Metha, Journal of Chemical Physics, 130, 164311 (2009).

The following publications are currently in preparation and will each contain some of the work presented in this thesis:

Structural and Electronic properties of Gas-Phase Neutral and Cationic $Rh_2Ho_2O_m$ (m = 0-2) Clusters Determined using Photoionisation Efficiency Spectroscopy, Density Functional Theory and Franck-Condon Factor Calculations.
A. S. Gentleman; M. A. Buntine; G.F. Metha (in preparation).

Photoionisation Efficiency Spectroscopy, Density Functional Theory Investigations and Franck-Condon Factor Calculations of Gas-Phase $Au_{3-k}Pr_k$ (k = 0-2) Clusters: How composition affects their structural and electronic properties.
A. S. Gentleman; M. A. Buntine; G.F. Metha (in preparation)

Elucidation of the Structural and Electronic Properties of the Gas-Phase $AuPr_2O_x$ (x = 0-2), $Au_2Pr_2O_m$ (m = 0-1) and $Au_3Pr_2O_n$ (n = 0-2) Bimetallic Clusters using Photoionisation Efficiency Spectroscopy, Density Functional Theory and Franck-Condon Factor Calculations.
A. S. Gentleman; M. A. Buntine; G.F. Metha (in preparation)

Abbreviations

AE	Appearance Energy
AO	Atomic Orbital
CGF	Contracted Gaussian Function
DFT	Density Functional Theory
ECP	Effective Core Potential
eV	Electron Volt
FC	Franck-Condon
FCF	Franck-Condon Factor
GTO	Gaussian-Type Orbital
HOMO	Highest Occupied Molecular Orbital
IE	Ionisation Energy
MO	Molecular Orbital
MP	Model Potential
PES	Potential Energy Surface
PIE	Photoionisation Efficiency
PFI-ZEKE	Pulsed Field Ionisation Zero-Electron Kinetic Energy
PGF	Primitive Gaussian Function
PP	Pseudopotential
SPI	Single Photon Ionisation
TMO	Transition Metal Oxide(s)
TOF	Time-of-Flight
TOF-MS	Time-of-Flight Mass Spectrometry
UPS	Ultra-violet Photoelectron Spectroscopy
ZEKE	Zero-Electron Kinetic Energy
ZPE	Zero-Point Energy

Table of Contents

1.1. Gas-Phase Transition Metal Oxide Clusters - Relevance to Catalysis

Transition metal oxides (TMOs) have been the topic of intense research over the last few decades due to their widespread use in the area of heterogeneous catalysis as both catalysts and catalytic supports. Industrially significant reactions such as the catalytic oxidation of alkanes and alkenes, oxidative dehydrogenation of light alkanes, and many others can be catalysed using TMOs.[1-5] However, despite TMOs being used extensively in heterogeneous catalysis, there still remains a dearth of understanding regarding the mechanistic details and structure-reactivity relationships behind how TMOs function as catalysts or as supports.[6] Gaining an enhanced understanding of these particular aspects of TMO catalysis is of vital importance as it will inevitably lead to more efficient and educated approaches in the design of next-generation TMO catalysts rather than the "trial and error" approach that is currently applied (not just for TMO catalyst design, but the design of all industrial heterogeneous catalysts in general).[7]

A valuable approach used to gain a fundamental understanding of the mechanistic details and structure-reactivity relationships underlying heterogeneous TMO catalysis is to investigate the structures of gas-phase TMO clusters and their reactivity with small molecules. TMO clusters are well-suited to model solid-state metal oxide surfaces as the chemical transformations involved in processes that utilise TMO catalysts occur on localised, active sites on the oxide surface that possess a spatial extension on the sub-nanometre scale. These catalytically active sites are characterised by steps, defects, ledges and/or corners on the metallic oxide surface that can differ significantly in charge density (i.e. they can be electron-rich or electron-deficient), thus allowing them to be considered as cationic and anionic TMO clusters of varying sizes and structures. Hence, if the reactivity of small molecules (e.g. methane in the partial oxidation (POX) process or *n*-butane in oxidative dehydrogenation) with gas-phase TMO clusters of various types, sizes and charge states is investigated, then molecular-level details regarding the energetics, kinetics and reaction mechanisms can

be attained, thus providing an overall understanding of how reactant molecules are activated in these catalytic processes.

An example of an industrial process where such insight has occurred is for the selective oxidation of hydrocarbons catalysed by vanadia surfaces. Castleman and co-workers investigated the formation of acetaldehyde via oxygen atom transfer from $V_xO_y^+$ clusters to ethylene.[8,9] Of the varied range of cationic vanadium oxide clusters experimentally investigated, only the $(V_2O_5)_n^+$ (n = 1,2) clusters were found to transfer an oxygen atom to ethylene to form acetaldehyde as the dominant reaction pathway. When the stoichiometry of these clusters differed by even just one oxygen atom (e.g. $V_2O_4^+$ and $V_2O_6^+$) then other reaction pathways became dominant (e.g. Association reactions with ethylene or molecular oxygen loss), resulting in no acetaldehyde production. Density functional theory (DFT) calculated reaction pathways provided the rationale behind these experimental observations showing that the $V_2O_5^+$ and $V_4O_{10}^+$ clusters possessed radical oxygen centres (M-O•) with elongated metal-oxygen bonds, which were ultimately responsible for their pronounced catalytic behaviour. Other cationic vanadium oxide clusters that did not have the 2:5 vanadium-to-oxygen ratio were found to lack these radical oxygen centres, making the catalytic oxygen atom transfer to ethylene unfeasible. Overall, this work was able to: (i) infer that the active sites on vanadia surfaces responsible for the selective oxidation of hydrocarbons can be envisioned as V_2O_5 clusters possessing radical oxygen centres, and (ii) provide the energetics, kinetics and reaction mechanisms underlying the chemical transformations involved in this industrial process. With such success in achieving fundamental insight into industrial processes catalysed by TMO surfaces, it is of no surprise that a vast number of experimental and computational studies aimed at investigating the structure of gas-phase TMO clusters and their reactivity have been performed to date.[8,10-131]

1.2. Emergence of Gas-Phase Bimetallic Transition Metal Oxide Clusters

To date, most experimental and computational studies aimed at investigating the structures and reactivity of gas-phase TMO clusters have been limited to monometallic oxide clusters. It is well known that introducing a second type of transition metal into transition metal surfaces can enhance their catalytic activity towards certain industrially-relevant processes such as CO oxidation and alkane hydrolysis.[132] Therefore, investigating the effects of introducing transition metal heteroatoms on the structure and reactivity of TMO clusters allows for the possibility of tailoring the composition of the TMO cluster to provide improved catalytic activity and provides a tractable way of exploring and designing more efficient TMO catalysts. Despite this, very little is known about the structures and reactivity of bimetallic cluster oxides composed of two different transition metals. With respect to structural investigations, Janssens and co-workers have performed infrared multiple photon dissociation spectroscopy in combination with DFT calculations on various titanium-vanadium oxide cluster anions to investigate how the electronic and geometric structures change by exchanging V atoms with Ti atoms.[133] In addition to this, Jarrold and co-workers have used anion photoelectron spectroscopy and DFT calculations to determine the lowest energy isomers of various neutral and anionic molybdenum-tungsten oxide, molybdenum-vanadium oxide and molybdenum-niobium oxide clusters, thus gaining insight into the effect that mixing W, V, and Nb atoms with Mo atoms has on the electronic and geometric properties of these clusters relative to their monometallic oxide counterparts.[134-136] DFT calculations have also been performed by Wang and co-workers aimed at investigating the structural and magnetic properties of the $TiVO_m$, $VMnO_m$ and $MnCoO_m$ (m = 3,4) bimetallic clusters, finding that pronounced magnetism is achieved for most of these bimetallic oxide clusters (with the exception of the $MnCoO_3$ cluster) relative to the monometallic oxide species.[137] With respect to reactivity studies, Castleman and co-workers have used DFT calculations to investigate the structure and reactivity of the $ZrNbO_5$ cluster relative to its

isoelectronic counterpart $Zr_2O_5^-$, which itself was found to readily oxidise carbon monoxide, strongly associate acetylene, and weakly associate ethylene.[138] They found that both the structure and reactivity of $ZrNbO_5$ should mimic that of $Zr_2O_5^-$, suggesting that investigations directed towards probing the structure and reactivity of anionic clusters could be used to infer the same properties for their neutral isoelectronic counterparts. In addition to this, Mafuné and co-workers have experimentally investigated the reactivity of cationic gold-titanium oxide clusters with CO, in conjunction with DFT calculations. They found that the reactivity was highest for those clusters consisting of one and three Au atoms bound to titanium oxide clusters possessing the same stoichiometry as bulk-phase titania (i.e. $(TiO_2)_n^+$ (n = 1-22)).[139] Recently, Bernstein and co-workers have used DFT calculations and the single photon ionisation technique coupled with time-of-flight mass spectrometry to also investigate CO reactivity but with various neutral cobalt-vanadium oxide clusters, finding that the $VCoO_4$ cluster displayed pronounced reactivity with CO to generate the $VCoO_3$ cluster and CO_2.[140] Also recently, He and co-workers have performed experimental work and DFT studies directed towards investigating C-H bond activation by cationic vanadium-silver bimetallic oxide clusters towards ethane,[141] and by the $AuNbO_3^+$ cluster towards methane, ethane and *n*-butane.[142] Regarding the former, they found that the reactivity of the various V-Ag oxide clusters towards ethane was greatly influenced by the presence of Ag atoms, with the reactivity decreasing with an increasing number of Ag atoms. Regarding the latter, they found that selective activation of a C-H bond in methane and multiple C-H bonds in ethane and *n*-butane were initiated by a radical oxygen centre in the $AuNbO_3^+$ cluster and promoted by the presence of the Au atom.

Overall, these experimental and theoretical studies clearly show an emerging interest in investigating the structure and reactivity of bimetallic cluster oxides as they provide an exciting new field of study with respect to catalysis.

1.3. Transition-Lanthanide Bimetallic Clusters and Their Oxide Counterparts – A Brief History of Previous Work Performed

Another variety of bimetallic oxide clusters are those composed of transition and lanthanide metal atoms. It has been found that doping TMO catalysts with lanthanide metal atoms can promote catalytic activity in industrial processes (such as the POX process), with greater conversion efficiency and selectivity.[4,143] Therefore, investigating the structure and reactivity of transition-lanthanide bimetallic clusters and their oxide counterparts can potentially provide an efficient and tractable way of helping to develop very efficient and selective catalysts in various industrial processes.

Although a great deal of previous experimental and computational studies have been done on gas-phase lanthanide and lanthanide oxide clusters,[101,144-165] very little work has been done on transition-lanthanide bimetallic clusters and their oxides. Zhang and co-workers have performed DFT investigations on Ni and Ti-doped La_{13} clusters where they found that substituting a La atom with a Ni or Ti atom lowered the binding energy of the cluster as a whole (relative to La_{13}), where Ni preferred to occupy a surface site and Ti preferred to occupy the central site.[166] In addition to this, Liu and co-workers have performed DFT calculations on La_mNi_n ($m+n \leq 7$) bimetallic clusters, reporting the lowest energetic isomers for each respective cluster.[167] In the 1970's, Cocke and Gingerich produced the dimers AgHo, AuHo and CePd in the gas-phase and determined their dissociation energies, standard heats of formation and appearance potentials.[168,169] More recently, Lievens and co-workers have generated gas-phase Au_nEr^+ ($3 \leq n \leq 20$) clusters and performed stability and dissociation pathway analyses on them.[170] They found that Au_6Er^+ and $Au_{16}Er^+$ were exceptionally stable due to them both containing 8 and 18 roaming valence electrons, respectively, which afford closed electronic shell structures for each of these species.[170] However, no specific inferences were made about whether there are geometric changes induced by Er-doping of the Au clusters. With respect to reactivity, Huang and co-workers have investigated the reactivity of the $LaFe^+$ dimer towards alkanes. It was observed that this dimer can

dehydrogenate two ethane molecules sequentially, whereas the separate cationic atoms are either non-reactive towards ethane (Fe^+) or can only dehydrogenate one ethane molecule (La^+).[171] With respect to work performed on the oxides of transition-lanthanide bimetallic clusters, Gibson produced these types of clusters in the gas-phase via the laser ablation of oxalates into vacuum.[172] It was proposed that ZrO_2 and HfO_2 act as coordinating ligands to the basic cluster structure of various lanthanide oxide clusters. These transition-lanthanide oxide clusters were proposed to form cubic structures based on the crystal structures of lanthanide monoxides. However, no computational work was performed to verify the proposed structure for each cluster. In addition to this work, Lievens, Asmis and co-workers have used vibrational predissociation spectroscopy and DFT calculations to investigate the geometric and electronic properties of the rare-gas-tagged $[(CeO_2)(VO_2)_n]^+$ (n=1,2) and $[(Ce_2O_3)(VO_2)]^+$ clusters, finding that the most stable structures had oxidation states of +3 and +5 for Ce and V, respectively, and not an oxidation state of +4 each.[173]

1.4. The Scope of this Thesis

With such little work performed to date, there is clearly still much to be learnt about the structure and reactivity of transition-lanthanide bimetallic clusters and their oxide counterparts. In particular, it would be of significant interest to understand the oxide chemistry of these types of clusters by investigating where the oxygen atoms prefer to bind and how this affects the electronic properties. The focus of the work presented in this thesis is to provide such an understanding by using a combined experimental and theoretical approach to determine the structural and electronic properties of various rhodium-holmium (Rh-Ho) and gold-praseodymium (Au-Pr) bimetallic clusters and their oxide counterparts. Rhodium and gold were chosen as the transition metals since they are catalytically relevant in the cluster regime.[174-191] However, due to the fact that the chemical properties across the lanthanide series are generally thought to be similar,[192] pragmatic reasons were used to select the lanthanide metals. Therefore, holmium and praseodymium were chosen as the lanthanide metals due to them being monoisotopic, thus minimizing complications in the mass spectra.

The clusters are experimentally generated via dual laser ablation and detected using time-of-flight mass spectrometry coupled with threshold laser ionisation. Upon successful formation and detection, the experimental adiabatic ionisation energies (AIEs) of the following clusters are determined using Photoionisation Efficiency (PIE) spectroscopy: $RhHo_2O_n$ (n = 0-2), $Rh_2Ho_2O_m$ (m = 0-2), $AuPr_2O_x$ (x = 0-2), $Au_2Pr_2O_m$ (m = 0-1), $Au_3Pr_2O_n$ (n = 0-2), and Au_2Pr. Chapter Two presents a discussion of the underlying theory and details behind the experimental setup and PIE experiments. Chapters Five and Eight present the PIE spectra and experimental AIEs obtained for the Rh-Ho and Au-Pr clusters, respectively. Overall, the experimental AIEs displayed in Chapters Five and Eight show how the two following trends influence the electronic properties of these clusters: (i) the sequential addition of oxygen atoms onto the base bimetallic cluster within each series, and (ii) the composition of the bimetallic clusters i.e. the transition: lanthanide metal atom ratio within each cluster.

In order to gain more insight into the nature of the observed experimental AIE trends mentioned on the previous page, DFT calculations are performed on the neutral and cationic species of the $RhHo_2O_n$ (n = 0-2), $Rh_2Ho_2O_m$ (m = 0-2) and the $Au_{3-k}Pr_k$ (k = 0-3) clusters. From these, the low-lying neutral and cationic geometries (in addition to other properties such as atomic charges and normal modes of vibration) are determined and subsequently, the theoretical AIEs of each cluster are calculated. In addition to these DFT calculations, Franck-Condon Factor (FCF) calculations are performed in order to simulate the Zero-Electron Kinetic Energy (ZEKE) and PIE spectra for each cluster in the $RhHo_2O_n$ (n = 0-2), $Rh_2Ho_2O_m$ (m = 0-2) and $Au_{3-k}Pr_k$ (k = 0-3) series. This is done in order to: (i) identify the most likely ionisation transition if there are two or more competing candidates for a particular cluster, and (ii) apply energy corrections to the experimental AIEs obtained from the PIE spectra in Chapters Five and Eight in order to account for thermal tailing resulting from vibrational "hot band" transitions at 300 K. Chapter Three presents a discussion of the underlying theory behind ZEKE spectroscopy and DFT calculations in addition to the details behind the computational procedure and the simulated ZEKE and PIE spectra. Chapters Six and Seven present and discuss the results from all the aforementioned theoretical work performed on the $RhHo_2O_n$ (n = 0-2) and $Rh_2Ho_2O_m$ (m = 0-2) clusters, respectively. Chapter Nine presents and discusses the results from the theoretical work performed on the $Au_{3-k}Pr_k$ (k = 0-3) clusters. Overall, comparison between the experimental and theoretical AIE trends as a function of: (i) sequential addition of oxygen atoms in the $RhHo_2O_n$ (n = 0-2) and $Rh_2Ho_2O_m$ (m = 0-2) cluster series, and (ii) substitution of a gold atom for a praseodymium atom in the $Au_{3-k}Pr_k$ (k = 0-3) cluster series ultimately allows for structural and electronic information to be inferred for each of these clusters.

1.5. References

(1) *Metal Oxides: Chemistry and Applications*; CRC Press, Taylor & Francis Group: Boca Raton, 2006.

(2) Zhen, K. J.; Khan, M. M.; Mak, C. H.; Lewis, K. B.; Somorjai, G. A. *J. Catal.* **1985**, *94*, 501.

(3) Khan, M. M.; Somorjai, G. A. *J. Catal.* **1985**, *91*, 263.

(4) Ashcroft, A. T.; Cheetham, A. K.; Foord, J. S.; Green, M. L. H.; Grey, C. P.; Murrell, A. J.; Vernon, P. D. F. *Nature* **1990**, *344*, 319.

(5) *Metal Oxide Catalysis*; Hargreaves, S. D. J. J. S. J., Ed.; Wiley-VCH Verlag GmbH & Co. KGaA: Weinheim, 2009.

(6) Zemski, K. A.; Justes, D. R.; Castleman Jr., A. W. *J. Phys. Chem. B* **2002**, *106*, 6136.

(7) Lang, S. M.; Bernhardt, T. M. *Phys. Chem. Chem. Phys.* **2012**, *14*, 9255.

(8) Justes, D. R.; Mitric, R.; Moore, N. A.; Bonacic-Koutecky, V.; Castleman Jr., A. W. *J. Am. Chem. Soc.* **2003**, *125*, 6289.

(9) Castleman Jr., A. W. *Catal. Lett.* **2011**, *141*, 1243.

(10) Asmis, K. R.; Sauer, J. *Mass Spectrom. Rev.* **2007**, *26*, 542.

(11) Asmis, K. R.; Wende, T.; Brummer, M.; Gause, O.; Santambrogio, G.; Stanca-Kaposta, E. C.; Dobler, J.; Niedziela, A.; Sauer, J. *Phys. Chem. Chem. Phys.* **2012**, *14*, 9377.

(12) Bell, R. C.; Castleman Jr., A. W. *J. Phys. Chem. A* **2002**, *106*, 9893.

(13) Bell, R. C.; Zemski, K. A.; Castleman Jr., A. W. *J. Phys. Chem. A* **1998**, *102*, 8293.

(14) Bell, R. C.; Zemski, K. A.; Justes, D. R.; Castleman Jr., A. W. *J. Chem. Phys.* **2001**, *114*, 798.

(15) Bell, R. C.; Zemski, K. A.; Kerns, K. P.; Deng, H. T.; Castleman Jr., A. W. *J. Phys. Chem. A* **1998**, *102*, 1733.

(16) Blumling, D. E.; Sayres, S. G.; Castleman Jr., A. W. *Int. J. Mass spectrom.* **2011**, *300*, 74.

(17) Brites, V.; Franzreb, K.; Harvey, J. N.; Sayres, S. G.; Ross, M. W.; Blumling, D. E.; Castleman Jr., A. W.; Hochlaf, M. *Phys. Chem. Chem. Phys.* **2011**, *13*, 15233.

(18) Cassady, C. J.; Mcelvany, S. W. *Organometallics* **1992**, *11*, 2367.

(19) Cassady, C. J.; Weil, D. A.; Mcelvany, S. W. *J. Chem. Phys.* **1992**, *96*, 691.

(20) Chen, W. J.; Zhai, H. J.; Huang, X.; Wang, L. S. *Chem. Phys. Lett.* **2011**, *512*, 49.

(21) Chen, W. J.; Zhai, H. J.; Zhang, Y. F.; Huang, X.; Wang, L. S. *J. Phys. Chem. A* **2010**, *114*, 5958.

(22) Da Silva, J. L. F.; Ganduglia-Pirovano, M. V.; Sauer, J. *Phys. Rev. B* **2007**, *76*.

(23) Dibble, C. J.; Akin, S. T.; Ard, S.; Fowler, C. P.; Duncan, M. A. *J. Phys. Chem. A* **2012**, *116*, 5398.

(24) Dinca, A.; Davis, T. P.; Fisher, K. J.; Smith, D. R.; Willett, G. D. *Int. J. Mass Spec.* **1999**, *182*, 73.
(25) Ding, X. L.; Xue, W.; Ma, Y. P.; Wang, Z. C.; He, S. G. *J. Chem. Phys.* **2009**, *130*.
(26) Dong, F.; Heinbuch, S.; He, S. G.; Xie, Y.; Rocca, J. J.; Bernstein, E. R. *J. Chem. Phys.* **2006**, *125*.
(27) Dong, F.; Heinbuch, S.; Xie, Y.; Rocca, J. J.; Bernstein, E. R.; Wang, Z. C.; Deng, K.; He, S. G. *J. Am. Chem. Soc.* **2008**, *130*, 1932.
(28) Engeser, M.; Schlangen, M.; Schroder, D.; Schwarz, H.; Yumura, T.; Yoshizawa, K. *Organometallics* **2003**, *22*, 3933.
(29) Engeser, M.; Weiske, T.; Schroder, D.; Schwarz, H. *J. Phys. Chem. A* **2003**, *107*, 2855.
(30) Feyel, S.; Dobler, J.; Schroder, D.; Sauer, J.; Schwarz, H. *Angew. Chem. Int. Ed.* **2006**, *45*, 4681.
(31) Feyel, S.; Schroder, D.; Rozanska, X.; Sauer, J.; Schwarz, H. *Angew. Chem. Int. Ed.* **2006**, *45*, 4677.
(32) Feyel, S.; Schroder, D.; Schwarz, H. *J. Phys. Chem. A* **2006**, *110*, 2647.
(33) Feyel, S.; Schwarz, H.; Schroder, D.; Daniel, C.; Hartl, H.; Dobler, J.; Sauer, J.; Santambrogio, G.; Woste, L.; Asmis, K. R. *Chemphyschem* **2007**, *8*, 1640.
(34) Feyel, S.; Waters, T.; O'Hair, R. A. J.; Wedd, A. G. *Dalton Trans.* **2004**, 4010.
(35) Fialko, E. F.; Kikhtenko, A. V.; Goncharov, V. B. *Organometallics* **1998**, *17*, 25.
(36) Fialko, E. F.; Kikhtenko, A. V.; Goncharov, V. B.; Zamaraev, K. I. *J. Phys. Chem. A* **1997**, *101*, 8607.
(37) Fialko, E. F.; Kikhtenko, A. V.; Goncharov, V. B.; Zamaraev, K. I. *J. Phys. Chem. B* **1997**, *101*, 5772.
(38) Fielicke, A.; Gruene, P.; Haertelt, M.; Harding, D. J.; Meijer, G. *J. Phys. Chem. A* **2010**, *114*, 9755.
(39) Fielicke, A.; Meijer, G.; von Helden, G. *Eur. Phys. J. D* **2003**, *24*, 69.
(40) Fielicke, A.; Meijer, G.; von Helden, G. *J. Am. Chem. Soc.* **2003**, *125*, 3659.
(41) Fielicke, A.; Rademann, K. *Phys. Chem. Chem. Phys.* **2002**, *4*, 2621.
(42) Fu, G.; Xu, X.; Lu, X.; Wan, H. L. *J. Phys. Chem. B* **2005**, *109*, 6416.
(43) Fu, G.; Xu, X.; Lu, X.; Wan, H. L. *J. Am. Chem. Soc.* **2005**, *127*, 3989.
(44) Fu, G.; Xu, X.; Wan, H. L. *Catal. Today* **2006**, *117*, 133.
(45) Gutsev, G. L.; Bauschlicher, C. W.; Zhai, H. J.; Wang, L. S. *J. Chem. Phys.* **2003**, *119*, 11135.
(46) Gutsev, G. L.; Jena, P.; Zhai, H. J.; Wang, L. S. *J. Chem. Phys.* **2001**, *115*, 7935.
(47) Harris, B. L.; Waters, T.; Khairallah, G. N.; O'Hair, R. A. J. *J. Phys. Chem. A* **2013**, *117*, 1124.

(48) He, S. G.; Xie, Y.; Dong, F.; Heinbuch, S.; Jakubikova, E.; Rocca, J. J.; Bernstein, E. R. *J. Phys. Chem. A* **2008**, *112*, 11067.
(49) Hermes, A. C.; Hamilton, S. M.; Cooper, G. A.; Kerpal, C.; Harding, D. J.; Meijer, G.; Fielicke, A.; Mackenzie, S. R. *Faraday Discuss.* **2012**, *157*, 213.
(50) Huang, X.; Zhai, H. J.; Li, J.; Wang, L. S. *J. Phys. Chem. A* **2006**, *110*, 85.
(51) Huang, X.; Zhai, H. J.; Waters, T.; Li, J.; Wang, L. S. *Angew Chem Int Edit* **2006**, *45*, 657.
(52) Jakubikova, E.; He, S. G.; Xie, Y.; Matsuda, Y.; Bernstein, E. R. *Abstr Pap Am Chem S* **2007**, *233*, 81.
(53) Jia, M. Y.; Xu, B.; Ding, X. L.; He, S. G.; Ge, M. F. *J Phys Chem C* **2012**, *116*, 24184.
(54) Jia, M. Y.; Xu, B.; Ding, X. L.; Zhao, Y. X.; He, S. G.; Ge, M. F. *J. Phys. Chem. C* **2012**, *116*, 9043.
(55) Johnson, G. E.; Reveles, J. U.; Reilly, N. M.; Tyo, E. C.; Khanna, S. N.; Castleman Jr., A. W. *J. Phys. Chem. A* **2008**, *112*, 11330.
(56) Justes, D. R.; Castleman Jr., A. W.; Mitric, R.; Bonacic-Koutecky, V. *Eur. Phys. J. D* **2003**, *24*, 331.
(57) Justes, D. R.; Moore, N. A.; Castleman Jr., A. W. *J. Phys. Chem. B* **2004**, *108*, 3855.
(58) Kerpal, C.; Harding, D. J.; Hermes, A. C.; Meijer, G.; Mackenzie, S. R.; Fielicke, A. *J. Phys. Chem. A* **2013**, *117*, 1233.
(59) Kimble, M. L.; Castleman Jr., A. W. *Int. J. Mass spectrom.* **2004**, *233*, 99.
(60) Kimble, M. L.; Castleman Jr., A. W.; Burgel, C.; Bonacic-Koutecky, V. *Int. J. Mass Spec.* **2006**, *254*, 163.
(61) Kimble, M. L.; Moore, N. A.; Johnson, G. E.; Castleman Jr., A. W.; Burgel, C.; Mitric, R.; Bonacic-Koutecky, V. *J. Chem. Phys.* **2006**, *125*.
(62) Kirilyuk, A.; Fielicke, A.; Demyk, K.; von Helden, G.; Meijer, G.; Rasing, T. *Phys. Rev. B* **2010**, *82*.
(63) Knight, A. M.; Bandyopadhyay, B.; Anfuso, C. L.; Molek, K. S.; Duncan, M. A. *Int. J. Mass Spec.* **2011**, *304*, 29.
(64) Lang, S. M.; Fleischer, I.; Bernhardt, T. M.; Barnett, R. N.; Landman, U. *J. Am. Chem. Soc.* **2012**, *134*, 20654.
(65) Lang, S. M.; Fleischer, I.; Bernhardt, T. M.; Barnett, R. N.; Landman, U. *Nano Lett.* **2013**, *13*, 5549.
(66) Lang, S. M.; Frank, A.; Bernhardt, T. M. *J. Phys. Chem. C* **2013**, *117*, 9791.
(67) Lang, S. M.; Schnabel, T.; Bernhardt, T. M. *Phys. Chem. Chem. Phys.* **2012**, *14*, 9364.
(68) Li, S. G.; Zhai, H. J.; Wang, L. S.; Dixon, D. A. *J. Phys. Chem. A* **2009**, *113*, 11273.
(69) Li, S. G.; Zhai, H. J.; Wang, L. S.; Dixon, D. A. *J. Phys. Chem. A* **2012**, *116*, 5256.

(70) Ma, J. B.; Wang, Z. C.; Schlangen, M.; He, S. G.; Schwarz, H. *Angew. Chem. Int. Ed.* **2013**, *52*, 1226.
(71) Ma, J. B.; Wu, X. N.; Zhao, X. X.; Ding, X. L.; He, S. G. *Phys. Chem. Chem. Phys.* **2010**, *12*, 12223.
(72) Ma, J. B.; Wu, X. N.; Zhao, Y. X.; Ding, X. L.; He, S. G. *J. Phys. Chem. A* **2010**, *114*, 10024.
(73) Ma, J. B.; Wu, X. N.; Zhao, Y. X.; Ding, X. L.; He, S. G. *Chinese J. Chem. Phys.* **2010**, *23*, 133.
(74) Ma, J. B.; Wu, X. N.; Zhao, Y. X.; He, S. G.; Ding, X. L. *Acta Phys-Chim Sin* **2010**, *26*, 1761.
(75) Ma, J. B.; Zhao, Y. X.; He, S. G.; Ding, X. L. *J. Phys. Chem. A* **2012**, *116*, 2049.
(76) Ma, Y. P.; Ding, X. L.; Zhao, Y. X.; He, S. G. *Chemphyschem* **2010**, *11*, 1718.
(77) Ma, Y. P.; Xue, W.; Wang, Z. C.; Ge, M. F.; He, S. G. *J. Phys. Chem. A* **2008**, *112*, 3731.
(78) Ma, Y. P.; Zhao, Y. X.; Li, Z. Y.; Ding, X. L.; He, S. G. *Chinese J. Chem. Phys.* **2011**, *24*, 586.
(79) Molek, K. S.; Anfuso-Cleary, C.; Duncan, M. A. *J. Phys. Chem. A* **2008**, *112*, 9238.
(80) Molek, K. S.; Jaeger, T. D.; Duncan, M. A. *J. Chem. Phys.* **2005**, *123*.
(81) Molek, K. S.; Reed, Z. D.; Ricks, A. M.; Duncan, M. A. *J. Phys. Chem. A* **2007**, *111*, 8080.
(82) Moore, N. A.; Mitric, R.; Justes, D. R.; Bonacic-Koutecky, V.; Castleman Jr., A. W. *J. Phys. Chem. B* **2006**, *110*, 3015.
(83) Pykavy, M.; van Wullen, C.; Sauer, J. *J. Chem. Phys.* **2004**, *120*, 4207.
(84) Reber, A. C.; Khanna, S. N.; Tyo, E. C.; Harmon, C. L.; Castleman Jr., A. W. *J. Chem. Phys.* **2011**, *135*.
(85) Reilly, N. M.; Reveles, J. U.; Johnson, G. E.; del Campo, J. M.; Khanna, S. N.; Koster, A. M.; Castleman Jr., A. W. *J Phys Chem C* **2007**, *111*, 19086.
(86) Reilly, N. M.; Reveles, J. U.; Johnson, G. E.; Khanna, S. N.; Castleman Jr., A. W. *J. Phys. Chem. A* **2007**, *111*, 4158.
(87) Reilly, N. M.; Reveles, J. U.; Johnson, G. E.; Khanna, S. N.; Castleman Jr., A. W. *Chem. Phys. Lett.* **2007**, *435*, 295.
(88) Reveles, J. U.; Johnson, G. E.; Khanna, S. N.; Castleman Jr., A. W. *J. Phys. Chem. C* **2010**, *114*, 5438.
(89) Romanyshyn, Y.; Guimond, S.; Kuhlenbeck, H.; Kaya, S.; Blum, R. P.; Niehus, H.; Shaikhutdinov, S.; Simic-Milosevic, V.; Nilius, N.; Freund, H. J.; Ganduglia-Pirovano, M. V.; Fortrie, R.; Dobler, J.; Sauer, J. *Top. Catal.* **2008**, *50*, 106.
(90) Ross, M. W.; Castleman Jr., A. W. *J. Phys. Chem. A* **2013**, *117*, 1030.
(91) Sayres, S. G.; Ross, M. W.; Castleman Jr., A. W. *J. Chem. Phys.* **2011**, *135*.

(92) Tyo, E. C.; Nossler, M.; Harmon, C. L.; Mitric, R.; Bonacic-Koutecky, V.; Castleman Jr., A. W. *J. Phys. Chem. C* **2011**, *115*, 21559.
(93) Tyo, E. C.; Nossler, M.; Mitric, R.; Bonacic-Koutecky, V.; Castleman Jr., A. W. *Phys. Chem. Chem. Phys.* **2011**, *13*, 4243.
(94) Vann, W. D.; Wagner, R. L.; Castleman Jr., A. W. *J. Phys. Chem. A* **1998**, *102*, 8804.
(95) Vann, W. D.; Wagner, R. L.; Castleman Jr., A. W. *J. Phys. Chem. A* **1998**, *102*, 1708.
(96) Vyboishchikov, S. F.; Sauer, J. *J. Phys. Chem. A* **2000**, *104*, 10913.
(97) Vyboishchikov, S. F.; Sauer, J. *J. Phys. Chem. A* **2001**, *105*, 8588.
(98) Wang, W. G.; Wang, Z. C.; Yin, S.; He, S. G.; Ge, M. F. *Chinese J. Chem. Phys.* **2007**, *20*, 412.
(99) Wang, Z. C.; Ding, X. L.; Ma, Y. P.; Cao, H.; Wu, X. N.; Zhao, Y. X.; He, S. G. *Chin. Sci. Bull.* **2009**, *54*, 2814.
(100) Waters, T.; Wedd, A. G.; O'Hair, R. A. J. *Chem. -Eur. J.* **2007**, *13*, 8818.
(101) Xu, B.; Zhao, Y. X.; Ding, X. L.; He, S. G. *Int. J. Mass Spec.* **2013**, *334*, 1.
(102) Xu, B.; Zhao, Y. X.; Ding, X. L.; Liu, Q. Y.; He, S. G. *J. Phys. Chem. A* **2013**, *117*, 2961.
(103) Xue, W.; Wang, Z. C.; He, S. G.; Xie, Y.; Bernstein, E. R. *J. Am. Chem. Soc.* **2008**, *130*, 15879.
(104) Xue, W.; Yin, S.; Ding, X. L.; He, S. G.; Ge, M. F. *J. Phys. Chem. A* **2009**, *113*, 5302.
(105) Yang, X.; Waters, T.; Wang, X. B.; O'Hair, R. A. J.; Wedd, A. G.; Li, J.; Dixon, D. A.; Wang, L. S. *J. Phys. Chem. A* **2004**, *108*, 10089.
(106) Yin, S.; He, S. G.; Ge, M. F. *Chin. Sci. Bull.* **2009**, *54*, 4017.
(107) Yin, S.; Ma, Y. P.; Du, L.; He, S. G.; Ge, M. F. *Chin. Sci. Bull.* **2008**, *53*, 3829.
(108) Yin, S.; Xue, W.; Ding, X. L.; Wang, W. G.; He, S. G.; Ge, M. F. *Int. J. Mass Spec.* **2009**, *281*, 72.
(109) Yuan, Z.; Zhao, Y. X.; Li, X. N.; He, S. G. *Int. J. Mass spectrom.* **2013**, *354*, 105.
(110) Zemski, K. A.; Bell, R. C.; Justes, D. R.; Castleman Jr., A. W. *Nobel Symp.* **2001**, *117*, 290.
(111) Zemski, K. A.; Justes, D. R.; Bell, R. C.; Castleman Jr., A. W. *J. Phys. Chem. A* **2001**, *105*, 4410.
(112) Zemski, K. A.; Justes, D. R.; Castleman Jr., A. W. *J. Phys. Chem. A* **2001**, *105*, 10237.
(113) Zhai, H. J.; Chen, W. J.; Lin, S. J.; Huang, X.; Wang, L. S. *J. Phys. Chem. A* **2013**, *117*, 1042.
(114) Zhai, H. J.; Dobler, J.; Sauer, J.; Wang, L. S. *J. Am. Chem. Soc.* **2007**, *129*, 13270.

(115) Zhai, H. J.; Huang, X.; Cui, L. F.; Li, X.; Li, J.; Wang, L. S. *J. Phys. Chem. A* **2005**, *109*, 6019.
(116) Zhai, H. J.; Kiran, B.; Cui, L. F.; Li, X.; Dixon, D. A.; Wang, L. S. *J. Am. Chem. Soc.* **2004**, *126*, 16134.
(117) Zhai, H. J.; Li, S.; Dixon, D. A.; Wang, L. S. *J. Am. Chem. Soc.* **2008**, *130*, 5167.
(118) Zhai, H. J.; Wang, B.; Huang, X.; Wang, L. S. *J. Phys. Chem. A* **2009**, *113*, 9804.
(119) Zhai, H. J.; Wang, B.; Huang, X.; Wang, L. S. *J. Phys. Chem. A* **2009**, *113*, 3866.
(120) Zhai, H. J.; Wang, L. S. *J. Chem. Phys.* **2002**, *117*, 7882.
(121) Zhai, H. J.; Wang, L. S. *J. Chem. Phys.* **2006**, *125*.
(122) Zhai, H. J.; Zhang, X. H.; Chen, W. J.; Huang, X.; Wang, L. S. *J. Am. Chem. Soc.* **2011**, *133*, 3085.
(123) Zhao, Y. X.; Yuan, J. Y.; Ding, X. L.; He, S. G.; Zheng, W. J. *Phys. Chem. Chem. Phys.* **2011**, *13*, 10084.
(124) Hossain, E.; Rothgeb, D. W.; Jarrold, C. C. *J. Chem. Phys.* **2010**, *133*.
(125) Mann, J. E.; Waller, S. E.; Rothgeb, D. W.; Jarrold, C. C. *J. Chem. Phys.* **2011**, *135*.
(126) Mann, J. E.; Waller, S. E.; Rothgeb, D. W.; Jarrold, C. C. *Chem. Phys. Lett.* **2011**, *506*, 31.
(127) Mayhall, N. J.; Rothgeb, D. W.; Hossain, E.; Jarrold, C. C.; Raghavachari, K. *J. Chem. Phys.* **2009**, *131*.
(128) Rothgeb, D. W.; Hossain, E.; Kuo, A. T.; Troyer, J. L.; Jarrold, C. C.; Mayhall, N. J.; Raghavachari, K. *J. Chem. Phys.* **2009**, *130*.
(129) Wyrwas, R. B.; Robertson, E. M.; Jarrold, C. C. *J. Chem. Phys.* **2007**, *126*.
(130) Wyrwas, R. B.; Yoder, B. L.; Maze, J. T.; Jarrold, C. C. *J. Phys. Chem. A* **2006**, *110*, 2157.
(131) Yoder, B. L.; Maze, J. T.; Raghavachari, K.; Jarrold, C. C. *J. Chem. Phys.* **2005**, *122*.
(132) Rodriguez, J. A. *Surf. Sci. Rep.* **1996**, *24*, 225.
(133) Janssens, E.; Santambrogio, G.; Brummer, M.; Wöste, L.; Lievens, P.; Sauer, J.; Meijer, G.; Asmis, K. R. *Phys. Rev. Lett.* **2006**, *96*.
(134) Waller, S. E.; Mann, J. E.; Rothgeb, D. W.; Jarrold, C. C. *J. Phys. Chem. A* **2012**, *116*, 9639.
(135) Mann, J. E.; Rothgeb, D. W.; Waller, S. E.; Jarrold, C. C. *J. Phys. Chem. A* **2010**, *114*, 11312.
(136) Mayhall, N. J.; Rothgeb, D. W.; Hossain, E.; Raghavachari, K.; Jarrold, C. C. *J. Chem. Phys.* **2009**, *130*.
(137) Wang, Y. B.; Yang, M. L.; Wang, J. L. *J .Mol. Struc. (THEOCHEM)* **2010**, *953*, 55.

(138) Nossler, M.; Mitric, R.; Bonacic-Koutecky, V.; Johnson, G. E.; Tyo, E. C.; Castleman Jr., A. W. *Angew. Chem. Int. Ed.* **2010**, *49*, 407.
(139) Himeno, H.; Miyajima, K.; Yasuike, T.; Mafune, F. *J. Phys. Chem. A* **2011**, *115*, 11479.
(140) Wang, Z. C.; Yin, S.; Bernstein, E. R. *J. Phys. Chem. Lett.* **2012**, *3*, 2415.
(141) Li, X. N.; Wu, X. N.; Ding, X. L.; Xu, B.; He, S. G. *Chem -Eur. J.* **2012**, *18*, 10998.
(142) Wu, X. N.; Li, X. N.; Ding, X. L.; He, S. G. *Angew Chem. Int. Ed.* **2013**, *52*, 2444.
(143) Slagtern, Å.; Olsbye, U. *Appl. Catal., A* **1994**, *110*, 99.
(144) Koretsky, G. M.; Knickelbein, M. B. *Eur. Phys. J. D* **1998**, *2*, 273.
(145) Reed, Z. A.; Duncan, M. A. *J. Phys. Chem. A* **2008**, *112*, 5354.
(146) Suzumura, J.; Hosoya, N.; Nagao, S.; Mitsui, M.; Nakajima, A. *J. Chem. Phys.* **2004**, *121*, 2649.
(147) Kurikawa, T.; Negishi, Y.; Hayakawa, F.; Nagao, S.; Miyajima, K.; Nakajima, A.; Kaya, K. *Eur. Phys. J. D* **1999**, *9*, 283.
(148) Nagao, S.; Negishi, Y.; Kato, A.; Nakamura, Y.; Nakajima, A.; Kaya, K. *J. Phys. Chem. A* **1999**, *103*, 8909.
(149) Nagao, S.; Negishi, Y.; Kato, A.; Nakamura, Y.; Nakajima, A.; Kaya, K. *J. Chem. Phys.* **2002**, *117*, 3169.
(150) Durakiewicz, T.; Halas, S. *Chem. Phys. Lett.* **2001**, *341*, 195.
(151) Luo, Y. H.; Wang, Y. Z. *Phys. Rev. A* **2001**, *64*.
(152) Wu, Z. J.; Guan, W.; Meng, J.; Su, Z. M. *J. Cluster Sci.* **2007**, *18*, 444.
(153) Wu, Z. J.; Shi, J. S.; Zhang, S. Y.; Zhang, H. J. *Phys. Rev. A* **2004**, *69*, 064502.
(154) Zhang, D. B.; Shen, J. *J. Chem. Phys.* **2004**, *120*, 5104.
(155) Bowlan, J.; Harding, D. J.; Jalink, J.; Kirilyuk, A.; Meijer, G.; Fielicke, A. *J. Chem. Phys.* **2013**, *138*.
(156) Da Silva, J. L. F.; Ganduglia-Pirovano, M. V.; Sauer, J.; Bayer, V.; Kresse, G. *Phys. Rev. B* **2007**, *75*.
(157) Ding, X. L.; Li, Z. Y.; Meng, J. H.; Zhao, Y. X.; He, S. G. *J. Chem. Phys.* **2012**, *137*.
(158) Ding, X. L.; Wu, X. N.; Zhao, Y. X.; Ma, J. B.; He, S. G. *Chemphyschem* **2011**, *12*, 2110.
(159) Meng, J. H.; Zhao, Y. X.; He, S. G. *J. Phys. Chem. C* **2013**, *117*, 17548.
(160) Ross, M. W.; Castleman Jr., A. W. *Chem. Phys. Lett.* **2013**, *565*, 22.
(161) Wu, L.; Liu, Y.; Zhang, C. H.; Li, S. G.; Dixon, D. A.; Yang, D. S. *J. Chem. Phys.* **2012**, *137*.
(162) Wu, L.; Zhang, C. H.; Krasnokutski, S. A.; Yang, D. S. *J. Chem. Phys.* **2012**, *137*.
(163) Wu, X. N.; Ding, X. L.; Bai, S. M.; Xu, B.; He, S. G.; Shi, Q. *J. Phys. Chem. C* **2011**, *115*, 13329.

(164) Wu, X. N.; Zhao, Y. X.; Xue, W.; Wang, Z. C.; He, S. G.; Ding, X. L. *Phys. Chem. Chem. Phys.* **2010**, *12*, 3984.
(165) Xu, B.; Zhao, Y. X.; Li, X. N.; Ding, X. L.; He, S. G. *J. Phys. Chem. A* **2011**, *115*, 10245.
(166) Zhang, D. B.; Shen, J.; Chen, N. X. *J. Chem. Phys.* **2005**, *123*, 154213.
(167) Liu, N.; Ma, Q. M.; Xie, Z.; Liu, Y.; Li, Y. C. *Chem. Phys. Lett.* **2007**, *436*, 184.
(168) Cocke, D. L.; Gingerich, K. A. *J. Phys. Chem.* **1971**, *75*, 3264.
(169) Cocke, D. L.; Gingerich, K. A. *J. Phys. Chem.* **1972**, *76*, 2332.
(170) Veldeman, N.; Janssens, E.; Hansen, K.; De Haeck, J.; Silverans, R. E.; Lievens, P. *Faraday Discuss.* **2008**, *138*, 147.
(171) Huang, Y. Q.; Freiser, B. S. *J. Am. Chem. Soc.* **1988**, *110*, 387.
(172) Gibson, J. K. *J. Phys. Chem.* **1996**, *100*, 507.
(173) Jiang, L.; Wende, T.; Claes, P.; Bhattacharyya, S.; Sierka, M.; Meijer, G.; Lievens, P.; Sauer, J.; Asmis, K. R. *J. Phys. Chem. A* **2011**, *115*, 11187.
(174) Parry, I. S.; Kartouzian, A.; Hamilton, S. M.; Balaj, O. P.; Beyer, M. K.; Mackenzie, S. R. *J. Phys. Chem. A* **2013**, *117*, 8855.
(175) Hamilton, S. M.; Hopkins, W. S.; Harding, D. J.; Walsh, T. R.; Gruene, P.; Haertelt, M.; Fielicke, A.; Meijer, G.; Mackenzie, S. R. *J. Am. Chem. Soc.* **2010**, *132*, 1448.
(176) Hamilton, S. M.; Hopkins, W. S.; Harding, D. J.; Walsh, T. R.; Haertelt, M.; Kerpal, C.; Gruene, P.; Meijer, G.; Fielicke, A.; Mackenzie, S. R. *J. Phys. Chem. A* **2011**, *115*, 2489.
(177) Hermes, A. C.; Hamilton, S. M.; Hopkins, W. S.; Harding, D. J.; Kerpal, C.; Meijer, G.; Fielicke, A.; Mackenzie, S. R. *J. Phys. Chem. Lett.* **2011**, *2*, 3053.
(178) Fukuoka, A.; Rao, L.-F.; Kosugi, N.; Kuroda, H.; Ichikawa, M. *Applied Catalysis* **1989**, *50*, 295.
(179) Wesendrup, R.; Schwarz, H. *Organometallics* **1997**, *16*, 461.
(180) Weber, W. A.; Gates, B. C. *J. Catal.* **1998**, *180*, 207.
(181) Argo, A. M.; Gates, B. C. *J. Phys. Chem. B* **2003**, *107*, 5519.
(182) Ishikawa, A.; Iglesia, E. *J. Catal.* **2007**, *252*, 49.
(183) Gilb, S.; Arenz, M.; Heiz, U. *Low Temperature Physics* **2006**, *32*, 1097.
(184) Hagen, J.; Socaciu, L. D.; Elijazyfer, M.; Heiz, U.; Bernhardt, T. M.; Woste, L. *Phys. Chem. Chem. Phys.* **2002**, *4*, 1707.
(185) Socaciu, L. D.; Hagen, J.; Bernhardt, T. M.; Woste, L.; Heiz, U.; Hakkinen, H.; Landman, U. *J. Am. Chem. Soc.* **2003**, *125*, 10437.
(186) Yoon, B.; Hakkinen, H.; Landman, U.; Worz, A. S.; Antonietti, J. M.; Abbet, S.; Judai, K.; Heiz, U. *Science* **2005**, *307*, 403.
(187) Landman, U.; Yoon, B.; Zhang, C.; Heiz, U.; Arenz, M. *Top. Catal.* **2007**, *44*, 145.

(188) Turner, M.; Golovko, V. B.; Vaughan, O. P. H.; Abdulkin, P.; Berenguer-Murcia, A.; Tikhov, M. S.; Johnson, B. F. G.; Lambert, R. M. *Nature* **2008**, *454*, 981.

(189) Tsunoyama, H.; Liu, Y. M.; Akita, T.; Ichikuni, N.; Sakurai, H.; Xie, S. H.; Tsukuda, T. *Catal. Surv. Asia* **2011**, *15*, 230.

(190) Liu, Y. M.; Tsunoyama, H.; Akita, T.; Xie, S. H.; Tsukuda, T. *ACS Catal.* **2011**, *1*, 2.

(191) Corma, A.; Concepcion, P.; Boronat, M.; Sabater, M. J.; Navas, J.; Yacaman, M. J.; Larios, E.; Posadas, A.; Lopez-Quintela, M. A.; Buceta, D.; Mendoza, E.; Guilera, G.; Mayoral, A. *Nat. Chem* **2013**, *5*, 775.

(192) Shriver, D. F.; Atkins, P. W.; Overton, T. L.; Rourke, J. P.; Weller, M. T.; Armstrong, F. A. *Inorganic Chemistry*; Fourth ed.; Oxford University Press: Oxford, 2006.

Chapter Two

Experimental Theory, Techniques and Apparatus

This chapter presents information on the experimental techniques and apparatus utilised to generate, detect and determine the adiabatic ionisation energies (IEs) of the gas-phase Rh-Ho and Au-Pr clusters and their oxide counterparts. The underlying theory behind the techniques and design of the apparatus will also be discussed. Firstly, a general introduction into metal cluster sources will be discussed followed by the presentation of, and discussion on, the design of the dual ablation source used to generate the aforementioned clusters in the gas-phase. Next, the general theory behind time-of-flight mass spectrometry (TOF-MS) will be discussed followed by how it is used collectively with the dual laser ablation source to generate and detect the clusters in the gas-phase. Lastly, the underlying spectroscopic theory behind the photoionisation process and photoionisation efficiency (PIE) spectroscopy will be discussed followed by the procedural details describing how the PIE experiments were performed on the Rh-Ho and Au-Pr clusters and their oxide counterparts. A discussion on how the PIE spectra were generated and experimental adiabatic IEs obtained from them will be presented at the end of this chapter.

2.1. Laser Ablation and Metal Cluster Sources

2.1.1. Metal Cluster Sources

In early cluster chemistry, small gas-phase metal clusters were produced by heating up a source chamber (containing the metal of interest) to a temperature higher than the boiling point of the metal. This method was very effective in producing small gas-phase metal clusters but was often limited to the boiling point of the metal and the limited extent to which the internal degrees of freedom were cooled.

In 1981, Smalley *et al.* developed a relatively simple laser vaporisation method of producing cold, highly concentrated molecular beams of small gas-phase metal clusters.[1] In their experimental setup, the 2nd harmonic (532nm) from a Nd:YAG laser is focussed onto a target metal rod which creates a hot, highly concentrated plasma containing neutral, anionic and cationic species. This process is called laser ablation and after it has occurred, the resulting metal vapour which is formed in the ablation process is supersonically expanded whilst entrained in a high density pulse of inert carrier gas from a pulsed supersonic nozzle. The supersonic expansion of the various types of metal cluster species cools them down to low temperatures. The development of this method was a great advance in metal cluster chemistry as it could be used to generate most types of metal cluster compounds in the gas-phase and ensured that only the lowest rotational, vibrational and electronic states of the clusters were occupied due to low temperatures caused by the supersonic expansion. This is of great importance to the spectroscopy of gas-phase metal clusters as the lowest states need to be occupied in order to be spectroscopically probed with minimal complications. It is for these various reasons that any experiments involving the formation and reactivity of any gas-phase metal clusters include a design that in some way mimics that of the Smalley-type laser ablation source. However, as the number of these studies are too numerous to list concisely, only those pertinent to development of the laser ablation source used to produce the Rh-Ho and Au-Pr clusters and their oxide counterparts will be discussed in this thesis.

2.1.2. Generation of Gas-Phase Transition-Lanthanide Bimetallic Clusters and their Oxide Counterparts

In 1983, Bondybey *et al.* implemented a Smalley-type laser ablation source in order to investigate the electronic structure and spectra of the bimetallic diatomic molecules CuGa, CuIn and SnBi.[2,3] In their design, the pertinent molecules of interest were generated via the laser ablation of metal alloy rods. However, the major disadvantages involving this procedure are: i) being limited to generating bimetallic clusters with certain metal-to-metal ratios by the percentage composition of the alloy rods, and ii) the complexity and high costs associated with alloying various metals. In order to surmount these disadvantages, Kaya et al. implemented an alternative design to generate bimetallic clusters in the gas-phase.[4] Their design involved laser ablating two individual metal rods (with two individual Nd:YAG lasers) separated by 5 mm and entraining the resulting metal vapours together in the same high density pulse of inert (He) carrier gas prior to supersonic expansion. Producing gas-phase bimetallic clusters via this dual ablation source design proved to be more advantageous than ablating metal alloy rods as the relative composition of bimetallic clusters could be controlled by adjusting the relative ablation-timing of each metal rod with time-delay instruments, and/or the individual laser fluences used to ablate each rod. Additionally, this dual ablation source design also allows (in principle) any type of gas-phase bimetallic cluster to be generated by placing the desired metals into the source without the cost and effort of alloying the two metals in randomly chosen percentage ratios depending on the metal-to-metal composition ratios desired in the bimetallic clusters of interest.

The various gas-phase Rh-Ho and Au-Pr clusters and their oxides counterparts presented and discussed in this thesis were generated using a dual laser ablation source similar in design to that developed by Kaya *et al.* to generate gas-phase bimetallic clusters (and investigate their reactivity with small molecules).[4] Figure 2.1 shows a cross-sectional depiction of two slightly different dual laser ablation sources used to generate the Rh-Ho (Figure 2.1(a)) and Au-Pr (Figure 2.1(b)) clusters and their oxide

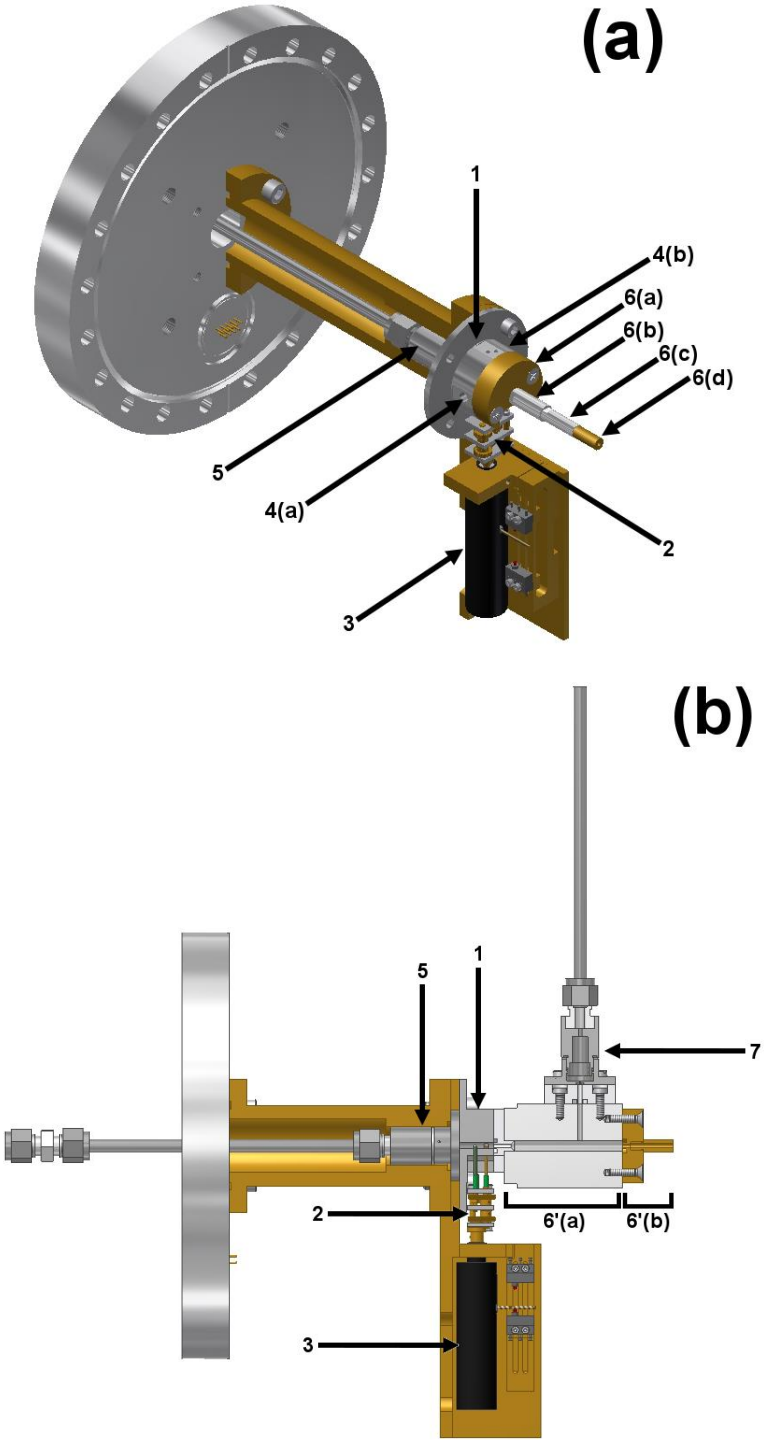

Figure 2.1. *(a) The dual laser ablation source used to generate the Au-Pr clusters and their oxide counterparts, and (b) A side-on, cross-sectional view of the dual laser ablation source used to generate the Rh-Ho clusters and their oxide counterparts. Refer to the text in Section 2.1.2 for the components/parts that correspond to each number.* <u>*NOTE:*</u> *Features 4(a) and (b) are not labelled in Figure 2.1(b) due to the side-on view, but are present.*

counterparts in the gas-phase. A general description the ablation source is given below.

As observed in Figures 2.1(a) and (b), the two pertinent metal rods (2 mm in diameter x 25 mm in length) are positioned 5 mm apart inside a stainless-steel ablation cap (**1**) and attached to a gearbox (**2**) that is connected to a screw mechanism (**3**) (Oriel, motor-mike 18014) which induces rotational motion such that the rods rotate in opposite directions relative to each other. In addition to this rotational motion, the screw mechanism also translates the two metal rods up and down along the rotational axis. The steel ablation cap that houses the metal rods also contains two 1 mm diameter holes each located on opposite sides of the cap through which the 2nd harmonic (532nm) output from two separate neodymium-doped yttrium aluminium garnet (Nd:YAG) lasers (Big Sky Laser, ULTRA-CFR) both running at 10 Hz are focussed onto the constantly rotating and translating metal rods using 250 mm focal length lenses (**4(a)** and **4(b)**), thus ablating them. This generates a hot metal vapour containing neutral, anionic and cationic species for which the temperature has been estimated to be as high as 10000 K.[5] The constant rotational and translational motion of metal rods ensures that a fresh surface is continuously ablated. The generation of the hot metal vapour via ablation is timed so that it occurs in the presence of a high density pulse of pure helium carrier gas (CIG gases 99.98%) delivered into a 3 mm diameter ablation channel via a pulsed nozzle (**5**) (General Valve, Series 9, 20 µm) driven by a home-made nozzle driver. As the metal rods readily oxidise before ablation, there are sufficient amounts of metal oxides inherently present to lead to the formation of the oxide cluster counterparts of the Rh-Ho and Au-Pr clusters, thus eliminating the need to seed the helium carrier gas with an oxidising gas (such as O_2 or N_2O). In all experiments, the lanthanide metal rod is positioned closer to the nozzle then the transition metal rod. Typical ablation powers used are 12 mJ pulse^{-1} for the holmium and praseodymium rods (both from DXL, 99.9%) and 2 mJ pulse^{-1} for the rhodium (DXL, 99.9%) and gold (Goodfellow, 99.9%) rods. Optimal signal of the bimetallic

clusters is achieved in both the Rh-Ho and Au-Pr experiments when the transition metal rod is ablated 4 µs after the lanthanide metal rod.

The hot metal vapour generated from the ablation process is entrained in the high density pulse of helium carrier gas and carried down the 3 mm diameter ablation channel and into a 'condensation tube assembly'. It is from this point where the cluster source design used differs significantly between the Rh-Ho and Au-Pr experiments.

The cluster source schematic shown in Figure 2.1(a) is used for the experiments involving the generation of the Au-Pr clusters and their oxide counterparts. In this design, the condensation tube assembly is made up of four sections; the first is 2 mm in diameter and 10 mm in length (**6(a)**), the second tapers out slowly from 2 mm in diameter to 5 mm in diameter and is 20 mm in length (**6(b)**), and the third and fourth are both 2 mm in diameter and 20 mm in length (**6(c)** and **6(d)**). The total length of the condensation tube assembly is 70 mm.

The cluster source schematic shown in Figure 2.1(b) is used for the experiments involving the generation of the Rh-Ho clusters and their oxide counterparts. In this design, the different species formed in the ablation process are carried by the helium into a Fast-Flow Block (FFB)/condensation tube assembly. The assembly is made up of two sections; the first is a stainless-steel FFB which has an internal diameter of 5 mm and a length of 50 mm (**6'(a)**), and the second is a brass condensation tube that has an internal diameter of 2mm and a length of 30 mm (**6'(b)**). The total length of the FFB/condensation tube assembly is 80 mm. The FFB was implemented into the design in order to eventually investigate the reactivities of bimetallic clusters in the gas-phase, where the reactant molecule of interest would be diluted in a mixture of helium gas and delivered into the FFB via a second pulsed nozzle (**7**). However, only preliminary experiments were performed and are not within the scope of this thesis.

In both cluster sources, as the ablated products entrained in the helium carrier gas reach the end of the 3 mm diameter ablation channel and move through either of the condensation tube assemblies, they experience collisional cooling and form various

types and sizes of transition metal clusters by association reactions (e.g. $M_2 + M_3 = M_5$, where M is a transition metal atom). Upon reaching the end of the condensation tube assembly, the clusters undergo supersonic expansion into a second chamber where they are ionised and detected (more details to follow in Sections 2.2 and 2.3). Upon supersonic expansion, all molecules experience varying degrees of cooling of their translational, rotational, and vibrational degrees of freedom; translation cooling is more effective than rotational cooling which itself is more effective than vibrational cooling.[6] This means that the translation temperatures (T_T) of the metal clusters in the molecular beam are cooled down the most efficiently, followed by their rotational temperatures (T_r) and then their vibrational temperatures (T_ν), which are the least effectively cooled upon supersonic expansion (equation 2.1.1):

$$T_T < T_r < T_\nu \tag{2.1.1}$$

Due to the inefficiency in vibrational cooling upon supersonic expansion, metal clusters in a supersonically-expanded molecular beam have been found to possess vibrational temperatures that are approximately the same as the condensation tube from which that expanded from.[7] Hence, the vibrational temperature of all clusters formed in the ablation process using the two cluster source designs presented in Figure 2.1 is *ca.* 300 K, as reported previously by our research group in the work involving the Nb_3C_n (n = 1-4), Nb_4C_n (n = 1-6) and Ta_3ZrC_y (y = 0-4) metal clusters.[8,9]

2.2. The Wiley-McLaren Time-of-Flight Mass Spectrometer

The technique of Time-of-Flight Mass Spectrometry (TOF-MS) first emerged on the mass spectrometry scene in the 1960s. However, due to the lack of suitable technology needed to record and process a time-of-flight (TOF) spectrum, it was quickly replaced with magnetic and quadrupole instruments.[10] In the 1970s-80s, advances in fast digital electronics, ionisation methods and the development of the 'reflectron'[11,12] lead to the re-emergence of TOF-MS. It is an extremely powerful spectrometric technique as it allows for a mass spectrum to be rapidly acquired with excellent resolution.[13] It is for this reason that TOF-MS is used in conjunction with the dual laser ablation sources discussed in Section 2.1.2 to detect and characterise the Rh-Ho and Au-Pr clusters and their oxide counterparts.

Figure 2.2 is a schematic showing the basic set-up of a Wiley-McLaren TOF mass spectrometer, which consists of: (i) a backing plate with an electrical potential across it, (ii) an extractor plate with an electrical potential across it, (iii) a ground plate held at ground potential, (iv) an ionisation region of length s, (v) an acceleration region of length d, (vi) a field-free drift region of length D, and (vii) a detector. This design is particularly advantageous as it provides higher overall resolution than a single-field TOF mass spectrometer (which has no extractor or ground plates), and allows for extra parameters to be adjusted so that optimal mass resolution can be attained. In this TOF mass spectrometer design, the TOF is defined as the time taken for all of the ions to travel from their initial position in the ionisation region to the detector.

The first stage of Wiley-McLaren TOF-MS involves the acceleration of all ions generated in the 'ionisation region' through the 'acceleration region' and into the 'field-free drift region'. When generated, the ions (all possessing the same charge q but different mass m) undergo acceleration in both the ionisation and acceleration regions as they experience two separate forces due to: (i) the electric field E_S generated by the

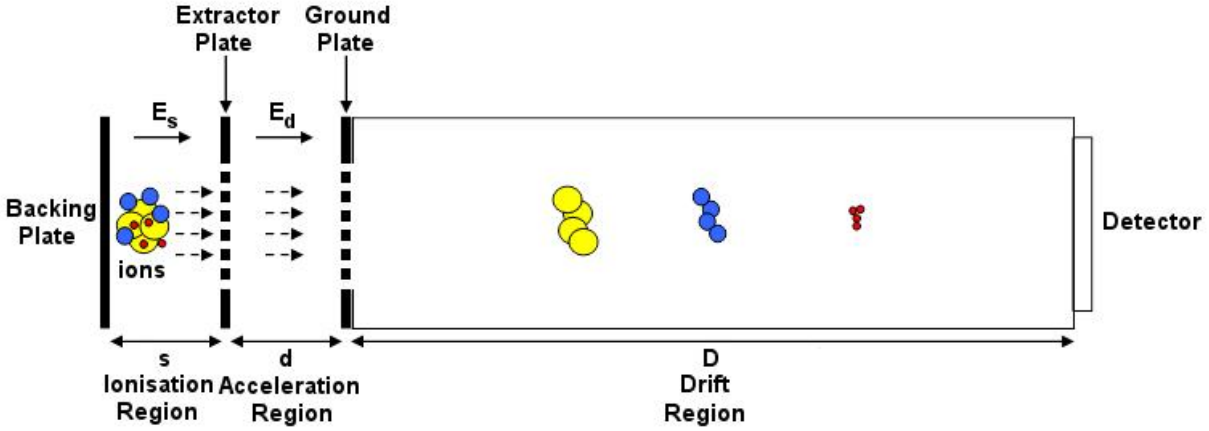

Figure 2.2. *Schematic showing the basis design of Wiley-McLaren time-of-flight mass spectrometer.*[14]

electric potential V_S applied across the backing plate, and (ii) the electric field E_d generated by the electric potential V_d applied across the extractor plate. As all the ions experience the same electric field in both regions, they are assumed to possess the same, constant kinetic energy E_k but with varying velocities v. Overall, this leads to the derivation of equation 2.2.3 from equations 2.2.1 and 2.2.2.

$$E_T = E_s + E_d = qV_s + qV_d = q(V_s + V_d) \tag{2.2.1}$$

$$E_k = \frac{1}{2}mv^2 \tag{2.2.2}$$

Therefore, by letting eq. 2.2.1 = eq. 2.2.2:

$$E_T = E_k$$

$$q(V_s + V_d) = \frac{1}{2}mv^2 \tag{2.2.3}$$

In the second stage of Wiley-McLaren TOF-MS, each ion enters the 'field-free drift region'. As they move across the field-free drift region, the ions separate out by their masses and velocities according to equation 2.2.3; the relationship between the

mass of each ion and its velocity is shown in equation 2.2.4. It shows that the velocity of each ion is inversely proportional to the square root of its mass.

$$v = \sqrt{\frac{2q(V_s + V_d)}{m}} \tag{2.2.4}$$

The time taken for ions to move across the field-free drift region of length D and reach the detector (a.k.a. the 'drift time' – denoted t_D) is given simply by equation 2.2.5:

$$t_D = \frac{D}{v} \tag{2.2.5}$$

Hence, substitution of eq. 2.2.4 into eq. 2.2.5 yields equation 2.2.6, which shows that the drift time of each ion is directly proportional to the square root of its mass. This is why heavier ions have a longer t_D than lighter ions, allowing for the separation of all ions by mass in the drift region.

$$t_D = D\sqrt{\frac{m}{2q(V_s + V_d)}} \tag{2.2.6}$$

In the third stage of Wiley-McLaren TOF-MS, there is a response time between when the ions hit the detector and when the corresponding signal is read by a digital oscilloscope (or some other type of digital output device).

As the response time of the detector and the time taken for the ions to accelerate from the ionisation and acceleration regions into the field-free drift region are considered negligible, the drift time of the ions is approximately equal to the observed TOF of the ions in Wiley-McLaren TOF-MS (Equation 2.2.7).

$$TOF \cong t_D$$

$$\therefore \quad TOF = D\sqrt{\frac{m}{2q(V_s + V_d)}} \tag{2.2.7}$$

Figure 2.3 shows an example of a TOF spectrum obtained using a Wiley-McLaren TOF mass spectrometer. As observed, the spectrum contains signals with varying intensities corresponding to each ion generated in the ionisation region, along with their corresponding TOF values. The width of each signal is governed by the velocity distribution associated with each ion, as a group of ions with the same mass will possess slightly different initial velocities prior to ionisation and acceleration.

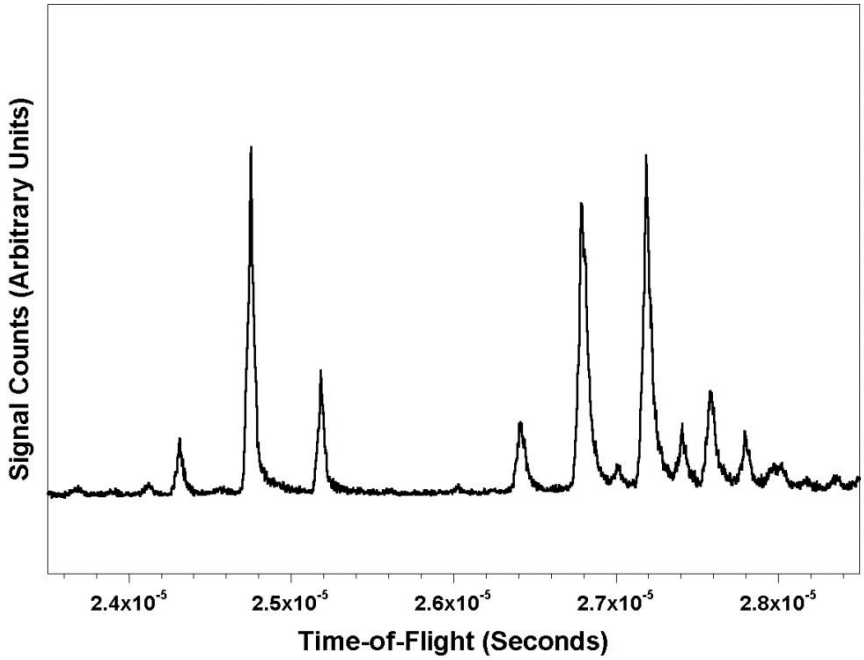

Figure 2.3. A typical example of a time-of-flight spectrum obtained using a Wiley-McLaren TOF mass spectrometer.

Each signal in a TOF spectrum can be assigned to a particular mass by graphing the $\sqrt{(m/q)}$ values of the proposed masses assigned to each signal versus their time-of-flight values (Note:[10] For positive ions, q = -ze where z is the charge number of the ion (+1 for the cluster ions in this thesis) and e is the elementary charge of an electron (-1.602×10^{-19} Coulombs). The charge number z is used instead of q in this thesis). If the relationship in this graph is observed to be exactly linear, then the correct masses have been assigned to each peak. After assigning the time-of-flight spectrum, a mass spectrum may then be obtained by placing the TOF values into the

linear equation obtained from the √(m/q) versus TOF graph. Plotting the intensity data from the time-of-flight spectrum versus this output will produce the mass spectrum. This is the procedure that was used to transform the time-of-flight spectra into the mass spectra shown in Chapters Five and Eight for the Rh-Ho and Au-Pr clusters and their oxide counterparts.

2.3. Experimental Setup and General Procedure

The experimental setup used to generate, detect and perform PIE experiments on the various Rh-Ho and Au-Pr clusters and their oxide counterparts in this thesis is shown in Figure 2.4. It consists of a source chamber and a flight/detection chamber.

The source and detection chambers are differentially pumped to a background pressure of *ca.* $1x10^{-7}$ Torr using two cryogenically-cooled 6-inch diffusion pumps (Varian VHS-6), which themselves are backed by two identical rotary pumps (Welch 1397) (**1**(**a**) and **1**(**b**)). Both background pressures are measured with separate ion gauges (Dunniway T100K) attached to each chamber (2(**a**) and 2(**b**)) which themselves are connected to two separate ion gauge controllers (Terranova 934).

The source chamber contains the dual ablation source used to generate the transition-lanthanide bimetallic clusters and their oxides, which is mounted on the end flange of the chamber (**3**). Pure helium gas (CIG gases, 99.98%) with a backing pressure of 60 psi is delivered behind the nozzle located inside the dual ablation source via a gas manifold. The nozzle, driven by a home-made nozzle driver, then delivers a dense pulse of helium gas into the source (typical gas pulse width is ca. 150 µs), thus increasing the pressure inside the source chamber to *ca.* $1x10^{-4}$ torr. This is the operational pressure that is maintained throughout the duration of the experiment. After the helium gas is introduced, the two metal rods housed in the source are then ablated with focussed 532 nm output from two separate Nd:YAG lasers running at 10 Hz through glass window ports that are attached to side flanges located on both sides of source chamber. The metal vapour created by the ablation of both metal rods is carried by the helium gas through the condensation tube assembly, where the clusters are formed. Upon reaching the end of the condensation tube assembly, the clusters then supersonically expand into vacuum and form a molecular beam which then enters the flight/detection chamber. The specific details regarding the ablation process, dual ablation source design, and rudimentary supersonic molecular beam dynamics have already been discussed in Section 2.1.2.

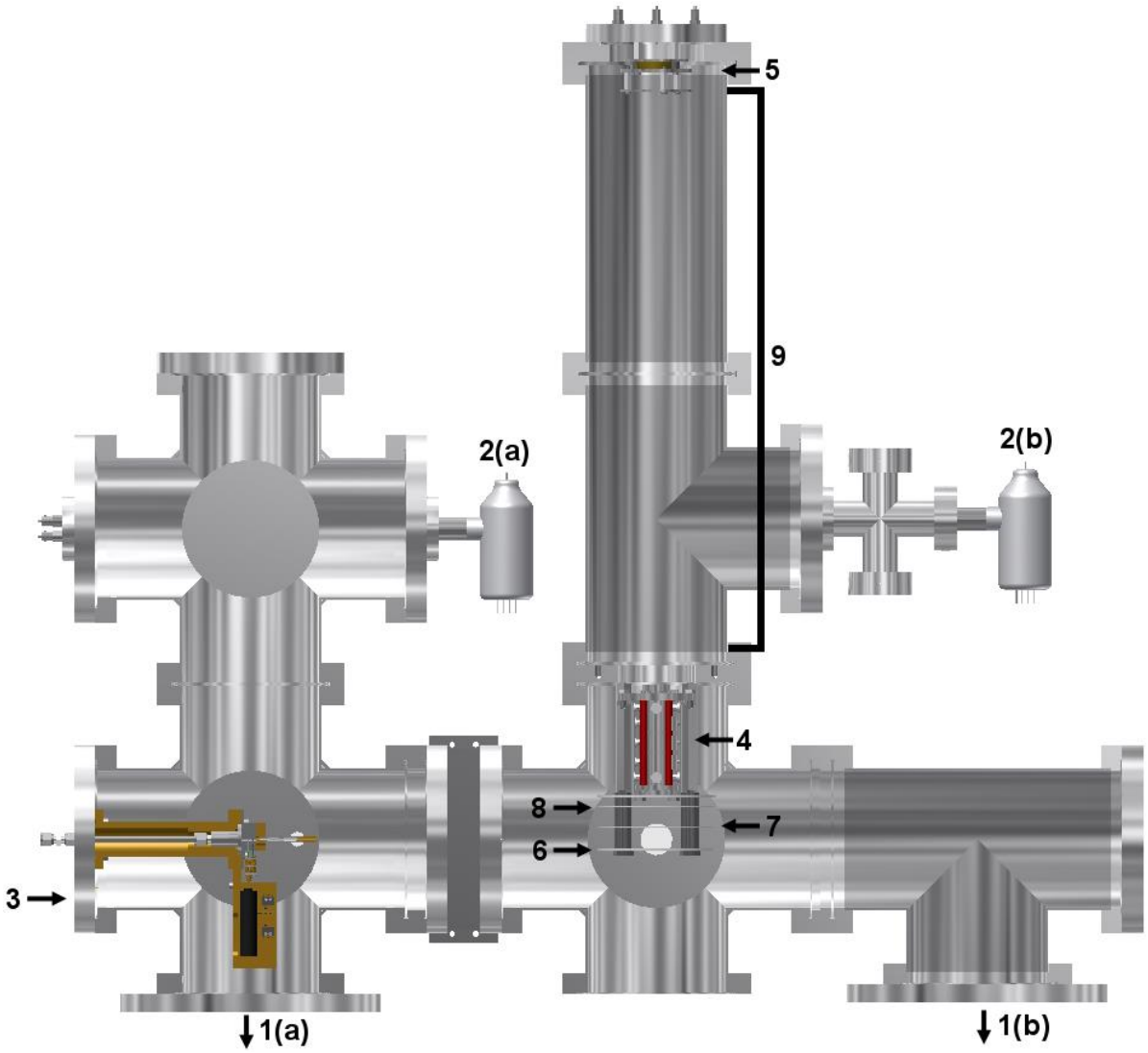

Figure 2.4. *The overall experimental setup used to generate, detect and perform PIE experiments on the Rh-Ho and Au-Pr clusters and their oxide counterparts (NOTE: The dual ablation source design used to generate the Au-Pr clusters and their oxides is shown). Refer to the text in Section 2.3 for the components/parts that correspond to each number.*

The flight/detection chamber contains a custom-built Wiley-McLaren TOF mass spectrometer[14] with a built-in ion optics assembly (**4**) and dual micro-channel plate (MCP) detector (**5**) (El Mul, MCP-M585) that are all used collectively to detect the clusters formed in the ablation process. The Wiley-McLaren TOF mass spectrometer itself (as discussed in Section 2.2) consists of a three electrode stack that is used to accelerate the cluster ions through the field-free drift region to the MCP detector (all three electrodes are labelled in Figure 2.4). These electrodes are all circular aluminium plates with a diameter of 70 mm and a width of 2 mm. The spacing between the repeller (**6**) and extractor (**7**) plates is 25 mm, and the spacing between the extractor and ground (**8**) plates is 20 mm. Throughout the entire experiment, voltages applied across the repeller and extractor plates are held at +2600 V and +2115 V, respectively, with the ground plate being held at ground potential. The extractor and ground plates both have 15 mm diameter holes in their centres covered with nickel mesh (90% transmission, Buckbee-Mears Inc.) in order to keep the electric fields created between all of the plates uniform.

The molecular beam containing the neutral clusters formed in ablation process enters the flight/detection chamber in the region between the repeller and extractor plates. The neutral clusters are then ionised in this region with unfocussed UV laser light generated by frequency-doubling the output from a tuneable dye laser (LAS GMBH, LDL 2051) pumped by the 3rd harmonic (355 nm) output from a Nd:YAG laser (Spectra-Physics GCR-10). The ionising light enters this region through a window port located on a side flange attached to the six-way cross that houses the three electrode stack and ion optics assembly. Once the clusters are ionised, the three electrode stack accelerates the cluster ions in a direction perpendicular to the molecular beam direction through the ion optics assembly and into the field-free drift region (**9**). The ion optics assembly, which consists of an einzel lens (with an internal diameter of 10 mm) and vertical and horizontal deflectors, helps focus and steer the cluster ions through the field-free drift region and towards the MCP detector. As the cluster ions

move through the field-free drift region, they are separated out due to their mass-to-charge ratio (as discussed in Section 2.2).

Once the cluster ions reach the end of the field-free drift region, they collide with the dual MCP detector, which consists of three plates: The front plate, the back plate, and the collection plate. The front and back plates are both typically held at *ca.* -1050 V, with the collection plate being held at ground. Upon collision, an output current is generated which is then amplified x25 using a pre-amplifier (Stanford Research SR445) before being delivered to a digital oscilloscope (LeCroy Model 9350AM, 500 MHz) for averaging over 1000 laser shots (1000 oscilloscope averages) and sent to a computer for further analysis. A TOF spectrum displaying all of the cluster ions is obtained (and then converted to a mass spectrum using the method discussed in Section 2.2). The timing between the pulsed nozzle, the ablation lasers and the ionisation laser is controlled with a digital delay generator (Griffith University, TARDIS II).

2.4. Spectroscopic Theory, Techniques and Procedures

2.4.1. The Born-Oppenheimer Approximation

In quantum chemistry, a molecule is represented by a total molecular wavefunction, Ψ_{ev} that contains within it all the electronic and vibrational information required to describe it in a particular state (neglecting rotation and spin contributions for the time being). However, as the electrons within the molecule are much lighter than the nuclei, any electronic movement occurs on a much faster time scale than the nuclei can vibrate. Hence, the nuclei can be approximated to remain fixed and the molecular wavefunction can be constructed in such a way that the electronic motion is treated separately from the vibrational motion. This is known as the Born-Oppenheimer (BO) approximation[15] and it allows the total molecular wavefunction to be written as a product of two separate wavefunctions; the electronic wavefunction, $\psi_e(q;Q)$ which is dependent on the electronic coordinates (q) and parametrically dependant on the nuclear coordinates (Q), and the vibrational wavefunction, $\psi_v(Q)$ which is dependent only on the nuclear coordinates and describes the vibrational motion of the molecule:

$$\Psi_{ev} = \psi_e(q;Q)\psi_v(Q) \tag{2.4.1}$$

In addition to separating the total molecular wavefunction, the BO approximation also allows the total energy of the molecule (E_{total}) to be separated into the sum of two terms; the electronic energy term (E_e), and the vibrational energy term (E_{vib}):

$$E_{total} = E_e + E_v \tag{2.4.2}$$

When rotation and spin contributions are considered for the molecule, the total molecular wavefunction (Equation 2.4.1) can be factorised further to include the wavefunctions that describe the rotational motion and spin contributions. Furthermore, the energetic contributions from the rotational motion and spin can also be included

additively into the total energy of the molecule (Equation 2.4.2). The expansion of the BO approximation to include these rotation and spin contributions further highlights that all the various types of properties of the molecule (electronic, vibrational, rotational and spin) can be treated separately. However, in the context of this thesis, only the electronic and vibrational contributions will be considered.

2.4.2. The Franck-Condon Principle

Consider a molecule that has undergone an electronic transition between two different states due to the absorption or emission of a photon of energy hν. Such a transition is bound to have underlying vibrational transitions occurring concurrently and as such, a range of vibronic signals will be observed with a varying range of intensities. The Franck-Condon (FC) principle[16,17] is one that is implemented to account for the observed intensity distribution of these vibronic signals. It states that as electrons are considered less massive than nuclei, an electronic transition will take place much faster than the nuclei can respond.[18] This means that all vibronic transitions that accompany the absorption or emission of a photon occur within a fixed nuclear framework, with the intensity of each observed vibronic signal depending entirely on the extent to which the vibrational wavefunctions in the lower and upper states overlap. In this quantum mechanical formalism of the FC principle, the intensity of a vibronic transition is proportional to the square of the transition moment $\boldsymbol{R}_{ev}$, which is expressed mathematically as:

$$\boldsymbol{R}_{ev} = \int \Psi'_{ev}{}^{*} \boldsymbol{\mu} \Psi''_{ev} d\tau_{ev} \tag{2.4.3}$$

where $\boldsymbol{\mu}$ is the electric dipole moment operator, Ψ_{ev}'' is the vibronic wavefunction in the lower state and Ψ_{ev}' is the vibronic wavefunction of the upper state. When the BO approximation is implemented, both vibronic wavefunctions can be written as a product of their separate electronic and vibrational wavefunctions, which transforms equation 2.4.3 into this:

$$\boldsymbol{R}_{e\nu} = \iint \psi_e^{'*} \psi_\nu^{'} \boldsymbol{\mu} \psi_e^{''} \psi_\nu^{''} d\tau_e dr \tag{2.4.4}$$

When integrating equation 2.4.4 over all electronic coordinates $d\tau_e$, it transforms into:

$$\boldsymbol{R}_{e\nu} = \int \psi_\nu^{'} \boldsymbol{R}_e \psi_\nu^{''} dr$$

$$\boldsymbol{R}_{e\nu} = \boldsymbol{R}_e \int \psi_\nu^{'} \psi_\nu^{''} dr = \boldsymbol{R}_e \left\langle \psi_\nu^{'} \middle| \psi_\nu^{''} \right\rangle \tag{2.4.5}$$

Where $\boldsymbol{R}_e$ is defined as the electronic transition moment and is considered to be constant as a consequence of the BO approximation. The integral in the centre of equation 2.4.5 (and shown in Dirac 'bra-ket' notation on the right hand side (r.h.s.) of eq. 2.4.5) is defined as the vibrational overlap integral and its value is an indication of the extent to which the two vibrational wavefunctions in the lower and upper states (denoted Ψ_v'' and Ψ_v', respectively) overlap. The square of this vibrational overlap integral is defined as the Franck-Condon Factor (FCF) for the vibronic transition in question:

$$\mathrm{FCF} = \left\langle \psi_\nu^{'} \middle| \psi_\nu^{''} \right\rangle^2 \tag{2.4.6}$$

As the intensity of each vibronic signal is proportional to $\boldsymbol{R}_{ev}$, the consequent implementation of the FC principle and BO approximation effectively culminates in each vibronic signal intensity (denoted I) being proportional to the magnitude of its corresponding FCF:

$$\mathrm{I} \propto \mathrm{FCF} \tag{2.4.7}$$

In addition to the value of a FCF for a given vibronic transition, the Boltzmann population of the lower vibration state at a given vibrational temperature T_ν also influences I of a vibronic signal. Therefore, I can be approximated by using Equation 2.4.8:

$$\mathrm{I} \cong \left\langle \psi_\nu^{'} \middle| \psi_\nu^{''} \right\rangle^2 \cdot e^{-(E_i^{''} - E_0^{''})/kT_\nu} \tag{2.4.8}$$

where E_i'' is the energy of the *ith* lower vibrational state, E_0'' is the energy of the ground vibrational state, and k is Boltzmann's constant (1.381×10^{-23} J K^{-1}). Hence, when considering the analysis of a vibronic spectrum, one must take into account a whole range of FCF values for various vibronic transitions in addition to the vibrational temperature of the molecular system in question.

2.4.3. Photoionisation Theory

Photoionisation is a process that involves the ejection of an electron from a neutral atom or molecule following an interaction with a photon possessing sufficient energy, $h\nu$.[19] The minimum photon energy required to eject the electron from a neutral molecule in its ground state is defined as the Ionisation Energy (IE).[19] The common unit used for IEs in the area of gas-phase metal cluster chemistry is the electron volt (eV), where 1 eV = 1.6022×10^{-19} J. Hence, all IEs presented and discussed in thesis will be in units of 'eV'.

When a molecule, M undergoes an ionisation transition due to photoionisation, it becomes a singly-charged molecular cation, M^+ with the general assumption that there are no additional processes involving excitation of electrons in M^+ after the transition has occurred. This means that M^+ is assumed to be produced in its lowest electronic state following photoionisation of M. Interestingly, ionisation transitions occur in a very similar manner to that of electronic transitions; there are underlying vibrational transitions that accompany the ionisation transition (i.e. transitions between vibrational states in the neutral and cationic structures, both in their ground electronic states). Hence, if one were to perform ultra-violet photoelectron spectroscopy (UPS) on M (a technique involving the ionisation of M with ultra-violet radiation followed by the separation of ejected photoelectrons based on their kinetic energy), a range of vibronic signals with varying intensities would be observed in its UPS spectrum. The FC principle can then be applied to account for the observed intensity distribution of these vibronic signals arising from the ionisation transition (just as for

electronic transitions). However, as opposed to electronic transitions, orbital selection rules for the photoionisation process described above are negligible – all ionisations are allowed.[19] The only selection rule encountered for ionisation transitions (without consideration of rotational contributions) is that $\Delta S = \pm 1/2$, where is S is the total spin quantum number associated with M and M^+.

With the knowledge that ionisation transitions are akin to electronic transitions in that they possess underlying vibrational structure, this allows for two types of IEs to be defined for M: (i) the adiabatic IE, and (ii) the vertical IE. The difference between the two is shown in Figure 2.5. Note that the Morse potential for diatomic molecules has been used to describe the PESs of M and M^+ to better highlight the difference between the two different types of IE.

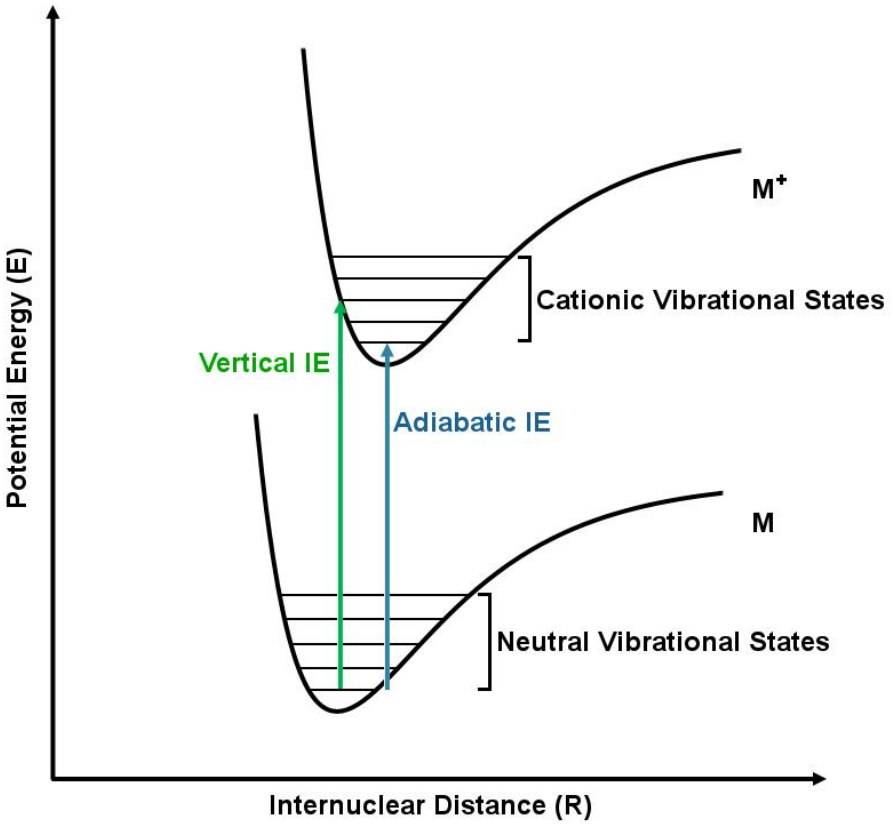

Figure 2.5. *Diagram illustrating the difference between vertical and adiabatic IEs. The Morse potential for diatomic molecules has been used to describe the PESs of M and M^+ to better highlight the difference between the two different types of IE.*

As observed in Figure 2.5, the vertical IE is defined as the energy difference between the lowest vibronic state on the PES of M and the vibronic state on the PES of M^+ that corresponds to the same nuclear positions as for M (i.e. the nuclear geometry remains fixed upon the ionisation transition). The corresponding ionisation transition is termed the 'vertical ionisation transition' and is expected to produce the largest value for the vibrational overlap integral (equation 2.4.5), thus resulting in the most intense vibronic signal. The adiabatic IE is defined as the energy difference between the lowest vibronic states on both PESs of M and M^+, with the corresponding ionisation transition termed as the 'adiabatic ionisation transition' or alternatively as the '0-0 transition'. As the nuclear geometry does not remain fixed upon an adiabatic ionisation transition, the associated vibrational overlap integral is expected to be lower in magnitude, thus resulting in lower vibronic signal intensity than that of the vibronic signal corresponding to the vertical ionisation transition. However, if the ground state geometries of M and M^+ are very similar, then there will be no discernable difference between the vertical and adiabatic ionisation transitions, thus resulting in no appreciable difference between the vertical and adiabatic IE values of M.

The IE, be it vertical or adiabatic, is one of the most important physical properties that can be measured for gas-phase metal clusters. Once a set of experimental IEs have been determined for individual metal clusters within a particular cluster system, IE trends as a function of cluster size, composition or sequential addition of non-metal/metal atoms onto a bare metal cluster can be used to investigate, with the aid of computational investigations, any changes in geometric and electronic properties that occur upon any of the aforementioned changes within a particular cluster system. Hence, in order to investigate the geometric and electronic properties of the various Rh-Ho and Au-Pr clusters and their oxide counterparts generated and detected via the techniques outlined in Section 2.3, the experimental adiabatic IEs of these clusters are determined using Photoionisation Efficiency (PIE) spectroscopy. For the $RhHo_2O_n$ (n = 0-2), $Rh_2Ho_2O_m$ (m = 0-2) and $Au_{3-k}Pr_k$ (k = 0-3)

clusters specifically, any observed experimental adiabatic IE trends within these cluster series are complemented by computational investigations in order to provide more rigorous insight into the nature of the trends.

2.4.4. Photoionisation Efficiency Spectroscopy

Photoionisation Efficiency (PIE) spectroscopy is used to determine the experimental adiabatic IEs of the various Rh-Ho and Au-Pr clusters and their oxide counterparts generated and detected via the techniques outlined in Sections 2.1.2 and 2.3. When performing a PIE experiment, the signal intensity of a molecular ion is recorded as the energy of the ionising laser is scanned in the vicinity of the ionisation threshold.[20] As the experiment is used to directly determine the minimum photon energy required to ionise the molecule, it is imperative that the photon fluence of the ionising light be sufficiently low so as to not induce multi-photon ionisation (MPI); the experiment must be performed under single-photon ionisation (SPI) conditions. Additionally, fragmentation of larger molecules induced by high photon fluences can also occur and contribute to the molecular (daughter) ion signal, potentially leading to false IE assignments. This adds to the requirement of keeping photon fluence low enough so that SPI is the dominant ionisation process in the experiment. Overall, if the PIE experiment is successfully performed on a molecule under SPI conditions, a spectrum similar to the form shown in Figure 2.6 will be obtained when the signal intensity of the molecular ion is plotted against ionising photon energy. The appearance energy of the molecule (AE) corresponds to the photon energy at which there is a sudden onset of molecular ion signal in the PIE spectrum (indicated by the arrow in Figure 2.6). This AE value is then corrected for field ionisation in order to obtain the experimental IE of the molecule (more details in Section 2.4.5 below).

When analysing the PIE spectrum of a molecule, the gradient of the ion signal intensity is qualitatively indicative of the amount of geometric change experienced by the molecule as it undergoes photoionisation. This is due to underlying vibronic

transitions that accompany the ionisation transition experienced by the molecule (see Section 2.3.3), with the length of the vibronic progression influencing how gradual or rapid the onset of ion signal is. Additionally, when the ion signal intensity is observed to plateau in the PIE spectrum, this indicates the end of the vibronic progression due to the highest energy FC-allowed vibronic transition being reached for the ionisation transition.

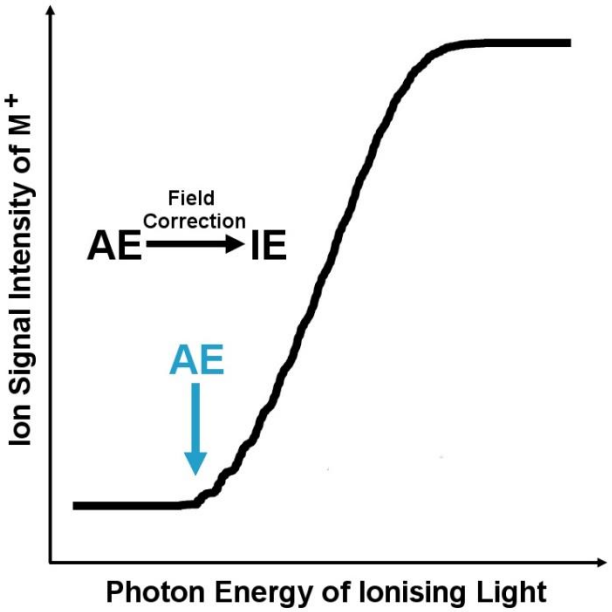

Figure 2.6. *A plot representing the ion signal onset of M^+ once the AE of the neutral molecule M has been reached. Once obtained, the AE is then field-corrected to obtain the experimental IE of the molecule.*

A short vibronic progression underlying the ionisation transition will result in a steep gradient of ion signal intensity being observed in the PIE spectrum. In contrast to this, a long vibronic progression underlying the ionisation transition produces shallow gradient of ion signal intensity. As short vibronic progressions are indicative of very minor geometric changes upon an electronic or ionisation transition, a steep gradient of ion signal intensity observed in a PIE spectrum also indicates little-to-no geometric change experienced by the molecule upon ionisation. The same rationalisation can be used for PIE spectra that have long vibronic progressions

underlying them; long vibronic progressions are indicative of a significant amount of geometric change experienced by the molecule upon an electronic or ionisation transition and hence, a shallow gradient of ion signal intensity will be observed in the PIE spectrum.

When the experimental IE of a metal cluster is determined using PIE spectroscopy (from field-correcting the experimental AE of the metal cluster), it is generally assumed that the value obtained represents the adiabatic IE of the metal cluster. This implies that the initial onset of ion signal observed in the PIE spectrum of a metal cluster is due to the band origin transition (i.e. no vibrational excitation in either state) and any additional onset observed thereafter is due to various other vibronic transitions that accompany the ionisation transition. However, as the vibrational temperature of all clusters generated in the laser ablation process described in Section 2.1.2 is *ca.* 300 K, it is likely that the initial onset of ion signal observed is actually due to vibronic 'hot band' transitions and not the band origin transition – a phenomenon characterised as 'thermal tailing'. This means that all experimental adiabatic IE values obtained for the various Rh-Ho and Au-Pr clusters and their oxide counterparts in this thesis are slightly red-shifted from the true adiabatic IE (i.e. the band origin transition). Fortunately, this effect can be accounted for by simulating the vibronic structure underlying the PIE spectra for each individual cluster at 300 K and adding a correction factor to the experimental AE once potential vibronic hot band candidates causing early ion signal onset have been identified (this is discussed in more detail in Chapter Three). This thermally-corrected experimental AE is then field-corrected to obtain the true adiabatic IE. However, an experimental PIE spectrum by itself gives little-to-no information regarding the extent to which thermal tailing affects ion signal onset. Hence, all experimental adiabatic IEs determined from the PIE spectra presented in Chapters Five and Eight are assumed to be due to the band origin transition and are subject to slight corrections to account for red-shifting attributed to thermal tailing.

2.4.5. Details behind the Photoionisation Efficiency Experiments

The PIE spectra of the $RhHo_2O_n$ (n = 0-2), $Rh_2Ho_2O_m$ (m = 0-2), $AuPr_2O_x$ (x = 0-2), $Au_2Pr_2O_m$ (m = 0-1), $Au_3Pr_2O_n$ (n = 0-2), Au_2Pr, and $Au_3Pr_2O_3H_2$ clusters presented in Chapters Five and Eight were recorded by monitoring their ion signals as a function of ionising UV wavelength under SPI conditions. All the data points in these PIE spectra were collected at 0.25 nm intervals in the wavelength regions investigated (222-280 nm and 218-265 nm for the Rh-Ho and Au-Pr experiments, respectively).

The ionising laser light used to perform all of the PIE experiments is generated by frequency-doubling the output from a tuneable dye laser (LAS GMBH, LDL 2051) pumped by the 3rd harmonic (355 nm) output from a Nd:YAG laser (Spectra-Physics GCR-10) running at 10 Hz. The frequency-doubling is achieved by using a β-barium borate (BBO) doubling crystal coupled with a compensator, with the output being separated from the residual fundamental output via an assembly made up of four Pellin-Broca prisms. This four-prism assembly is also advantageous for the PIE experiments as it allows for the beam direction of the frequency-doubled output to remain constant whilst the wavelength of the dye laser is scanned.

As mentioned in Section 2.4.4, it is imperative that the photon fluence of the ionising laser beam used for the PIE experiments be sufficiently low so as to not induce MPI or fragmentation processes. In order to help ensure this, the ionisation laser beam is expanded by x5 and collimated using a telescope assembly comprising of two lenses with focal lengths of 50 mm and 250 mm. After leaving the telescope, the central part of the newly expanded and collimated beam then passes through an adjustable iris set to a diameter of 5 mm, which creates a 5mm-diameter ionising laser beam with reduced photon density (and photon fluence) that then enters the flight/detection chamber. Variations in output efficiencies from the dye laser are minimised by a home-made computer program which incorporates the stepper motor controlling the BBO doubling crystal and compensator angles, pyroelectric power meter (Ophir Nova II), boxcar integrator (Stanford Research Systems SR250) and a digital oscilloscope (LeCroy 9350

AM, 500 MHz) to attenuate the ionisation laser power to the value desired and hold it constant at each wavelength.

After entering the flight/detection chamber, the ionising laser beam overlaps perpendicularly with the molecular beam, exits the chamber and then hits the pyroelectric power meter. Each ionising laser pulse that hits the power meter generates a flat-top pulse with a rise time of *ca.* 3 ms that is proportional to the laser pulse energy. This output pulse is then sent to the boxcar integrator where a small section of the flat part of the pulse is integrated and the value sent to the oscilloscope, where the voltage value displayed is proportional to the laser pulse energy. This was necessary as the rise time of the flat-top pulse is much longer than the µs flight time of the cluster ions, such that both signals cannot be displayed on the oscilloscope simultaneously (which is required by the home-made computer program that drives the PIE experiments). The optimal ionising laser powers used for the Rh-Ho and Au-Pr PIE experiments are *ca.* 80 µJ pulse^{-1} (*ca.* 400 µJ cm^{-2}) and *ca.* 60 µJ pulse^{-1} (*ca.* 300 µJ cm^{-2}), respectively. These laser powers are consistent with those recommended for performing PIE experiments involving transition metal clusters to ensure SPI conditions (400 µJ cm^{-2} or less), as suggested by Knickelbein and co-workers.[21] Overall, expansion and collimation of the ionising laser beam in addition to the attenuation of its laser power effectively ensures that SPI is the dominant ionisation process in all the PIE experiments.

As mentioned in Section 2.3, a digital delay generator (Griffith University, TARDIS II) is used to control the timing between the pulsed nozzle, the ablation lasers and the ionisation laser in order to attain decent cluster ion signal. Once the cluster signal appears on the digital oscilloscope, the home-made computer program is then started to run the wavelength scans and eventually obtain a PIE spectrum.

Before starting a wavelength scan, the program first requires two things: (i) that the voltage level proportional to the laser power desired to run a wavelength scan is set to a pre-determined value in the program and indicated by amplitude on the digital

oscilloscope, and (ii) a polynomial function for the stepper motor that controls the BBO doubling crystal and compensator angles in order to attain maximum frequency-doubled output at each wavelength to be used in the scan. Once these two requirements have been met, the program is then started at the shortest wavelength of the scan. At first, the ionising laser power is attenuated over 10 laser pulses (10 oscilloscope averages) by the program driving the stepper motor positions. Once the integrated voltage output from the pyroelectric power meter is within ±7 % of the pre-determined voltage set in the program and indicated on the digital oscilloscope, the crystal and compensator angles remain at their current positions and a mass spectrum is then collected and averaged over 1000 laser pulses (i.e. 1000 oscilloscope averages). The laser power is also averaged over 1000 laser pulses. Once completed, the averaged mass spectrum, laser power and wavelength are all downloaded and stored on a computer before the program moves the dye laser to the next wavelength position.

Once a wavelength scan has been completed, it is then opened by another program which displays all the mass spectra collected individually at each wavelength and the corresponding average laser power over the 1000 pulses. In order to generate the data points needed to create the PIE spectrum of a particular cluster, the program is used to integrate the area under the peak corresponding to the cluster of interest. This generates a data file which has columns that contains the following information corresponding to each data point in the scan: (i) the integrated area of the cluster peak, (ii) the wavelength, and (iii) the average laser power used. The integrated area at each data point is then divided by the corresponding laser power to normalise it and give the cluster ion signal intensity at each wavelength in the scan. Overall, this procedure is used to generate a range of data points for a series of wavelength scans across different laser dye regions. In order to create a complete data set for the cluster of interest, overlapping scans are concatenated by scaling the cluster ion signal intensities until they are consistent.

Whilst the wavelength scans are being performed, there are two issues that could potentially affect the quality of the PIE spectra obtained: (i) Large pulse-to-pulse cluster ion signal fluctuations caused by inhomogeneities on the surface of the metal rods as they are ablated,[22] and (ii) long-term cluster ion signal drift. To compensate for issue (i), the time taken to average out the mass spectrum over 1000 laser pulses at each wavelength corresponds to one complete translation/rotation cycle of the two metal rods (*ca.* 100 s at 10 Hz). Therefore, any fluctuation of cluster ion signal due to these inhomogeneities should be moderately constant at each wavelength data point. To compensate for issue (ii), the wavelength scans are always performed from shortest to longest wavelength, with the laser returned to the starting wavelength at the end of the scan. If the cluster ion signal intensities, relative to laser power, are similar in the two mass spectra collected at the shortest wavelength, then the cluster ion signal drift is considered negligible and the scan is deemed acceptable for analysis.

Once a complete data set for the cluster of interest is obtained, the wavelength corresponding to every data point in the set is converted to the actual wavelength. This is determined by measuring the fundamental output from the dye laser using an opto-galvanic cell. These actual wavelength values are then converted to vacuum wavenumbers. The cluster ion signal intensity is then plotted against the photon energy in vacuum wavenumbers, thus generating the PIE spectrum for the cluster of interest. Two lines are then fitted to the baseline and the linear rise of the signal in this spectrum, with the intersection of these two lines being denoted as the appearance energy (AE) of the cluster. From this, the adiabatic IE of the cluster is determined using a correction factor of $IE=AE+6.1\sqrt{V}$ (where V is the voltage difference between the repeller and extractor plates = 485 V cm^{-1} for the experimental design) as recommended by Schlag and co-workers in order to account for the slight red-shifting in IE caused by the dc extraction field.[23] This procedure of IE determination has an conservatively estimated error of ±0.05 eV associated with it, as first postulated by

Knickelbein and Yang in their work involving photoionisation studies of niobium clusters.[24]

2.5. References

(1) Dietz, T. G.; Duncan, M. A.; Powers, D. E.; Smalley, R. E. *J. Chem. Phys.* **1981**, *74*, 6511.

(2) Bondybey, V. E.; Schwartz, G. P.; English, J. H. *J. Chem. Phys.* **1983**, *78*, 11.

(3) Bondybey, V. E.; English, J. H. *J. Chem. Phys.* **1983**, *79*, 4746.

(4) Nonose, S.; Sone, Y.; Onodera, K.; Sudo, S.; Kaya, K. *J. Phys. Chem.* **1990**, *94*, 2744.

(5) Meiwes-Broer, K.-H. In *Advances in Metal and Semiconductor Clusters*; Duncan, M. A., Ed.; JAI Press Inc.: Greenwich, Conneticut, 1993; Vol. 1 - Spectroscopy and Dynamics.

(6) Koperski, J.; Fry, E. S. *J. Phys. B - at Mol. Opt.* **2006**, *39*, S1125.

(7) Collings, B. A.; Amrein, A. H.; Rayner, D. M.; Hackett, P. A. *J. Chem. Phys.* **1993**, *99*, 4174.

(8) Dryza, V.; Addicoat, M. A.; Gascooke, J. R.; Buntine, M. A.; Metha, G. F. *J. Phys. Chem. A* **2008**, *112*, 5582.

(9) Dryza, V.; Metha, G. F. *J. Chem. Phys.* **2009**, *130*, 244301.

(10) Guilhaus, M. *J. Mass Spec.* **1995**, *30*, 1519.

(11) Mamyrin, B. A. S., D. V.; Zagulin, V. A. *Sov. Phys.-JETP (English Translation)* **1973**, *37*, 45.

(12) Mamyrin, B. A. S., D. V.; *Sov. Phys.-JETP (English Translation)* **1979**, *49*, 762.

(13) Dawson, J. H. J. G., M. *Rapid Commun. Mass Spec.* **1989**, *3*, 155.

(14) Wiley, W. C.; Mclaren, I. H. *Rev. Sci. Instrum.* **1955**, *26*, 1150.

(15) Born, M. O., J. R. *Annalen Der Physik* **1927**, *84*, 457.

(16) Franck, J. *Trans. Faraday Soc.* **1926**, *21*, 0536.

(17) Condon, E. U. *Phys. Rev.* **1928**, *32*, 0858.

(18) Atkins, P. W. D. P., J. *Physical Chemistry*; 9th ed.; Oxford University Press: Great Britain, 2010.

(19) Hollas, J. M. *High Resolution Spectroscopy*; John Wiley & Sons Ltd: West Sussex, England, 1998.

(20) Simard, B. M., S. A.; Rayner, D. M.; Yang, D. S. In *Nato Adv Sci I C-Mat*; Russo, N. S., D. R., Ed.; Springer: the Netherlands, 2000, p 239.

(21) Knickelbein, M. B.; Yang, S.; Riley, S. J. *J. Chem. Phys.* **1990**, *93*, 94.

(22) Pedersen, D. B.; Rayner, D. M.; Simard, B.; Addicoat, M. A.; Buntine, M. A.; Metha, G. F.; Fielicke, A. *J. Phys. Chem. A* **2004**, *108*, 964.

(23) Németh, G. I.; Ungar, H.; Yeretzian, C.; Selzle, H. L.; Schlag, E. W. *Chem. Phys. Lett.* **1994**, *228*, 1.

(24) Knickelbein, M. B.; Yang, S. *J. Chem. Phys.* **1990**, *93*, 5760.

Chapter Three

Theoretical Background and Methodology

This chapter presents background information on all of the theoretical techniques that were utilised to determine the structural and electronic properties of the transition-lanthanide bimetallic clusters and their oxide counterparts. Procedural details regarding how these theoretical techniques were implemented is also presented. Firstly, a general introduction into the central tenets behind density functional theory will be discussed, followed by a general discussion on basis sets. Next, the discussion will focus more specifically on the B3P86 density functional and how it is coupled with the Stuttgart-Dresden (SDD) basis set with utilisation of various Effective Core Potentials (ECPs) to theoretically investigate the structural and electronic properties of the transition-lanthanide bimetallic clusters and their oxide counterparts. Lastly, a rigorous discussion on Zero-Electron Kinetic Energy (ZEKE) spectroscopy will be presented followed by the procedural details behind how vibrational overlap integrals and their corresponding Franck-Condon Factors (FCFs) are calculated and used to simulate ZEKE spectra and PIE spectra for the transition-lanthanide bimetallic clusters and their oxide counterparts.

3.1. The Schrödinger Equation

The ultimate objective of most molecular structure calculations is to solve the time-independent Schrödinger equation in order to attain the total ground state energy (and numerous other properties) for a given molecular system containing N electrons and M nuclei:

$$\hat{H}\Psi_0(\vec{r}_N,\vec{R}_M)=E_0^{tot}\Psi_0(\vec{r}_N,\vec{R}_M) \tag{3.1.1}$$

where $\hat{H}$, $\Psi_0(\vec{r}_N,\vec{R}_M)$ and E_0^{tot} are the total Hamiltonian operator, ground state wavefunction and total ground state energy of the molecular system, respectively. In the absence of external electric and magnetic fields, the total molecular Hamiltonian is generally comprised of five fundamental operators, each one representing either kinetic or potential energy contributions to the molecule:

$$\hat{H} = \hat{T}_e + \hat{T}_N + \hat{V}_{Ne} + \hat{V}_{NN} + \hat{V}_{ee} \tag{3.1.2}$$

where the first two operators correspond to the kinetic energies contributions of the electrons and nuclei ($\hat{T}_e$ and $\hat{T}_N$), and the last three correspond to potential energy contributions from nucleus-electron, nucleus-nucleus and electron-electron interactions ($\hat{V}_{Ne}$, $\hat{V}_{NN}$ and $\hat{V}_{ee}$). The total energy of the molecular system is therefore also comprised of five different energy contributions, each relative to the five different operators in the total Hamiltonian:

$$E_0^{tot} = E_{T_e} + E_{T_N} + E_{Ne} + E_{NN} + E_{ee} \tag{3.1.3}$$

In practice, solving the Schrodinger equation accurately in the form presented in Equation 3.1.1 with the total molecular Hamiltonian (eq 3.1.2) is quite onerous. This is because molecular wavefunctions that are variably dependent on the co-ordinates of the N electrons and M nuclei are often difficult to express accurately due to the correlated motion of all these particles within the molecule (meaning that no particle is moving

independently of all the others). Simplification is thus required in order to tractably solve for E_0^{tot} and is achieved by implementation of the Born-Oppenheimer (BO) approximation (Section 2.3.1). When this approximation is applied, the electrons within the molecule are treated as moving in a field of stationary nuclei; which is justified as nuclear motion occurs more slowly than electronic motion due to nuclei being much heavier than electrons. This allows for the following three simplifications to be made: (i) the molecular, ground state wavefunction $\Psi_0(\vec{r}_N,\vec{R}_M)$ becomes dependant only on the electronic co-ordinates, with dependence on the nuclear co-ordinates becoming parametric i.e. $\Psi_0(\vec{r}_N,\vec{R}_M) \xrightarrow{BO} \Psi_0^{el}(\vec{r}_N)$, (ii) all kinetic energy contributions due to nuclear motion equate to zero i.e. $\hat{T}_N = E_{T_N} = 0$, and (iii) all potential energy contributions due to nucleus-nucleus interactions (E_{NN}) equate to a constant for fixed nuclear positions. Collectively, these three simplifications allow for the total energy of the molecular system to be expressed as follows:

$$E_0^{tot} = E_{NN} + E_0^{el} \tag{3.1.4}$$

Where E_{NN} is the potential energy contribution due to nucleus-nucleus interactions, and E_0^{el} is the ground state electronic energy contribution to E_0^{tot}. The latter value is obtained by solving the electronic Schrodinger equation:

$$\hat{H}_{el}\Psi_0^{el}(\vec{r}_N) = E_0^{el}\Psi_0^{el}(\vec{r}_N) \tag{3.1.5}$$

Where $\Psi_0^{el}(\vec{r}_N)$ is the ground state electronic wavefunction (which is normalised and anti-symmetric with respect to the interchange of electronic co-ordinates), and $\hat{H}_{el}$ is the electronic Hamiltonian operator which has the form:

$$\hat{H}_{el} = \hat{T}_e + \hat{V}_{Ne} + \hat{V}_{ee} \tag{3.1.6}$$

Alternatively, the determined value of E_0^{el} via the use of $\Psi_0^{el}(\vec{r}_N)$ and the Schrödinger equation is also known as the expectation value (denoted by $\langle \hat{H}_{el} \rangle$) of $\hat{H}_{el}$. This is because E_0^{el} is the observable that is represented by the quantum mechanical operator $\hat{H}_{el}$ and in Dirac bra-ket notation, this alternative representation can be expressed as:

$$\langle \hat{H}_{el} \rangle = \langle \Psi_0^{el}(\vec{r}_N) | \hat{H}_{el} | \Psi_0^{el}(\vec{r}_N) \rangle = E_0^{el} \tag{3.1.7}$$

As shown in Equation 3.1.6, the electronic Hamiltonian is dependant only on the kinetic energy contributions of the electrons, and the potential energy contributions due to nucleus-electron and electron-electron interactions. Hence, this allows E_0^{el} to be expressed as a summation of the individual energy contributions corresponding to each operator in the electronic Hamiltonian displayed in Equation 3.1.6:

$$E_0^{el} = E_{T_e} + E_{Ne} + E_{ee} \tag{3.1.8}$$

Once the BO approximation has been implemented, the approach to attain E_0^{tot} proceeds as follows: (i) the electronic Schrodinger equation (Eq. 3.1.5) is solved for a given $\Psi_0^{el}(\vec{r}_N)$ at fixed nuclear positions in order to attain E_0^{el} of the molecular system, (ii) E_{NN} is calculated via the following formula for fixed nuclear coordinates of the M of nuclei:

$$E_{NN} = \sum_{A=1}^{M} \sum_{B>A}^{M} \frac{Z_A Z_B}{r_{AB}} \tag{3.1.9}$$

where Z_A and Z_B are the respective nuclear charges of nuclei A and B, and r_{AB} is the distance between them, and (iii) E_0^{tot} is then calculated via the simple summation expressed in Equation 3.1.4.

Overall, the objective of molecular structure calculations, once applying the BO approximation, is still the same: to calculate E_0^{tot} of the molecular system. However,

the main part of achieving this goal is now to solve the electronic Schrodinger equation (Eq. 3.1.5) for a given ground state electronic wavefunction $\Psi_0^{el}(\vec{r}_N)$. There are two overall approaches that can be used to achieve this: (i) wavefunction-based methods, and (ii) electron density-based methods. As all results presented from the molecular structure calculations were performed using the latter method, only the background theory to electron-density based methods will be discussed.

3.2. Density Functional Theory

3.2.1. Brief Background

In the framework of Density Functional Theory (DFT), the ground state electron density of the molecular system $\rho_0(\vec{r}_N)$ is used to construct $\Psi_0^{el}(\vec{r}_N)$ and $\hat{H}_{el}$ in order to solve Equation 3.1.5 to obtain E_0^{el}. This effectively means that E_0^{el} is a functional (i.e. a function that maps some other function to a number) of $\rho_0(\vec{r}_N)$, which is denoted $E_0^{el}\left[\rho_0(\vec{r}_N)\right]$ to represent this fact. This is because $\left\langle \hat{H}_{el} \right\rangle = E_0^{el}$ through Equation 3.1.7, where the expectation value $\left\langle \hat{H}_{el} \right\rangle$ is a functional as it is a function which maps $\Psi_0^{el}(\vec{r}_N)$ (which itself is a function $\rho_0(\vec{r}_N)$ in the context of DFT) onto E_0^{el}, thus making $\left\langle \hat{H}_{el} \right\rangle$ and E_0^{el} both functionals which ultimately rely on $\rho_0(\vec{r}_N)$. Therefore, since E_0^{el} is a functional of $\rho_0(\vec{r}_N)$, the individual energy components of which E_0^{el} is comprised (Eq. 3.1.8) must also be functionals of $\rho_0(\vec{r}_N)$. Hence:

$$E_0^{el}\left[\rho_0(\vec{r}_N)\right] = E_{T_e}\left[\rho_0(\vec{r}_N)\right] + E_{Ne}\left[\rho_0(\vec{r}_N)\right] + E_{ee}\left[\rho_0(\vec{r}_N)\right] \tag{3.2.1}$$

However, straight-forward determination of $E_0^{el}\left[\rho_0(\vec{r}_N)\right]$ from Equation 3.2.1 is problematic due to complications arising from electron-electron interactions that affect the first and third terms on the right hand side (r.h.s) of the equation. In order to simplify matters, Kohn and Sham proposed treating all electrons in the molecule as a fictitious system of non-interacting electrons which have the same $\rho_0(\vec{r}_N)$ as a real system of interacting electrons. This simplification allows for: (i) the first term in Equation 3.2.1 to be separated into specific components which relate to the kinetic energy of the fictitious non-interacting electrons (denoted $E_{T_e}^{NI}\left[\rho_0(\vec{r}_N)\right]$) and corrections to this value arising from electron interactions (denoted $\Delta E_{T_e}^{I}\left[\rho_0(\vec{r}_N)\right]$), and (ii) the third term in Equation 3.2.1 to be separated into specific components relating to the

energies associated with classical (denoted $E_{ee}^{CL}\left[\rho_0(\vec{r}_N)\right]$) and quantum mechanical (denoted $\Delta E_{ee}^{QM}\left[\rho_0(\vec{r}_N)\right]$) electron-electron interactions:

$$E_0^{el}\left[\rho_0(\vec{r}_N)\right]=E_{T_e}^{NI}\left[\rho_0(\vec{r}_N)\right]+E_{Ne}\left[\rho_0(\vec{r}_N)\right]+E_{ee}^{CL}\left[\rho_0(\vec{r}_N)\right] \\ +\Delta E_{T_e}^{I}\left[\rho_0(\vec{r}_N)\right]+\Delta E_{ee}^{QM}\left[\rho_0(\vec{r}_N)\right] \tag{3.2.2}$$

With this separation shown in equation 3.2.2, the first three terms on the r.h.s can all be determined exactly and are representative of the specific energy contributions arising from the fictitious non-interacting electron system. The last two terms are coined the 'difficult' terms and as such are combined into a single energy component called the exchange-correlation energy (denoted $E_{XC}\left[\rho_0(\vec{r}_N)\right]$). Hence, E_0^{el} can now be expressed as this:

$$E_0^{el}\left[\rho_0(\vec{r}_N)\right]=E_{T_e}^{NI}\left[\rho_0(\vec{r}_N)\right]+E_{Ne}\left[\rho_0(\vec{r}_N)\right]+E_{ee}^{CL}\left[\rho_0(\vec{r}_N)\right]+E_{XC}\left[\rho_0(\vec{r}_N)\right] \tag{3.2.3}$$

It is important to point out that if $E_{XC}\left[\rho_0(\vec{r}_N)\right]$ were known exactly, then the electronic Schrodinger equation would be solved exactly for the molecular system of interest. However, the explicit form of $E_{XC}\left[\rho_0(\vec{r}_N)\right]$ is thus far unknown, making how the exchange and correlation components of this term are treated the distinguishing factor between all available DFT functionals. The first three terms on the r.h.s of equation 3.2.3 are treated in the same manner by all DFT functionals.

3.2.2. Types of Density Functionals

There are three main types of DFT functionals used widely in computational chemistry to treat the exchange and correlation terms in $E_{XC}\left[\rho_0(\vec{r}_N)\right]$: (i) Local density functionals, (ii) Gradient-corrected (or non-local) density functionals, and (iii) Hybrid functionals. Those from types (i) and (ii) that specifically treat the exchange and

correlation components of $E_{XC}\left[\rho_0(\vec{r}_N)\right]$ are called exchange functionals and correlation functionals, respectively.

Local density functionals require that the electron density used in the calculation be single-valued at every position in the molecule. Functionals that conform to this requirement are those that have effectively been derived from the analysis of the uniform electron gas; a system which has the same density value at all positions. An example of a widely used local density exchange functional is the Slater (S) functional[1] (also known as the Local Spin Density (LSD) exchange functional). An example of a widely used local density correlation functional is the Vosko, Wilk and Nusair (VWN) functional[2] (also known as the LSD correlation functional). These two examples can be combined to form a local exchange-correlation functional known as the SVWN functional.

Gradient-corrected density functionals involve the use of the electron density and its gradient in calculations. These functionals are generally more chemically realistic and accurate than local density functionals due to the fact that electron density is non-uniform in atoms and molecules. An example of a gradient-corrected exchange functional is the Becke (B88) functional.[3] An example of a gradient-corrected correlation functional is the Lee, Yang and Parr (LYP) functional.[4] As with local exchange-correlation functionals, these two examples can be combined to form a non-local exchange-correlation functional known as the BLYP functional.

Out of the three types of DFT functionals that are available for use in calculations, hybrid functionals are the most accurate and computationally expensive. They define the exchange functional using a linear combination of HF, local and gradient-corrected exchange terms. This combined exchange functional is then coupled with a local and/or a non-local correlation functional to give a hybrid exchange-correlation functional. A typical example of a hybrid functional is the B3LYP functional. This functional is composed of the Becke three-parameter (B3) combined exchange functional[5] and is coupled with the gradient-corrected LYP functional.

Hybrid functionals are used in a large percentage of computational investigations involving transitions metal clusters (despite the fact that they are the most computationally expensive) due to the high accuracy that they can provide.

3.2.3. The B3P86 Density Functional

The B3P86 is a hybrid exchange-correlation density functional. The exchange term is defined by the B3 combined exchange functional. The correlation term is defined by the Perdew 86 (P86) gradient-corrected correlation functional.[6] The mathematical expression of the exchange-correlation term of the B3P86 density functional is shown in equation 3.2.4 (NOTE: The dependency on $\rho_0(\vec{r}_N)$ is implicit in the equation).[5]

$$E_{XC}^{B3P86} = (1-A)E_X^S + AE_X^{HF} + B\Delta E_X^{B88} + CE_C^{P86} + (1-C)E_C^{VWN} \qquad (3.2.4)$$

Where, E_x^S is the local exchange term defined by the S (or LSD exchange) functional, E_x^{HF} is the exchange term from the HF method, ΔE_x^{B88} is the gradient-corrected exchange term defined by the B88 functional, E_c^{P86} is the gradient-corrected correlation term defined by the P86 functional, E_c^{VWN} is the local correlation term defined by the VWN (or LSD correlation) functional and constants A, B, and C are equal to 0.20, 0.72 and 0.81, respectively as determined by Becke.[5]

As observed from Equation 3.2.4, the exchange term in the B3P86 functional is a linear combination of HF, local and gradient-corrected exchange terms coupled with local and gradient-corrected correlation terms. The mixture of these different types of functionals helps gives rise to the high accuracy of all calculations performed using this functional and as such, has been chosen for investigating the geometric and electronic properties of the $RhHo_2O_n$ (n = 0-2), $Rh_2Ho_2O_m$, (m = 0-2) and $Au_{3-k}Pr_k$ (k = 0-3) clusters.

3.3. Basis Sets

3.3.1. Mathematical Formalism and Molecular Orbitals

In the context of this thesis, a basis set is defined as a set of mathematical functions (called basis functions) that are used to represent the atomic orbitals (AOs) of each atom in a given molecular system. For the most popular basis sets used in computational chemistry, Gaussian functions are chosen as the basis functions and as such, the atomic orbitals (AOs) approximated by them are called Gaussian-type orbitals (GTOs). A normalised GTO in its general form is expressed (in atom-centred Cartesian coordinates) as this:[7]

$$\phi\left(x,y,z;\alpha,i,j,k\right)=\left(\frac{2\alpha}{\pi}\right)^{3/4}\left[\frac{(8\alpha)^{i+j+k}\,i!j!k!}{(2i)!(2j)!(2k)!}\right]^{1/2}x^{i}y^{j}z^{k}e^{-\alpha(x^2+y^2+z^2)} \tag{3.3.1}$$

Where α is the exponent (which controls the width of the GTO), and i, j, k are non-negative integers that determine the nature of the orbital (i.e. s-type, p-type etc. orbitals).

In practice, the best computational results are obtained when the basis set used consists of a set of basis functions which themselves are composed of a certain number of linearly combined GTOs. Such basis functions are called Contracted Gaussian Functions (CGFs) and the GTOs from which they are composed are called Primitive Gaussian Functions (PGFs). Hence, each CGF that is a basis function χ for a chosen basis set can be expressed mathematically as:[7]

$$\chi\left(x,y,z;\{\alpha\},i,j,k\right)=\sum_{a=1}^{M}c_a\phi\left(x,y,z;\alpha_a,i,j,k\right) \tag{3.3.2}$$

Where M is the number of GTOs (or PGFs) used in the linear combination (a.k.a. the 'degree of contraction') and c_a is the contraction coefficient for each individual PGF (i.e. how much each PGF contributes to the linear combination).

It is important to point out that most basis sets used in computational chemistry contain a mixture of CGFs and uncontracted PGFs to approximate the various AOs of a given atom (e.g. a basis set may contain 8*s* basis functions but only two of them may be CGFs and the six will remain as uncontracted PGFs). As such, the general notation used to describe a basis set is: (x*s*x*p*x*d*...x*l*)/[y*s*y*p*y*d*...x*l*], where the information in parentheses represents the total number of PGFs in the basis set (segregated into x PGFs of each angular momentum(*l*)-type), and the information in square brackets represents that number of Gaussian functions after contraction has taken place (segregated into y CGFs/uncontracted PGFs of each *l*-type). Unfortunately though, this notation does not explicitly show how the CGFs have been constructed from the available PGFs. Such information (if required) is obtained by viewing all the basis function information within the given basis set (such as exponents, contraction coefficients, degree of contraction for each CGF etc.).

There are two ways of contracting PGFs to construct CGFs: (i) Segmented contraction, and (ii) Generalised contraction. In segmented contraction, a set of PGFs are contracted to make a set of CGFs but each PGF can only be used once to construct a particular CGF (i.e. you cannot use the same PGF to construct two different CGFs). In generalised contraction, a set of PGFs are still contracted to make CGFs. However, all PGFs representing GTOs of a particular *l*-type enter all CGFs representing GTOs of the same *l*-type, but with different contraction coefficients (e.g. a PGF that is representing an *s*-orbital needs to be contracted into every CGF that represents an *s*-orbital). Basis sets that contain CGFs constructed via segmented contraction are called 'segmented contracted basis sets'. Basis sets that contain CGFs constructed via generalised contraction are called 'general contracted basis sets'.

Regardless of how many CGFs and uncontracted PGFs are used to represent a set of basis functions $\{\chi\}$ in a given basis set, the ultimate purpose of assigning them to approximate AOs is so they can be used to construct basis functions that approximate the molecular orbitals (MOs) of a given molecular system. This is done by

constructing each individual MO by linearly combining the appropriate atomic basis functions χ (be they CGFs or uncontracted PGFs):

$$\Phi_i = \sum_{\mu=1}^{N} c_{i\mu}\chi_\mu \tag{3.3.3}$$

Where Φ_i is the ith MO, χ_μ is the set of N basis functions representing each contributing AO and $c_{i\mu}$ are the MO expansion coefficients (which control how much each individual basis function χ_μ contributes to the overall construction of the MO in question).

Once all of the individual MOs within a molecular system are constructed, they can be used to form the electronic wavefunction for the molecular system. Hence, if the ground state electronic wavefunction of a given molecular system needs to be determined (in order to obtain E_0^{el} by solving equation 3.1.5), then the set of MOs that correspond to it must first be determined. An iterative process called the Self-Consistent Field (SCF) method is used to find this set of MOs $\{\Phi\}$, which effectively aims at determining the values of $c_{i\mu}$ for each basis function that gives rise to each individual MO within this sought-after set.

In the context of DFT, the MOs corresponding to a given molecular system are called Kohn-Sham Molecular Orbitals (KS-MOs). In order to obtain $E_0^{el}\left[\rho_0(\vec{r}_N)\right]$ for the molecular system, the SCF method is used to determine the KS-MOs corresponding to $\Psi_0^{el}(\vec{r}_N)$ of the molecular system. The formalism behind the SCF method is not reviewed here and interested readers are directed towards references 7, 8 and 9 for more specific details regarding this iterative process.

3.3.2. Effective Core Potentials (ECPs)

In chemical systems involving heavy atoms, calculations can take long periods of time due to the large number of basis functions that are needed to describe the large

number of electrons. However, because the core electrons of heavy atoms are said to be inert and play no significant part in chemical interactions, computational time can be decreased by replacing the core electrons with analytical functions that represent the interaction between the nucleus and the core electrons as seen by the valence electrons. These functions are called Effective Core Potentials (ECPs) and once implemented leave only valence electrons to be treated explicitly in the quantum chemical calculation, reducing the number of basis functions needed and the computational time required to complete the calculation. Additionally, ECPs can be modified to account for the relativistic effects experienced by the inner-most core electrons of a heavy atom that can arise from their high (near light-speed) velocities.[7]

There are two types of ECPs available for use in computational chemistry (used in conjunction with an appropriate basis set): (i) model potentials (MPs), and (ii) pseudo-potentials (PPs). MPs attempt to model the all-electron potential for valence electrons occupying orbitals that possess the correct radial nodal structure.[10] PPs attempt to model the same potential but for valence electrons that occupy pseudo-valence orbitals i.e. orbitals generated via a formal transformation of regular valence orbitals that yield correct orbital energies but possess a more simplified radial nodal structure.[10] In this thesis, all calculations were performed using the SDD basis set, which uses PPs to treat the core electrons.

3.3.3. The SDD Basis Set

The Stuttgart-Dresden (SDD) basis set is one that incorporates PPs into quantum chemical calculations. When used in conjunction with any type of method, it treats each element up to Ar with the D95V basis set[11] and the remainder of the periodic table with Stuttgart-Dresden PPs coupled with either segmented or general contracted basis sets (depending on the element after Ar that is chosen). There are three different theoretical levels of reference data for the Stuttgart-Dresden PPs; The Hartree-Fock PP (HF), the Woods-Boring quasi-relativistic PP (WB) and the Dirac-

Fock relativistic PP (DF). The notation for each particular PP is: XYn, where X is the reference system for generating the PP (S for a single-valence electron ion or M for a neutral atom), Y is the theoretical level of reference data (HF, WB or DF for each respective PP) and n denotes the number of core electrons replaced by the PP. When the SDD basis set is used in chemical calculations, any of these different Stuttgart-Dresden PPs can be implemented depending on which elements are present in the molecular system of interest. Table 3.1 shows various ranges of elements and the corresponding default Stuttgart-Dresden PP that is implemented in an SDD calculation.[12]

In this thesis, the SDD basis set is used on the following elements: Rh, Au, Ho, Pr, and O. Table 3.2 shows the respective segmented contracted basis sets and the corresponding PPs (if applicable) used on each element.[11,13,14] As observed in Table 3.2, the praseodymium and holmium atoms are not treated with the default MWB28 PP, but with the MWB48 and MWB56 PPs, respectively. These two PPs are part of a class known as the large-core $4f^n$/Q=11 quasi-relativistic PPs (where Q is the number of valence electrons treated explicitly by the quantum chemical calculation and n = number of *f*-electrons) and regard all orbitals of lanthanide atoms with principle quantum numbers n = 1-4 as core orbitals, thus replacing the corresponding electrons (48 and 56 electrons for praseodymium and holmium, respectively) with an effective potential.[15,16] The 5s, 5p, 6s and 5d orbitals are left untreated and are thus considered to be valence orbitals when the large-core PPs are implemented. Since *f*-electrons of lanthanide atoms are known to take little-to-no part in chemical bonding and can make calculations very complicated and time-consuming, the implementation of these two large-core PPs to treat praseodymium and holmium in calculations involving the $RhHo_2O_n$ (n = 0-2), $Rh_2Ho_2O_m$ (m = 0-2) and $Au_{3-k}Pr_k$ (k = 0-3) clusters is chemically sound. More specific details regarding these 'large-core' PPs and their use on praseodymium and holmium are discussed in more detail in Section 4.1.1.

Element	Stuttgart-Dresden PP used by default
K,Ca	MWB10
Sc to Zn	MDF10
Ga to In	MWB28
Sn to Ba	MWB46
La to Yb	MWB28
Lu to Hg	MWB60
Tl to Rn	MWB78
Ac to Lr	MWB60

Table 3.1. *The elements and the corresponding default Stuttgart-Dresden PPs that are implemented when used in a calculation involving the SDD basis set.*[12]

Element	Segmented Contracted Basis Set	Stuttgart-Dresden PP Used
Rh	$(8s7p6d)/[6s5p3d]$[a]	MWB28[a]
Au	$(8s7p6d)/[6s5p3d]$[a]	MWB60[a]
Pr	$(14s13p10d8f6g)/[10s8p5d4f3g]$[b]	MWB48[d,e]
Ho	$(14s13p10d8f6g)/[10s8p5d4f3g]$[b]	MWB56[d,e]
O	$(9s5p)/[4s2p]$[c]	None

A – Reference 13
B – Reference 14
C – Reference 11
D – Reference 15
E – Reference 16

Table 3.2. *The elements pertinent to all of the clusters discussed in this thesis and the corresponding segmented contracted basis sets and Stuttgart-Dresden PPs used on them in all of the calculations performed for this thesis using the SDD basis set.*

3.4. Computational Procedure and Details

Initial optimisations were performed on various starting geometries of the $RhHo_2O_n$ (n = 0-2), $Rh_2Ho_2O_m$ (m = 0-2) and $Au_{3-k}Pr_k$ (k = 0-3) clusters using the B3P86 hybrid DFT method coupled with the SDD basis set in the Gaussian 09 suite of programs[17] without symmetric constraints. In each calculation, large-core $4f^{n)}$/Q=11 quasi-relativistic PPs developed by Dolg *et al.*[15,16] were used for the holmium and praseodymium atoms. The conventional SDD PPs were used on the rhodium and gold atoms (see Table 3.2). Harmonic vibrational frequency calculations were subsequently performed on all unique structures located to determine if they were true minima (zero imaginary frequencies). For all unique minima within *ca.* 1 eV of the lowest energy structures (including the lowest energy structures themselves) found to possess higher symmetry, re-optimisation and harmonic frequency calculations within the highest possible symmetric point group were performed. This was done in order to ensure that there were no significant differences between the symmetry-constrained and unconstrained energies, and to properly analyse and assign the ground states and vibrational modes of each relevant structure. Hirshfeld atomic charges[18] were also calculated for the low-lying neutral and cationic candidate structures of interest to the assignment of the ionisation transition for each cluster. Hirshfeld charge analysis was chosen as it is found to yield more chemical meaningful atomic charges than those calculated via other methods such as Mulliken, Bader or Weinhold charge analysis.[19] In addition, stability tests were also performed on the corresponding wavefunctions of all neutral and cationic minima discussed and displayed in this thesis to ensure that there were no instabilities present.

For the $RhHo_2$, Au_3, $AuPr_2$, Au_2Pr and Pr_3 clusters, the various starting geometries considered for initial optimisation consisted of differing types of linear and triangular configurations. The starting geometries considered for $RhHo_2O$ consisted of the oxygen atom interacting with a holmium or rhodium atom, a Ho-Rh or Ho-Ho edge or all three atoms in the optimised structure of the $RhHo_2$ trimer base. The starting

geometries for $RhHo_2O_2$ consisted of the O_2 molecule interacting associatively (O_2 molecule intact) or dissociatively (two separate O atoms) with the optimized structure of the $RhHo_2$ trimer base. Among the associatively bound starting geometries, the O_2 molecule was made to interact with the $RhHo_2$ cluster singly bound to either a holmium or rhodium atom, doubly bound to either a Ho-Rh or Ho-Ho edge, or triply bound to all three atoms. The dissociatively bound starting geometries contained various combinations of the two separate oxygen atoms being singly bound to either a holmium or rhodium atom, doubly bound to either the Ho-Rh or Ho-Ho edge, or triply bound to all three atoms in the $RhHo_2$ cluster.

The starting geometries for Rh_2Ho_2 consisted of differing types of two dimensional and three dimensional configurations. The starting geometries for Rh_2Ho_2O consisted of the oxygen atom interacting with a holmium or rhodium atom, a Rh-Ho, Ho-Ho or Rh-Rh edge or with one of the $RhHo_2$ trimer faces in the optimized structure of the Rh_2Ho_2 tetramer base. Starting geometries for $Rh_2Ho_2O_2$ consisted of the O_2 molecule interacting associatively or dissociatively with the optimized structure of the Rh_2Ho_2 tetramer base. Amongst the associatively bound starting geometries, the O_2 molecule was made to interact with the Rh_2Ho_2 cluster singly bound to either a holmium or rhodium atom, doubly bound to either a Rh-Ho, Ho-Ho or Rh-Rh edge or triply bound to all three atoms across one of the $RhHo_2$ trimer faces. The dissociatively bound starting geometries contained various combinations of the two separate oxygen atoms binding in the same fashion as all the multiple starting configurations considered for Rh_2Ho_2O.

For all calculations involving the neutral $RhHo_2O_n$ (n = 0-2) and $Au_{3-k}Pr_k$ (k = 0-3) clusters, the doublet, quartet, sextet and octet spin multiplicities were considered. For the $Rh_2Ho_2O_m$ (m = 0-2) clusters, the singlet, triplet, quintet and septet multiplicities were considered. Once the lowest energy spin states of each neutral cluster were found, the pertinent multiplicities of the cationic species were calculated with consideration of the $\Delta S = \pm 1/2$ selection rule for ionisation. By considering all the

multiple starting geometries and various multiplicities, it is expected that the lowest energy part of the potential energy surface of each cluster was successfully explored.

The Cartesian coordinates and energetic data for the $RhHo_2O_n$ (n = 0-2), $Rh_2Ho_2O_m$ (m = 0-2) and $Au_{3-k}Pr_k$ (k = 0-3) structures presented in this thesis are located in the Appendix sections B, D and F for reference.

3.5. Simulated Zero-Electron Kinetic Energy and PIE Spectra Details

3.5.1. Zero-Electron Kinetic Energy (ZEKE) Spectroscopy

In Section 2.3.3, it was mentioned that ultra-violet photoelectron spectroscopy (UPS) can be used to probe the vibronic structure associated with an ionisation transition undertaken by a molecule M. The UPS spectrum of M, which will display a range of vibronic signals with varying intensities, is generally obtained by measuring the varied kinetics energies of the ejected photoelectrons. These kinetic energy values will ultimately depend on: (i) The energies of the MOs in neutral M from which they are ejected, and (ii) the energies of the vibronic transitions that occur from M to M^+. Although UPS can provide such detailed information, there is one drawback to the technique; it suffers from being a low resolution technique due to its limited ability to measure the kinetic energies of photoelectrons with sufficient accuracy.[20]

In 1984, a technique known as Zero-Electron Kinetic Energy (ZEKE) Spectroscopy was developed to provide higher-resolution detail of the underlying vibronic structure.[21,22] This is achieved by focussing only on those electrons that possess zero kinetic energy once ejected from M. Electrons that possess non-zero kinetic energies (a.k.a. kinetic electrons) are discriminated against and are not detected. Figure 3.1 illustrates the difference in the ionisation processes involved in UPS and ZEKE Spectroscopy.

As shown in Figure 3.1(a), UPS involves irradiating M with a photon that possesses more energy than is required to specifically access either the zero-point energy level or a particular vibrational energy level of M^+ (indicated by the green arrow). After interacting with this photon, the photoelectrons that are ejected from M will possess a varying range of kinetic energies (red arrows – Figure 3.1(a)) that are equal to the energy differences between the photon energy used, and the energies of the numerous vibronic transitions that accompany the ionisation transition. This is slightly contrasted to ionisation process involved in one-photon ZEKE spectroscopy, shown in Figures 3.1(b).

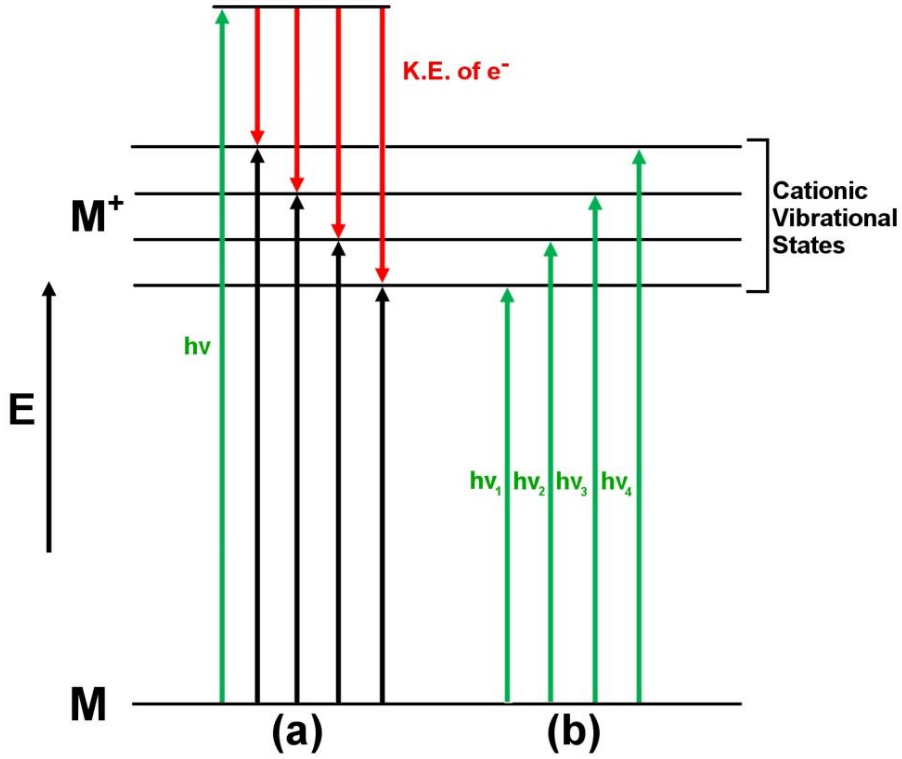

Figure 3.1. *The ionisation processes involved in: (a) Ultra-violet Photoelectron Spectroscopy (UPS), and (b) one-photon Zero-Electron Kinetic Energy (ZEKE) spectroscopy. The green arrows represent the photon energies used in each type of spectroscopy. The black arrows in process (a) represent the energy of the vibronic transition, and the red arrows in process (a) represent the range of kinetic energies the electrons can possess once ejected from M. NOTE: The kinetic energy of an ejected electron is the difference between the photon energy used, and the energy of any of the vibronic transitions.*

As observed in Figure 3.1(b), ZEKE spectroscopy involves scanning a monochromatic, tuneable light source (such as a laser) across the various vibronic states of the cation. If the energy of an incident photon is equal to that of a vibronic transition during the scan (green arrows in Figure 3.1(b)), a photoelectron will be ejected that possesses zero kinetic energy (within a certain bandwidth). These ZEKE electrons are then extracted as they are produced via a pulsed electric extraction field that is applied a short time after ionisation and helps discriminate against kinetic electrons using TOF-MS. Overall, collecting all of the ZEKE electrons produced over

the entire scan will result in the obtainment of a ZEKE spectrum, which will display a range of vibronic signals with varying intensities and higher resolution than can be achieved using UPS. Unfortunately, though this approach to ZEKE spectroscopy seems simple in theory, it has proven difficult to implement experimentally.[23] This lead to the development of pulsed field ionisation ZEKE (PFI-ZEKE) spectroscopy, which is easier to implement experimentally and provides even higher resolution ZEKE spectra than the approach illustrated in Figure 3.1(b).

In the PFI-ZEKE approach, a laser is used to excite M into long-lived, high-lying ($n > 150$) Rydberg states that converge onto rotational, vibrational, and electronic states of the cation above the ionisation threshold (i.e. in the ionisation continuum).[23-25] A few microseconds after laser excitation, a pulsed field is applied to remove the electrons from these Rydberg states, thus ionising M and giving rise to ZEKE electrons. At the same time these ZEKE electrons are produced, kinetic electrons are already present due to direct ionisation that can occur from the laser excitation. However, as these kinetic electrons are generated microseconds before the ZEKE electrons (due to the excitation laser being fired microseconds before the pulsed ionisation field is applied), TOF-MS can be used to distinguish the former electrons from the latter. Additionally, resolution of ZEKE spectra obtained with the PFI-ZEKE approach can be varied simply by controlling the speed at which the ionising pulsed field voltage is ramped up from 0 V to the desired voltage; the slower the ramp speed, the higher resolution that can be achieved (up to 0.2 cm^{-1}).[24] Irrespective of this, PFI-ZEKE spectroscopy mostly provides spectroscopic information about M^+. If vibronic hot band transitions occur, then spectroscopic information about M can also be attained.

Since its emergence, PFI-ZEKE spectroscopy has been used extensively to successfully probe the structures of various transition metal clusters.[26-31] In this previous work, DFT calculations, Franck-Condon Factor (FCF) calculations and ZEKE spectral simulations have all been used to help aid in the interpretation of the experimental

ZEKE spectra. More specifically, DFT calculations are first performed in order to determine the geometries and harmonic vibrational modes of the neutral and cationic species of the pertinent cluster. FCF calculations are then performed using the geometries and harmonic vibrational modes of the neutral and cationic species of interest in order to predict the range of vibronic signals that can occur with varying intensities (with the assumption that the neutral and ionic potentials are both harmonic). Lastly, these signals are then convoluted with Lorentzian (or alternatively, Gaussian) functions at a particular Full-Width Half-Maximum (FWHM) in order to account for spectral broadening due to unresolved rotational transitions, thus producing the simulated ZEKE spectra. Overall, if the simulated spectrum compares well with the experimental spectra, then geometric information of the neutral and cationic structures of the cluster can be inferred.

Another feature of PFI-ZEKE spectroscopy that remains relatively unexplored is its potential to be used to simulate the PIE spectra of molecules. According to Wigner's threshold law for single photoionisation, the rovibronic states of the cationic structure of a molecule should appears as "steps" in a PIE spectrum.[32] Hence, as PFI-ZEKE spectroscopy is used to probe the rovibronic states of cations, this implies that signals observed in a PFI-ZEKE spectrum should correlate well with "steps" that can be observed in PIE spectra.[24] This correlation has been noted before in previous work involving PFI-ZEKE spectroscopy.[33] Therefore, if the PFI-ZEKE spectrum (whether experimental or theoretical) is known, then a PIE spectrum can be generated simply by integrating the ZEKE signal intensities with respect to photon energy. Taatjes and co-workers have performed work akin to this in their study of the photoionisation efficiency of HONO.[34] In their work, they calculated FCFs for the photoionisation transition of *trans*-HONO from DFT-calculated neutral and cationic structures, convoluted the resulting signals with Gaussian functions with a FWHM of 0.04 or 0.06 eV to simulate spectral line broadening, and then integrated these signals with respect to photon energy to generate the simulated PIE spectrum. The resulting simulated

spectrum was found to compare fairly well with that obtained experimentally, thus inferring geometrical information about the neutral and cationic structures of HONO. More recently, Ahmed and co-workers have used the same method in their work involving PIE spectroscopy of the $PtCH_2$ and H-Pt-CH_3 clusters.[35] In a similar fashion to Taatjes and co-workers, they used DFT to determine the neutral and cationic structures of $PtCH_2$ and H-Pt-CH_3, calculated FCFs for the photoionisation transitions of both clusters, convoluted the resulting signals with Gaussian functions with a FWHM of 0.025 eV, and then integrated these signals in order to generate simulated PIE spectra for both clusters. The simulated PIE spectra were observed to compare very well with experimental PIE spectra, thus allowing the authors to infer structural information of $PtCH_2$ and H-Pt-CH_3 in their neutral and cationic states.

In this thesis, FCFs are calculated for ionisation transitions of interest for the $RhHo_2O_n$ (n = 0-2), $Rh_2Ho_2O_m$ (m = 0-2) and $Au_{3-k}Pr_k$ (k = 0-3) clusters with the intention of using them to simulate PFI-ZEKE spectra corresponding to these transitions. As discussed in Chapter Two, the implementation of the FC principle and BO approximation effectively culminates in vibronic signal intensities being proportional to the magnitude of their corresponding FCFs, justifying the use of the calculated FCFs to simulate the PFI-ZEKE spectra corresponding to the ionisation transitions of the aforementioned clusters (as PFI-ZEKE signals represent the vibronic transitions that underlie ionisation transitions). In this way, all of the simulated spectra presented in Chapters Six, Seven and Nine are produced. In a similar fashion to the work performed by Taatjes, Ahmed and their respective co-workers, the simulated PFI-ZEKE spectra are then used to simulate the PIE spectra for ionisation transitions of interest, which themselves are also presented in Chapters Six, Seven and Nine. Overall, the simulated PFI-ZEKE (termed 'ZEKE' from here onwards) and PIE spectra for the $RhHo_2O_n$ (n = 0-2), $Rh_2Ho_2O_m$ (m = 0-2) and $Au_{3-k}Pr_k$ (k = 0-3) clusters will be used to: (i) identify the most likely transition from two or more competing candidates that occurs upon ionisation for each cluster, (ii) infer geometric information about the

neutral and cationic structures of each cluster, and (iii) apply slight corrections to the experimental adiabatic IEs obtained from the PIE spectra in order to account for thermal tailing resulting from vibrational hot band transitions at 300 K.

3.5.2. Procedural details for the ZEKE and PIE Spectral Simulations

The vibronic spectral lines that constitute the ZEKE spectra presented in this thesis were simulated via multi-dimensional vibrational overlap integrals and their corresponding FCFs that were calculated for ionisation transitions of interest for the $RhHo_2O_n$ (n = 0-2), $Rh_2Ho_2O_m$ (m = 0-2) and $Au_{3-k}Pr_k$ (k = 0-3) clusters (NOTE: The relationship between vibrational overlap integrals and their FCFs is expressed mathematically in Section 2.4.2 – Equation 2.4.6). The calculations are performed using the ezSpectrum 3.0 program developed by Mozhayskiy and Krylov.[36] The program allows for the two quantities to be calculated in the following two ways: (i) If the normal coordinates of the neutral and cationic structures are the same or very similar, then the normal modes of these two structures will be parallel and thus, the vibrational wavefunctions corresponding to them can be expressed as products of one dimensional harmonic oscillator wavefunctions (the harmonic approximation). This allows for the multi-dimensional vibrational overlap integrals, and subsequently their FCFs, to be evaluated as products of one-dimensional vibrational overlap integrals,[37] and (ii) If the normal coordinates of the neutral and cationic structures are significantly different, then their corresponding normal modes will be non-parallel. This means that the multi-dimensional vibrational overlap integrals (and subsequently, their FCFs) cannot be evaluated via the products of one dimensional integrals and thus are evaluated directly, with the inclusion of Duschinsky rotations[38,39] of the normal modes of the neutral and cationic structures as full-dimensional integrals.[37] Method (ii) was preferred over method (i) and as such, all vibronic spectral lines (and their spectral intensities) constituting the ZEKE spectra presented in this thesis were simulated from multi-dimensional vibrational overlap integrals and FCFs calculated using method (ii).

The input file for the program requires the following information to calculate the vibrational overlap integrals and their corresponding FCFs so that a ZEKE "stick spectrum" can be generated for an ionisation transition of interest: (i) Optimised geometries of the neutral and cationic clusters pertinent to the ionisation transition (in Cartesian coordinates), (ii) the harmonic vibrational frequencies corresponding to these neutral and cationic structures, and (iii) the normal mode vectors for each of these harmonic vibrational frequencies. Once all of this information has been placed into the input file, various spectral parameters are set (such as adiabatic IE (a.k.a. the band origin transition), temperature, whether or not combinations bands are allowed, the maximum number of excitations allowed in the neutral and cationic states etc.) and the calculations are performed. Upon completion, an output file is generated which contains the following information regarding each ZEKE spectral line: (i) the energy position relative to the adiabatic IE set, (ii) the corresponding value of the vibrational overlap integral, (iii) the energy of the neutral vibrational state from where the vibronic transition starts relative to the ground vibrational state of the neutral cluster, (iv) the assignment of the vibronic transition underlying it (in terms of the number of quanta of one or more of the normal modes from the neutral and cationic structures), and (v) the spectral intensity, I (which is calculated by the program using Equation 2.4.8 displayed in Section 2.4.2).

All of the vibrational overlap integral and FCF calculations were performed with the allowance of combination bands and with the maximum number of excitations allowed in the neutral and cationic states set to 3 and 6, respectively. Additionally, all calculations were performed with the temperature set to 300 K, which is the approximate vibrational temperature of the neutral clusters entrained in the molecular beam (refer to Section 2.1.2). Lastly, for each ZEKE transition, the adiabatic IE (a.k.a the band origin transition) was set to the experimental appearance energy (AE) determined from the PIE spectrum of the cluster of interest. The AE value was used

instead of the experimental adiabatic IE value as it not field-corrected, thus allowing for more accurate corrections to be applied due to thermal tailing (*vide infra*).

Once the ZEKE stick spectrum corresponding to an ionisation transition of interest has been generated, it is then convoluted with a 0.00062 eV (ca. 5 cm^{-1}) FWHM Gaussian line shape in order to account for the broadening of each ZEKE signal due to underlying rotational transitions that are expected to arise from thermally populated rotational states (NOTE: Gaussian functions were chosen for convolution as Taatjes *et al.* and Ahmed *et al.* used them to simulate spectral line broadening before integration to yield their simulated PIE spectra – See Section 3.5.1). This value of FWHM was chosen so as to maintain consistency with the FWHM of ZEKE signals simulated and experimentally determined by Yang *et al.* for various other transition metal cluster species.[28,30] This convolution process then gives rise to a ZEKE spectrum that can be directly compared to a ZEKE spectra obtained experimentally.

As mentioned in Section 3.5.1, the signals observed in a ZEKE spectrum correlate well with the "steps" that can be observed in a PIE spectrum. There are two benefits that arise from this simple fact: (i) It allows for the identification of the vibronic hot band transitions at 300 K that can give rise to early onset of cluster ion signal in the PIE spectrum, thus allowing for energy corrections to be applied to the simulated ZEKE signals and subsequently, the experimental adiabatic IE of the cluster (which by definition, corresponds to the band origin transition), and (ii) once this energy correction has been applied to all energies in the simulated ZEKE spectrum, the signal intensities from the resulting corrected ZEKE spectrum can then be integrated with respect to their photon energy to yield a simulated PIE spectrum for the ionisation transition of interest, which can then be compared to that obtained experimentally. The following procedure below describes how all of this is performed so as to obtain the simulated PIE spectra and corrected experimental adiabatic IEs for the $RhHo_2O_n$ (n = 0-2), $Rh_2Ho_2O_m$ (m = 0-2), Au_2Pr and $AuPr_2$ clusters. The experimental AEs of the Au_3 and Pr_3 clusters were not determined as part of this work

so no correction could be made to their experimental adiabatic IEs. However, their ZEKE spectra were still simulated with the adiabatic IE set to previously determined experimental values for structural identification purposes.

Firstly, the lowest energy vibronic hot band signal present in the simulated ZEKE spectrum with considerable intensity is identified visually. An energy correction factor is then calculated by taking the difference between the band origin transition energy (which is set to the experimental AE of the cluster), and the energy of this vibronic hot band transition. This energy correction factor is then applied to all transition energies in the simulated ZEKE spectrum to generate a corrected ZEKE spectrum. In this corrected ZEKE spectrum, the energies of the vibronic hot band transition asserted to be responsible for thermal onset and the band origin transition are shifted higher in energy, with the new band origin transition energy corresponding to the thermally-corrected experimental AE of the cluster at 300 K (denoted $AE^{\dagger}$ in Chapters Six, Seven and Nine). Once obtained, this experimental $AE^{\dagger}$ is then field-corrected via the equation described in Section 2.4.5 to yield the corrected experimental adiabatic IE for the cluster (denoted $IE^{\dagger}$ in Chapters Six, Seven and Nine). Once this value has been determined, the corrected ZEKE spectrum is then used to simulate the PIE spectrum for the cluster as described previously (*vide supra*). It is worth noting that in some of the ZEKE spectra, it is not possible to identify the specific vibronic hot band transition that is responsible for thermal onset of the PIE spectrum due to a dense array of vibronic hot band signals being simulated. On these occasions, different arbitrary energy correction factors are used to shift the resulting simulated PIE spectrum until a good match is observed to the experimental PIE spectrum (this is after both the simulated and experimental spectra are normalised).

Once the simulated PIE spectrum has been generated for the ionisation transition of interest, it is then compared to the experimental PIE spectrum of the cluster. Both the simulated and experimental spectra are first independently normalised before the comparison is made. The experimental PIE spectrum is normalised to either

one of these two values: (i) a mean value of cluster ion signal intensity calculated by averaging all the cluster ion signal intensities from the beginning to end of a plateau region in the experimental PIE spectrum, or (ii) if the highest energy FC-allowed vibronic transition had not been reached experimentally (resulting in no observed plateau of the cluster ion signal in the experimental PIE spectrum), then the PIE spectrum is normalised to the highest cluster ion signal intensity value in the experimental PIE spectrum. The normalisation procedure for the simulated PIE spectrum is performed in the same manner as normalisation procedure (i) listed above for the experimental PIE spectra (as all simulated PIE spectra must plateau within the energy range defined by the allowed transitions). Overall, the comparison between the normalised simulated and experimental PIE spectra is indicative of how accurately the neutral and cationic structures have been calculated. If excellent qualitative comparison between the two spectra is observed, then it indicates that the neutral and cationic structures that were used to simulate the ZEKE and PIE spectra are the most likely structures of the pertinent cluster in the experiment.

3.6. References

(1) Slater, J. C. *The Self-Consistent Field for Molecules and Solids* McGraw-Hill: New York, 1974; Vol. 4.

(2) Vosko, S. H.; Wilk, L.; Nusair, M. *Can. J. Phys.* **1980**, *58*, 1200.

(3) Becke, A. D. *Phys. Rev. A* **1988**, *38*, 3098.

(4) Lee, C. T.; Yang, W. T.; Parr, R. G. *Phys. Rev. B* **1988**, *37*, 785.

(5) Becke, A. D. *J. Chem. Phys.* **1993**, *98*, 5648.

(6) Perdew, J. P. *Phys. Rev. B* **1986**, *33*, 8822.

(7) Cramer, C. J. *Essentials of Computational Chemistry*; 2nd ed.; John Wiley & Sons Ltd.: West Sussex, England, 2004.

(8) Jensen, F. *Introduction to Computational Chemistry*; 2nd ed.; John Wiley & Sons Ltd: West Sussex, England, 2007.

(9) Szabo, A.; Ostlund., N. S. *Modern Quantum Chemistry: Introduction to Advanced Electronic Structure Theory*; McGraw-Hill Publishing Company: New York, 1989.

(10) Dolg, M.; Cao, X. Y. *Chem. Rev.* **2012**, *112*, 403.

(11) Dunning, T. H. *J. Chem. Phys.* **1970**, *53*, 2823.

(12) Gaussian Website, URL: http://www.gaussian.com/ [Last Date Accessed: 22/01/2014]

(13) Andrae, D.; Haussermann, U.; Dolg, M.; Stoll, H.; Preuss, H. *Theor. Chim. Acta* **1990**, *77*, 123.

(14) Cao, X. Y.; Dolg, M. *J. Mol. Struc. (THEOCHEM)* **2002**, *581*, 139.

(15) Dolg, M.; Stoll, H.; Savin, A.; Preuss, H. *Theor. Chim. Acta* **1989**, *75*, 173.

(16) Dolg, M.; Stoll, H.; Preuss, H. *Theor. Chim. Acta* **1993**, *85*, 441.

(17) Frisch, M. J. T., G. W.; Schlegel, H. B.; Scuseria, G. E.; Robb, M. A.; Cheeseman, J. R.; Scalmani, G.; Barone, V.; Mennucci, B.; Petersson, G. A.; Nakatsuji, H.; Caricato, M.; Li, X.; Hratchian, H. P.; Izmaylov, A. F.; Bloino, J.; Zheng, G.; Sonnenberg, J. L.; Hada, M.; Ehara, M.; Toyota, K.; Fukuda, R.; Hasegawa, J.; Ishida, M.; Nakajima, T.; Honda, Y.; Kitao, O.; Nakai, H.; Vreven, T.; Montgomery, J. A., Jr.; Peralta, J. E.; Ogliaro, F.; Bearpark, M.; Heyd, J. J.; Brothers, E.; Kudin, K. N.; Staroverov, V. N.; Kobayashi, R.; Normand, J.; Raghavachari, K.; Rendell, A.; Burant, J. C.; Iyengar, S. S.; Tomasi, J.; Cossi, M.; Rega, N.; Millam, N. J.; Klene, M.; Knox, J. E.; Cross, J. B.; Bakken, V.; Adamo, C.; Jaramillo, J.; Gomperts, R.; Stratmann, R. E.; Yazyev, O.; Austin, A. J.; Cammi, R.; Pomelli, C.; Ochterski, J. W.; Martin, R. L.; Morokuma, K.; Zakrzewski, V. G.; Voth, G. A.; Salvador, P.; Dannenberg, J. J.; Dapprich, S.; Daniels, A. D.; Farkas, Ö.; Foresman, J. B.; Ortiz, J. V.; Cioslowski, J.; Fox, D. J. *Gaussian 09, Revisions B.01, C.01 and D.01* Wallingford CT, 2009.

(18) Hirshfeld, F. L. *Theor. Chim. Acta* **1977**, *44*, 129.

(19) Guerra, C. F.; Handgraaf, J. W.; Baerends, E. J.; Bickelhaupt, F. M. *J. Comp. Chem.* **2004**, *25*, 189.
(20) Hollas, J. M. *High Resolution Spectroscopy*; John Wiley & Sons Ltd: West Sussex, England, 1998.
(21) Müller-Dethlefs, K.; Sander, M.; Schlag, E. W. *Chem. Phys. Lett.* **1984**, *112*, 291.
(22) Müller-Dethlefs, K.; Sander, M.; Schlag, E. W. *Z Naturforsch A* **1984**, *39*, 1089.
(23) Simard, B. M., S. A.; Rayner, D. M.; Yang, D. S. In *Metal-Ligand Interactions in Chemistry, Physics, and Biology,* Russo, N.; Salahub., D. R., Ed.; Springer: the Netherlands, 2000, p 239.
(24) Müller-Dethlefs, K.; Schlag, E. W. *Angew. Chem. Int. Ed.* **1998**, *37*, 1346.
(25) Held, A.; Schlag, E. W. *Acc. Chem. Res.* **1998**, *31*, 467.
(26) Yang, D. S.; James, A. M.; Rayner, D. M.; Hackett, P. A. *Chem. Phys. Lett.* **1994**, *231*, 177.
(27) Yang, D. S.; Zgierski, M. Z.; Berces, A.; Hackett, P. A.; Roy, P. N.; Martinez, A.; Carrington, T.; Salahub, D. R.; Fournier, R.; Pang, T.; Chen, C. F. *J. Chem. Phys.* **1996**, *105*, 10663.
(28) Yang, D. S.; Zgierski, M. Z.; Rayner, D. M.; Hackett, P. A.; Martinez, A.; Salahub, D. R.; Roy, P. N.; Carrington, T. *J. Chem. Phys.* **1995**, *103*, 5335.
(29) Yang, D. S.; James, A. M.; Rayner, D. M.; Hackett, P. A. *J. Chem. Phys.* **1995**, *102*, 3129.
(30) Yang, D. S.; Zgierski, M. Z.; Berces, A.; Hackett, P. A.; Martinez, A.; Salahub, D. R. *Chem. Phys. Lett.* **1997**, *277*, 71.
(31) Yang, D. S.; Zgierski, M. Z.; Hackett, P. A. *J. Chem. Phys.* **1998**, *108*, 3591.
(32) Müller-Dethlefs, K. S., E. W. *Annu. Rev. Phys. Chem.* **1991**, *42*, 109.
(33) Dopfer, O.; Melf, M.; Müller-Dethlefs, K. *Chem. Phys.* **1996**, *207*, 437.
(34) Taatjes, C. A.; Osborn, D. L.; Cool, T. A.; Nakajima, K. *Chem. Phys. Lett.* **2004**, *394*, 19.
(35) Perera, M.; Metz, R. B.; Kostko, O.; Ahmed, M. *Angew. Chem. Int. Ed.* **2013**, *52*, 888.
(36) Mozhayskiy, V. A.; Krylov, A. I. ezSpectrum, http://iopenshell.usc.edu.
(37) Mozhayskiy, V. A.; Krylov, A. I. ezSpectrum v3.0 Manual.
(38) Sharp, T. E. R., H. M. *J. Chem. Phys.* **1964**, *41*, 3452.
(39) Duschinsky, F. *Acta Physicochim URSS* **1937**, *7*, 551.

Chapter Four

Benchmarking Chapter

In this chapter, the coupling of the B3P86 density functional with the SDD/SDD† basis set is benchmarked against known parameters of diatomic molecules pertinent to the $RhHo_2O_n$ (n = 0-2), $Rh_2Ho_2O_m$ (m = 0-2) and $Au_{3-k}Pr_k$ (k = 0-3) clusters. This was done in order to test the validity of using this computational methodology to calculate the electronic and geometric properties of the aforementioned clusters and subsequently, their theoretical IEs. Additionally, the use of this methodology in accurately simulating ZEKE and PIE spectra from FCF calculations between the neutral and cationic geometries is benchmarked against the experimental ZEKE and PIE spectra measured for the Nb_3O cluster.

4.1. Justification of Basis Set

In order to explain the observed trend in experimental IEs, DFT calculations (specifically employing the B3P86 density functional) are performed on the neutral and cationic $RhHo_2O_n$ (n = 0-2), $Rh_2Ho_2O_m$ (m = 0-2) and $Au_{3-k}Pr_k$ (k = 0-3) clusters. Since *f*-electrons of lanthanide atoms are known to take little to no part in chemical interaction and can make calculations very complicated and time-consuming, the large-core $4f^n$/Q=11 quasirelativistic pseudopotential (PP) version of the Stuttgart-Dresden (denoted SDD†) basis set developed by Dolg *et al.*[1-4] is used for the lanthanide atoms in the aforementioned clusters. For holmium and praseodymium, in the $[Xe]4f^{10}6s^25d^1$ and $[Xe]4f^26s^25d^1$ electron configurations respectively, all electrons apart from the 5s, 5p, 6s and 5d are taken into the PP. The $4f^n$/Q=11 notation denotes the number of *f*-electrons (n) and the number of valence electrons (11) considered for the calculations involving the Ho and Pr atoms. Thus, the SDD† basis set on Ho and Pr affords a valence electron configuration of $5s^25p^66s^25d^1$ for both lanthanide atoms. An example of where this basis set has been used to calculate various structural and electronic properties of lanthanide-containing clusters is by Nemukhin *et al.* for the Ho_2 cluster.[5] In this work, various *ab initio* methods were used (with the $4f^n$/Q=11 PP) to predict and assign the optical UV-Vis spectral transitions observed for Ho_2 suspended in an argon matrix. They found that the predicted UV-Vis transitions correlated extremely well with the experimentally observed transitions, thus confirming the assumption that *f*-electrons play no significant part in chemical interaction and that the SDD† basis set is suitable to predict and verify experimental data.

The SDD† basis set is used only for the Ho and Pr atoms in this thesis and the standard SDD basis set is used on the Rh, Au and O atoms. Therefore, it is necessary to benchmark the use of the SDD/SDD† basis set (in combination with the B3P86 density functional) against known parameters for pertinent diatomic molecules containing all atoms mentioned previously.

To test this, seven diatomic molecules were chosen to benchmark against; HoO, Ho_2, RhO, Rh_2, Pr_2, AuPr and Au_2. The former four diatomic molecules were chosen as they have known parameters and chemical bonds relevant to the $RhHo_2O_n$ (n = 0-2) and $Rh_2Ho_2O_m$ (m = 0-2) clusters. The latter three diatomic molecules were chosen for the same reason for the $Au_{3-k}Pr_k$ (k = 0-3) clusters.

Table 4.1 shows various experimental[6-17] and previously calculated[12,18-27] parameters of Ho_2, HoO, RhO and Rh_2 in addition to those calculated using our computational method. Even though there are no known experimental parameters for RhHo, the geometry of this dimer was also calculated so that relative bond strengths could be compared to the other four diatomics. In general, all of our calculated parameters were found to compare well with experimental and other previously calculated values. Notably good agreement between experimental and our calculated values are obtained for the ω_e and r values, which deviate by no more than *ca.* 67 cm^{-1} and 0.150 Å, respectively. Regarding the other parameters, the calculated D_o and IE values are also in reasonable agreement with the known experimental parameters. In the case of HoO, the IE calculated using the SDD/SDD† basis set compares better with experimental values than that calculated by Wu *et. al.*[19] Thus, our choice of coupling the B3P86 density functional with the SDD/SDD† basis set is supported.

Table 4.2 shows various experimental[28-39] and previously calculated[40-43] parameters of Au_2, AuPr and Pr_2 in addition to those calculated using our computational method. In general, all the calculated parameters were found to compare well with experimental and other previously calculated values. As with the parameters in Table 4.1, notably good agreement between experiment and our calculated values are obtained for the ω_e and r values, which deviate by no more than *ca.* 61 cm^{-1} and 0.079 Å, respectively. Of the other parameters, the calculated D_o and IE values are also in good agreement with the known parameter values. In the case of AuPr, the D_o calculated using our computational method compares extremely well with the known experimental value,[31] which is the only known parameter for this diatomic molecule.

Dimer	Calc ω_e (cm^{-1})	Known ω_e (cm^{-1})	Calc. r (Å)	Known r (Å)	Calc. Bond Strength (eV)	Known Bond Strength (eV)	Calc. IE (eV)	Known IE (eV)
Ho_2	118.1	112.0[a] 135.2[b]	3.176	3.317[a]	1.24	0.87 ± 0.18[b]	5.76	6.0 ± 1.0[b]
HoO	855.4	839[c] 828.1[d] 834[e]	1.788	1.792[c]	7.33	5.12[c] 6.33 ± 0.18[f]	6.84	7.372[c] 6.1 ± 0.5[g] 6.2 ± 0.1[h]
RhO	827.1	838.3[i] 799.0[i]	1.745	1.739[i] 1.887[j]	3.84	4.20 ± 0.43[k]	9.71	8.63 ± 0.43[l]
RhHo	322.6	-	2.711	-	4.81	-	7.07	-
Rh_2	351.0	351.7[m] 283.9 ± 1.8[o] 311.0[p] 275[q] 282[r] 204[s] 191[s] 238[t] 266[u]	2.216	2.219[m] 2.203[p] 2.25[q] 2.331[r] 2.589[s] 2.564[s] 2.673[t] 2.28[u]	1.66	1.629[m] 1.4 ± 0.3[o] 1.76[p] 1.19[q] 2.4059 ± 0.0005[v] 2.92 ± 0.22[n] 2.765[r] 1.33[s] 2.08[s] 1.500[t] 2.1[u]	7.99	7.1 ± 1.0[n] 7.82[q]

a – Reference 5 | e – Reference 8 | i – Reference 12 | m – Reference 21 | q – Reference 23 | u – Reference 24
b – Reference 6 | f – Reference 9 | j – Reference 20 | n – Reference 15 | r – Reference 25 | v – Reference 17
c – Reference 19 | g – Reference 10 | k – Reference 13 | o – Reference 16 | s – Reference 26
d – Reference 7 | h – Reference 11 | l – Reference 14 | p – Reference 22 | t – Reference 27

Table 4.1. List of the various parameters of Ho_2, HoO, RhO, RhHo and Rh_2 calculated using the B3P86 density functional and the SDD/SDD† basis sets. Also listed are the experimentally and theoretically known parameters for the pertinent dimers.

Dimer	Calc ω_e (cm^{-1})	Known ω_e (cm^{-1})	Calc. r (Å)	Known r (Å)	Calc. Bond Strength (eV)	Known Bond Strength (eV)	Calc. IE (eV)	Known IE (eV)
Au_2	173.1	180.0[a] 172.0[a] 190.9[b,c] 183[e]	2.551	2.4719[b,c] 2.547[f] 2.526[a] 2.473[a] 2.513[e] 2.512[g]	1.97	2.306 ± 0.0005[h] 2.301-2.311[j] 2.29 ± 0.02[k] 2.23 ± 0.10[e] 2.52[a] 2.28[a] 2.330[e] 2.12[g] 2.20[f]	9.81	8.82±0.18[l] 9.16 ± 0.10[m] 9.5 ± 0.3[d] 9.85[a] 9.50[a] 9.20[i] 9.15[g]
AuPr	173.9	-	2.640	-	3.01	3.144 ± 0.217[n]	6.09	-
Pr_2	183.5	244.9 ± 1.2[o]	2.631	-	1.94	-	5.47	4.52 ± 0.05[p]

a – Reference 40 e – Reference 41 i – Reference 33 m – Reference 30
b – Reference 28 f – Reference 42 j – Reference 34 n – Reference 31
c – Reference 29 g – Reference 43 k – Reference 35 o – Reference 37
d – Reference 38 h – Reference 32 l – Reference 39 p – Reference 36

Table 4.2. List of the various parameters of Au_2, AuPr and Pr_2 calculated using the B3P86 density functional and the SDD/SDD† basis sets. Also listed are the experimentally and theoretically known parameters for the pertinent dimers.

Thus, our choice of coupling the B3P86 density functional with the SDD/SDD† basis set is further supported.

4.2. ZEKE and PIE Benchmark to the Nb_3O Cluster

In order to validate the theoretical methodology employed to investigate the geometric properties of the $RhHo_2O_n$ (n = 0-2), $Rh_2Ho_2O_m$ (m = 0-2) and $Au_{3-k}Pr_k$ (k = 0-3) clusters, it is necessary to test the effectiveness of coupling the B3P86 density functional with the SDD/SDD† basis set in accurately determining structural data and in turn, simulating the ZEKE and PIE spectra of a well-characterised cluster system. The system that was chosen to benchmark against was the Nb_3O cluster. This is due to the fact that: (i) the neutral and cationic structures of Nb_3O have previously been characterised by ZEKE and PIE spectroscopy, and (ii) it is a transition metal cluster oxide and thus far, is the only one that has been characterised with combined PIE, ZEKE and DFT investigations.

4.2.1. B3P86/SDD Calculations on the Nb_3O Cluster

Figure 4.1 shows the lowest energy neutral and cationic structures calculated using B3P86 density functional coupled with the SDD basis set, together with the corresponding bond lengths for each cluster. The same structures (and their corresponding bond lengths) calculated by Yang *et al.* using the same density functional and the LANL2DZ basis set are also displayed for comparison.[44] Additionally, Table 4.3 displays the calculated normal modes of vibration for both the neutral and cationic forms of Nb_3O, together with those previously calculated at the B3P86/LANL2DZ level of theory and experimentally determined by Yang *et al.* (experimental values presented in bold).

Nb_3O	Nb_3O^+
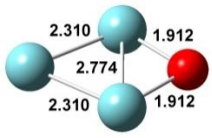	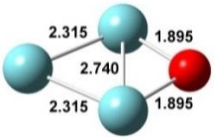
B3P86/SDD	B3P86/SDD
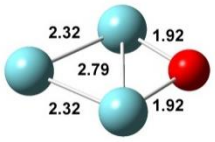	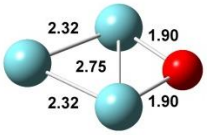
B3P86/LANL2DZ	B3P86/LANL2DZ

Figure 4.1. *Lowest energy neutral and cationic structures of the Nb_3O cluster calculated with the B3P86 density functional and the SDD basis set. The same structures calculated by Yang et al. using the same density functional and the LANL2DZ basis set are also included (Nb atoms in blue and O atoms in red).[44] Bond lengths have also been labelled for each structure (in Å - labelled to two d.p. for the B3P86/LANL2DZ structures as reported by Yang et al.).*

Mode	Symmetry[a]	Motion[b]	Value for Nb_3O (cm^{-1})	Value for Nb_3O^+ (cm^{-1})
ν_1	a_1	ν_s Nb-O	729 (733, **710 ± 20**)	757 (764)
ν_2	a_1	ν_s Nb-Nb	348 (350)	374 (379)
ν_3	a_1	δ_s Nb-Nb-Nb	313 (310, **320 ± 1**)	319 (315, **312 ± 1**)
ν_4	b_1	ν_a Nb-O	568 (572)	600 (608)
ν_5	b_1	ν_a Nb-Nb	226 (233)	259 (260)
ν_6	b_2	π Nb_3O	284 (286)	267 (274)

Table 4.3. *Calculated vibrational modes of the lowest energy neutral and cationic minima of Nb_3O at the B3P86/SDD level of theory. Presented in parentheses for comparison are the vibrational mode data calculated by Yang et al. at the B3P86/LANL2DZ level of theory. The values determined experimentally are also presented in the parentheses and are shown in boldface.[44]*

[a] *All structures possess C_{2v} symmetry.*

[b] ν_s: symmetric stretch; ν_a: asymmetric stretch; δ_s: symmetric bend; π: *Out-of-Plane Deformation.*

As observed, the bond lengths and vibrational modes calculated using the B3P86/SDD level of theory compare extremely well with those determined previously by Yang *et al.*

4.2.2. The ZEKE Spectrum of the Nb_3O Cluster

The next step is to verify whether ZEKE spectra simulated using the neutral and cationic structures of Nb_3O calculated at the B3P86/SDD level of theory can reproduce results that can rationalise, and compare well with, the experimental ZEKE spectrum of Nb_3O (just as Yang and co-workers did with their B3P86/LANL2DZ calculations).

Figure 4.2 shows the ZEKE spectrum for the $^1A_1 \leftarrow {}^2B_2$ transition of Nb_3O simulated at 300 K using the neutral and cationic structures, and their corresponding vibrational modes, calculated at the B3P86/SDD level of theory (Figure 4.1 and Table 4.3). The band origin (0_0^0) transition energy for the simulation was set at 5.526 eV (*ca.* 44747 cm^{-1}), which is the dc field-corrected experimental IE determined by Yang *et al.* for the Nb_3O cluster. Shown inset is the experimental ZEKE spectra of Nb_3O collected at 100 K and 300 K by the same authors for comparison.[44] As observed, the simulated ZEKE spectrum compares extremely well with the experimental ZEKE spectrum, with the signal intensities and band positions of the relevant transitions reproduced exceedingly well.

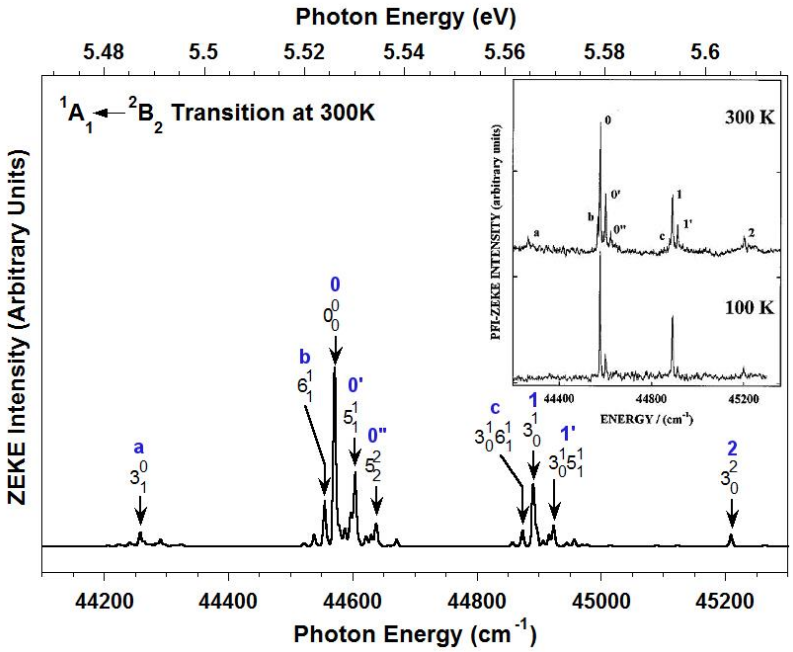

Figure 4.2. *ZEKE spectrum simulated at 300 K for the* $^1A_1 \leftarrow {}^2B_2$ *transition of the* Nb_3O *cluster. For the simulated ZEKE signals that are relevant to the experimental ZEKE spectrum, they have been labelled according to their corresponding experimental ZEKE signals. Inset: The* experimental ZEKE spectra of Nb_3O collected at 100 K and 300 K by Yang *et al.*[44]

4.2.3. The PIE Spectrum of the Nb_3O Cluster

The final benchmarking test to be carried out relates to the potential of the simulated ZEKE spectrum of Nb_3O to produce a PIE spectrum, which is obtained by integrating the simulated ZEKE signal intensities with respect to photon energy. Comparison between the experimental and simulated PIE spectra will ultimately show how accurately the neutral and cationic geometries have been calculated, in addition to providing information regarding their FC overlap. Characteristics of each spectrum to compare include the shape of the PIE curve, the gradient of cluster signal onset (or its steepness), and the energy region in which each spectrum is observed to plateau due to the last FC-allowed transition being attained.

Figure 4.3 shows the simulated PIE spectrum attained by integrating the simulated ZEKE spectrum for the $^1A_1 \leftarrow {}^2B_2$ transition with respect to photon energy. Shown inset is the experimental PIE spectrum of Nb_3O measured by Yang *et al.* with the experimental appearance energy (AE) determined to lie at 44475 cm^{-1} (*ca.* 5.514

eV).[44] For this particular simulated PIE spectrum, the corresponding ZEKE spectrum is simulated with the 0_0^0 transition set to this experimental AE value, as opposed to the dc-field corrected IE used for simulating the ZEKE spectrum shown in Figure 4.2. This is done so that the thermal-tailing effect observed in experimental PIE spectra measured at 300 K can be eventually be accounted for (*vide infra* – Section 4.2.4). Upon comparison, it is observed that the simulated PIE spectrum compares extremely well with the experimental PIE spectrum, with both displaying sharp onset at around the same energy and plateauing at around 44600 cm^{-1} (*ca.* 5.530 eV). This further indicates that the neutral and cationic geometries of Nb_3O have accurately been calculated at the B3P86/SDD level of theory, that the FC overlap between these two structures has been accurately accounted for, and that this level theory can reliably PIE spectra that compares well with those attained experimentally.

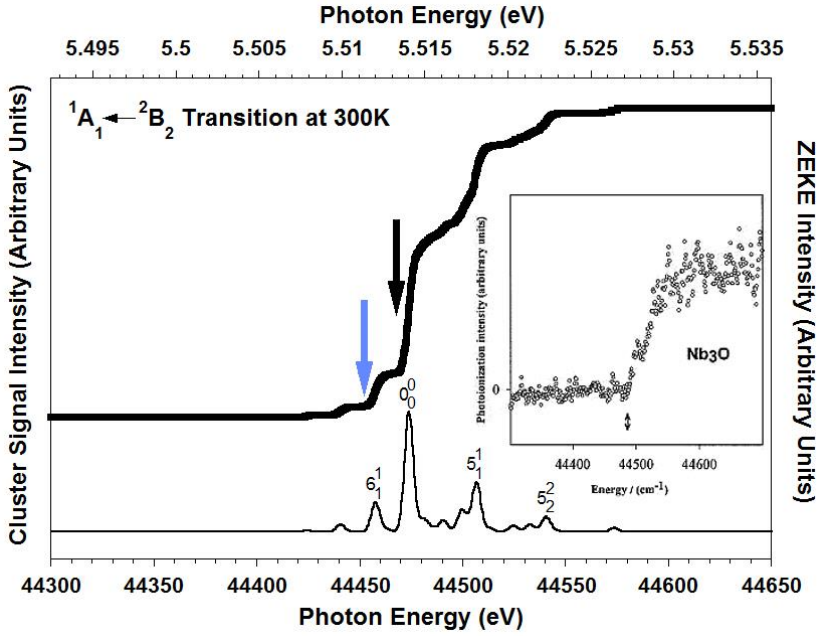

Figure 4.3. *The corrected ZEKE and PIE spectra for the* $^1A_1 \leftarrow {}^2B_2$ *transition of* Nb_3O *simulated at 300 K. The blue arrow indicates the energy of the most significant hot band transition that initiates thermal onset of the PIE spectrum. The black arrow indicates the energy of the band origin and the corrected adiabatic ionisation energy of* Nb_3O*. Inset: The* experimental PIE spectrum of Nb_3O collected at 300 K by Yang *et al.*[44]

4.2.4. Accounting for the Thermal Tailing Effect in PIE Spectra

In addition to providing information regarding the neutral and cationic structures and their FC overlap, the simulated ZEKE and PIE spectra can also be used to account for the thermal-tailing effect. More specifically, since the PIE experiments are conducted at 300 K, the obtained spectra will exhibit earlier than anticipated cluster signal onset as a result of the vibrational hot band transitions that can occur at this temperature (known the "thermal-tailing effect"). This can lead to attaining experimental IE values that are slightly lower than the true adiabatic IE values (i.e. due to the 0_0^0 transition). Hence, it is also necessary to test the potential of determining and applying the necessary correction factors to the experimental IEs obtained from the PIE spectra in order to account for this phenomenon.

The simulation of the ZEKE spectrum that yields the simulated PIE spectrum shown in Figure 4.3 is performed with the 0_0^0 transition set to the experimental AE of Nb_3O (as mentioned earlier in Section 4.2.3). This is based on the assumption that the initial onset observed in the PIE spectrum occurs due to the 0_0^0 transition, with any additional onset observed thereafter being due to various other vibronic transitions. However, the presence of the strong hot band feature at 44457 cm^{-1} (the 6_1^1 vibronic transition - indicated with the blue arrow in Figure 4.3) indicates that the initial cluster signal onset is most likely due to this vibronic transition and not the 0_0^0 transition. Hence, the initial experimental cluster signal onset observed at 44475 cm^{-1} may actually be due to the 6_1^1 vibronic transition and not the 0_0^0 transition. Therefore, the initial experimental cluster signal onset observed at 44475 cm^{-1} is asserted to be due to the 6_1^1 vibronic transition and the experimental AE (i.e. the 0_0^0 transition) of Nb_3O lies slightly higher in energy. By adding a correction factor of 18 cm^{-1} (ca. 0.00223 eV - the difference between the energy assigned to the theoretical 0_0^0 transition (44475 cm^{-1}) and the energy simulated for the 6_1^1 vibronic transition (44457 cm^{-1})) to all of the transitions energies in the simulated ZEKE spectrum, the energy of the 6_1^1 vibronic transition shifts to 44475 cm^{-1} (*ca.* 5.514 eV) and the energy of the 0_0^0 transition shifts

to 44493 cm^{-1} (*ca.* 5.516 eV), with the latter being the thermally-corrected experimental AE of Nb_3O. Applying the appropriate dc-field correction factor of +95 cm^{-1} (the IE shift caused by the dc extraction field in the experimental setup of Yang *et al.*) to this new 0_0^0 transition energy yields a value of 44588 cm^{-1} (*ca.* 5.528 eV), the field- and thermally-corrected experimental IE for Nb_3O.

Upon comparison of the corrected experimental IE value with the dc field-corrected experimental IE value determined by Yang *et al.* (44570 cm^{-1} – *ca.* 5.526 eV), there is no significant difference observed between the two values. However, this is only because the energy difference between the 6_1^1 vibronic transition and the 0_0^0 transition is minuscule. If the energy difference between the hot band transition asserted to give rise to thermal onset and the 0_0^0 transition is considerably larger, then there will be larger correction factors that would need to applied to experimental IE values; which could apply to the $RhHo_2O_n$ (n = 0-2), $Rh_2Ho_2O_m$ (m = 0-2) and $Au_{3-k}Pr_k$ (k = 0-3) clusters discussed throughout this thesis.

4.3. Conclusion

In summary, this chapter has shown that the coupling of the B3P86 density functional with the SDD/SDD† basis set to accurately calculate the electronic and geometric properties of the $RhHo_2O_n$ (n = 0-2), $Rh_2Ho_2O_m$ (m = 0-2) and $Au_{3-k}Pr_k$ (k = 0-3) clusters is valid. In addition, it was also demonstrated that the neutral and cationic geometries calculated using this methodology can be used to accurately simulate the ZEKE and PIE spectra of the aforementioned clusters from FCF calculations. These conclusions were verified as: (i) calculated geometric and electronic parameters of diatomic molecules pertinent to the clusters at the B3P86/(SDD/SDD†) level of theory were found to compare well with previously determined experimental and theoretical values, and (ii) simulated ZEKE and PIE spectra simulated from neutral and cationic geometries of the Nb_3O cluster calculated at the B3P86/SDD level of theory were found to compare well with those obtained experimentally in previous work. Lastly, it was also demonstrated that the simulated ZEKE and PIE spectra can also be used to determine the correction factors that need to be applied to experimental IE values obtained at 300 K in order to account for the slight red-shift of them due to the thermal-tailing effect.

4.4. References

(1) Dolg, M.; Stoll, H. *Theor. Chim. Acta* **1989**, *75*, 369.
(2) Dolg, M.; Stoll, H.; Preuss, H. *Theor. Chim. Acta* **1993**, *85*, 441.
(3) Dolg, M.; Stoll, H.; Preuss, H. *J. Mol. Struc. (THEOCHEM)* **1992**, *96*, 239.
(4) Dolg, M.; Stoll, H.; Savin, A.; Preuss, H. *Theor. Chim. Acta* **1989**, *75*, 173.
(5) Nemukhin, A. V.; Ermilov, A. Y.; Petrukhina, M. A.; Klotzbucher, W. E.; Smets, J. *Spectrochim. Acta A* **1997**, *53*, 1803.
(6) Cocke, D. L.; Gingerich, K. A. *J. Phys. Chem.* **1971**, *75*, 3264.
(7) Willson, S. P.; Andrews, L. *J. Phys. Chem. A* **1999**, *103*, 6972.
(8) Gatterer, A. *Ric. Spettroscop.* **1942**, *1*, 139.
(9) Dulick, M.; Murad, E.; Barrow, R. F. *J. Chem. Phys.* **1986**, *85*, 385.
(10) Murad, E.; Hildenbrand, D. L. *J. Chem. Phys.* **1980**, *73*, 4005.
(11) Ackermann, R. J.; Rauh, E. G.; Thorn, R. J. *J. Chem. Phys.* **1976**, *65*, 1027.
(12) Citra, A.; Andrews, L. *J. Phys. Chem. A* **1999**, *103*, 4845.
(13) Pedley, J. B.; Marshall, E. M. *J. Phys. Chem. Ref. Data* **1983**, *12*, 976.
(14) Chen, Y.-M.; Armentrout, P. B. *J. Chem. Phys.* **1995**, *103*, 618.
(15) Cocke, D. L.; Gingeric.Ka *J. Chem. Phys.* **1974**, *60*, 1958.
(16) Wang, H. M.; Haouari, H.; Craig, R.; Liu, Y. F.; Lombardi, J. R.; Lindsay, D. M. *J. Chem. Phys.* **1997**, *106*, 2101.
(17) Langenberg, J. D.; Morse, M. D. *J. Chem. Phys.* **1998**, *108*, 2331.
(18) Nemukhin, A. V.; Ermilov, A. Y.; Petrukhina, M. A.; Klotzbucher, W. E.; Smets, J. *Spectrochim. Acta, Part A* **1997**, *53*, 1803.
(19) Wu, Z. J.; Guan, W.; Meng, J.; Su, Z. M. *J. Cluster Sci.* **2007**, *18*, 444.
(20) Mains, G. J.; White, J. M. *J. Phys. Chem.* **1991**, *95*, 112.
(21) Wu, Z. J. *Chem Phys Lett* **2004**, *383*, 251.
(22) Yanagisawa, S.; Tsuneda, T.; Hirao, K. *J. Comp. Chem.* **2001**, *22*, 1995.
(23) Lacaze-Dufour, C.; Mineva, T.; Russo, N. *Int. J. Quantum Chem.* **2001**, *85*, 162.
(24) Balasubramanian, K.; Liao, D. W. *J. Phys. Chem.* **1989**, *93*, 3989.
(25) Chien, C. H.; Blaisten-Barojas, E.; Pederson, M. R. *Phys. Rev. A* **1998**, *58*, 2196.
(26) Harada, M.; Dexpert, H. *J. Phys. Chem.* **1996**, *100*, 565.
(27) Illas, F.; Rubio, J.; Canellas, J.; Ricart, J. M. *J. Chem. Phys.* **1990**, *93*, 2603.
(28) Huber, K. P.; Herzberg, G. *Molecular Spectra and Molecular Structure IV. Constants of Diatomic Molecules*; Van Nostrand Reinhold Company, 1979.
(29) Ames, L. L.; Barrow, R. F. *Trans. Faraday Soc.* **1967**, *63*, 39.
(30) Cheeseman, M. A.; Eyler, J. R. *J. Phys. Chem.* **1992**, *96*, 1082.
(31) Gingericich, K. A.; Finkbeiner, H. C. *J. Chem. Phys.* **1970**, *52*, 2956.
(32) Hopkins, W. S.; Hamilton, S. M.; McNaughter, P. D.; Mackenzie, S. R. *Chem. Phys. Lett.* **2009**, *483*, 10.

(33) Jackschath, C.; Rabin, I.; Schulze, W. *Ber. Bunsen Phys. Chem.* **1992**, *96*, 1200.
(34) James, A. M.; Kowalczyk, P.; Simard, B.; Pinegar, J. C.; Morse, M. D. *J. Mol. Spec.* **1994**, *168*, 248.
(35) Kordis, J.; Gingerich, K. A.; Seyse, R. J. *J. Chem. Phys.* **1974**, *61*, 5114.
(36) Koretsky, G. M.; Knickelbein, M. B. *Eur. Phys. J. D* **1998**, *2*, 273.
(37) Shen, X. L.; Fang, L.; Chen, X. Y.; Lombardi, J. R. *J. Chem. Phys.* **2000**, *113*, 2233.
(38) Stearns, C. A.; Kohl, F. J. *J. Phys. Chem.* **1973**, *77*, 136.
(39) Takahashi, L. K.; Zhou, J.; Wilson, K. R.; Leone, S. R.; Ahmed, M. *J. Phys. Chem. A* **2009**, *113*, 4035.
(40) Bonacic-Koutecky, V.; Burda, J.; Mitric, R.; Ge, M. F.; Zampella, G.; Fantucci, P. *J. Chem. Phys.* **2002**, *117*, 3120.
(41) Liu, W. J.; van Wullen, C. *J. Chem. Phys.* **2000**, *113*, 2506.
(42) Mills, G.; Gordon, M. S.; Metiu, H. *Chem. Phys. Lett.* **2002**, *359*, 493.
(43) Wesendrup, R.; Hunt, T.; Schwerdtfeger, P. *J. Chem. Phys.* **2000**, *112*, 9356.
(44) Yang, D. S.; Zgierski, M. Z.; Rayner, D. M.; Hackett, P. A.; Martinez, A.; Salahub, D. R.; Roy, P. N.; Carrington, T. *J. Chem. Phys.* **1995**, *103*, 5335.

Chapter Five

Photoionisation Efficiency Spectroscopy of Gas-Phase $RhHo_2O_n$ (n = 0-2) and $Rh_2Ho_2O_m$ (m = 0-2) Clusters.

This chapter presents the experimentally determined adiabatic IEs of the gas-phase $RhHo_2O_n$ (n = 0-2) and $Rh_2Ho_2O_m$ (m = 0-2) clusters attained using PIE spectroscopy. Generation of a whole variety of Rh-Ho bimetallic bare and oxide clusters in the laser ablation process is initially discussed, followed by presentation and discussion of the PIE spectra of each pertinent cluster and how observed IE trends in as a function of sequential addition of oxygen atoms differ between each series.

5.1. Mass Spectra and Photoionisation Measurements

Figure 5.1 shows a TOF mass spectrum of holmium and rhodium-holmium clusters and their oxide counterparts recorded at 222 nm under single-photon ionisation conditions (see Appendix A for linear √Mass vs. TOF conversion graph). As observed in Figure 5.1, holmium oxide clusters of the form Ho_2O_x (x = 0-3) and Ho_3O_y (y = 1-5) were generated in abundance. The Ho_2 dimer was found to form with very little intensity and the Ho_3 trimer did not appear in the mass spectrum. This lack of aggregation of holmium atoms to form molecular clusters is consistent with what has been observed previously by Nagao *et al.* and is attributed to the Coulombic repulsion that arises from their ability to act as three-electron donors.[1,2] As also observed in Figure 5.1, the holmium-rhodium species $RhHo_2O_n$ (n = 0-2), $Rh_2Ho_2O_m$ (m = 0-2), $RhHo_3O_b$ (b = 0-5) and $Rh_3Ho_2O_a$ (a = 1-2) are generated with moderate to strong signal intensities. The RhHo dimer is also observed to form with very weak intensity. However, the rhodium dominated species Rh_2HoO_n and Rh_3HoO_n are not present in the mass spectrum. This is either due to their absence in the molecular beam or the IE of these clusters being greater in energy than the minimum ionisation wavelength the mass spectrum was collected at (< 222 nm). Due to the fact that the $Rh_3Ho_2O_a$ (a = 1-2) clusters appear in the mass spectrum at 222 nm, it is most likely the latter reason that accounts for their non-appearance.

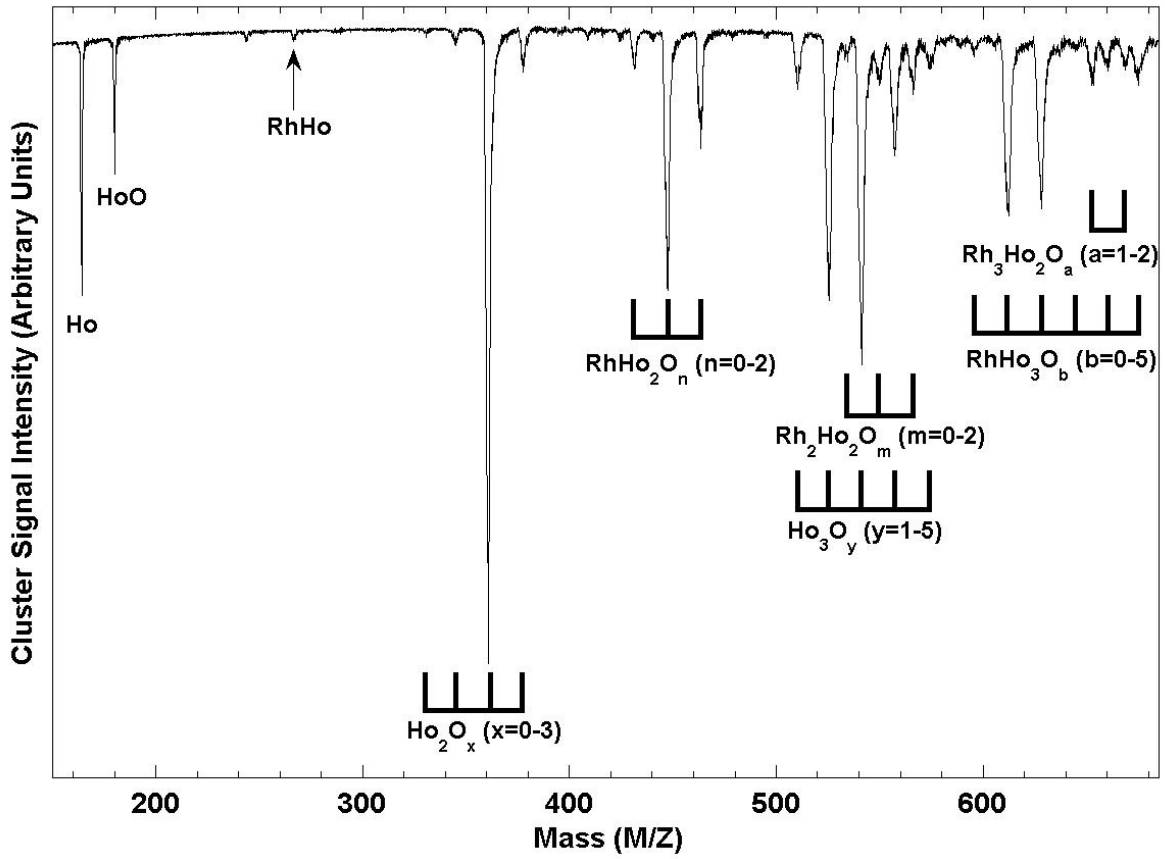

Figure 5.1. *Mass spectrum of various holmium and holmium-rhodium bimetallic clusters and their oxides recorded at 222 nm under single photon ionisation conditions.*

5.2. Mass and PIE Spectra of the $RhHo_2O_n$ (n = 0-2) Clusters

Figures 5.2(a)-(c) show the portion of the mass spectrum of that contains the $RhHo_2O_n$ (n = 0-2) clusters recorded three different ionising wavelengths; 262 nm, 242 nm and 222 nm. In the spectrum at 222 nm (Figure 5.2(c)), it is clearly seen that all three clusters appear with moderate to high intensities. The cluster $RhHo_2O$ has the most intense peak, followed by $RhHo_2O_2$ then $RhHo_2$. Ionisation at 242 nm (Figure 5.2(b)) yields only $RhHo_2O$, with a slight decrease in intensity. At 262 nm (Figure 2a), all signals have decreased to baseline, implying that none of these species are ionised at this wavelength.

The PIE spectra for the $RhHo_2O_n$ (n = 0-2) species are shown in Figures 5.3(a)-(c), respectively. As observed in Figure 5.3(b), $RhHo_2O$ shows a dramatic increase in intensity from baseline. This signifies excellent Franck-Condon (FC) overlap between the electronic states of the neutral and the cation and is indicative of minor geometric change upon ionisation. The PIE spectrum for this species is also observed to level off after 5.4 eV, satisfying that the highest energy FC-allowed transition was attained. Interestingly, the PIE spectrum for this species displays structure before levelling off, which is not usually observed for molecules this large. We have confirmed that this is not due to a change in cluster abundance as PIE curves of other, simultaneously-recorded species with low IEs (i.e. $RhHo_3O_2$) did not show this behaviour. Contrary to $RhHo_2O$, the PIE spectra for $RhHo_2$ and $RhHo_2O_2$ show very gradual onsets of ionisation from baseline, signifying poor FC overlap between the neutral and the cation for these two clusters. In addition, the PIE curves for these two species also show no levelling off after 5.6 eV (222 nm) towards the higher energy parts, indicating that the highest FC-allowed transition has not yet been attained.

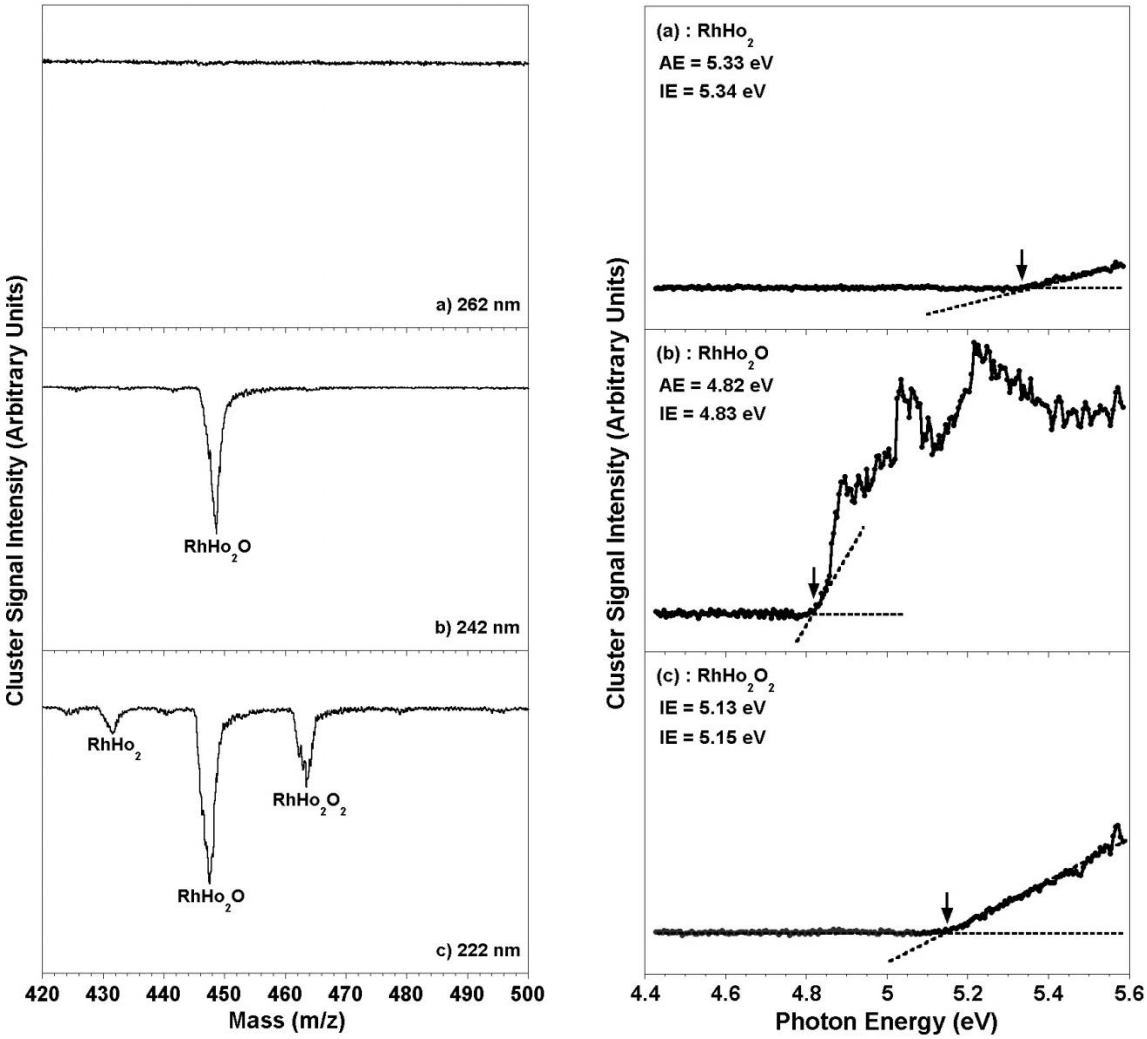

Figure 5.2. (Left) *Mass spectra of the $RhHo_2O_n$ (n=0-2) clusters recorded at three different ionisation wavelengths: (a) 262 nm, (b) 242 nm, and (c) 222 nm.*
Figure 5.3. (Right) *PIE spectra of the $RhHo_2O_n$ (n=0-2) clusters. The determined AEs and IEs are also displayed (uncertainty in IEs = ±0.05 eV), with the black arrows indicating the values of the IEs.*

In addition to the PIE Curves for the $RhHo_2O_n$ (n = 0-2) species, Figures 5.3(a)-(c) also show the experimentally determined appearance energies (AEs) and adiabatic IEs for the $RhHo_2O_n$ (n = 0-2) clusters. The IE for $RhHo_2$ is determined to be 5.34 eV, which is low for a Rh containing cluster considering that pure Rh clusters are known to have very high IEs (Rh_{1-4}, IE = 6.42 eV-7.87 eV, Rh_{5-18}, IE $<$ 6.42 eV).[3] The addition of an oxygen atom to the $RhHo_2$ bare metal cluster to yield $RhHo_2O$ results in the IE changing by -0.51 eV. The addition of a second oxygen atom then results in an IE change of +0.32 eV relative to $RhHo_2O$. In comparing the IEs of $RhHo_2$ and $RhHo_2O_2$, it is observed that the addition of two oxygen atoms changes the IE by only -0.19 eV.

5.3. Mass and PIE Spectra of the $Rh_2Ho_2O_m$ (m = 0-2) Clusters

Figures 5.4(a)-(c) show the portion of the mass spectrum containing the $Rh_2Ho_2O_m$ (m = 0-2) clusters recorded at three different ionising wavelengths: 262 nm, 242 nm and 222 nm. As observed in the mass spectrum recorded at 222 nm (Figure 5.4(c)), all three of the $Rh_2Ho_2O_m$ clusters appear with minimal to moderate signal intensities accompanied by the Ho_3O_y (y = 1-5) clusters, which themselves appear with moderate to strong signal intensities. Ionisation at 242 nm and 262 nm (Figure 5.4(b) and 5.4(a)) yields only the Ho_3O_y clusters, with the signals due to all of the $Rh_2Ho_2O_m$ clusters decreasing to baseline in both mass spectra. This implies that none of the $Rh_2Ho_2O_m$ clusters are ionised at these wavelengths.

The PIE spectra for the $Rh_2Ho_2O_m$ (m = 0-2) clusters are shown in Figures 5.5(a)-(c). The PIE spectrum for Rh_2Ho_2 (Figure 5.5(a)) shows a weak to moderate increase in intensity from baseline. This signifies a reasonable amount of FC overlap between the electronic states of the neutral and cationic species and is indicative of a moderate amount of geometric change upon ionisation. Contrary to this, the PIE spectra of Rh_2Ho_2O and $Rh_2Ho_2O_2$ (Figures 5.5(b) and 5.5(c)) both display a relatively sharp increase of cluster signal intensity from baseline. This signifies excellent FC overlap between the electronic states of the neutral and cationic species for both Rh_2Ho_2O and $Rh_2Ho_2O_2$ and is indicative of no appreciable geometric change upon ionisation of these clusters. As also observed in Figures 5.5(a)-(c), none of the clusters appear to have reached a constant level of signal intensity in their PIE spectra. This indicates that the highest energy FC-allowed transitions were not attained for any of the clusters.

In addition to the PIE spectra, Figures 5.5(a)-(c) also show the experimentally determined AEs and adiabatic IEs for the $Rh_2Ho_2O_m$ (m = 0-2) clusters. The experimental IE for Rh_2Ho_2 was determined to be 5.47 eV, which as stated previously, is low for a rhodium-containing metal cluster. The addition of an oxygen atom to Rh_2Ho_2 to yield Rh_2Ho_2O results in the IE changing by -0.01 eV. The addition of a

second sequential oxygen atom to yield $Rh_2Ho_2O_2$ results in an IE change of -0.05 eV relative to the IE of Rh_2Ho_2O. In comparing the experimentally determined IEs of Rh_2Ho_2 and $Rh_2Ho_2O_2$, the IE is found to change by -0.06 eV.

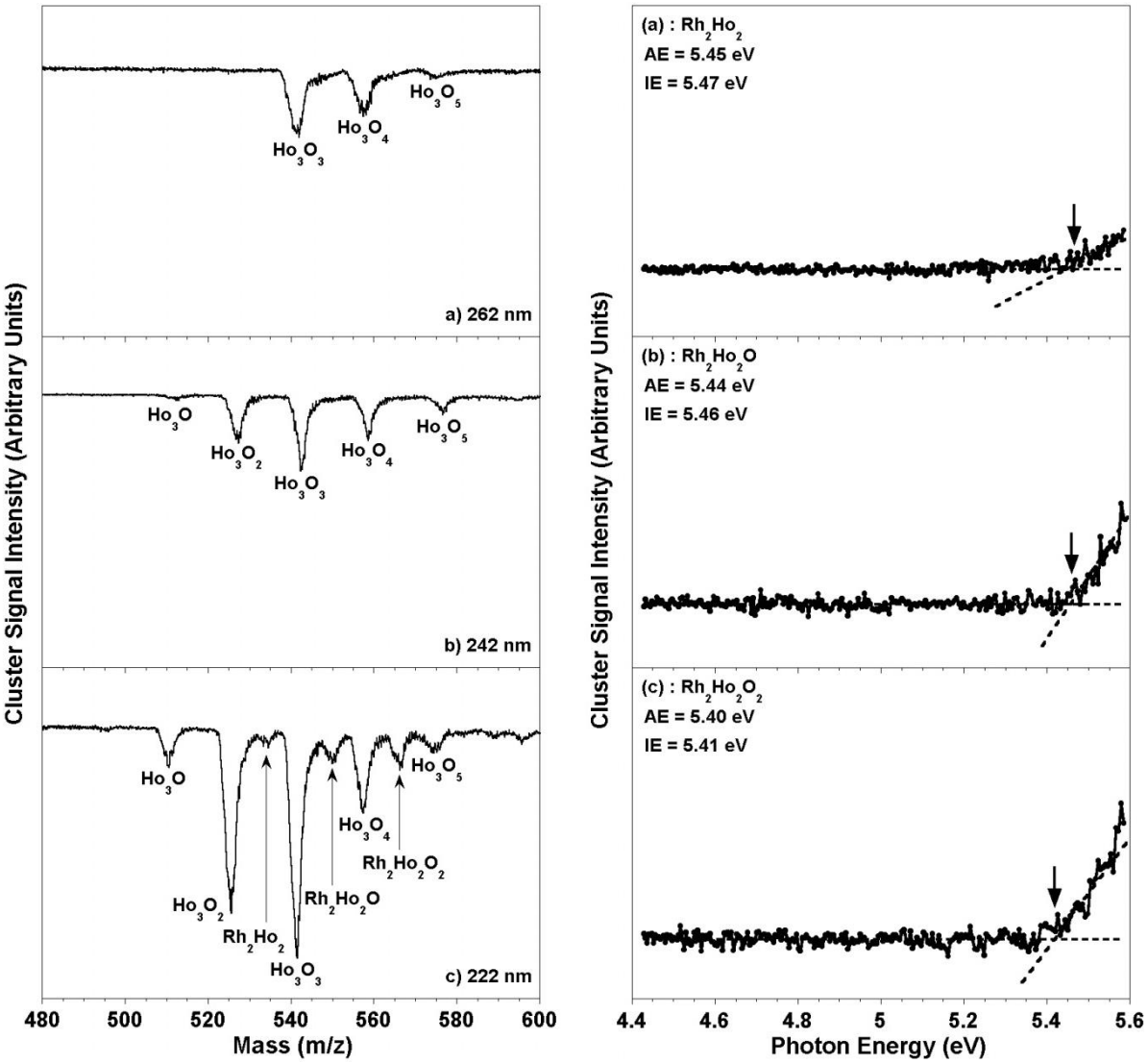

Figure 5.4. (Left) *Mass spectra of the $Rh_2Ho_2O_m$ (m = 0-2) clusters recorded at three different ionisation wavelengths: (a) 262 nm, (b) 242 nm, and (c) 222 nm.*

Figure 5.5. (Right) *PIE spectra of the $Rh_2Ho_2O_m$ (m = 0-2) clusters. The determined AEs and IEs are also displayed (uncertainty in IEs = ±0.05 eV), with the black arrows indicating the values of the IEs.*

5.4. Comparison between the $RhHo_2O_n$ and $Rh_2Ho_2O_m$ Clusters

Figure 5.6 displays the experimental adiabatic IEs determined for the $RhHo_2O_n$ (n = 0-2) and $Rh_2Ho_2O_m$ (m = 0-2) clusters. Relative to the bare clusters, the IE of Rh_2Ho_2 is found to be 0.10 eV higher than $RhHo_2$. As observed for the $Rh_2Ho_2O_m$ (m = 0-2) cluster series, it appears that the sequential addition of oxygen atoms onto Rh_2Ho_2 has little to no effect on the IE. This is contrary to the IE trend observed for the $RhHo_2O_n$ (n = 0-2) clusters, in which the addition of one and two oxygen atoms onto $RhHo_2$ is found to change the IE by -0.51 eV and -0.19 eV relative to the IE of $RhHo_2$, respectively. Therefore, this experimental data implies that the addition of a rhodium atom onto $RhHo_2$ inhibits the significant change in electronic structure that is accompanied by oxidation.

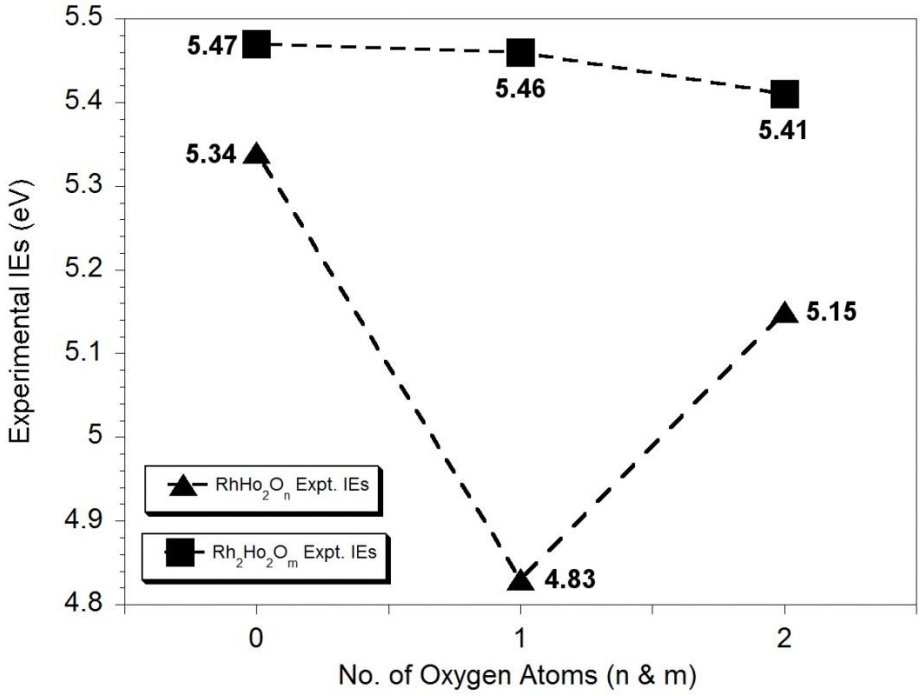

Figure 5.6. *Graph showing the experimentally determined adiabatic IE values for the $RhHo_2O_n$ (n = 0-2) and $Rh_2Ho_2O_m$ (m = 0-2) clusters as a function of constituent oxygen atoms. The experimental uncertainty associated with these IE values is conservatively estimated to be ±0.05 eV.*[4]

5.5. Conclusion

The gas-phase $RhHo_2O_n$ (n = 0-2) and $Rh_2Ho_2O_m$ (m = 0-2) bimetallic bare and oxide clusters have been generated and detected experimentally using a dual laser ablation source coupled with a TOF-MS, and their experimental adiabatic IEs determined using PIE spectroscopy. Concerning the $RhHo_2On$ (n = 0-2) clusters, the experimental IE of $RhHo_2O$ was found to be significantly red-shifted in comparison to the experimental IEs of $RhHo_2$ and $RhHo_2O_2$. This implies that there must be significant changes in the electronic properties of the $RhHo_2$ cluster upon the sequential addition of oxygen atoms. Contrary to the IE trend observed for the $RhHo_2O_n$ (n =0-2) clusters, the experimental adiabatic IEs for all $Rh_2Ho_2O_m$ (m = 0-2) clusters were found to remain effectively constant upon the sequential addition of oxygen atoms. This suggested that the addition of a rhodium atom onto the $RhHo_2$ cluster inhibits the significant change in electronic structure experienced by this cluster when it undergoes oxidation.

5.6. References

(1) Nagao, S.; Negishi, Y.; Kato, A.; Nakamura, Y.; Nakajima, A.; Kaya, K. *J. Phys. Chem. A* **1999**, *103*, 8909.

(2) Nagao, S.; Negishi, Y.; Kato, A.; Nakamura, Y.; Nakajima, A.; Kaya, K. *J. Chem. Phys.* **2002**, *117*, 3169.

(3) Zakin, M. R.; Cox, D. M.; Kaldor, A. *J. Chem. Phys.* **1988**, *89*, 1201.

(4) Knickelbein, M. B.; Yang, S. *J. Chem. Phys.* **1990**, *93*, 5760.

Chapter Six

DFT Investigations, FCF Calculations and Spectral Simulations of the Gas-Phase $RhHo_2O_n$ (n = 0-2) Clusters

This chapter presents the theoretical insight attained from DFT investigations and FCF calculations performed on the $RhHo_2O_n$ (n = 0-2) clusters. Various neutral and cationic structures calculated to lie within *ca.* 1 eV of the lowest energy structures of each charge state (including their intrinsic properties such as Hirshfeld charges, calculated vibrational modes etc.) are presented and discussed. Following this, ZEKE and PIE spectral simulations developed from FCF calculations performed for ionisation transitions of interest are presented, discussed and compared to the experimentally obtained PIE spectra shown in Chapter Five. Overall, all theoretical data obtained from these investigations are used to: (i) assign the vibronic transitions that are most likely to occur upon ionisation for each cluster, (ii) apply slight corrections to the experimental IEs of these clusters in order to account for thermal tailing that results from vibrational hot band transitions at 300 K, and (iii) determine the calculated IEs of the $RhHo_2O_n$ (n = 0-2) clusters and compare them to those obtained experimentally.

6.1. DFT Results for the $RhHo_2$ Cluster

6.1.1. Lowest Energy Neutral and Cationic Structures

For the neutral $RhHo_2$ species, the lowest energy structure is determined to be a doublet C_{2v} isosceles triangle in a $^2A_1$ state (Structure **IA** – Figure 6.1) with Ho-Ho and Rh-Ho bond lengths of 3.498 Å and 2.386 Å, respectively. For the cationic $RhHo_2$ species, there are two isomers calculated that are of significant interest. The lowest energy structure of these two cationic isomers is a singlet C_{2v} isosceles triangle in a $^1A_1$ state (Structure $\mathbf{IA}^+$ – Figure 6.1) with Ho-Ho and Rh-Ho bond lengths of 3.923 Å and 2.380 Å, respectively. The other is a triplet C_{2v} isosceles triangle in a $^3B_2$ state (structure $\mathbf{IB}^+$ – Figure 6.1) with Ho-Ho and Rh-Ho bond lengths of 3.391 Å and 2.380 Å, respectively. The triplet structure is calculated to lie 0.02 eV higher in energy than the singlet structure. Other neutral and cationic minima (Structures **IB-ID** and $\mathbf{IC}^+$-$\mathbf{ID}^+$ - Figure 6.1) were also calculated, but are found to lie higher in energy; especially the linear structure of the neutral species which is calculated to lie +2.01 eV above the lowest energy neutral structure. In addition to the geometric data and Hirshfeld charges presented in Figure 6.1, Table 6.1 shows the calculated vibrational modes and symmetries of **IA**, $\mathbf{IA}^+$ and $\mathbf{IB}^+$. The Cartesian coordinates and electronic parameters of all the calculated neutral and cationic $RhHo_2$ structures presented in Figure 6.1 can be found in Appendix B.

6.1.2. Geometric Changes and Hirshfeld Charges

For the lowest energy neutral minimum (**IA**) and the two low-lying cationic minima ($\mathbf{IA}^+$ and $\mathbf{IB}^+$) discussed in Section 6.1.1, there are two ionisation transitions considered possible for $RhHo_2$: (i) a $^1A_1 \leftarrow {}^2A_1$ ($\mathbf{IA}^+ \leftarrow \mathbf{IA}$) transition, and (ii) a $^3B_2 \leftarrow {}^2A_1$ ($\mathbf{IB}^+ \leftarrow \mathbf{IA}$) transition.

In analysing the change in atomic Hirshfeld charges (labelled in Figure 6.1) upon ionisation, the Rh and Ho atoms gain a net charge of +0.402 and +0.295, respectively upon the **IA** to $\mathbf{IA}^+$ ($^1A_1 \leftarrow {}^2A_1$) transition. Upon ionisation from **IA** to $\mathbf{IB}^+$ ($^3B_2 \leftarrow {}^2A_1$),

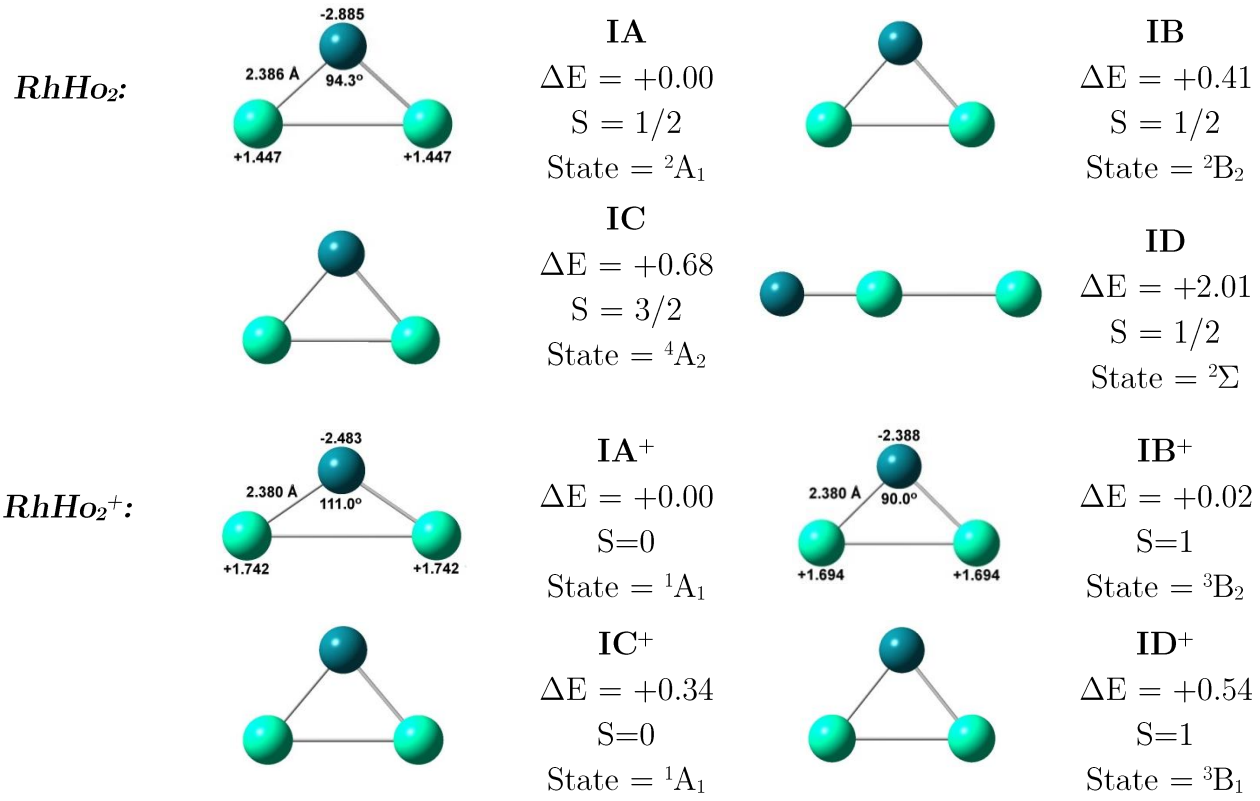

Figure 6.1. *Calculated structures for the neutral and cationic isomers of the $RhHo_2$ cluster (Rh atoms in dark green, Ho atoms in light green). The relative energies (ΔE in eV) are calculated with respect to the lowest energy neutral and cationic isomers and are zero-point energy corrected. Hirshfeld charges and geometric data have also been provided for structures of relevance to the discussion.*

Mode	Symmetry	Normal mode[a]	**IA** (cm^{-1})	**IA**$^+$ (cm^{-1})	**IB**$^+$ (cm^{-1})
ν_1	a_1	ν_s Rh-Ho	235	223	244
ν_2	a_1	δ_s Ho-Rh-Ho	94	75	105
ν_3	b_2	ν_a Rh-Ho	151	190	156

Table 6.1. *Calculated vibrational modes of the lowest energy neutral and cationic minima of $RhHo_2$.*

[a] ν_s: symmetric stretch; ν_a:asymmetric stretch; δ_s: symmetric bend.

the Rh and Ho atoms gain a net charge of +0.497 and +0.247, respectively. For the former transition, the increased electrostatic repulsion experienced between the two Ho atoms is consistent with the Ho-Ho bond length increasing by 0.425 Å in $\mathbf{IA}^+$. For the latter transition, the magnitude of positive charge gained by the Ho atoms is less, thus being consistent with a smaller increase of 0.108 Å for the Ho-Ho bond length in $\mathbf{IB}^+$.

For both transitions, the corresponding bond length changes are significant and indicate that both transitions involve significant motion along the appropriate FC co-ordinate. This should ultimately result in long vibronic progressions which will manifest as a gradual onset of cluster signal in the PIE spectrum. However, since there is significantly less geometric change experienced by the $RhHo_2$ cluster upon the $^3B_2 \leftarrow {}^2A_1$ transition, there should be a faster onset of signal if this is the dominant transition. As it is difficult to discern the extent to which geometric change affects the observed rate of signal onset, both ionisation transitions are potential candidates to explain the experimental PIE spectrum of $RhHo_2$ (Figure 5.3(a)) as it exhibits gradual cluster signal onset following ionisation.

6.2. DFT Results for the $RhHo_2O$ Cluster

6.2.1. Lowest Energy Neutral and Cationic Structures

For the neutral $RhHo_2O$ species, the lowest energy structure is calculated to be a planar doublet C_{2v} structure in a $^2B_2$ state, where the O atom is bound across the Ho-Ho bond (Structure **IIA** – Figure 6.2). The lowest energy cationic structure is a singlet C_{2v} structure in a $^1A_1$ state with the O atom bound in the same manner (Structure $\mathbf{IIA}^+$ - Figure 6.2). In addition to the geometric data and Hirshfeld charges presented for **IIA** and $\mathbf{IIA}^+$ in Figure 6.2, Table 6.2 shows the calculated vibrational modes and symmetries of these two clusters. Overall, both structures are consistent with the increased stability of the Ho-O bond relative to the Rh-O bond (refer to bond strengths in Table 4.1, Chapter 4) which results in the oxygen atom binding to the Ho-Ho edge rather than the Ho-Rh edge. Other neutral and cationic minima (Structures **IIB** and $\mathbf{IIB}^+$ - Figure 6.2) are also calculated, but found to lie much higher in energy. The Cartesian coordinates and electronic parameters of all the calculated neutral and cationic $RhHo_2O$ structures presented in Figure 6.2 can be found in Appendix B.

6.2.2. Geometric Changes and Hirshfeld Charges

For $RhHo_2O$, there is only one possible ionisation transition to be considered: the $^1A_1 \leftarrow {}^2B_2$ ($\mathbf{IIA}^+ \leftarrow \mathbf{IIA}$) transition. Upon ionisation from **IIA** to $\mathbf{IIA}^+$ ($^1A_1 \leftarrow {}^2B_2$), the Ho, Rh and O atoms all gain a net charge of +0.259, +0.430 and +0.044, respectively. Despite the gain in positive charge by the holmium atoms, the Ho-Ho bond length decreases by 0.04 Å. The Ho-O and Ho-Rh bond lengths also decrease by 0.02 Å and 0.01 Å, respectively. The slight shortening of the latter two bonds keeps the cationic structure rigid and inhibits the lengthening of the Ho-Ho bond upon ionisation. All these structural changes are relatively small and indicate strong FC overlap between the neutral and cationic structures, which will result in short vibronic progressions and thus a sharp onset of cluster signal in the PIE spectrum. This is entirely consistent with the experimental PIE spectrum for $RhHo_2O$ (Figure 5.3(b)) which exhibits sharp onset following ionisation.

$RhHo_2O$:	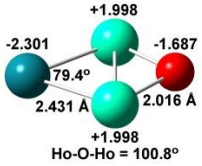	**IIA** ΔE = 0.00 S = 1/2 State = $^2B_2$	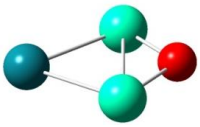	**IIB** ΔE = +1.37 S = 3/2 State = $^4B_2$
$RhHo_2O^+$:	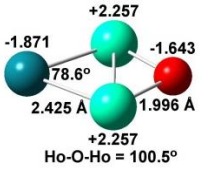	**IIA$^+$** ΔE = 0.00 S=0 State =$^1A_1$	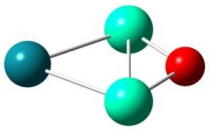	**IIB$^+$** ΔE = +1.46 S=1 State = $^3B_2$

Figure 6.2. *Calculated structures for the neutral and cationic isomers of the $RhHo_2O$ cluster (Rh atoms in dark green, Ho atoms in light green and O atoms in red). The relative energies (ΔE in eV) are calculated with respect to the lowest energy neutral and cationic isomers. Hirshfeld charges and geometric data have also been provided for structures of relevance to the discussion.*

Mode	Symmetry	Normal Mode[a]	**IIA** (cm^{-1})	**IIA$^+$** (cm^{-1})
ν_1	a_1	ν_s Ho-O	568.1	595.2
ν_2	a_1	ν_s Rh-Ho	225.9	236.9
ν_3	a_1	δ_s Ho-Rh-Ho	185.7	195.0
ν_4	b_1	π $RhHo_2O$	177.1	181.4
ν_5	b_2	ν_a Ho-O	528.1	567.4
ν_6	b_2	ν_a Rh-Ho	123.3	146.9

Table 6.2. *Calculated vibrational modes of the lowest energy neutral and cationic minima of $RhHo_2O$.*

[a]ν_s: symmetric stretch; ν_a: asymmetric stretch; δ_s: symmetric bend; *π: Out-of-Plane Deformation.*

6.3. DFT Results for the $RhHo_2O_2$ Cluster

6.3.1. Lowest Energy Neutral and Cationic Structures

For the neutral $RhHo_2O_2$ species, there are two isomers calculated to lie within the estimated experimental IE error. The lowest energy neutral structure is a doublet non-planar C_{2v} structure in a $^2A_1$ state with each individual oxygen atom doubly bridged to a Ho-Ho bond in a dissociative manner (Structure **IIIA** – Figure 6.3). The other neutral isomer is calculated to lie only +0.04 eV higher in energy than **IIIA** and is a doublet C_s structure in a $^2A'$ state with a structural motif similar to that of **IIIA** (Structure **IIIB** – Figure 6.3); the main structural difference being the location of an oxygen atom close to the rhodium atom in **IIIB**, thus lowering its symmetry and differentiating it from **IIIA**. The lowest energy neutral structure with associatively-bound O_2 is a doublet C_{2v} structure in the $^2B_1$ state with O_2 bound perpendicular to the $RhHo_2$ trimer base across the Ho-Ho bond (Structure **IIIE** - Figure 6.3). This structure is calculated to lie +4.01 eV higher in energy than **IIIA**. The lowest energy cationic structure is found to be a singlet non-planar C_s dissociative structure in a $^1A'$ state with a structural motif very similar to that of **IIIB** (Structure $\mathbf{IIIA}^+$ - Figure 6.3). A cationic C_{2v} structure akin to **IIIA** was calculated, but is found to possess an imaginary frequency. Viewing the motion of atoms corresponding to this imaginary mode shows this structure connecting to $\mathbf{IIIA}^+$, thus inferring that $RhHo_2O_2$ favours C_s symmetry in the cationic state. The lowest energy cationic structure with associatively-bound O_2 is found to be a singlet C_{2v} structure in a $^1A_1$ state with a structural motif very similar to that of **IIIE** (Structure $\mathbf{IIIC}^+$ - Figure 6.3) and +3.73 eV higher in energy than $\mathbf{IIIA}^+$. Overall, as the neutral and cationic associatively bound structures are calculated to lie much higher in energy than the lower energy dissociative structures, it is contended that only the latter are present in the molecular beam.

As with $RhHo_2O$, the increased stability of the Ho-O bond compared to the Rh-O bond results in both oxygen atoms binding preferably to the Ho-Ho edge rather than the Rh-Ho edge in both the lower energy neutral and cationic structures. Other dissociative neutral and cationic minima at the same or higher multiplicities were also calculated

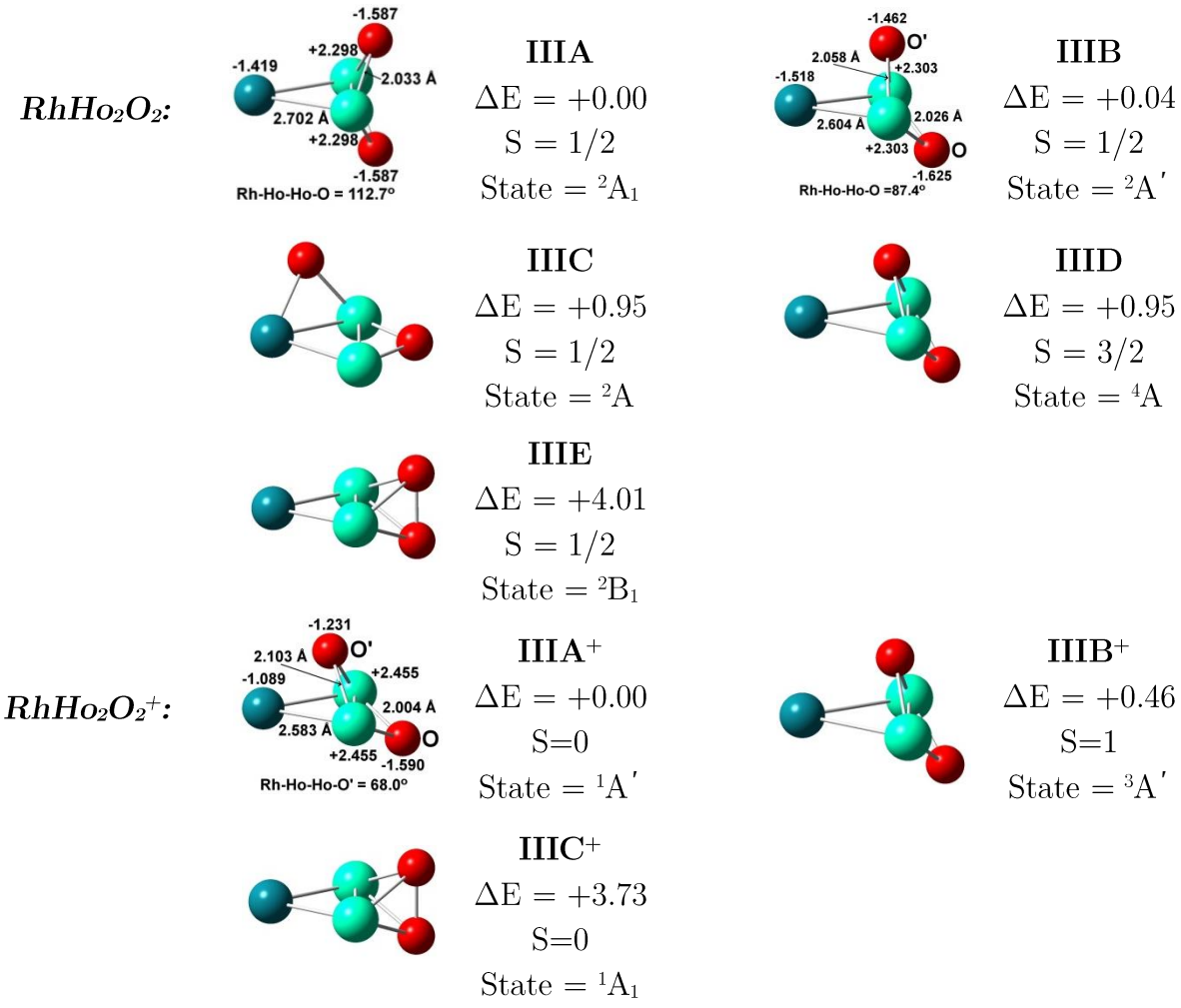

Figure 6.3. *Calculated structures for the neutral and cationic isomers of the $RhHo_2O_2$ cluster (Rh atoms in dark green, Ho atoms in light green and O atoms in red). The relative energies (ΔE in eV) are calculated with respect to the lowest energy neutral and cationic isomers. Hirshfeld charges and geometric data have also been provided for structures of relevance to the discussion.*

Mode	Symmetry[a]	Normal Mode[b]	**IIIA** (cm^{-1})	**IIIB** (cm^{-1})	**IIIA**$^+$ (cm^{-1})
ν_1	a_1/a'	$\nu_s^\dagger$ Ho-O	619	607	616
ν_2	a_1/a'	δ_s O-Ho-Ho-O	297	283	419
ν_3	a_1/a'	δ_s Ho-Rh-Ho	211	205	225
ν_4	a_1/a'	ν_s Rh-Ho	157	175	181
ν_5	a_2/a''	$\nu_a^\ddagger$ Ho-O	378	384	384
ν_6	b_1/a''	$\nu_a^\dagger$ Ho-O	561	548	576
ν_7	b_1/a''	ν_a Rh-Ho	85	100	108
ν_8	b_2/a'	$\nu_s^\ddagger$ Ho-O	568	553	564
ν_9	b_2/a'	π $RhHo_2$	88	42	199

Table 6.3. *Calculated vibrational modes of the lowest energy neutral and cationic minima of $RhHo_2O_2$.*

[a]*Structure **IIIA** has C_{2v} symmetry. Structures **IIIB** and **IIIA**$^+$ both have C_s symmetry. Label format: C_{2v}/C_s (NOTE: Mode numbering is relative to Structure **IIIA**)*

[b]νs: symmetric stretch; ν_a: asymmetric stretch; δ_s: symmetric bend; *π: Out-of-Plane Deformation;* $\nu_s^\dagger$: symmetric stretch of individual bonds with both O atoms stretching symmetrically relative to each other; $\nu_s^\ddagger$: symmetric stretch of individual bonds with both O atoms stretching asymmetrically relative to each other; $\nu_a^\dagger$: asymmetric stretch of individual bonds with both O atoms stretching symmetrically relative to each other; $\nu_a^\ddagger$: asymmetric stretch of individual bonds with both O atoms stretching asymmetrically relative to each other.

(Structures **IIIC-IIID** and **IIIB**$^+$ - Figure 6.3) but are found to lie much higher in energy than those discussed on the previous page. In addition to the geometric data and Hirshfeld charges presented in Figure 6.3, Table 6.3 shows the calculated vibrational modes and symmetries of **IIIA**, **IIIB** and **IIIA**$^+$. The Cartesian coordinates and electronic parameters of all the calculated neutral and cationic $RhHo_2O_2$ structures presented in Figure 6.3 can be found in Appendix B.

6.3.2. Hirshfeld Charges and Geometric Changes

For the two low-lying neutral minima (**IIIA** and **IIIB**) and the lowest energy cationic minimum (**IIIA**$^+$) discussed in Section 6.3.1, there are two ionisation transitions considered possible for $RhHo_2O_2$: (i) a $^1A' \leftarrow {}^2A_1$ (**IIIA**$^+ \leftarrow$ **IIIA**) transition, and (ii) a $^1A' \leftarrow {}^2A'$ (**IIIB**$^+ \leftarrow$ **IIIA**) transition.

In analysing the change in atomic Hirshfeld charges (labelled in Figure 6.3) upon ionisation, the rhodium and holmium atoms gain a net charge of +0.330 and +0.157, respectively upon the **IIIA** to **IIIA**$^+$ ($^1A' \leftarrow {}^2A_1$) transition. The change in charge of each individual oxygen atom is -0.003 for the oxygen atom that is furthest away from the rhodium atom in **IIIA**$^+$ (labelled O in **IIIA** and **IIIA**$^+$ - Figure 6.3), and +0.356 for the oxygen atom that migrates closer to the rhodium atom upon ionisation in **IIIA**$^+$ (labelled O' in **IIIA** and **IIIA**$^+$ - Figure 6.3). Upon ionisation from **IIIB** to **IIIA**$^+$ ($^1A' \leftarrow {}^2A'$), the rhodium and holmium atoms are observed to gain a net charge of +0.429 and +0.157, respectively. For the same transition, the gain in charge is +0.035 and +0.231 for oxygen atoms O and O', respectively.

For both transitions, the most significant geometric change is of the Rh-Ho-Ho-O dihedral angle of the oxygen atom that moves closer to the rhodium atom upon ionisation (labelled O' in **IIIA** and **IIIA**$^+$ - Figure 6.3). This dihedral angle is observed to change by 44.7° for the $^1A' \leftarrow {}^2A_1$ transition and 19.4° for the $^1A' \leftarrow {}^2A'$ transition, with both showing the pertinent oxygen atom shifting closer to the rhodium atom upon ionisation. Both geometric changes are considered significant and indicate moderate-to-poor FC

overlap between the neutral and cationic structures, which should ultimately result in a gradual onset of cluster signal upon ionisation. However, the smaller geometric change experienced by the $RhHo_2O_2$ cluster in the $^1A' \leftarrow {}^2A'$ transition should result in a faster onset of signal if this is the dominant transition. As stated previously, it is difficult to discern the extent to which geometric change affects the observed rate of signal onset. Therefore, it is contended at this stage that both ionisation transitions are equally possible and that both would have a gradual onset of signal following ionisation. This is consistent with the PIE spectrum of $RhHo_2O_2$ (Figure 5.3(c)), which exhibits this behaviour.

6.4. Simulated ZEKE and PIE Spectra for the $RhHo_2O_n$ (n = 0-2) Clusters

6.4.1. Simulated ZEKE Spectra for the $RhHo_2$ Cluster

Due to the two lowest energy cationic minima of $RhHo_2$ being separated by only 0.02 eV and both the $^1A_1 \leftarrow {}^2A_1$ (**IA**$^+ \leftarrow$ **IA**) and $^3B_2 \leftarrow {}^2A_1$ (**IB**$^+ \leftarrow$ **IA**) transitions predicting slow ionisation onsets, it is difficult to assign one, or both, to the experimental data. In addition, as the vibrational temperature is *ca.* 300 K in the molecular beam, it is possible that the initial onset of experimental cluster signal is due to vibronic "hot band" transitions.

Figure 6.4 shows the ZEKE spectra for the $^1A_1 \leftarrow {}^2A_1$ and $^3B_2 \leftarrow {}^2A_1$ transitions that are simulated at 300 K. The ZEKE spectrum for the $^1A_1 \leftarrow {}^2A_1$ transition (Figure 6.4(a)) exhibits six progressions which contain signals that appear with very weak to strong intensities, with the highest energy FC-allowed transition predicted to appear at *ca.* 5.396 eV (due to the 2_0^6 vibronic transition). The other progression possesses a constant energy spacing of approximately 0.0116 eV (94 cm^{-1}), which corresponds to the energy of the same symmetric bending mode of **IA**. Additionally, there are two other signals that appear with weak intensities due to the $2_2^5 3_1^1$ and $1_0^1 2_3^4$ vibronic transitions. Overall, the most intense peaks that arise in the calculated spectrum are present in the 2_3^n the 2_2^n progressions i.e. only progressions that involve quanta of the symmetric bending mode of **IA**$^+$. This indicates that the most significant FC co-ordinate change upon the $^1A_1 \leftarrow {}^2A_1$ transition is for the Ho-Ho bond length, which is observed to be the main structural difference between structures **IA** and **IA**$^+$. The band origin (0_0^0) for this transition is noticeably absent from the ZEKE spectrum (the position of the band origin is labelled in Figure 6.2(a)) since its calculated intensity is significantly lower than the other peaks in the ZEKE spectrum. Such a weak intensity for the band origin transition indicates that there should be a very long progression observed in the ZEKE spectrum; specifically involving the symmetric bending mode of **IA**$^+$ as the highest energy FC-allowed transition that appears in the spectrum is part of a progression involving this mode. Re-simulation of the ZEKE spectrum at 300 K with an increase in vibrational

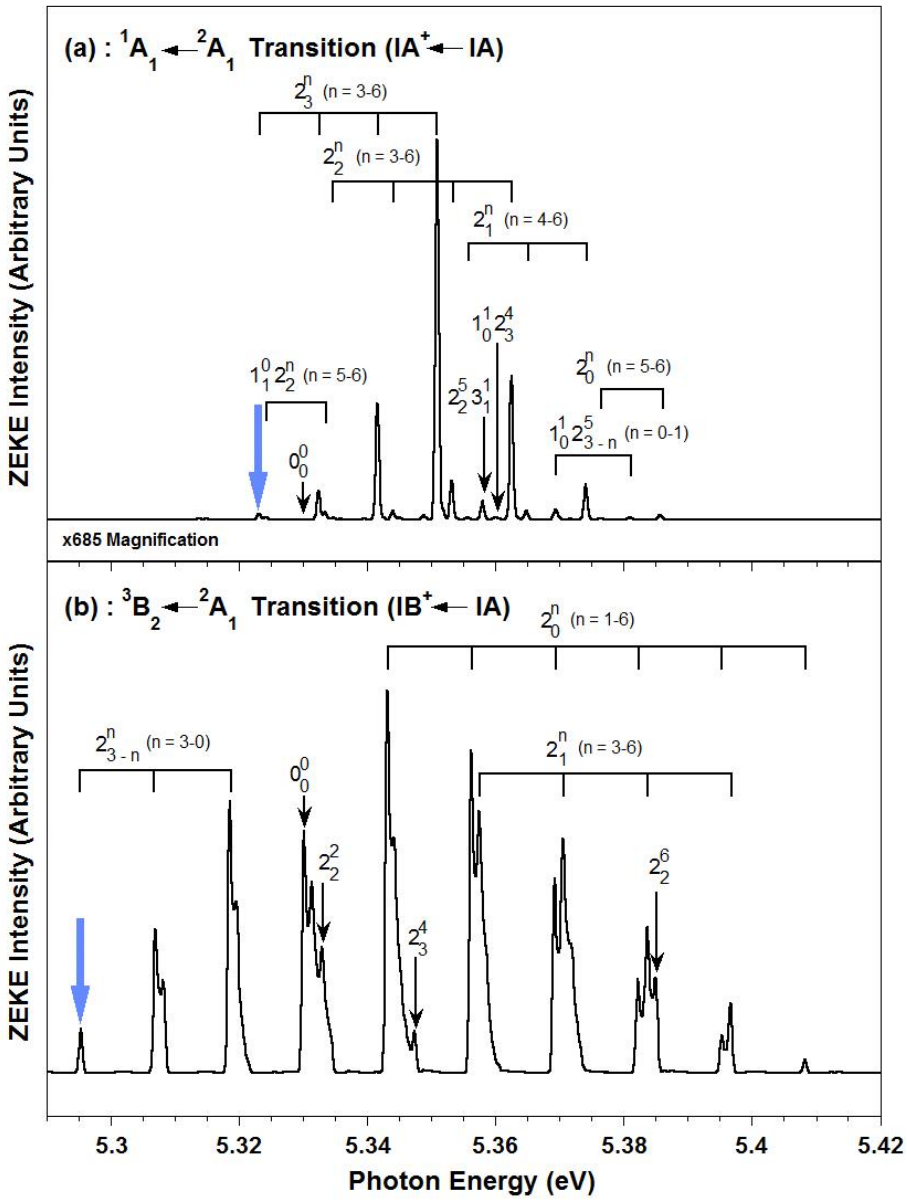

Figure 6.4. *ZEKE spectra simulated at 300 K for the: (a) $^1A_1 \leftarrow {}^2A_1$ ($IA^+ \leftarrow IA$), and (b) $^3B_2 \leftarrow {}^2A_1$ ($IB^+ \leftarrow IA$) transitions for the $RhHo_2$ cluster. The theoretical band origins and possible thermal onset starting positions (blue arrows) are indicated. For clarity, the $^1A_1 \leftarrow {}^2A_1$ ZEKE spectrum has been magnified ×685 relative to the $^3B_2 \leftarrow {}^2A_1$ ZEKE spectrum (with the y-axis for each spectrum on the same scale).*

quantum number of the neutral and cationic structures and expansion of the energy window yields a ZEKE spectrum with the most intense signals appearing in the 2_0^n progression (located in Appendix C of this thesis). The intensities of the signals in this progression increase steadily from the 2_0^6 vibronic transition at *ca.* 5.396 eV with increasing photon energy, with the highest intensity signals appearing at *ca.* 5.55 eV. After this photon energy, the corresponding signals begin to steadily decrease in intensity until the progression terminates at *ca.* 5.65 eV. Overall, this re-simulated ZEKE spectrum of the $^1A_1 \leftarrow {}^2A_1$ transition shows how the very weak intensity of the band origin transition leads to a very long vibronic progression involving the symmetric bending mode of $\mathbf{IA}^+$.

Figure 6.4(b) shows the ZEKE spectrum simulated for the $^3B_2 \leftarrow {}^2A_1$ ionisation transition. As observed, there are three progressions containing signals that appear with moderate to strong intensities, with the highest FC-allowed transition simulated to arise at *ca.* 5.418 eV (which is due to the 2_0^6 vibronic transition). Two of the progressions possess a constant energy spacing of approximately 0.0130 eV (105 cm^{-1}), which corresponds to the energy of the symmetric bending mode of structure $\mathbf{IB}^+$. The last progression possesses a constant energy spacing of approximately 0.0116 eV (94 cm^{-1}), which corresponds to the energy of the symmetric bending mode of structure **IA**. Additionally, there are several other signals that appear in the spectrum with intensities that range from moderate to strong due to the 2_2^2, 2_3^4 and 2_2^6 vibronic transitions. Interestingly, all signals in this spectrum arise from transitions between vibrational energy levels in the neutral and cationic structures that comprise only of various quanta of the symmetric bending modes of structures **IA** and $\mathbf{IB}^+$. Overall, both progressions appear to contain the most intense signals, with the band origin signal also appearing with an intensity level that rival those of the signals in each progression. However, as the entire ZEKE spectrum is dominated by transitions between vibrational energy levels which comprise of various quanta of the symmetric bending modes of structures **IA** and $\mathbf{IB}^+$, this indicates that the most significant FC co-ordinate change upon the $^3B_2 \leftarrow {}^2A_1$

transition is the same as for the $^1A_1 \leftarrow {}^2A_1$ transition, which is the change in the Ho-Ho bond length upon ionisation.

Upon comparison of the ZEKE spectra in Figure 6.4, it is clear that the signals simulated for the $^3B_2 \leftarrow {}^2A_1$ transition have far greater overall intensities than those simulated for the $^1A_1 \leftarrow {}^2A_1$ transition. Even the re-simulated ZEKE spectrum for the $^1A_1 \leftarrow {}^2A_1$ transition located in Appendix C had to be magnified x2 in order to compare it on the same scale as the ZEKE spectrum for the $^3B_2 \leftarrow {}^2A_1$ transition shown in Figure 6.4(b), thus further justifying this statement. This is due to the change experienced by the Ho-Ho bond length upon ionisation being much larger for the latter transition (0.425 Å) than the former transition (0.108 Å), thus leading to a more enhanced FC overlap between structures **IA** and $\mathbf{IB}^+$ than for structures **IA** to $\mathbf{IA}^+$ in the energy region considered. Therefore, the $^3B_2 \leftarrow {}^2A_1$ transition is assigned to be the observed ionisation transition for $RhHo_2$.

6.4.2. Comparison of Experimental and Simulated PIE Spectra for $RhHo_2$

In simulating the ZEKE spectrum for the $^3B_2 \leftarrow {}^2A_1$ transition at 300 K, the theoretical 0_0^0 transition was set to the experimental appearance energy (denoted AE in Chapter 5) of $RhHo_2$ (5.33 eV). This was done based on the assumption that the initial onset of cluster signal in the experiment is due to the 0_0^0 transition and hence, any additional onset observed thereafter is due to various vibronic transitions that accompany the pure adiabatic ionisation transition. However, the presence of the strong hot band feature simulated to arise at *ca.* 5.295 eV (due to the 2_0^3 vibronic transition – indicated by the blue arrow in Figure 6.4(b)) indicates that the initial cluster signal onset is most likely due to this vibronic transition and not the 0_0^0 transition. Hence, the initial experimental cluster signal onset observed at 5.33 eV is asserted to actually be due to the 2_0^3 vibronic transition and the experimental AE (i.e. the 0_0^0 transition) of $RhHo_2$ lies slightly higher energy.

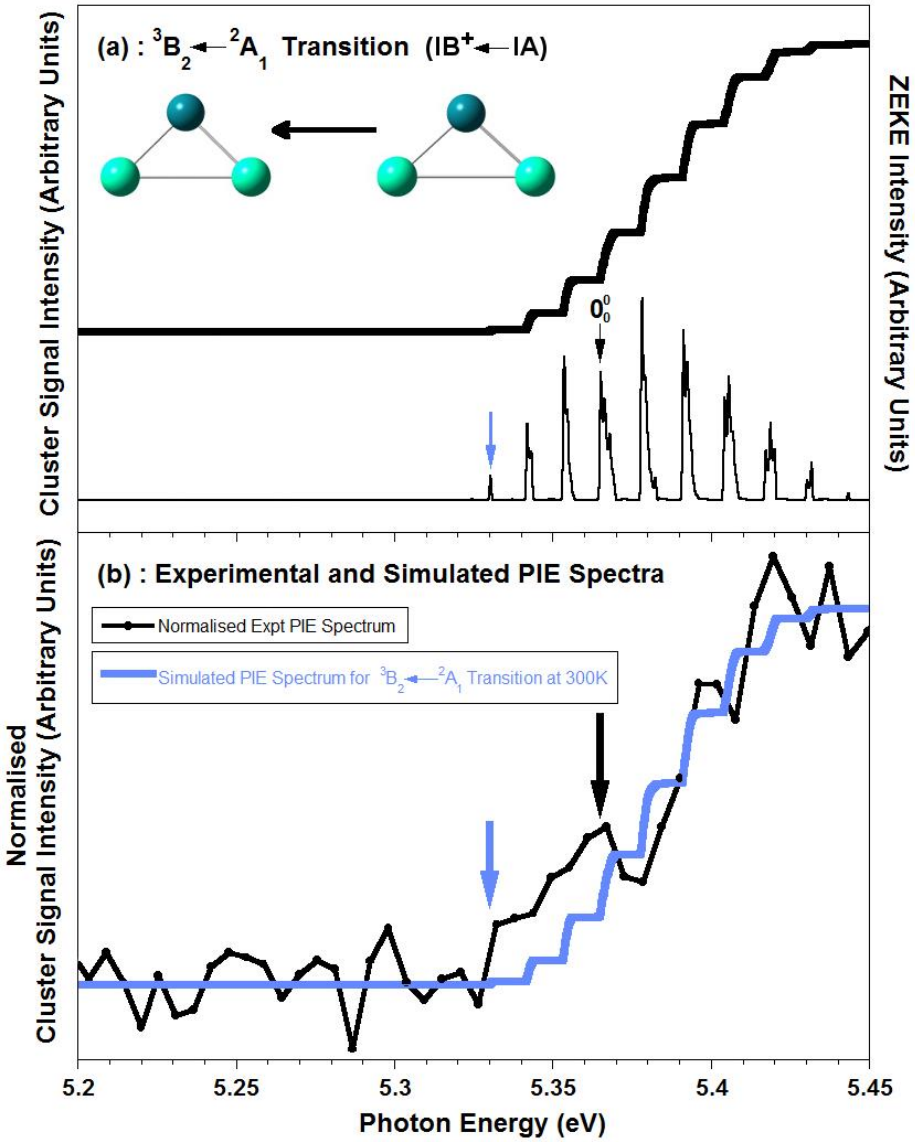

Figure 6.5. *(a) The corrected ZEKE and PIE spectra for the $^3B_2 \leftarrow {}^2A_1$ ($IB^+ \leftarrow IA$) transition of $RhHo_2$ simulated at 300 K, and (b) The normalised experimental and corrected PIE spectra for the $^3B_2 \leftarrow {}^2A_1$ ($IB^+ \leftarrow IA$) transition of $RhHo_2$ simulated at 300 K. The blue arrow indicates the energy of the most significant hot band transition that initiates thermal onset of the PIE spectrum. The black arrow indicates the energy of the band origin and the thermally-corrected experimental appearance energy (AE^t) of $RhHo_2$.*

For the ZEKE spectrum arising from the $^3B_2 \leftarrow {}^2A_1$ transition, a correction factor of 0.035 eV (the difference between the energy assigned to the theoretical 0_0^0 transition (5.33 eV) and the energy simulated for the 2_0^3 vibronic transition (5.295 eV)) needs to be applied to all transition energies in order to attain the thermally-corrected experimental AE (denoted $AE^\dagger$) for $RhHo_2$ upon this ionisation transition. Figure 6.5 shows the comparison of the resulting corrected ZEKE and corresponding PIE spectra simulated for the $^3B_2 \leftarrow {}^2A_1$ transition with the experimental PIE spectrum of $RhHo_2$.

As observed in Figure 6.5(a), the addition of the 0.035 eV correction factor to all transition energies in the simulated ZEKE spectrum causes an initial cluster signal onset at 5.33 eV in the simulated PIE spectrum due to the 2_0^3 vibronic transition (blue arrow) and shifts the energy of the 0_0^0 transition to 5.365 eV (black arrow), the latter being the experimental $AE^\dagger$ for $RhHo_2$ upon the $^3B_2 \leftarrow {}^2A_1$ transition. In addition, the 0.035 eV correction factor shifts the energy of the 2_0^6 vibronic transition (the highest energy FC-allowed vibronic transition) to 5.443 eV, causing the simulated PIE spectrum to level off at around this point.

As observed in Figure 6.5(b), the simulated and experimental PIE spectra have been independently normalised and compared. As observed, the shifting of the simulated ZEKE by 0.035 eV results in an excellent fit of the corresponding simulated PIE curve to the experimental PIE curve, with both displaying very similar levels of cluster signal onset upon ionisation and both appearing to level off at *ca.* 5.44 eV. Overall, such excellent comparison between the experimental and theoretical PIE spectra strongly indicates that structures **IA** and $\mathbf{IB}^+$ are the most likely neutral and cationic $RhHo_2$ structures, respectively.

6.4.3. Simulated ZEKE Spectrum for the $RhHo_2O$ cluster

As opposed to the $RhHo_2$ cluster, there is only one possible candidate for each of the neutral (**IIA**) and cationic (**IIA**$^+$) structures of the $RhHo_2O$ cluster as all other structures are calculated to lie much higher in energy.

Figure 6.6 shows the ZEKE spectrum simulated for the $^1A_1 \leftarrow {}^2B_2$ (**IIA**$^+ \leftarrow$ **IIA**) transition at 300 K. As observed, there are five overall progressions which contain signals that appear with weak to strong intensities, with the highest energy FC-allowed signal occurring *ca.* 4.917 eV for the $1_0^1 3_0^1$ vibronic transition. Within each of the five progressions, the ZEKE signals are found to possess a constant energy spacing of *ca.* 0.0242 eV (195 cm^{-1}) between them, which corresponds to the energy of the symmetric bending mode (mode ν_3 - δ_s Ho-Rh-Ho) of structure **IIA**$^+$. The simulation also yielded numerous other ZEKE signals not part of any of the five progressions arising from transitions between various vibrational energy levels of structures **IIA** and **IIA**$^+$ that are comprised of various quanta of modes ν_1, ν_3 and ν_6 from both of these structures. Additionally, the most intense signal that arises in the ZEKE spectrum for the $^1A_1 \leftarrow {}^2B_2$ transition is due to the 0_0^0 transition. This indicates that the vertical and adiabatic IEs for $RhHo_2O$ are equal and that there should be very little geometric change experienced by this cluster upon ionisation, which is substantiated by the minute structural differences observed between structures **IIA** and **IIA**$^+$ in section 6.2.2.

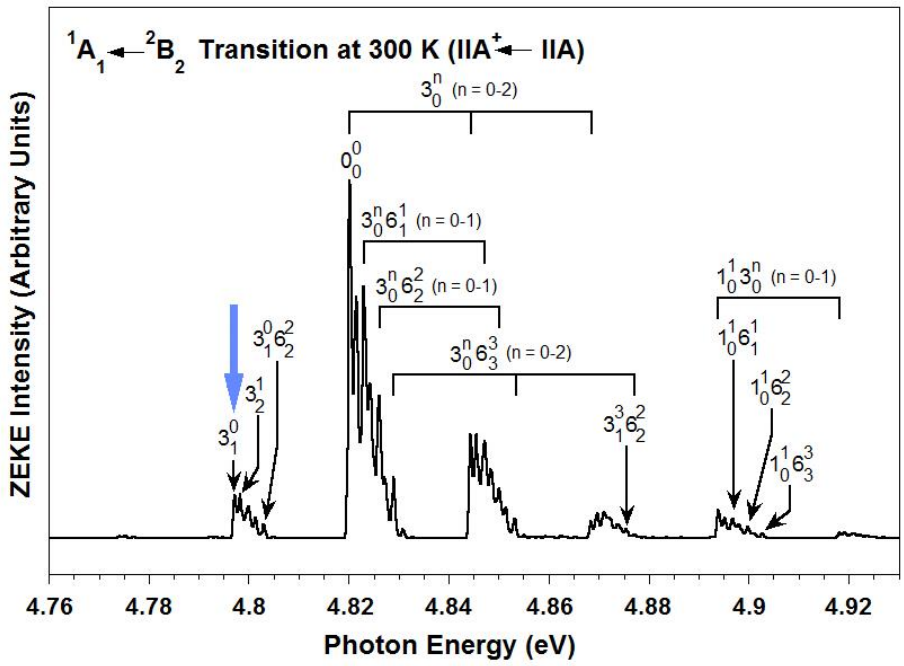

Figure 6.6. *ZEKE spectrum simulated at 300 K for the $^1A_1 \leftarrow {}^2B_2$ transition for the $RhHo_2O$ cluster. The energies of the theoretical band origin and possible thermal onset starting position (blue arrow) are indicated. The ZEKE signals whose origins are unambiguously known have been labelled accordingly with number of quanta of each vibrational mode from the neutral and cationic structures contributing to each of them.*

6.4.4. Comparison of Experimental and Simulated PIE Spectra for $RhHo_2O$

In simulating the ZEKE spectrum for the $^1A_1 \leftarrow {}^2B_2$ transition at 300 K, the theoretical 0_0^0 transition was set to the experimental AE of $RhHo_2O$ (4.82 eV). This was done based on the assumption that the initial onset of cluster signal in the experiment is due to the 0_0^0 transition and hence, any additional onset observed thereafter is due to various other vibronic transitions that accompany the pure adiabatic ionisation transition. However, the presence of the strong hot band feature simulated to arise at *ca.* 4.797 eV (due to the 3_1^0 vibronic transition – indicated by the blue arrow in Figure 6.6) indicates that the initial cluster signal onset is most likely due to this vibronic transition and not the 0_0^0 transition. Hence, the initial experimental cluster signal onset observed at 4.82 eV is asserted to actually be due to the 3_1^0 vibronic transition and the experimental AE (i.e. 0_0^0 transition) of $RhHo_2O$ lies slightly higher in energy.

For the ZEKE spectrum arising from the $^1A_1 \leftarrow {}^2B_2$ transition, a correction factor of 0.023 eV (the difference between the energy assigned to the theoretical 0_0^0 transition (4.82 eV) and the energy simulated for the 3_1^0 vibronic transition (*ca.* 4.797 eV)) needs to be applied to all of the transitions energies in order to attain the experimental $AE^\dagger$ for $RhHo_2O$ for this ionisation transition. Figure 6.7 shows the comparison of the resulting corrected ZEKE and corresponding PIE spectra simulated for the transition with the experimental PIE spectrum of $RhHo_2O$.

As observed in Figure 6.7(a), the addition of the 0.023 eV correction factor to all transition energies in the simulated ZEKE spectrum causes an initial cluster signal onset at 4.82 eV in the simulated PIE spectrum due to the 3_1^0 vibronic transition (blue arrow) and shifts the energy of the 0_0^0 transition to 4.843 eV (black arrow), the latter being the experimental $AE^\dagger$ for $RhHo_2O$. In addition, the 0.023 eV correction factor shifts the energy of the $1_0^1 3_0^1$ vibronic transition (the highest energy FC-allowed vibronic transition) to 4.940 eV, causing the simulated PIE spectrum to level off at around this point. However, from *ca.* 4.89 eV onwards, the level of cluster signal onset with increasing

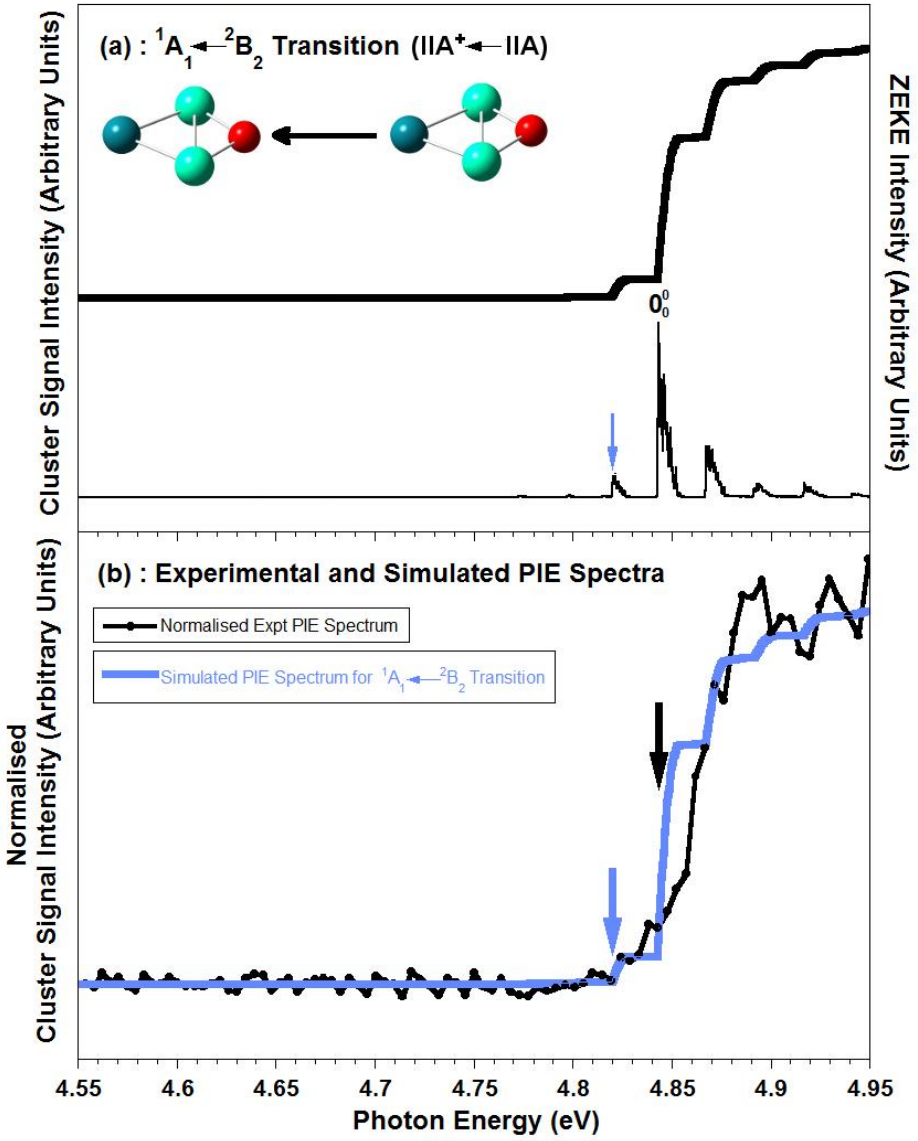

Figure 6.7. *(a) The corrected ZEKE and PIE spectra for the $^1A_1 \leftarrow {}^2B_2$ ($IIA^+ \leftarrow IIA$) transition of $RhHo_2O$ simulated at 300 K, and (b) The normalised experimental and corrected PIE spectra for the $^1A_1 \leftarrow {}^2B_2$ ($IIA^+ \leftarrow IIA$) transition of $RhHo_2O$ simulated at 300 K. The blue arrow indicates the energy of the most significant hot band transition that initiates thermal onset of the PIE spectrum. The black arrow indicates the energy of the band origin and the thermally-corrected experimental appearance energy ($AE^\dagger$) of $RhHo_2O$.*

photon energy begins to drastically decrease due to the low intensity of the ZEKE signals simulated to arise in this region. Hence, it can be argued that the simulated PIE spectrum effectively levels off from *ca.* 4.89 eV onwards as the level of increasing cluster signal intensity around this region is minuscule relative to the level observed immediately after ionisation at 4.82 eV.

In Figure 6.7(b), the simulated and experimental PIE spectra have been independently normalised and compared. As observed, both spectra compare extremely well, with both displaying very similar levels of cluster signal onset upon ionisation and both appearing to level off at *ca.* 4.89 eV. Overall, such excellent comparison between the experimental and theoretical PIE spectra strongly indicates that structures **IIA** and **IIA**$^+$ are the most likely neutral and cationic structures of $RhHo_2O$, respectively.

6.4.5. Simulated ZEKE Spectrum for the $RhHo_2O_2$ cluster

The two lowest energy neutral minima of $RhHo_2O_2$ are structures **IIIA** and **IIIB**, separated by only 0.04 eV so with both the $^1A' \leftarrow {}^2A_1$ (**IIIA**$^+ \leftarrow$ **IIIA**) and $^1A' \leftarrow {}^2A'$ (**IIIA**$^+ \leftarrow$ **IIIB**) transitions predicting slow ionisation onsets, it is difficult to discern which particular neutral isomer is the most prominent in the molecular beam prior to ionisation. Hence, the ZEKE spectra for the $^1A' \leftarrow {}^2A_1$ and $^1A' \leftarrow {}^2A'$ transitions were simulated at 300 K in order to ascertain which transition dominates (and to correct the experimental IE value due to "hot band transitions").

Figure 6.8 displays the ZEKE spectrum simulated for the $^1A' \leftarrow {}^2A'$ transition at 300 K. The ZEKE spectrum simulated for the $^1A' \leftarrow {}^2A_1$ transition yielded signals that have extremely low intensities due to extremely low calculated FCF values. As observed in Figure 6.8, the simulation yields a dense array of vibronic signals comprised of various quanta of various modes from both structures. Due to the large number of simulated transitions, specific labelling has been omitted except for the band origin (0_0^0 – black arrow) and the vibronic "hot band" transition ($3_1^0 7_2^0$ vibronic transition – blue arrow) potentially responsible for the initial onset of experimental cluster signal.

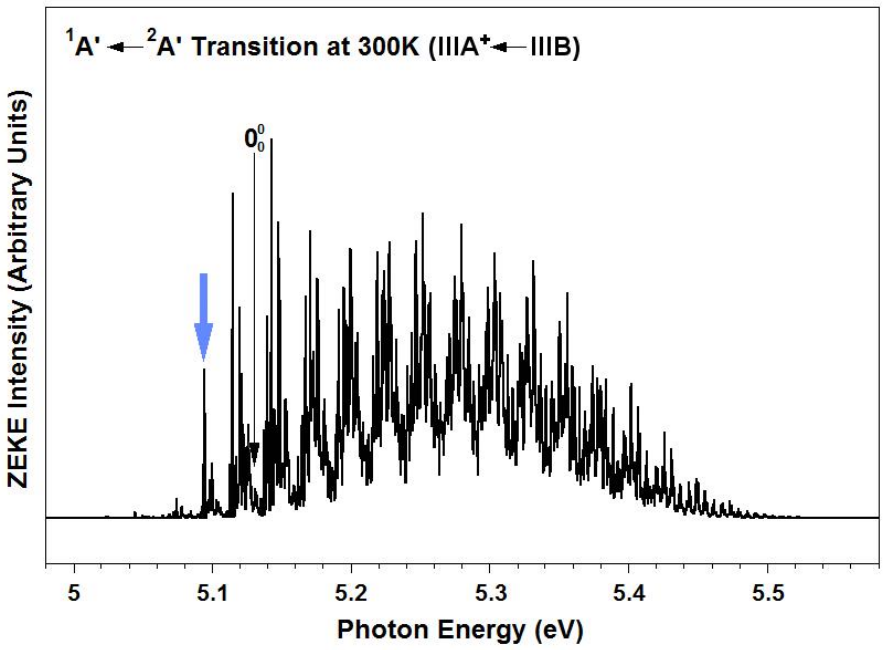

Figure 6.8. *ZEKE spectrum simulated at 300 K for the $^1A' \leftarrow {}^2A'$ transition (**IIIA$^+$ ← IIIB**) for the $RhHo_2O_2$ cluster. Due to the large number of ZEKE signals simulated, specific labelling has been omitted except for the theoretical band origin (black arrow) and the $3_1^0 7_2^0$ transition (the possible thermal onset starting position - blue arrow).*

6.4.6. Comparison of Experimental and Simulated PIE Spectra for $RhHo_2O_2$

In simulating the ZEKE spectrum for the $^1A' \leftarrow {}^2A'$ transition at 300 K, the theoretical 0_0^0 transition was set to the experimental AE of $RhHo_2O_2$ (5.13 eV). This was done based on the assumption that the initial onset of cluster signal in the experiment is due to the 0_0^0 transition and hence, any additional onset observed thereafter is due to various other vibronic transitions that accompany the pure adiabatic ionisation transition. However, the presence of the strong hot band feature simulated to arise at *ca.* 5.094 eV (due to the $3_1^0 7_2^0$ vibronic transition – indicated by the blue arrow in Figure 6.8) indicates that the initial cluster signal onset is most likely due to this vibronic transition and not the 0_0^0 transition. Hence, the initial experimental cluster signal onset observed at 5.13 eV is asserted to actually be due to the $3_1^0 7_2^0$ vibronic transition and the experimental AE (i.e. 0_0^0 transition) of $RhHo_2O_2$ lies slightly higher in energy.

For the ZEKE spectrum arising from the $^1A' \leftarrow {}^2A'$ transition, a correction factor of 0.036 eV (the difference between the energy assigned to the theoretical 0_0^0 transition (5.13 eV) and the energy simulated for the $3_1^0 7_2^0$ vibronic transition (*ca.* 5.094 eV)) needs to be applied to all of the transitions energies in order to attain the experimental $AE^\dagger$ for $RhHo_2O_2$ for this ionisation transition. Figure 6.9 shows the comparison of the resulting corrected ZEKE and corresponding PIE spectra simulated for the transition with the experimental PIE spectrum of $RhHo_2O_2$.

As observed in Figure 6.9(a), the addition of the 0.036 eV correction factor to all transition energies in the simulated ZEKE spectrum causes an initial cluster signal onset at 5.13 eV in the simulated PIE spectrum due to the $3_1^0 7_2^0$ vibronic transition (blue arrow) and shifts the energy of the 0_0^0 transition to 5.166 eV (black arrow), the latter being the experimental $AE^\dagger$ for $RhHo_2O_2$. Additionally, the 0.036 eV correction factor causes the simulated PIE spectrum to level off at *ca.* 5.51 eV. However, from *ca.* 5.43 eV onwards, the level that the cluster signal intensity increases with photon energy begins to drastically decrease due to the relatively low intensity of the vibronic signals simulated to arise in this region. Hence, it can be argued that the simulated PIE spectrum effectively levels off from *ca.* 5.43 eV onwards as the level of increasing cluster signal intensity around this region is lower than the level observed immediately after ionisation at 5.13 eV.

In Figure 6.9(b), the simulated and experimental PIE spectra have been independently normalised and compared. As observed, both spectra compare extremely well, with both displaying very similar levels of cluster signal onset upon ionisation and both appearing to level off at *ca.* 5.43 eV. Overall, such excellent comparison between the experimental and theoretical PIE spectra indicates that structures **IIIB** and $\mathbf{IIIA}^+$ are the most likely neutral and cationic structures of $RhHo_2O_2$, respectively.

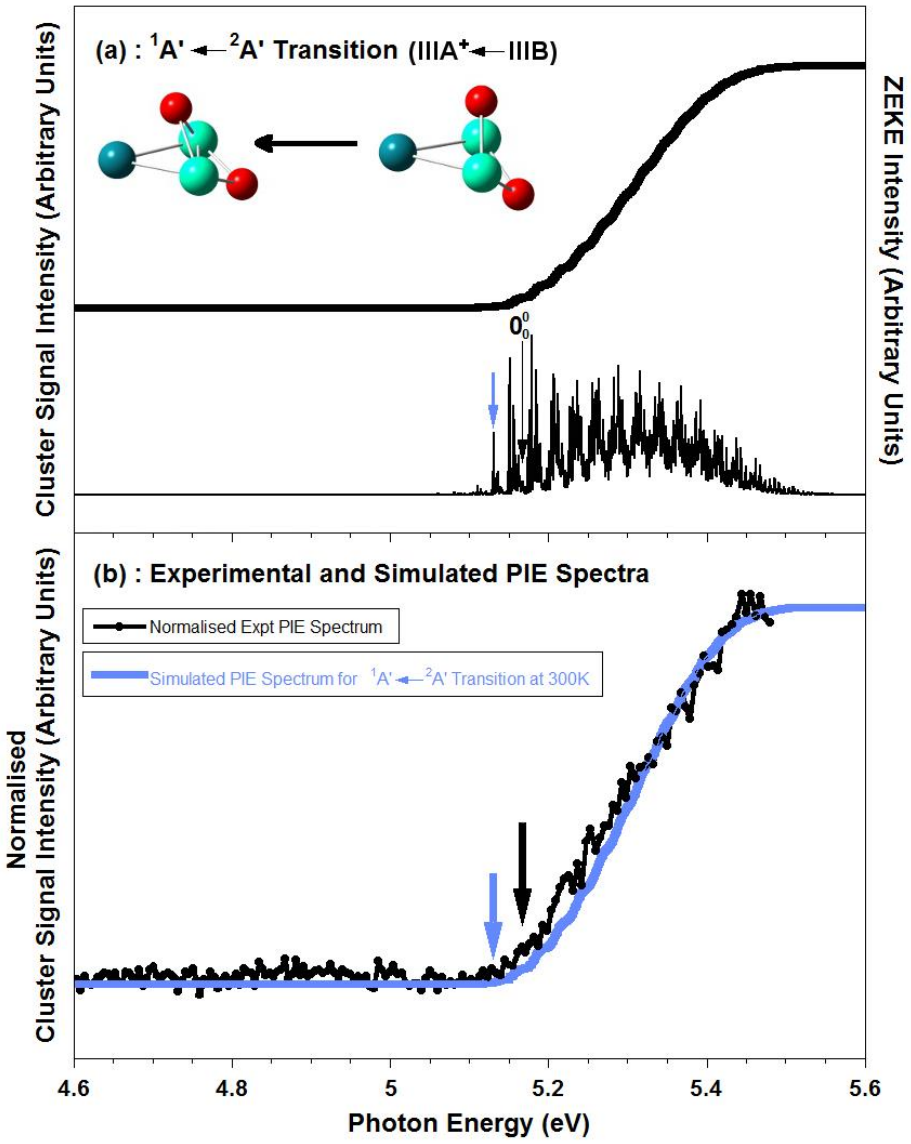

Figure 6.9. *(a) The corrected ZEKE and PIE spectra for the $^1A' \leftarrow {}^2A'$ ($IIIA^+ \leftarrow IIIB$) transition of $RhHo_2O_2$ simulated at 300 K, and (b) The normalised experimental and corrected PIE spectra for the $^1A' \leftarrow {}^2A'$ ($IIIA^+ \leftarrow IIIB$) transition of $RhHo_2O_2$ simulated at 300 K. The blue arrow indicates the energy of the most significant hot band transition that initiates thermal onset of the PIE spectrum. The black arrow indicates the energy of the band origin and the thermally-corrected experimental appearance energy (AE^t) of $RhHo_2O_2$.*

6.5. Field-Correction to the Experimental IEs of the $RhHo_2O_n$ Clusters

From the various ZEKE and PIE spectral simulations presented in the previous section, the thermally-corrected experimental AEs (denoted $AE^{\dagger}$) have been determined for the $RhHo_2O_n$ (n = 0-2) clusters. By applying a correction factor of 0.017 eV (derived from IE =AE+6.1$\sqrt{E}$; where E= 485 V/cm for the experimental setup)[1] to these experimental $AE^{\dagger}$ values, the field- and thermally-corrected experimental IEs (rounded-off to two decimal places) become 5.38 eV, 4.86 eV and 5.18 eV for $RhHo_2$, $RhHo_2O$ and $RhHo_2O_2$, respectively. These values for the $RhHo_2O_n$ (n = 0-2) clusters are listed in Table 6.4 and denoted $IE^{\dagger}$ to differentiate them from the experimental IEs determined in Chapter 5 (denoted IE in that chapter).

6.6. Calculated IEs of the $RhHo_2O_n$ Clusters and Comparison to Experimental IEs

The calculated IEs of each cluster within the $RhHo_2O_n$ (n = 0-2) series are determined by taking the energy difference (in eV and including zero-point energy correction) between the assigned neutral and cationic structures determined by the ZEKE and PIE spectral simulations presented and discussed in Section 6.4 (and obeying the $\Delta S = \pm 1/2$ selection rule). These calculated IE values for the $RhHo_2O_n$ (n = 0-2) clusters are listed in Table 6.4. As observed, the calculated IE for $RhHo_2$ is 5.82 eV upon the $^3B_2 \leftarrow {}^2A_1$ transition. The addition of an oxygen atom to the bare metal cluster decreases the IE by 0.44 eV, yielding a calculated IE of 5.38 eV upon the $^1A_1 \leftarrow {}^2B_2$ transition for $RhHo_2O$. Furthermore, the addition of another oxygen atom increases the IE by 0.26 eV relative to $RhHo_2O$, yielding a calculated IE of 5.64 eV upon the $^1A' \leftarrow {}^2A'$ transition for $RhHo_2O_2$. Relative to the bare metal cluster, the addition of two oxygen atoms to form $RhHo_2O_2$ decreases the calculated IE by 0.18 eV.

Cluster	Expt. AE†	Expt. IE†	Structures	Calc. Transition	E of Neutral HOMO	Calc. IE (Incl. ZPE)	Offset IE
$RhHo_2$	5.365	5.38	$IB^+ \leftarrow IA$	$^3B_2 \leftarrow {}^2A_1$	-4.49	5.82	5.38
$RhHo_2O$	4.843	4.86	$IIA^+ \leftarrow IIA$	$^1A_1 \leftarrow {}^2B_2$	-4.02	5.38	4.94
$RhHo_2O_2$	5.166	5.18	$IIIA^+ \leftarrow IIIB$	$^1A' \leftarrow {}^2A'$	-4.60	5.64	5.20

Table 6.4. *List of the thermally-corrected experimental AEs (AE†) and field- and thermally-corrected experimental IEs (IE†) determined for the $RhHo_2O_n$ (n = 0-2) clusters. Also shown are the calculated transitions, energies of the neutral HOMOs and IEs (offset and including ZPE) determined using the B3P86 density functional and the SDD basis set (uncertainty in Expt. IE† = ±0.05 eV). The offset IE was calculated by subtracting the difference between the calculated and corrected experimental IEs for the $RhHo_2$ cluster (0.44 eV) from all the calculated IEs. All numerical values are in units of 'eV'.*

As observed in previous studies on gas-phase metal carbide clusters by the Metha group, the calculated IEs listed in Table 6.4 are determined to be higher in energy than the experimental IE† values.[2-5] This is attributed to the nature of the B3P86 functional rather than that of the Stuttgart-Dresden ECP, which has been concluded previously from the comparison of the experimental IEs of the Ta_4C_y (y = 0-4) clusters with those calculated using the B3P86/LANL2DZ and B3P86/SDD levels of theory.[3] Hence, in order to account for this over-estimation, the calculated IEs are corrected with respect to the experimental IE† value of $RhHo_2$ as the main focus of this work is how the IE changes with respect to the sequential addition of oxygen atoms onto the bare metal cluster. Accordingly, the difference between the calculated IE and experimental IE† of $RhHo_2$ is determined to be +0.44 eV. This value is then subtracted from the calculated IE values for $RhHo_2O$ and $RhHo_2O_2$ to give the offset IE values that are listed in the final column of Table 6.4.

Figure 6.10 shows the comparison of the experimental $IE^{\dagger}$ and calculated offset IE values, both plotted against the number of constituent oxygen atoms for each cluster. The general trend in IE as a function of oxygen atoms is the same in both sets of data; both show that the addition of one oxygen atom significantly red-shifts the IE. Additionally, the difference between the experimental $IE^{\dagger}$ and offset IE values is only +0.090 eV for $RhHo_2O$ and +0.017 for $RhHo_2O_2$, indicating good quantitative comparison between theory and experiment especially since the experimental IE error is ±0.05 eV.

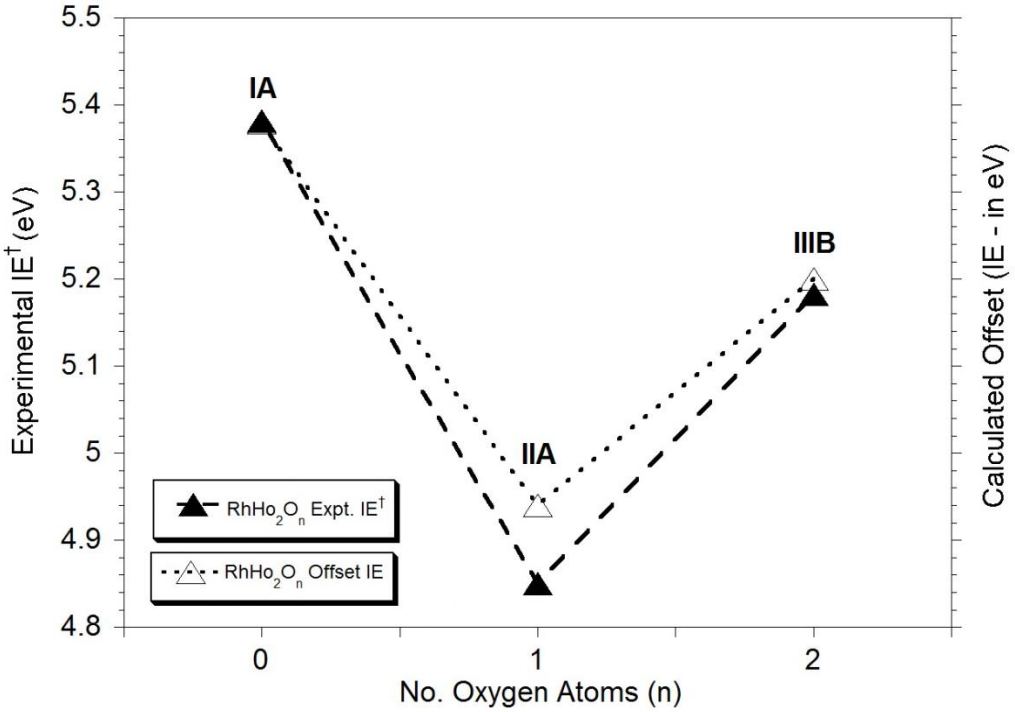

Figure 6.10. *Graph showing the experimental IE values for the $RhHo_2O_n$ (n = 0-2) clusters as a function of constituent oxygen atoms. Also shown are the offset IE values calculated using DFT. Note that the "Calculate Offset" value for $RhHo_2$ is arbitrarily set to the corrected experimental value and this difference is used as the offset correction for the other calculated IE values. The corresponding neutral isomer of each cluster from which ionisation is most likely to occur has also been labelled.*

Overall, a significant IE change following the addition of one oxygen atom rather than two onto the bare metal cluster is indicative of significant changes in the electronic structure of each cluster upon sequential oxidation. More specifically, any changes in the energies, bonding/non-bonding/anti-bonding characteristics and the composition of the HOMOs of each neutral cluster that occur upon oxidation will have a direct effect on the IE, assuming that the electron is removed from the HOMO of the neutral cluster in the photoionisation process. Hence, Figure 6.11 shows the comparison between the neutral HOMO energy and the experimental IE† of each cluster, both plotted against the number of constituent oxygen atoms. The axes have been shifted but represent a linear relationship. The corresponding pictures of the neutral HOMO of each cluster have also been included in order to help explain any observed change in bonding/non-bonding/anti-bonding character upon oxidation.

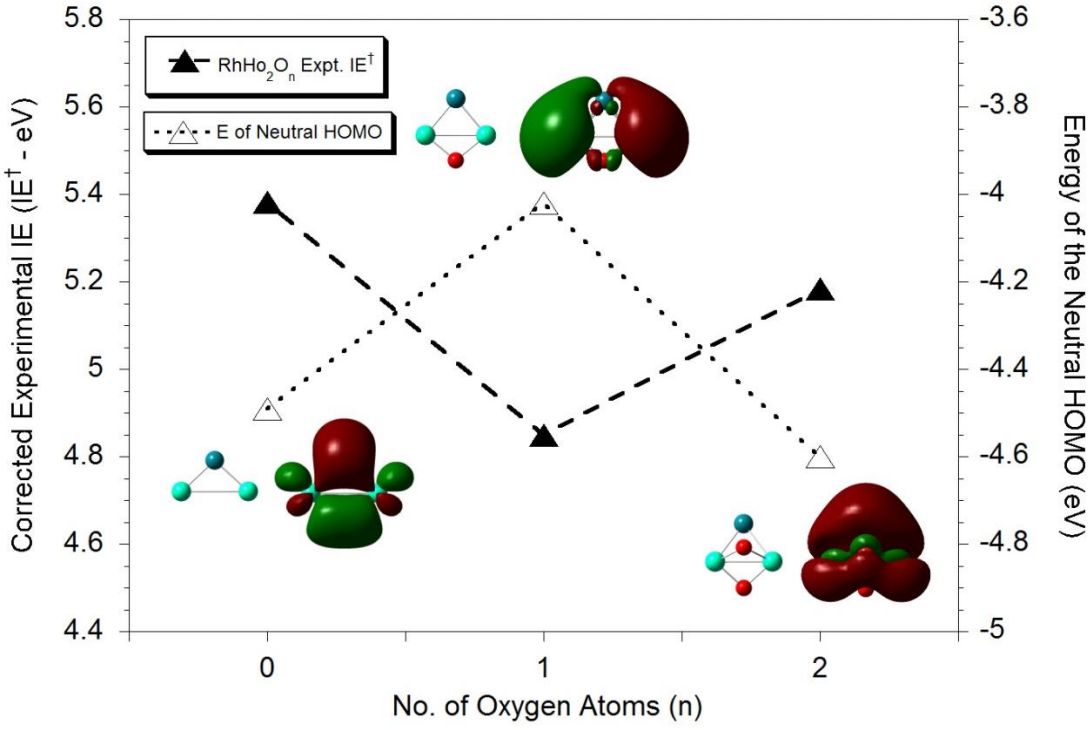

Figure 6.11. *Graph showing the comparison between the experimental IE† values and the HOMO energies of the lowest energy neutral structures for the $RhHo_2O_n$ (n = 0-2) clusters. Also displayed are pictures of each HOMO showing how the bonding/anti-bonding character changes with additional oxygen atoms.*

As seen in Figure 6.11, there is an anti-correlation observed between the energy of the neutral HOMO and the corresponding experimental IE† of each cluster. This is expected as the IE of a neutral molecule should be low if the energy of its HOMO is high, keeping consistency with the assumption that electrons are removed from the neutral HOMO of each cluster in the photoionisation process. This is observed upon the addition of an oxygen atom to the $RhHo_2$ cluster, which results in the energy of the neutral HOMO increasing by 0.47 eV and the experimental IE† decreasing by 0.53 eV. The subsequent addition of another oxygen atom decreases the neutral HOMO energy by 0.58 eV, which causes the IE† of $RhHo_2O_2$ to increase by 0.33 eV (both relative to $RhHo_2O$). Such a large variation in the energies of the neutral HOMOs can be attributed to their bonding/anti-bonding characteristics; with the neutral HOMO of $RhHo_2O$ displaying more anti-bonding character than the neutral HOMOs of $RhHo_2$ and $RhHo_2O_2$, which subsequently contributes to the observed experimental IE trend.

In addition to changes in HOMO bonding characteristics upon sequential oxidation, the observed IE changes are also related to the composition of the neutral HOMOs of each cluster in the $RhHo_2O_n$ series (which can be inferred from the HOMO pictures in Figure 6.11). Ionisation from the HOMOs of the $RhHo_2O_n$ clusters removes a metal-based (largely on Ho) *d* electron for $RhHo_2$, a metal-based (largely on Ho) *s* electron for $RhHo_2O$, and an electron delocalised across the metal and O atoms for $RhHo_2O_2$. These assigned characters of each electron removed upon ionisation is justified by the changes in atomic Hirshfeld charges observed upon transition from the assigned neutral state to the assigned cationic state of each cluster (*vide supra* Sections 6.1.2, 6.2.2 and 6.3.2 for changes in atomic Hirshfeld charges for $RhHo_2$, $RhHo_2O$ and $RhHo_2O_2$, respectively). Overall, these different electronic characters coupled with the changes in neutral HOMO energy (due to changes in bonding/non-bonding/anti-bonding characteristics upon sequential oxidation) collectively lead to the experimental IE trend observed.

Finally, the good comparison between the experimental and theoretical data in Figures 6.10 and 6.11 (in addition to Figures 6.5(b), 6.7(b) and 6.9(b)) indicates that incorporating the *f*-electrons of the Ho atom into the ECP as part of the computational method is valid. This infers that *f*-electrons seem to play no significant part in the valence active space of the neutral and cationic $RhHo_2O_n$ (n = 0-2) clusters.

6.7. Conclusion

In summary, this chapter has presented theoretical insight gained from DFT calculations, FCF calculations and ZEKE and PIE spectral simulations performed on the $RhHo_2O_n$ (n = 0-2) clusters. From these studies, it is concluded that: (i) the most likely neutral and cationic structures of each individual cluster have been inferred from comparison between the experimental and simulated PIE spectra of each cluster, (ii) the experimental IEs of each cluster have been corrected for thermal tailing that results from vibronic hot band transitions at 300 K, and (iii) the calculated IEs of the $RhHo_2O_n$ (n = 0-2) clusters have been determined and after an applied offset, were found to compare well with the field- and thermally-corrected experimental IEs; with both sets of data showing the IE of $RhHo_2O$ to be significantly red-shifted in comparison to the IEs of $RhHo_2$ and $RhHo_2O_2$. Overall, such good comparison between the experimental and theoretical data has indicated that *f*-electrons play no significant part in the valence active space of the neutral and cationic $RhHo_2O_n$ (n = 0-2) clusters.

6.8. References

(1) Németh, G. I.; Ungar, H.; Yeretzian, C.; Selzle, H. L.; Schlag, E. W. *Chem. Phys. Lett.* **1994**, *228*, 1.

(2) Dryza, V.; Addicoat, M. A.; Gascooke, J. R.; Buntine, M. A.; Metha, G. F. *J. Phys. Chem. A* **2008**, *112*, 5582.

(3) Dryza, V.; Metha, G. F. *J. Chem. Phys.* **2009**, *130*, 1.

(4) Dryza, V.; Gascooke, J. R.; Buntine, M. A.; Metha, G. F. *Physical Chemistry Chemical Physics : PCCP* **2009**, *11*, 1060.

(5) Dryza, V.; Alvino, J. F.; Metha, G. F. *J. Phys. Chem. A* **2010**, *114*, 4080.

Chapter Seven

DFT Investigations, FCF Calculations and Spectral Simulations of the Gas-Phase $Rh_2Ho_2O_m$ (m = 0-2) Clusters.

This chapter presents all the theoretical insight attained from DFT investigations and FCF calculations performed on the $Rh_2Ho_2O_m$ (m = 0-2) clusters. Initially, various neutral and cationic structures calculated within *ca.* 1 eV of the lowest energy structures of each charge state as well as their properties such as Hirshfeld charges and vibrational modes etc., are presented and discussed. Following this, ZEKE and PIE spectra simulations developed from FCF calculations are presented, discussed and compared to the experimentally obtained PIE spectra shown in Chapter Five. Overall, all theoretical data obtained from these investigations were used to: (i) assign the vibronic transitions that are the most likely to occur upon ionisation for each cluster, (ii) apply slight corrections to the experimental IEs of these clusters in order to account for thermal tailing resulting from vibrational hot band transitions at 300 K, and (iii) calculate the theoretical IEs of the $Rh_2Ho_2O_m$ (m = 0-2) clusters and compare them to those obtained experimentally. Furthermore, the theoretical insight attained for the $Rh_2Ho_2O_m$ (m = 0-2) clusters is used to explain the contrasting IE trend these clusters display against the $RhHo_2O_n$ (n = 0-2) clusters observed in Chapters Five and Six.

7.1. DFT Results for the Rh_2Ho_2 Cluster

7.1.1. Lowest Energy Neutral and Cationic Structures

For the Rh_2Ho_2 cluster, the lowest energy neutral structure is determined to be a singlet C_{2v} butterfly structure in a $^1A_1$ state (Structure **IVA** – Figure 7.1) with Rh-Rh and Rh-Ho bond lengths of 2.756 Å and 2.499 Å, respectively. As this structure possesses a Rh-Rh bond and not a Ho-Ho bond, this indicates preferential formation of the former bond, which is consistent with the increased stability of the Rh-Rh bond compared to the Ho-Ho bond (Chapter 4 – Table 4.1). A planar, D_{2h} analogue of **IVA** is calculated to lie +0.09 eV higher in energy than **IVA**. However, upon performing a harmonic vibrational frequency calculation on this structure, it is found to possess one imaginary frequency thus indicating that it is not a true minimum. An additional neutral singlet structure is also calculated and is found to lie +0.14 eV higher in energy than **IVA**. This D_{2h} isomer in a ^1A_g state (Structure **IVB**) has Rh-Ho and Ho-Ho bond lengths of 2.450 Å and 3.054 Å, respectively. As this structure possesses a Ho-Ho bond and not a Rh-Rh bond, this bonding motif results in the increased overall instability of **IVB** compared to **IVA**. Various other singlet and triplet neutral minima, including other C_{2v} butterfly structures (Structures **IVD** and **IVE** – Figure 7.1), D_{2h} planar structures (Structures **IVC** – Figure 7.1) and a planar C_s structure (Structure **IVF** – Figure 7.1) were also calculated for the neutral Rh_2Ho_2 cluster, but are found to lie higher in energy than **IVA**. In addition to the geometric data and Hirshfeld charges presented in Figure 7.1, Table 7.1 shows the calculated vibrational modes and symmetries of **IVA** and **IVB**. The Cartesian coordinates and electronic parameters of all the calculated neutral Rh_2Ho_2 structures presented in Figure 7.1 can be found in Appendix D.

The lowest energy cationic structure for the Rh_2Ho_2 cluster was determined to be a doublet C_{2v} butterfly structure in a $^2B_1$ state (Structure $\mathbf{IVA}^+$ - Figure 7.1) with Rh-Rh and Rh-Ho bond lengths of 2.768 Å and 2.445 Å, respectively. An additional cationic minimum is calculated +0.07 eV higher in energy; a doublet D_{2h} planar

structure in a $^2B_{2u}$ state (Structure **IVB**$^+$ - Figure 7.1) with Rh-Ho and Ho-Ho bond lengths of 2.449 Å and 3.114 Å, respectively. As with **IVA** and **IVB**, the increased stability of the Rh-Rh bond compared to the Ho-Ho bond results in a more energetically favourable bonding motif for **IVA**$^+$ over **IVB**$^+$. Other doublet cationic minima were also calculated, such as an additional C_{2v} structure (Structure **IVC**$^+$ - Figure 7.1) and a planar C_s structure (Structure **IVD**$^+$) but are found to lie higher in energy than **IVA**$^+$ and **IVB**$^+$. In addition to the geometric data and Hirshfeld charges presented in Figure 7.1, Table 7.1 shows the calculated vibrational modes and symmetries of **IVA**$^+$ and **IVB**$^+$. The Cartesian coordinates and electronic parameters of all the calculated cationic Rh_2Ho_2 structures presented in Figure 7.1 can be found in Appendix D.

7.1.2. Geometric Changes and Hirshfeld Charges

For the two lowest energy neutral (**IVA** and **IVB**) and cationic (**IVA**$^+$ and **IVB**$^+$) minima discussed in Section 7.1.1, there are four ionisation transitions considered possible for Rh_2Ho_2: (a) the $^2B_1 \leftarrow {}^1A_1$ (**IVA**$^+ \leftarrow$ **IVA**) transition, (b) the $^2B_{2u} \leftarrow {}^1A_g$ (**IVB**$^+ \leftarrow$ **IVB**) transition, (c) the $^2B_{2u} \leftarrow {}^1A_1$ (**IVB**$^+ \leftarrow$ **IVA**), and (d) the $^2B_1 \leftarrow {}^1A_g$ (**IVA**$^+ \leftarrow$ **IVB**) transition. However, for the sake of brevity, only geometric and atomic Hirshfeld charge changes for transitions (a) and (b) will be discussed as transitions (c) and (d) do not yield a ZEKE spectrum due to extremely low FCF values (*vide infra* – Section 7.4.1).

In analysing the change in atomic Hirshfeld charges (labelled in Figure 7.1) upon ionisation, the rhodium and holmium atoms gain a net charge of +0.320 and +0.108, respectively upon transition (a). Despite the large gain in positive charge by the holmium atoms, the Ho-Rh-Rh-Ho dihedral angle decreases by 8.8^o upon ionisation. Additionally, the Rh-Ho bond length is found to decrease by 0.004 Å and the Rh-Rh bond length increases by 0.012 Å. Upon transition (b), the rhodium and holmium atoms gain a net charge of +0.448 and +0.053, respectively. Despite the large gain in positive charge by the holmium atoms, the Ho-Ho bond length only increases by

Rh_2Ho_2:	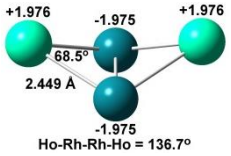	**IVA** $\Delta E = 0.00$ $S = 0$ State = $^1A_1$	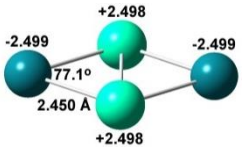	**IVB** $\Delta E = +0.14$ $S = 0$ State = ^1A_g
	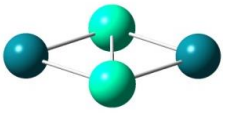	**IVC** $\Delta E = +0.22$ $S = 1$ State = $^3B_{3g}$	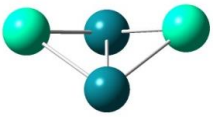	**IVD** $\Delta E = +0.28$ $S = 1$ State = $^3A_2$
	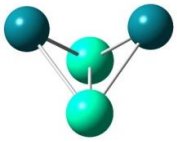	**IVE** $\Delta E = +0.59$ $S = 1$ State = $^3B_1$	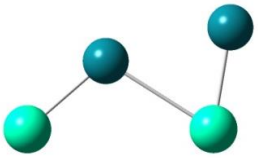	**IVF** $\Delta E = +0.71$ $S = 0$ State = $^1A'$
$Rh_2Ho_2^+$:	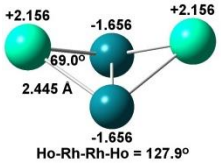	**IVA$^+$** $\Delta E = 0.00$ $S = 1/2$ State = $^2B_1$	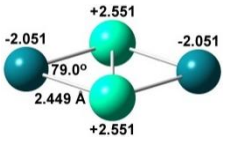	**IVB$^+$** $\Delta E = +0.07$ $S = 1/2$ State = $^2B_{2u}$
	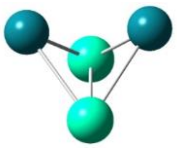	**IVC$^+$** $\Delta E = +0.45$ $S = 1/2$ State = $^2A_1$	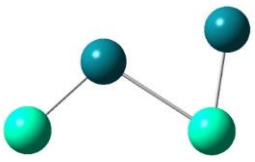	**IVD$^+$** $\Delta E = +0.99$ $S = 1/2$ State = $^2A'$

Figure 7.1. *Calculated structures for the neutral and cationic isomers of the Rh_2Ho_2 cluster (rhodium atoms in dark green, holmium atoms in light green). The relative energies (ΔE in eV) are calculated with respect to the lowest energy neutral and cationic isomers and are zero-point energy corrected. Hirshfeld charges and geometric data have also been provided for structures of relevance to the discussion.*

Mode	Symmetry[a]	Motion[b]	**IVA** (cm^{-1})	**IVA$^+$** (cm^{-1})	**IVB** (cm^{-1})	**IVB$^+$** (cm^{-1})
ν_1	a_g/a_1	$\nu_s^{\dagger}$ Rh-Ho	240	244	225	218
ν_2	a_g/a_1	δ_s Rh-Ho-Rh / δ_s Ho-Rh-Ho	131	130	157	143
ν_3	b_{3g}/a_2	$\nu_a^{\dagger}$ Rh-Ho	94	90	73	89
ν_4	b_{1u}/b_1	$\nu_a^{\S}$ Rh-Ho	197	201	223	175
ν_5	b_{2u}/b_2	$\nu_a^{\ddagger}$ Rh-Ho	185	188	184	207
ν_6	b_{3u}/a_1	δ_s Rh-Ho-Ho-Rh / δ_s Ho-Rh-Rh-Ho	48	59	64	49

Table 7.1. *Calculated vibrational modes of the lowest energy neutral and cationic minima of Rh_2Ho_2.*

[a] *Structures **IVA** and **IVA$^+$** have C_{2v} symmetry and Structures **IVB** and **IVB$^+$** have D_{2h} symmetry.*

*Label format: D_{2h}/C_{2v} (NOTE: Mode numbering is relative to Structures **IVB** and **IVB$^+$**).*

[b] *ν_s: symmetric stretch; ν_a: asymmetric stretch; δ_s: symmetric bend;*

$\nu_s^{\dagger}$: symmetric stretch of individual bonds with both Rh/Ho atoms stretching symmetrically relative to each other; $\nu_a^{\dagger}$: asymmetric stretch of individual bonds with both Rh/Ho atoms* stretching asymmetrically relative to each other; $\nu_a^{\ddagger}$: asymmetric stretch of individual bonds with both Ho/Rh atoms* stretching symmetrically relative to each other; $\nu_a^{\S}$: asymmetric stretch of individual bonds with both Rh/Ho atoms* stretching symmetrically relative to each other.*

Note:* Rh/Ho = Rh atoms for **IVA and **IVA$^+$**/Ho atoms for **IVB** and **IVB$^+$**.*

*Ho/Rh = Ho for **IVA** and **IVA$^+$**/Ho atoms for **IVB** and **IVB$^+$**.*

0.060 Å, which is accompanied by the Rh-Ho bond decreasing minutely by 0.002 Å upon ionisation.

For transition (a), the Rh-Ho-Ho-Rh dihedral angle change is considered to be fairly significant and indicates moderate-to-poor FC overlap between **IVA** and $\mathbf{IVA}^+$. This should ultimately result in a slow onset of cluster signal following ionisation. Contrary to this, the Ho-Ho and Rh-Ho bond length changes experienced upon transition (b) are considered to be relatively minute and indicate strong FC overlap between **IVB** and $\mathbf{IVB}^+$, thus predictively resulting in a rapid onset of cluster signal following ionisation. Unfortunately, the PIE spectrum of Rh_2Ho_2 (Chapter 5 – Figure 5.5(a)) has an AE that is close to the highest photon energy used experimentally; thus making it difficult to identify whether the cluster signal onset observed experimentally is rapid or gradual. Therefore, it is asserted at this stage that transitions (a) and (b) are both viable candidates for the Rh_2Ho_2 cluster.

7.2. DFT Results for the Rh_2Ho_2O Cluster

7.2.1. Lowest Energy Neutral and Cationic Structures

For the Rh_2Ho_2O species, the lowest energy neutral structure was determined to be a singlet C_{2v} structure in the $^1A_1$ state with the O atom bound across the Ho-Ho bond (Structure **VA**) and Rh-Rh, Rh-Ho, Ho-Ho and Ho-O bond lengths of 2.627 Å, 2.570 Å, 2.975 Å and 2.028 Å, respectively. The lowest energy cationic structure (Structure $\mathbf{VA}^+$) was found to be a doublet C_{2v} structure in the $^2B_2$ state with the O atom bound in the same manner as structure **VA** and Rh-Rh, Rh-Ho, Ho-Ho and Ho-O bond lengths of 2.470 Å, 2.665 Å, 3.052 Å and 1.997 Å, respectively. As with the lowest energy neutral and cationic minima of $RhHo_2O$ present in Chapter Six, the O atom is observed to only interact with the Ho-Ho bond in both structures. This is ascribed to the increased stability of the Ho-O bond relative to the Rh-O bond (refer to bond strengths in Table 4.1, Chapter Four) which results in the oxygen atom binding to the Ho-Ho edge rather than the Rh-Ho and Rh-Rh edges. Other neutral and cationic minima of Rh_2Ho_2O with the same, or very similar, structural motifs as **VA** and $\mathbf{VA}^+$ were also determined at higher multiplicities (Structures **VB** and $\mathbf{VB}^+$) but were found to lie higher in energy. In addition to the geometric data and Hirshfeld charges presented in Figure 7.2, Table 7.2 shows the calculated vibrational modes and symmetries of **VA** and $\mathbf{VA}^+$. The Cartesian coordinates and electronic parameters of all the calculated neutral and cationic Rh_2Ho_2O structures presented in Figure 7.2 can be found in Appendix D.

7.2.2. Geometric Changes and Hirshfeld Charges

Upon ionisation from structure **VA** to $\mathbf{VA}^+$ ($^2B_2 \leftarrow {}^1A_1$), the holmium, rhodium and oxygen atoms gain net charges of +0.090, +0.403 and +0.015, respectively. Despite the significant gain in positive charge by the rhodium atoms, the Rh-Rh bond length decreases by 0.157 Å. The Ho-O bond length is also observed to decrease by 0.031 Å but this is attributed to the increased positive charge on the holmium atoms, causing a

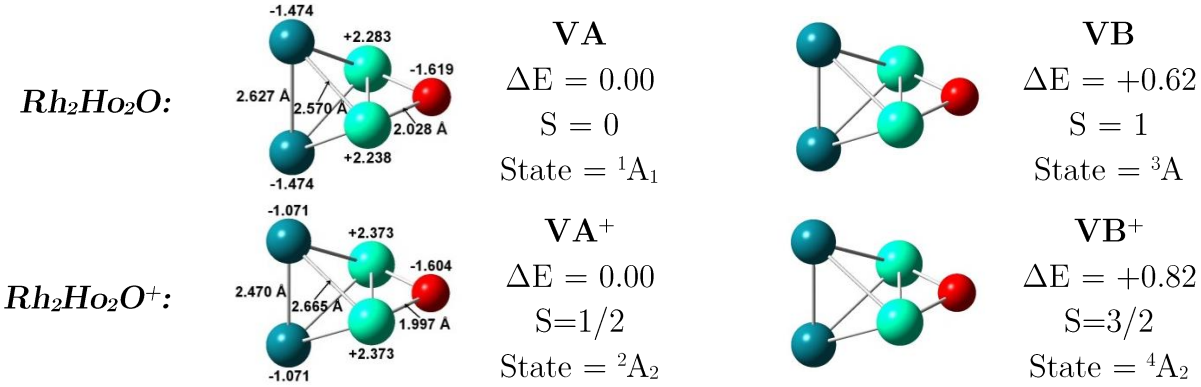

Figure 7.2. *Calculated structures for the neutral and cationic isomers of the Rh_2Ho_2O cluster (rhodium atoms in dark green, holmium atoms in light green and oxygen atoms in red). The relative energies (ΔE in eV) are calculated with respect to the lowest energy neutral and cationic isomers and are zero-point energy corrected. Hirshfeld charges and geometric data have also been provided for structures of relevance to the discussion.*

Mode	Symmetry[a]	Motion[b]	**VA** (cm^{-1})	**VA$^+$** (cm^{-1})
ν_1	a_1	ν_s Ho-O	574	588
ν_2	a_1	ν Rh-Rh	243	263
ν_3	a_1	δ_s Ho-O-Ho	192	190
ν_4	a_1	$\nu_s^{\dagger}$ Rh-Ho	138	153
ν_5	a_2	$\nu_a^{\ddagger}$ Rh-Ho	60	62
ν_6	b_1	ν_a Ho-O	507	562
ν_7	b_1	$\nu_a^{\dagger}$ Rh-Ho	138	107
ν_8	b_2	δ Rh-Ho-Ho-O	186	184
ν_9	b_2	$\nu_s^{\ddagger}$ Rh-Ho	147	83

Table 7.2. *Calculated vibrational modes of the lowest energy neutral and cationic minima of Rh_2Ho_2O.*

[a] *Structures **VA** and **VA$^+$** both possess C_{2v} symmetry.*

[b] *ν: stretch; ν_s: symmetric stretch; ν_a: asymmetric stretch; δ_s: symmetric bend; θ: rocking motion; δ: bend.*

$\nu_a^{\dagger}$: asymmetric stretch of individual bonds with both Rh atoms stretching symmetrically relative to each other; $\nu_a^{\ddagger}$: asymmetric stretch of individual bonds with both Rh atoms stretching asymmetrically relative to each other; $\nu_s^{\dagger}$: symmetric stretch of individual bonds with both Rh atoms stretching symmetrically relative to each other; $\nu_s^{\ddagger}$: symmetric stretch of individual bonds with both Rh atoms stretching asymmetrically relative to each other;

stronger electrostatic attractive force between the two atoms. This increase in positive charge also causes the Ho-Ho bond length to increase by 0.077 Å and the Rh-Ho bond length also increases by 0.095 Å. Overall, all of these bond length changes are considered to be significant and indicate moderate-to-poor FC overlap between **VA** and $\mathbf{VA}^+$. This should ultimately result in a slow onset of cluster signal following ionisation, which is consistent with the observed behaviour in the experimental PIE spectrum of Rh_2Ho_2O (Chapter 5 – Figure 5.5(b)).

7.3. DFT Results for the $Rh_2Ho_2O_2$ Cluster

7.3.1. Lowest Energy Neutral and Cationic Structures

For the neutral $Rh_2Ho_2O_2$ species, there are three isomers calculated that are of significant interest. The lowest energy of these is a singlet C_s dissociative structure in a $^1A'$ state with one oxygen atom doubly bridged to a Ho-Ho bond (labelled O), and the other (labelled O′) triply bound to a $RhHo_2$ face (Structure **VIA** – Figure 7.3). The next lowest energy neutral isomer is calculated to lie +0.02 eV higher in energy than **VIA** and is a triplet C_{2v} structure in a $^3B_2$ state with a structural motif similar to that of **VIA** (Structure **VIB** – Figure 7.3); except that both oxygen atoms are located equidistantly from their nearest rhodium atom neighbour, thus raising its symmetry and differentiating it from **VIA**. The last low-lying neutral isomer of interest is calculated to lie +0.03 eV higher in energy than **VIA** and is a triplet C_s structure in a $^3A''$ state with a structural motif that is very similar to **VIA** (Structure **VIC** – Figure 7.3). The lowest energy neutral structure with associatively-bound O_2 is a singlet C_{2v} structure in a $^1A_1$ state with O_2 bound perpendicular to the Ho-Ho bond, and parallel with the Rh-Rh bond (Structure **VIH** - Figure 7.3). This structure is calculated to lie +3.58 eV higher in energy than **VIA**. In addition to the geometric data and Hirshfeld charges presented in Figure 7.3, Table 7.3 shows the calculated vibrational modes and symmetries of **VIA**, **VIB and VIC**. The Cartesian coordinates and electronic parameters of all the calculated neutral $Rh_2Ho_2O_2$ structures presented in Figure 7.3 can be found in Appendix D.

For the cationic $Rh_2Ho_2O_2$ species, there are also three isomers calculated that are of significant interest. The lowest energy cationic structure is a quartet C_{2v} dissociative structure in a $^4B_1$ state with each individual oxygen atom doubly bridged to a Ho-Ho bond and located equidistantly from their nearest rhodium atom neighbour (Structure $\mathbf{VIA}^+$ – Figure 7.3). The next low-lying cationic isomer is calculated to lie +0.10 eV higher in energy than $\mathbf{VIA}^+$ and is a doublet C_s structure in a $^2A''$ state with a structural motif similar to that of $\mathbf{VIA}^+$ (Structure $\mathbf{VIB}^+$ – Figure 7.3); but that one

of the oxygen atoms (labelled O′) is located closer to its nearest rhodium atom neighbour than the other, thus lowering the symmetry and differentiating it from **VIA**$^+$. The last low-lying neutral isomer of interest is calculated to lie +0.14 eV higher in energy than **VIA**$^+$ and is a quartet C_s structure in a ^{4}A" state with a structural motif that is very similar to **VIB**$^+$ (Structure **VIC**$^+$ – Figure 7.3). The lowest energy cationic structure with associatively-bound O_2 is a singlet C_{2v} structure in a $^2A_2$ state with O_2 bound perpendicular to the Ho-Ho bond, and parallel with the Rh-Rh bond (Structure **VIG**$^+$ - Figure 7.3). This structure is calculated to lie +3.76 eV higher in energy than **VIA**$^+$. In addition to the geometric data and Hirshfeld charges presented in Figure 7.3, Table 7.3 shows the calculated vibrational modes and symmetries of **VIA**$^+$, **VIB**$^+$ and **VIC**$^+$. The Cartesian co-ordinates and electronic parameters of all the calculated cationic $Rh_2Ho_2O_2$ structures presented in Figure 7.3 can be found in Appendix D.

As with $RhHo_2O$ (Chapter 6) and Rh_2Ho_2O, the increased stability of the Ho-O bond compared to the Rh-O bond results in both oxygen atoms binding preferably to the Ho-Ho edge rather than the Rh-Ho edges in both the lower energy neutral and cationic structures. Other dissociative neutral and cationic minima at higher multiplicities were calculated (Structures **VID-VIG and VID**$^+$**-VIF**$^+$) but are found to lie much higher in energy than those presented in Figure 7.3. Lastly, as the neutral and cationic associatively bound structures are calculated to lie much higher in energy than the lower energy dissociative structures, it is contended that (as with $RhHo_2O_2$) only the latter are present in the molecular beam.

7.3.2. Hirshfeld Charges and Geometric Changes

For the three lowest energy neutral (**VIA-VIC**) and cationic (**VIA**$^+$**-VIC**$^+$) minima presented in Figure 7.3 and discussed in Section 7.3.1, there are seven ionisation transitions considered possible for $Rh_2Ho_2O_2$: (a) the ^{2}A" ← ^{1}A' (**VIB**$^+$ ← **VIA**) transition, (b) the $^4B_1 \leftarrow {}^3B_2$ (**VIA**$^+$ ← **VIB**) transition, (c) the ^{2}A" ← $^3B_2$

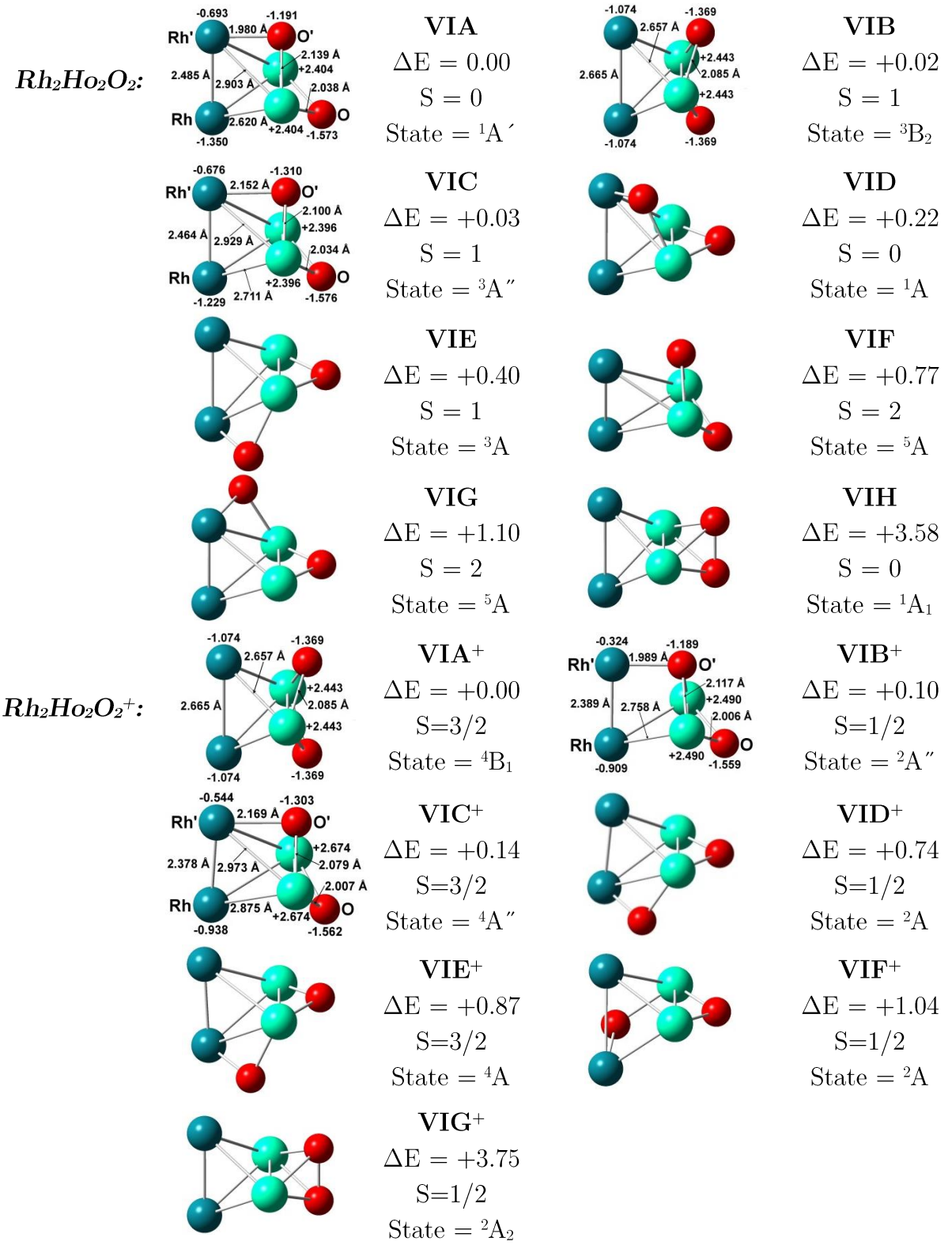

Figure 7.3. *Calculated structures for the neutral and cationic isomers of the $Rh_2Ho_2O_2$ cluster (rhodium atoms in dark green, holmium atoms in light green and oxygen atoms in red). The relative energies (ΔE in eV) are calculated with respect to the lowest energy neutral and cationic isomers and are zero-point energy corrected. Hirshfeld charges and geometric data have also been provided for structures of relevance to the discussion.*

Mode	Symmetry[a]	Motion[b]	**VIA** (cm^{-1})	**VIA$^+$** (cm^{-1})	**VIB** (cm^{-1})	**VIB$^+$** (cm^{-1})	**VIC** (cm^{-1})	**VIC$^+$** (cm^{-1})
ν_1	a_1/a'	$\nu_s^\dagger$ Ho-O	593	584	559	618	596	615
ν_2	a_1/a'	δ_s O-Ho-Ho-O	566	337	343	564	394	399
ν_3	a_1/a'	ν Rh-Rh	247	238	224	271	247	242
ν_4	a_1/a'	ν Ho-Ho,						
		ν Rh-Rh	200	208	194	199	184	215
		/ $\delta^\dagger$ Rh-Ho-Ho-O						
ν_5	a_1/a'	$\nu_s^\dagger$ Rh-Ho	158	131	127	146	145	110
ν_6	a_2/a"	$\nu_a^\ddagger$ Ho-O	346	405	370	373	359	390
ν_7	a_2/a"	$\nu_a^\ddagger$ Rh-Ho	38	63	52	32	35	43
ν_8	b_1/a"	$\nu_a^\dagger$ Ho-O	496	551	482	560	513	578
ν_9	b_1/a"	$\nu_a^\dagger$ Rh-Ho	103	103	112	89	83	90
ν_{10}	b_2/a'	$\nu_s^\ddagger$ Ho-O	470	527	510	490	509	522
ν_{11}	b_2/a'	θ O-Ho-Ho-O	231	190	190	227	218	165
ν_{12}	b_2/a'	$\nu_s^\ddagger$ Rh-Ho	117	79	127	109	83	89

Table 7.3. *Calculated vibrational modes of the lowest energy neutral and cationic minima of $Rh_2Ho_2O_2$.*

[a] *Structures **VIA$^+$** and **VIB** both possess C_{2v} symmetry. Structures **VIA**, **VIB$^+$** and **VIC** all possess C_s symmetry.*

*Label format: C_{2v}/C_s (NOTE: Mode numbering is relative to Structures **VIA$^+$** and **VIB**)*

[b] *ν: stretch; ν_s: symmetric stretch; ν_a: asymmetric stretch; δ_s: symmetric bend; θ: rocking motion; δ: bend.*

$\nu_a^\dagger$: asymmetric stretch of individual bonds with both Rh/O atoms stretching symmetrically relative to each other; $\nu_a^\ddagger$: asymmetric stretch of individual bonds with both Rh/O atoms stretching asymmetrically relative to each other; $\nu_s^\dagger$: symmetric stretch of individual bonds with both Rh/O atoms stretching symmetrically relative to each other; $\nu_s^\ddagger$: symmetric stretch of individual bonds with both Rh/O atoms stretching asymmetrically relative to each other; $\delta^\dagger$: Involves O atom bound further away from a Rh atom in the C_s structures.

(**VIB**$^+$ ← **VIB**) transition, (d) the $^4A'' \leftarrow {}^3B_2$ (**VIC**$^+$ ← **VIB**) transition, (e) the $^4B_1 \leftarrow {}^3A''$ (**VIA**$^+$ ← **VIC**) transition, (f) the $^2A'' \leftarrow {}^3A''$ (**VIB**$^+$ ← **VIC**) transition, and (g) the $^4A'' \leftarrow {}^3A''$ (**VIC**$^+$ ← **VIC**) transition. However, for the sake of brevity, only geometric and atomic Hirshfeld charge changes for transitions (a) and (f) will be discussed. These two were chosen as the five other transitions were found to either yield a simulated ZEKE spectrum with significantly lower signal intensity, or not yield a ZEKE spectrum at all due to extremely low FCF values (*vide infra* – Section 7.4.5).

In analysing the change in atomic Hirshfeld charges (labelled in Figure 7.3) upon transition (a), the holmium atoms gain a net charge of +0.086 and each individual rhodium atom gains a net charge of +0.369 for the oxygen-bound atom (labelled Rh' in **VIA** and **VIB**$^+$ - Figure 7.3), and +0.352 for the other atom (labelled Rh in **VIA** and **VIB**$^+$ - Figure 7.3) upon ionisation. Additionally, the change in charge of each individual oxygen atom is -0.002 for the atom that is bound to Rh' (labelled O' in **VIA** and **VIB**$^+$ - Figure 7.3), and +0.014 for the other atom upon ionisation (labelled O in **VIA** and **VIB**$^+$ - Figure 7.3). Upon transition (f), the holmium atoms gain a net charge of +0.094 and the rhodium atoms Rh and Rh' gain a net charge of +0.320 and +0.352, respectively. Additionally, the gain in charge is +0.017 and +0.121 for oxygen atoms O and O', respectively.

For transition (a), the most significant geometric changes upon ionisation are of the Rh-Ho and Rh'-Ho bonds, which are both observed to increase by 0.138 Å and 0.105 Å, respectively upon ionisation. Interestingly, these geometric changes create the impression of a "Rh_2" cluster moving away from a "Ho_2O_2" cluster, with the interaction between the two weakening upon ionisation. For transition (f), the most significant geometric change upon ionisation is the Rh'-O' bond, which is observed to decrease by 0.164 Å upon ionisation. Both sets of geometric changes that occur upon transitions (a) and (f) are considered significant and indicate moderate-to-poor FC overlap between the neutral and cationic structures, which should ultimately result in a gradual onset of cluster signal upon ionisation. However, as stated previously in Section 6.1.2, it can be

difficult to discern the extent to which geometric change affects the observed rate of signal onset. Therefore, it is contended at this stage that both ionisation transitions are equally possible and that both would have a gradual onset of signal following ionisation. This is consistent with the PIE spectrum of $Rh_2Ho_2O_2$ (Figure 5.3(c)), which exhibits this behaviour.

7.4. Simulated ZEKE and PIE Spectra for the $Rh_2Ho_2O_m$ (m= 0-2) Clusters

7.4.1. Simulated ZEKE Spectra for Rh_2Ho_2

Figure 7.4 shows the ZEKE spectra for the $^2B_1 \leftarrow {}^1A_1$ (**IVA**$^+$ ← **IVA**) and $^2B_{2u} \leftarrow {}^1A_g$ (**IVB**$^+$ ← **IVB**) transitions that were simulated at 300 K. The ZEKE spectrum for the $^2B_1 \leftarrow {}^1A_1$ transition (Figure 7.4(a)) exhibits nine progressions that appear with very weak to strong intensities, with the highest energy FC-allowed transition with appreciable intensity predicted to appear at *ca.* 5.511 eV (due to the $2_0^2 6_0^4$ vibronic transition). Of these nine progressions, six are due to the excitation of quanta corresponding to vibrational modes of **IVA**$^+$; with four of the progressions possessing an energy spacing of *ca.* 0.0161 eV (130 cm^{-1}) and corresponding to the symmetric bending mode of the Ho-Rh-Ho angle (ν_2 - δ_s Ho-Rh-Ho), and the other two possessing a spacing of *ca.* 0.00730 eV (59 cm^{-1}) and corresponding to the symmetric bending mode of the Ho-Rh-Rh-Ho dihedral angle (ν_6 - δ_s Ho-Rh-Rh-Ho). The rest of the progressions possess an energy spacing of *ca.* 0.00598 eV (48 cm^{-1}), which corresponds to the energy of the symmetric bending mode of the Ho-Rh-Rh-Ho dihedral angle (ν_6 - δ_s Ho-Rh-Rh-Ho) of **IVA**. Overall, the most intense peaks that arise in the calculated spectrum are mostly present in the 6_0^n the $2_0^1 6_0^n$ progressions i.e. only progressions that involve quanta of the symmetric bending mode of the Ho-Rh-Rh-Ho dihedral angle of **IVA**$^+$. This indicates that the most significant FC co-ordinate change upon the $^2B_1 \leftarrow {}^1A_1$ transition is for the Ho-Rh-Rh-Ho dihedral angle, which is observed to be the main structural difference between structures **IVA** and **IVA**$^+$**.** The band origin (0_0^0) for this transition was simulated to have a lower intensity than the other signals and as such, is concealed under the other ZEKE signals. The position of the band origin transition is labelled in Figure 7.4(a)) for reference.

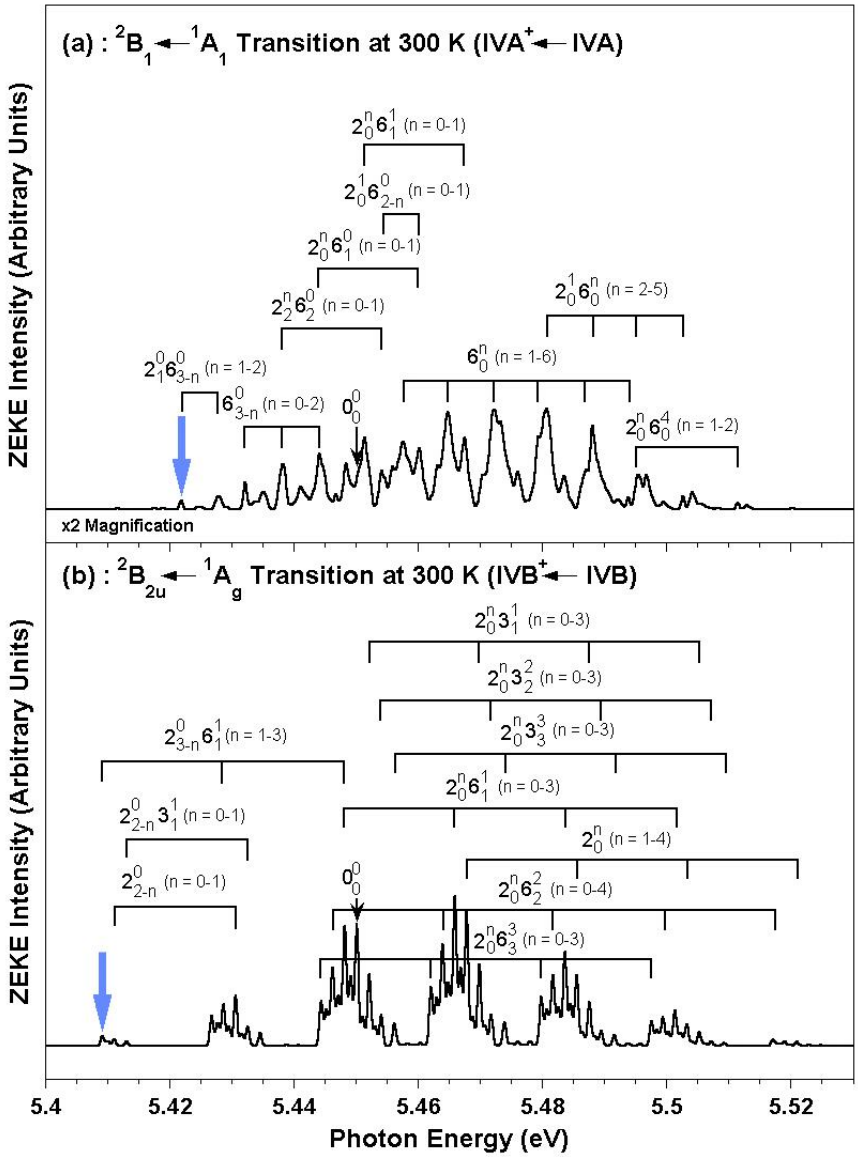

Figure 7.4. *ZEKE spectra simulated at 300 K for: (a) the $^2B_1 \leftarrow {}^1A_1$ (**$IVA^+ \leftarrow IVA$**), and (b) the $^2B_{2u} \leftarrow {}^1A_g$ (**$IVB^+ \leftarrow IVB$**) transitions for the Rh_2Ho_2 cluster. The theoretical band origins (black arrows) and possible thermal onset starting positions (blue arrows) are indicated. For clarity, the $^2B_1 \leftarrow {}^1A_1$ ZEKE spectrum has been magnified ×2 relative to the $^2B_{2u} \leftarrow {}^1A_g$ ZEKE spectrum (with the y-axis for each spectrum on the same scale).*

Figure 7.4(b) shows the ZEKE spectrum simulated for the $^2B_{2u} \leftarrow {}^1A_g$ transition. There are ten progressions that appear with weak to strong intensities, with the highest energy FC-allowed transition predicted to arise at *ca.* 5.521 eV (due to the 2_0^4 vibronic transition). Seven of these progressions possess a constant energy spacing of *ca.* 0.0177 eV (143 cm^{-1}), which corresponds to the energy of the symmetric bending mode of the Rh-Ho-Rh angle (ν_2 - δ_s Rh-Ho-Rh) for **IVB$^+$**. The other three progressions possess a constant energy spacing of *ca.* 0.0195 eV (157 cm^{-1}), which corresponds to the energy of the symmetric bending mode of the Rh-Ho-Rh angle (mode ν_2 - δ_s Rh-Ho-Rh) for **IVB**. Overall, the former seven progressions contain most of the highest intensity signals, with the 0_0^0 transition also predicted to appear in the ZEKE spectrum with comparable intensity. This indicates that the vertical and adiabatic IEs for Rh_2Ho_2 are equal for the $^2B_{2u} \leftarrow {}^1A_g$ transition and that there should be minimal geometric change experienced by this cluster upon ionisation, which is substantiated by the minute structural differences observed between **IVB** and **IVB$^+$** in Section 7.1.2.

Upon comparison of the ZEKE spectra in Figure 7.4, it is noticed that the signals simulated for the $^2B_{2u} \leftarrow {}^1A_g$ have slightly greater overall intensities than those simulated for the $^2B_1 \leftarrow {}^1A_1$ transition (due to the x2 magnification of the latter transition). However, as **IVA** is more energetically stable than **IVB**, it is more likely to be formed in the experiment. At this stage therefore, it is contended that both transitions are equally viable ionisation transitions for Rh_2Ho_2.

7.4.2. Comparison of Experimental and Simulated PIE Spectra for Rh_2Ho_2

In simulating the ZEKE spectra for the $^2B_1 \leftarrow {}^1A_1$ and $^2B_{2u} \leftarrow {}^1A_g$ transitions at 300 K, the theoretical 0_0^0 transition was set to the experimental appearance energy (denoted AE in Chapter 5) of Rh_2Ho_2 (5.45 eV). This was done based on the assumption that the initial onset of cluster signal in the experiment is due to the 0_0^0 transition and hence, any additional onset observed thereafter is due to various vibronic transitions that accompany the pure adiabatic ionisation transition. However,

the presence of strong hot band features simulated to arise at *ca.* 5.422 eV for the $^2B_1 \leftarrow {}^1A_1$ transition (due to the $2_1^0 6_2^0$ vibronic transition – indicated by the blue arrow in Figure 7.4(a)) and *ca.* 5.409 eV for the $^2B_{2u} \leftarrow {}^1A_g$ transition (due to the $2_2^0 6_1^1$ vibronic transition – indicated by the blue arrow in Figure 7.4(b)) indicates that the initial cluster signal onset is most likely due to these vibronic transitions and not the 0_0^0 transition. Hence, the initial experimental cluster signal onset observed at 5.45 eV is asserted to actually be due to either of the aforementioned vibronic transitions (depending on the assigned ionisation transition) and the experimental AE (i.e. the 0_0^0 transition) of Rh_2Ho_2 lies slightly higher energy.

For the ZEKE spectra arising from the $^2B_1 \leftarrow {}^1A_1$ and $^2B_{2u} \leftarrow {}^1A_g$ transitions, correction factors of 0.028 eV and 0.041 eV (the difference between the assigned theoretical 0_0^0 transition energy (5.45 eV) and the simulated transition energies of the aforementioned vibronic hot band transitions within each ZEKE spectrum) need to be applied, respectively to all transitions energies in order to attain the thermally-corrected experimental AE (denoted $AE^{\dagger}$) for Rh_2Ho_2 for each ionisation transition. Figures 7.5 and 7.6 show the comparison of the resulting corrected ZEKE and corresponding PIE spectra simulated for each transition with the experimental PIE spectrum of Rh_2Ho_2.

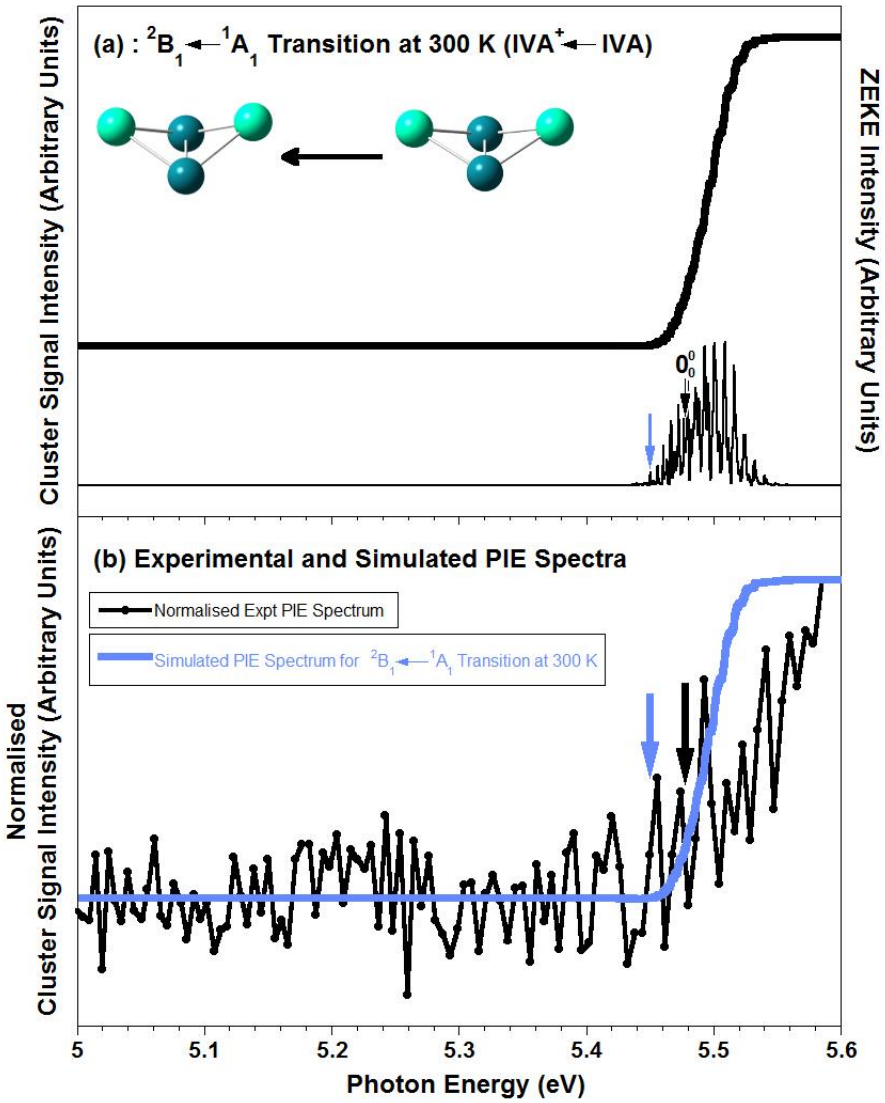

Figure 7.5. *(a) The corrected ZEKE and PIE spectra for the $^2B_1 \leftarrow {}^1A_1$ (IVA$^+ \leftarrow$ IVA) transition of Rh_2Ho_2 simulated at 300 K, and (b) The normalised experimental and corrected PIE spectra for the $^2B_1 \leftarrow {}^1A_1$ (IVA$^+ \leftarrow$ IVA) transition of Rh_2Ho_2 simulated at 300 K. The blue arrow indicates the energy of the most significant hot band transition that initiates thermal onset of the PIE spectrum. The black arrow indicates the energy of the band origin and the thermally-corrected experimental appearance energy ($AE^\dagger$) of Rh_2Ho_2.*

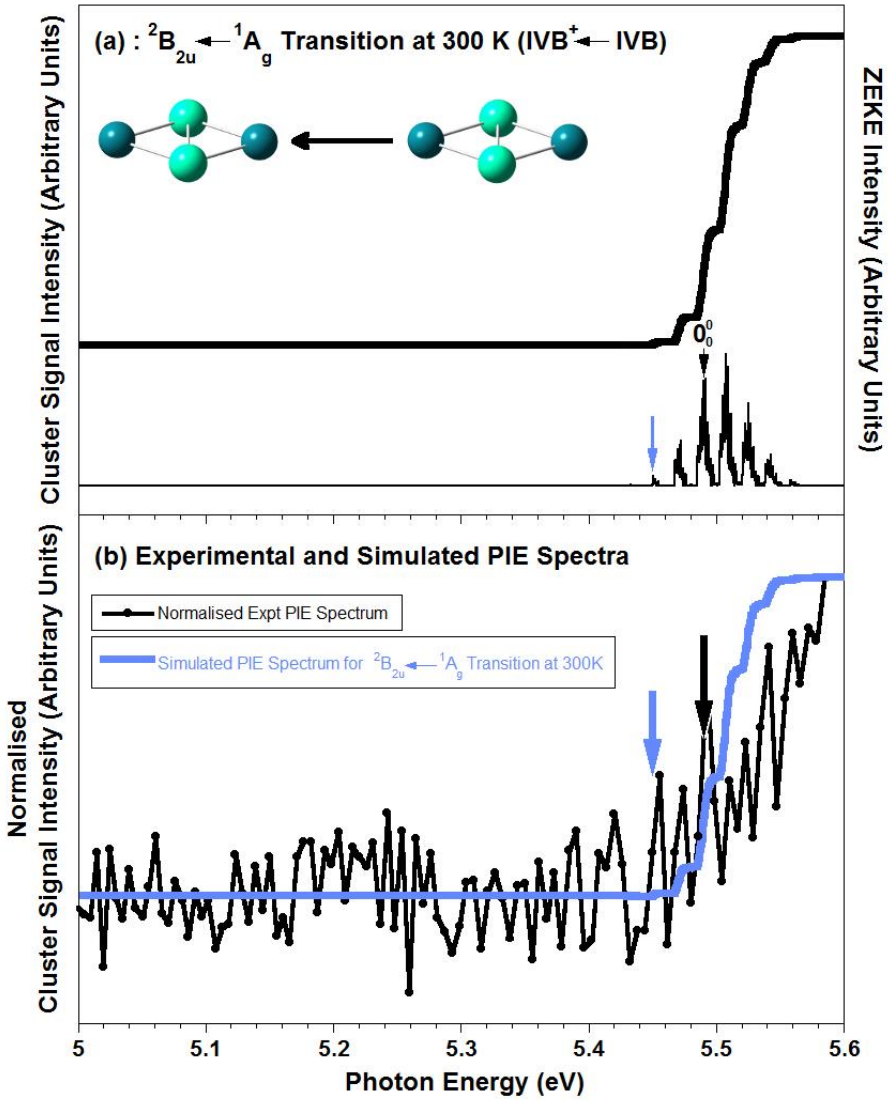

Figure 7.6. *(a) The corrected ZEKE and PIE spectra for the $^2B_{2u} \leftarrow {}^1A_g$ ($IVB^+ \leftarrow IVB$) transition of Rh_2Ho_2 simulated at 300 K, and (b) The normalised experimental and corrected PIE spectra for the $^2B_{2u} \leftarrow {}^1A_g$ ($IVB^+ \leftarrow IVB$) transition of Rh_2Ho_2 simulated at 300 K. The blue arrow indicates the energy of the most significant hot band transition that initiates thermal onset of the PIE spectrum. The black arrow indicates the energy of the band origin and the thermally-corrected experimental appearance energy (AE^t) of Rh_2Ho_2.*

As observed in Figure 7.5(a), the addition of the 0.028 eV correction factor to all transition energies in the simulated ZEKE spectrum causes an initial cluster signal onset at 5.45 eV in the simulated PIE spectrum due to the $2_1^0 6_2^0$ vibronic transition (blue arrow) and shifts the energy of the 0_0^0 transition to 5.478 eV (black arrow), the latter being the experimental AE† for Rh_2Ho_2 upon the $^2B_1 \leftarrow {}^1A_1$ transition. In addition, the 0.028 eV correction factor shifts the energy of the $2_0^2 6_0^4$ vibronic transition (the highest energy FC-allowed vibronic transition) to 5.549 eV, causing the simulated PIE spectrum to level off at around this point.

As observed in Figure 7.6(a), the addition of the 0.041 eV correction factor to all transition energies in the simulated ZEKE spectrum causes an initial cluster signal onset at 5.45 eV in the simulated PIE spectrum due to the $2_2^0 6_1^1$ vibronic transition (blue arrow) and shifts the energy of the 0_0^0 transition to 5.491 eV (black arrow), the latter being the experimental AE† for Rh_2Ho_2 upon the $^2B_{2u} \leftarrow {}^1A_g$ transition. In addition, the 0.041 eV correction factor shifts the energy of the 2_0^4 vibronic transition (the highest energy FC-allowed vibronic transition) to 5.562 eV, causing the simulated PIE spectrum to level off at around this point.

In Figures 7.5(b) and 7.6(b), the simulated and experimental PIE spectra have been independently normalised and compared. As observed, the simulated and experimental spectra do not compare particularly well as both simulated PIE spectra appear to exhibit a steeper signal onset than the experimental PIE spectrum. However, the experimental PIE spectrum does not plateau, thus indicating that the highest energy FC-allowed vibronic transition was not reached experimentally for Rh_2Ho_2. Additionally, the experimental PIE spectrum does not display much cluster signal onset due to having an AE that is close to the highest photon energy used experimentally. These two factors could affect the normalisation of the experimental PIE spectrum, thus leading to the discrepancies observed.

From the comparison between the simulated and experimental PIE spectra alone, it is not possible to assign either ionisation transition to Rh_2Ho_2. However, when

observing how well the HOMO energies of **IVA** and **IVB** compare with the overall trend of neutral HOMO energy versus experimental IE (*vide infra* – Figure 7.12), it is observed that the HOMO energy of **IVA** compares better with the overall trend than **IVB**. Hence, structures **IVA** and $\mathbf{IVA}^+$ are asserted to be the most likely neutral and cationic structures of Rh_2Ho_2, respectively.

7.4.3. Simulated ZEKE Spectrum for the Rh_2Ho_2O Cluster

In contrast to the Rh_2Ho_2 cluster, there is only one possible candidate for each of the neutral (**VA**) and cationic ($\mathbf{VA}^+$) structures of the Rh_2Ho_2O cluster as all other structures are calculated to lie much higher in energy.

Figure 7.6 shows the ZEKE spectrum simulated for the $^2A_2 \leftarrow {}^1A_1$ ($\mathbf{VA}^+ \leftarrow \mathbf{VA}$) transition at 300 K. As observed, the simulation yields a dense array of vibronic signals comprised of various quanta of various modes from both structures. Due to the large number of simulated transitions, specific labelling has been omitted except for the band origin (0_0^0 – black arrow). Additionally, a range bar has also been placed on the spectrum to indicate that the vibronic "hot band" transition of interest lies somewhere within this range. This is done as it is unclear from the ZEKE spectrum which particular vibronic transition is responsible for the thermal onset of the PIE spectrum.

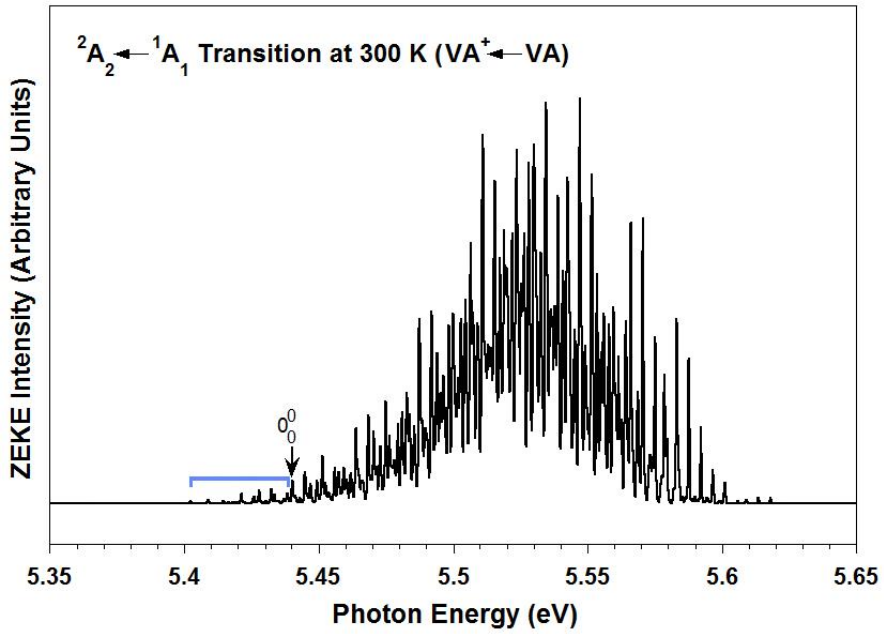

Figure 7.6. *ZEKE spectrum simulated at 300 K for the* $^2A_2 \leftarrow {}^1A_1$ ($\mathbf{VA^+ \leftarrow VA}$) *transition for the* Rh_2Ho_2O *cluster. Due to the large number of ZEKE signals simulated, specific labelling has been omitted except for the theoretical band origin (black arrow) and possible range of the thermal onset starting position (blue range bar).*

7.4.4. Comparison of Experimental and Simulated PIE Spectra for Rh_2Ho_2O

In simulating the ZEKE spectrum for the $^2A_2 \leftarrow {}^1A_1$ transition at 300 K, the theoretical 0_0^0 transition was set to the experimental AE of Rh_2Ho_2O (5.44 eV). This was done based on the assumption that the initial onset of cluster signal in the experiment is due to the 0_0^0 transition and hence, any additional onset observed thereafter is due to various other vibronic transitions that accompany the pure adiabatic ionisation transition. However, as with Rh_2Ho_2 (and the $RhHo_2O_n$ clusters in Chapter 6), the vibrational temperature of the molecular beam at *ca.* 300 K could lead to an early onset of Rh_2Ho_2O cluster signal due to vibronic "hot band" transitions rather than the origin band. The presence of hot band features simulated to arise between *ca.* 5.401 – 5.439 eV (indicated by the blue range bar in Figure 7.6) indicates that the initial cluster signal onset is most likely due to one of the vibronic transitions within this range and not the 0_0^0 transition. Hence, the initial experimental cluster

signal onset observed 5.44 eV is asserted to actually be due to a vibronic hot band transition and the experimental AE (i.e. 0_0^0 transition) of Rh_2Ho_2O lies slightly higher in energy.

For the ZEKE spectrum arising from the $^2A_2 \leftarrow {}^1A_1$ transition, an arbitrary correction factor of 0.030 eV needs to be applied to all of the transitions energies in order to attain the experimental AE† for Rh_2Ho_2O for this ionisation transition.[1] Figure 7.7 shows the comparison of the resulting corrected ZEKE and corresponding PIE spectra simulated for the transition with the experimental PIE spectrum of Rh_2Ho_2O. As observed in Figure 7.7(a), the addition of the 0.030 eV correction factor to all transition energies in the simulated ZEKE spectrum causes an initial cluster signal onset at 5.44 eV in the simulated PIE spectrum (blue arrow) and shifts the energy of the 0_0^0 transition to 5.470 eV (black arrow), the latter being the experimental AE† for Rh_2Ho_2O. In addition, the 0.030 eV correction factor shifts the highest energy FC-allowed vibronic transition with considerable intensity to *ca.* 5.600 eV, causing the simulated PIE spectrum to level off at around this point.

In Figure 7.7(b), the simulated and experimental PIE spectra have been independently normalised and compared. As observed, the shifting of the simulated ZEKE by 0.030 eV results in an excellent fit of the corresponding simulated PIE curve to the experimental PIE curve, with both displaying very similar levels of cluster signal onset upon ionisation and both appearing to level off at *ca.* 5.60 eV. Overall, such excellent comparison between the experimental and theoretical PIE spectra strongly indicates that structures **VA** and **VA**$^+$ are the most likely neutral and cationic Rh_2Ho_2O structures, respectively.

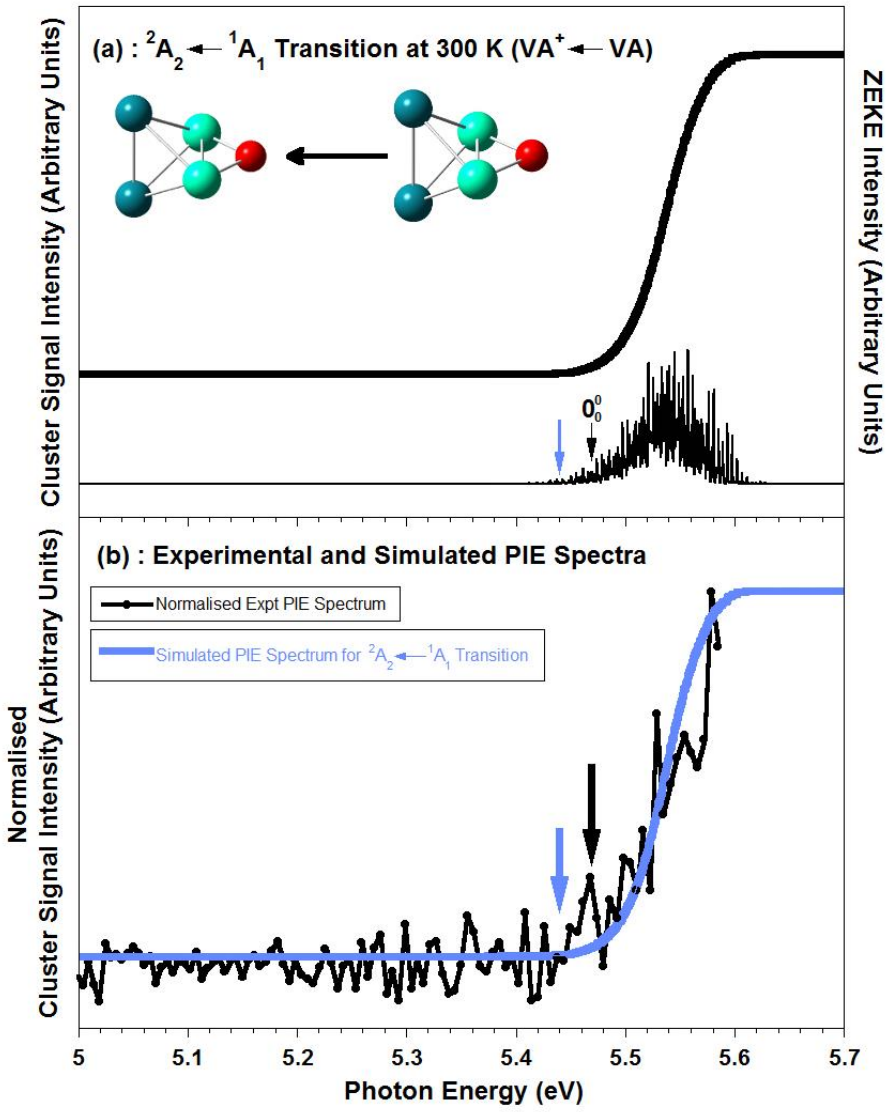

Figure 7.7. *(a) The corrected ZEKE and PIE spectra for the $^2A_2 \leftarrow {}^1A_1$ ($VA^+ \leftarrow VA$) transition of Rh_2Ho_2O simulated at 300 K, and (b) The normalised experimental and corrected PIE spectra for the $^2A_2 \leftarrow {}^1A_1$ ($VA^+ \leftarrow VA$) transition of Rh_2Ho_2O simulated at 300 K. The blue arrow indicates the energy at which the thermal onset of the PIE spectrum is initiated. The black arrow indicates the energy of the band origin and thermally-corrected experimental appearance energy (AE^t) of Rh_2Ho_2O.*

7.4.5. Simulated ZEKE Spectra for the $Rh_2Ho_2O_2$ cluster

Figure 7.8 shows the ZEKE spectra simulated at 300 K for four of the seven possible ionisation transitions for $Rh_2Ho_2O_2$ (*vide supra* – Section 7.3.2): (a) the $^2A'' \leftarrow {}^1A'$ (**VIB**$^+ \leftarrow$ **VIA**) transition, (b) the $^4B_1 \leftarrow {}^3B_2$ (**VIA**$^+ \leftarrow$ **VIB**) transition, (c) the $^2A'' \leftarrow {}^3A''$ (**VIB**$^+ \leftarrow$ **VIC**) transition, and (d) the $^4A'' \leftarrow {}^3A''$ (**VIC**$^+ \leftarrow$ **VIC**) transition. The ZEKE spectra simulated for the $^2A'' \leftarrow {}^3B_2$ (**VIC**$^+ \leftarrow$ **VIB**), $^4A'' \leftarrow {}^3B_2$ (**VIC**$^+ \leftarrow$ **VIB**) and $^4B_1 \leftarrow {}^3A''$ (**VIA**$^+ \leftarrow$ **VIC**) transitions yielded signals that have extremely low intensities due to very low calculated FCF values and thus, produced much weaker ZEKE spectra than those displayed in Figure 7.8. As observed in Figure 7.8, all simulations yield a dense array of ZEKE signals arising from transitions between numerous vibrational energy levels that are comprised of multiple quanta of various modes from both neutral and cationic states. Due to the large number of ZEKE signals simulated, specific labelling has been omitted from all spectra except for the band origin (0_0^0 – black arrow). Additionally, as in the ZEKE spectrum for Rh_2Ho_2O, range bars have been placed on each spectrum to indicate that the vibronic "hot band" transition responsible for the thermal onset of the PIE spectrum lies somewhere within this range.

Upon comparison of the ZEKE spectra in Figure 7.8, it is clear that the signals simulated for the $^2A'' \leftarrow {}^1A'$ (ZEKE spectrum (a)) and $^2A'' \leftarrow {}^3A''$ (ZEKE spectrum (c)) transitions have slightly greater overall intensities than those simulated for the other two transitions (as the ZEKE spectra arising from the latter two transitions have been magnified). Hence, these transitions are the only two that will be considered (as mentioned in Section 7.3.2 above) and thus, only comparison of the resulting simulated PIE spectra with the experimental PIE spectrum will ultimately determine which transition will be assigned for the $Rh_2Ho_2O_2$ cluster.

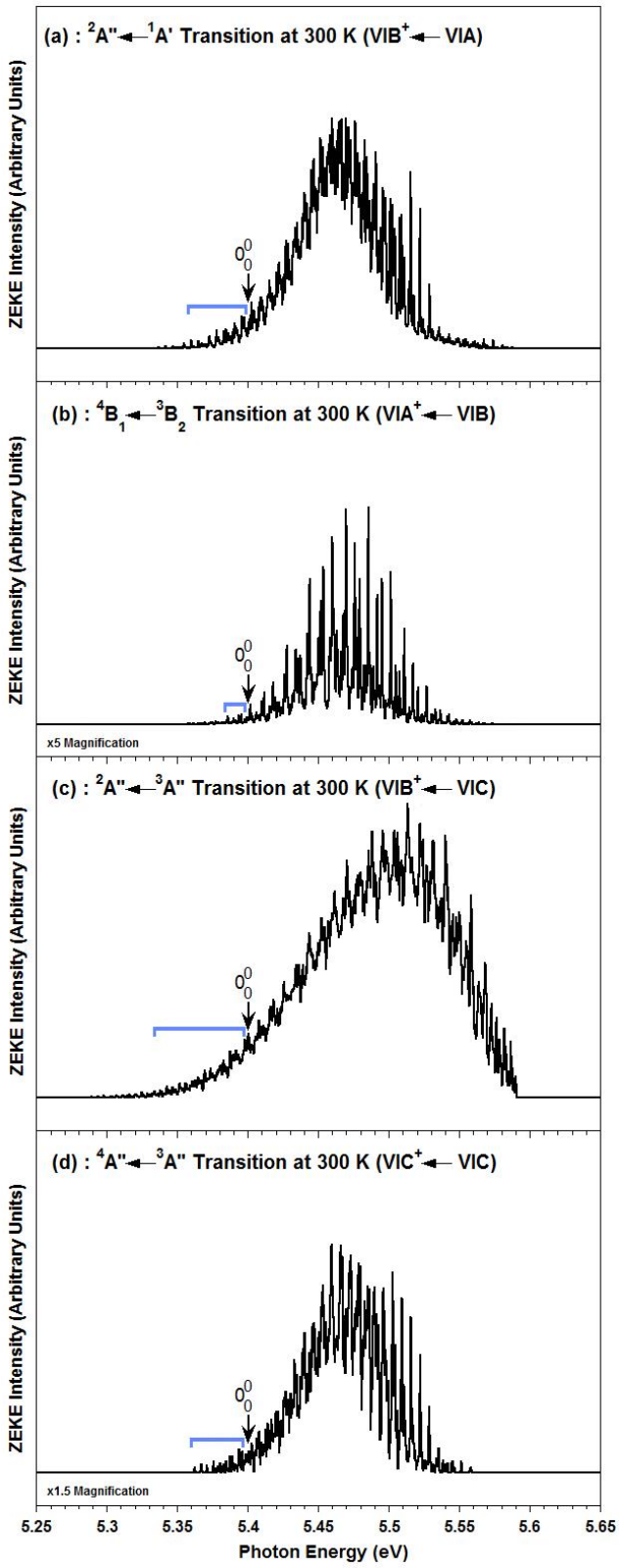

Figure 7.8. *ZEKE spectra simulated at 300 K for the various competing transition for the $Rh_2Ho_2O_2$ cluster. The energies of the theoretical band origin (black arrow) and approximate range of thermal onset starting position (blue bracket) have been indicated. Due to the large number of ZEKE signals simulated, specific labelling has been omitted except for the band origin (0_0^0).*

7.4.6. Comparison of Experimental and Simulated PIE Spectra for $Rh_2Ho_2O_2$

In simulating the ZEKE spectra for the $^2A'' \leftarrow {}^1A'$ and $^2A'' \leftarrow {}^3A''$ transitions at 300 K, the theoretical 0_0^0 transition was set to the experimental AE of $Rh_2Ho_2O_2$ (5.40 eV). This was done based on the assumption that the initial onset of cluster signal in the experiment is due to the 0_0^0 transition and hence, any additional onset observed thereafter is due to various vibronic transitions that accompany the pure adiabatic ionisation transition. However, the presence of the hot band features simulated to arise between *ca.* 5.351 - 5.398 eV for the $^2A'' \leftarrow {}^1A'$ transition and *ca.* 5.334 – 5.398 eV for the $^2A'' \leftarrow {}^3A''$ transition (indicated by the blue range bars in Figures 7.6(a) and (c)) indicates that the initial cluster signal onset is most likely due to one of the vibronic transitions in these ranges and not the 0_0^0 transition. Hence, the initial experimental cluster signal onset observed 5.40 eV is asserted to actually be due to a vibronic hot-band transition and the experimental AIE (i.e. 0_0^0 transition) of $Rh_2Ho_2O_2$ lies slightly higher in energy.

For the ZEKE spectra arising from the $^2A'' \leftarrow {}^1A'$ and $^2A'' \leftarrow {}^3A''$ transitions, a correction factor of 0.030 eV (the difference between the assigned theoretical 0_0^0 transition energy (5.45 eV) and the simulated transition energies of the aforementioned vibronic hot band transitions within each ZEKE spectrum) needs to be applied to all transitions energies in order to attain the experimental AE† for $Rh_2Ho_2O_2$ for each ionisation transition. Figures 7.9 and 7.10 show the comparison of the resulting corrected ZEKE and corresponding PIE spectra simulated for each transition with the experimental PIE spectrum of $Rh_2Ho_2O_2$.

As observed in Figures 7.9(a) and 7.10(a), the addition of the 0.030 eV correction factor to all transition energies causes an initial cluster signal onset at 5.40 eV in each simulated PIE spectra (blue arrow) and shifts the energy of the 0_0^0 transition to 5.430 eV (black arrow), the latter being the experimental AE† for $Rh_2Ho_2O_2$ for both ionisation transitions. In addition, the 0.030 eV correction factor

shifts the highest energy FC-allowed vibronic transition with considerable intensity to *ca.* 5.560 eV for the $^2A'' \leftarrow {}^1A'$ transition, and to *ca.* 5.620 for the $^2A'' \leftarrow {}^3A''$ transition, thus causing the simulated PIE spectrum for the former transition to level off at an earlier photon energy than the latter.

In Figures 7.9(b) and 7.10(b), the simulated PIE spectra from each transition have been normalised and compared to the normalised experimental PIE spectrum. As observed, the corresponding simulated PIE spectrum for the $^2A'' \leftarrow {}^3A''$ transition (Figure 7.9(b)) compares better with the experimental PIE spectrum than that of the $^2A'' \leftarrow {}^1A'$ transition (Figure 7.10(b)), with the former displaying a much similar level of cluster signal onset to that observed experimentally than the latter. Additionally, the simulated PIE spectrum yielded from the former transition levels off at around the same photon energy as that attained experimental, thus also contributing to the better comparison. Overall, the better comparison between the experimental PIE spectrum and that simulated from the $^2A'' \leftarrow {}^3A''$ transition indicates that structures **VIC** and $\mathbf{VIB}^+$ are the most likely neutral and cationic $Rh_2Ho_2O_2$ structures, respectively.

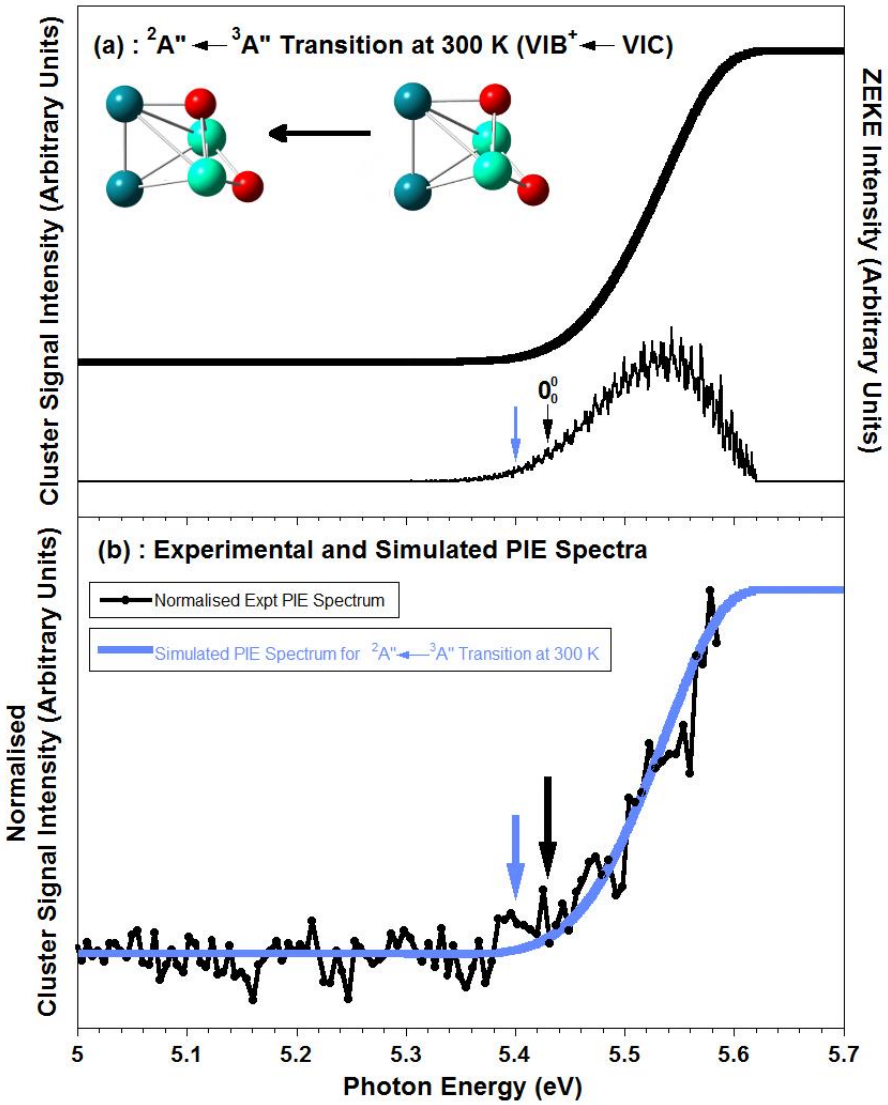

Figure 7.9. *(a) The corrected ZEKE and PIE spectra for the $^2A'' \leftarrow {}^3A''$ (VIB$^+$ ← VIC) transition of $Rh_2Ho_2O_2$ simulated at 300 K, and (b) The normalised experimental and corrected PIE spectra for the $^2A'' \leftarrow {}^3A''$ (VIB$^+$ ← VIC) transition of $Rh_2Ho_2O_2$ simulated at 300 K. The blue arrow indicates the energy of the most significant hot band transition that initiates thermal onset of the PIE spectrum. The black arrow indicates the energy of the band origin and the thermally-corrected experimental appearance energy (AE^t) of $Rh_2Ho_2O_2$.*

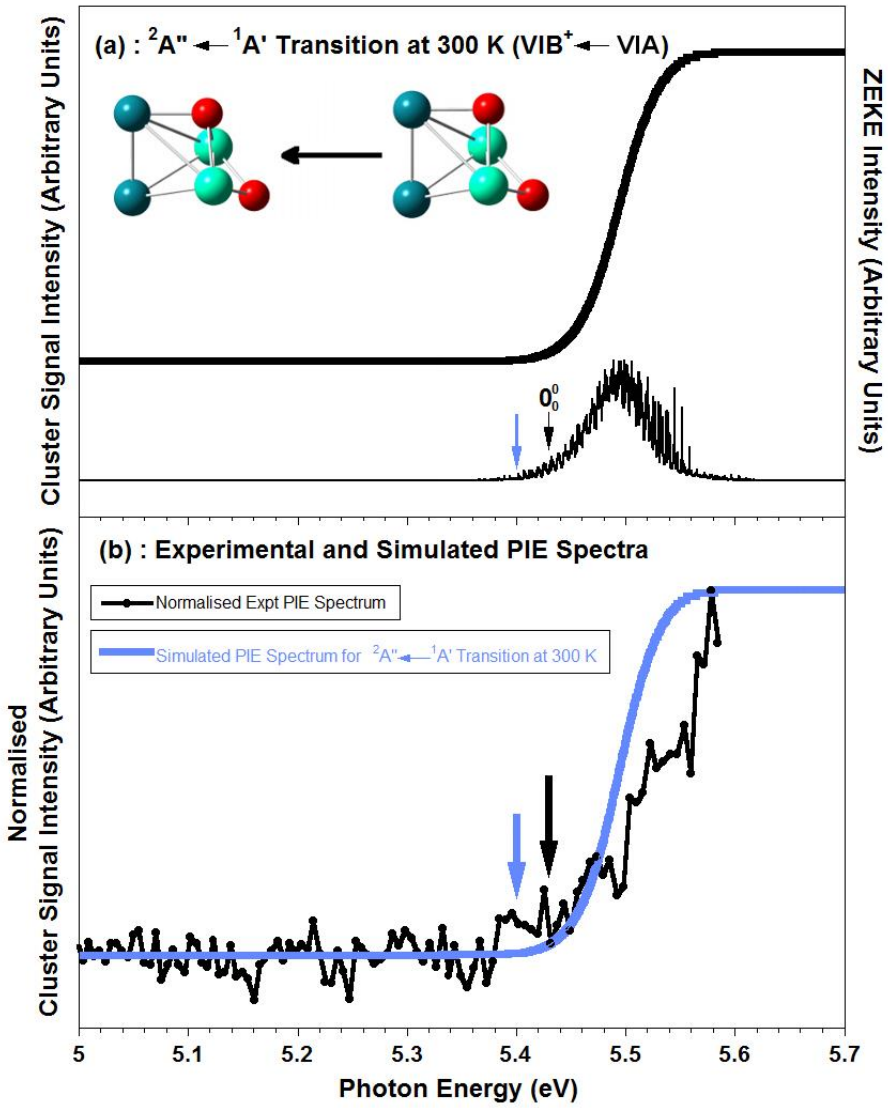

Figure 7.10. *(a) The corrected ZEKE and PIE spectra for the $^2A'' \leftarrow {}^1A'$ (VIB$^+$ ← VIA) transition of $Rh_2Ho_2O_2$ simulated at 300 K, and (b) The normalised experimental and corrected PIE spectra for the $^2A'' \leftarrow {}^1A'$ (VIB$^+$ ← VIA) transition of $Rh_2Ho_2O_2$ simulated at 300 K. The blue arrow indicates the energy of the most significant hot band transition that initiates thermal onset of the PIE spectrum. The black arrow indicates the energy of the band origin and thermally-corrected experimental appearance energy ($AE^\dagger$) of $Rh_2Ho_2O_2$.*

7.5. Field-Correction to the Experimental IEs of the $Rh_2Ho_2O_m$ Clusters

From the various ZEKE and PIE spectral simulations presented in the previous section, the thermally-corrected experimental AEs (denoted $AE^{\dagger}$) have been determined for the $Rh_2Ho_2O_m$ (m = 0-2) clusters. By applying a correction factor of 0.017 eV (derived from IE =AE+6.1$\sqrt{E}$; where E= 485 V/cm for the experimental setup)[2] to these experimental $AE^{\dagger}$ values, the field- and thermally-corrected experimental IEs (rounded-off to two decimal places) become 5.50 eV, 5.49 eV and 5.45 eV for Rh_2Ho_2, Rh_2Ho_2O and $Rh_2Ho_2O_2$, respectively. These values for the $Rh_2Ho_2O_m$ (m = 0-2) clusters are listed in Table 7.4 and denoted $IE^{\dagger}$ to differentiate them from the experimental IEs determined in Chapter 5 (denoted IE in that chapter).

7.6. Calculated IEs of the $Rh_2Ho_2O_m$ Clusters and Comparison to Experimental IEs

As for the $RhHo_2O_n$ (n = 0-2) clusters in Chapter 6, the calculated IEs of each cluster within the $Rh_2Ho_2O_m$ (m = 0-2) series are determined by taking the energy difference (in eV and including zero-point energy correction) between the assigned neutral and cationic structures determined by the ZEKE and PIE spectral simulations presented and discussed in Section 7.4 (and obeying the $\Delta S = \pm 1/2$ selection rule). These calculated IE values for the $Rh_2Ho_2O_m$ (m = 0-2) clusters are listed in Table 7.4. As observed, the calculated IE for Rh_2Ho_2 is 5.75 eV for the $^2B_1 \leftarrow {}^1A_1$ transition. The addition of an oxygen atom to the bare metal cluster increases the IE by 0.08 eV, yielding a calculated IE of 5.83 eV for the $^2A_1 \leftarrow {}^1A_1$ transition of Rh_2Ho_2O. Furthermore, the addition of another oxygen atom decreases the IE by 0.10 eV relative to Rh_2Ho_2O, yielding a calculated IE of 5.73 eV for the $^2A'' \leftarrow {}^3A''$ transition of $Rh_2Ho_2O_2$. Relative to the bare metal cluster, the addition of two oxygen atoms to form $Rh_2Ho_2O_2$ decreases the calculated IE by 0.02 eV.

Cluster	Expt. AE†	Expt. IE†	Structures	Calc. Transition	E of Neutral HOMO	Calc. IE (Incl. ZPE)	Offset IE
Rh_2Ho_2	5.478	5.50	$IVA^+ \leftarrow IVA$	$^2B_1 \leftarrow {}^1A_1$	-4.41	5.75	5.50
Rh_2Ho_2O	5.470	5.49	$VA^+ \leftarrow VA$	$^2A_1 \leftarrow {}^1A_1$	-4.56	5.83	5.58
$Rh_2Ho_2O_2$	5.430	5.45	$VIB^+ \leftarrow VIC$	$^2A" \leftarrow {}^3A"$	-4.45	5.73	5.48

Table 7.4. *List of the thermally-corrected experimental AEs (*AE†*) and field- and thermally-corrected experimental IEs (IE†) determined for the $Rh_2Ho_2O_m$ (m = 0-2) clusters. Also shown are the calculated transitions, energies of the neutral HOMOs and IEs (offset and including ZPE) determined using the B3P86 density functional and the SDD basis set (uncertainty in IEs = ±0.05 eV). The offset IE was calculated by subtracting the difference between the calculated and corrected experimental IEs for the Rh_2Ho_2 cluster (0.26 eV) from all the calculated IEs. All numerical values are in units of 'eV'.*

As observed for the $RhHo_2O_n$ (n = 0-2) clusters in Chapter 6 and in previous studies on gas-phase metal carbide clusters by the Metha group, the calculated IEs listed in Table 7.4 are determined to be higher in energy than the experimental IE† values.[3-6] This is attributed to the nature of the B3P86 functional rather than that of the Stuttgart-Dresden ECP, which has been concluded previously from the comparison of the experimental IEs of the Ta_4C_y (y = 0-4) clusters with those calculated using the B3P86/LANL2DZ and B3P86/SDD levels of theory.[4] Hence, in order to account for this over-estimation, the calculated IEs are corrected with respect to the experimental IE† value of Rh_2Ho_2 as the main focus of this work is how the IE changes with respect to the sequential addition of oxygen atoms onto the bare metal cluster. Accordingly, the difference between the calculated and experimental IE† of Rh_2Ho_2 is determined to be +0.25 eV. This value is then subtracted from the calculated IE values for Rh_2Ho_2O and $Rh_2Ho_2O_2$ to give the offset IE values that are listed in the final column of Table 7.4.

Figure 7.11 shows the comparison of the experimental IE† and calculated offset IE values, both plotted against the number of constituent oxygen atoms for each cluster. The general trend in IE as a function of oxygen atoms is the same in both sets of data; both show that the sequential addition of oxygen atoms onto Rh_2Ho_2 has little to no effect on the IE. This is in stark contrast to the IE trend observed for the $RhHo_2O_n$ (n = 0-2) clusters in Chapters Five and Six, where the sequential addition of oxygen atoms onto $RhHo_2$ significantly affects the IEs. Additionally, the difference between the experimental IE† and offset IE values is only +0.09 eV for Rh_2Ho_2O and +0.03 for $Rh_2Ho_2O_2$, indicating good quantitative comparison between theory and experiment, especially since the experimental IE error is ±0.05 eV.

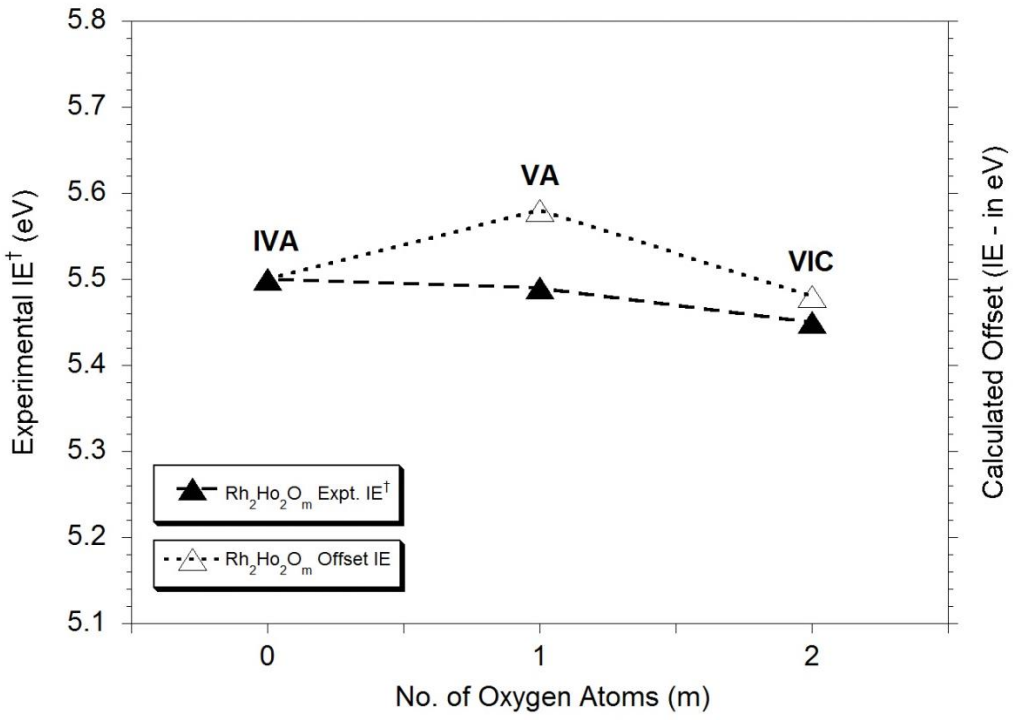

Figure 7.11. *Graph showing the corrected experimental IE values (denoted IE†) for the $Rh_2Ho_2O_m$ (m = 0-2) clusters as a function of constituent oxygen atoms. Also shown are the offset IE values calculated using DFT. Note that the "Calculated Offset" value for Rh_2Ho_2 is arbitrarily set to the corrected experimental value and this difference is used as the offset correction for the other calculated IE values. The corresponding neutral isomer of each cluster from which ionisation is most likely to occur has also been labelled.*

Overall, observing no substantial IE change following the sequential addition of oxygen atoms onto Rh_2Ho_2 suggests that there is no significant change in the electronic structure of each cluster upon sequential oxidation. Assuming that the electron is removed from the HOMO of the neutral cluster in the photoionisation process, this specifically indicates that there should be no substantial changes in the energies, bonding/non-bonding/anti-bonding characteristics and the composition of the HOMOs of each neutral cluster upon the sequential addition of oxygen atoms onto Rh_2Ho_2. Figure 7.12 shows the comparison between the neutral HOMO energy and the experimental IE† of each cluster, both plotted against the number of constituent oxygen atoms. The axes have been shifted but represent a linear relationship. The corresponding pictures of the neutral HOMO of each cluster have also been included in order to help explain any observed change in bonding/non-bonding/anti-bonding character upon oxidation. Additionally, the Rh_2Ho_2 HOMO energies for structures **IVA** and **IVB** have both been included in order to provide the rationale for exclusion of the latter as a contending structure.

As seen in Figure 7.12, there is a rather good relationship between the energy of the neutral HOMO and the corresponding experimental IE† of each cluster; both trends show little to no change in energy upon sequential addition of oxygen atoms onto the Rh_2Ho_2 cluster (all relative to the HOMO energy of **IVA**). This is expected as the IE of a neutral molecule should remain unchanged if the energy of its HOMO is relatively unaffected upon oxidation, keeping consistency with the assumption that electrons are removed from the neutral HOMO of each cluster in the photoionisation process. As such, the lack in variation of the energies of the neutral HOMOs upon oxidation can then be attributed to their characteristics; with the neutral HOMO of each cluster displaying the same amount of non-bonding/anti-bonding character, subsequently resulting in the observed experimental IE trend.

Additionally, it is observed that the HOMO energy for structure **IVA** matches better to the experimental IE† trend than that of structure **IVB**, thus validating the

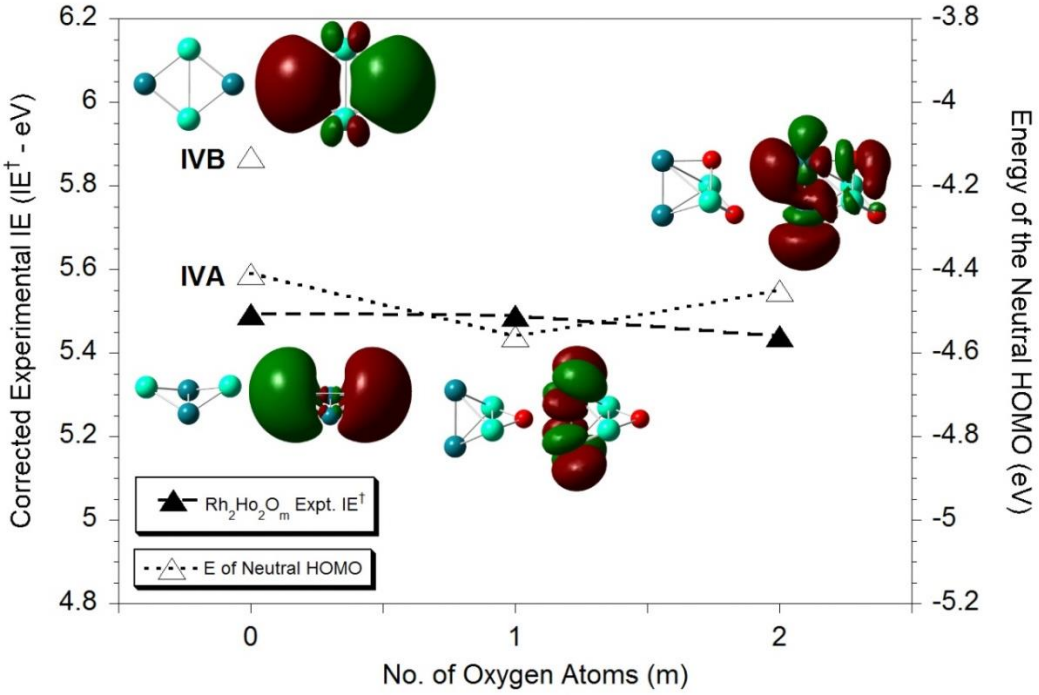

Figure 7.12. *Graph showing the comparison between the experimental IE† values and the HOMO energies of the assigned neutral structures for the $Rh_2Ho_2O_m$ (m = 0-2) clusters. Also displayed are pictures of each HOMO showing how the bonding/anti-bonding character changes with additional oxygen atoms. Note that the Rh_2Ho_2 HOMO energies for* ***IVA*** *and* ***IVB*** *are both included in order to provide the rationale for the exclusion of* ***IVB*** *as a contending structure.*

assignment of **IVA** in Sections 7.4.1 and 7.4.2 (*vide supra*) as the neutral structure of the Rh_2Ho_2 cluster.

In addition to the lack of change in HOMO bonding characteristics upon sequential oxidation, the observed IE trend is also related to the composition of the neutral HOMOs of each cluster in the $Rh_2Ho_2O_m$ series (which can be inferred from the HOMO pictures in Figure 7.12). Ionisation from the HOMOs of the $Rh_2Ho_2O_m$ clusters removes a metal-based (largely on Ho) *s* electron for Rh_2Ho_2, a metal-based (solely on Rh) *d* electron for Rh_2Ho_2O, and a metal-based (largely on Rh) *d* electron for $Rh_2Ho_2O_2$. These assigned characters of each electron removed upon ionisation is justified by the changes in atomic Hirshfeld charges observed upon transition from the assigned neutral state to the assigned cationic state of each cluster (*vide supra* Sections

7.1.2, 7.2.2 and 7.3.2 for changes in atomic Hirshfeld charges for Rh_2Ho_2, Rh_2Ho_2O and $Rh_2Ho_2O_2$, respectively). Overall, these electronic characters coupled with the lack of change in neutral HOMO energy (due to changes in bonding/non-bonding/anti-bonding characteristics upon sequential oxidation) collectively lead to the experimental IE trend observed.

Finally, the good comparison between the experimental and theoretical data in Figures 7.11 and 7.12 (in addition to Figures 7.7(b) and 7.9(b)) indicates that incorporating the *f*-electrons of the Ho atom into the ECP as part of the computational method is just as valid for the $Rh_2Ho_2O_m$ (m = 0-2) clusters as it is for the $RhHo_2O_n$ (n = 0-2) clusters. This infers that *f*-electrons seem to play no significant part in the valence active space of the neutral and cationic $Rh_2Ho_2O_m$ (m = 0-2) clusters.

7.7. Conclusion

In summary, this chapter has presented theoretical insight gained from DFT calculations, FCF calculations and ZEKE and PIE spectral simulations performed on the $Rh_2Ho_2O_m$ (m = 0-2) clusters. From these studies, it is concluded that: (i) the most likely neutral and cationic structures of each individual cluster have been inferred from comparison between the experimental and simulated PIE spectra of each cluster, (ii) the experimental IEs of each cluster have been corrected for thermal tailing that results from vibronic hot band transitions at 300 K, and (iii) the calculated IEs of the $Rh_2Ho_2O_m$ (m = 0-2) clusters have been determined and after an applied offset, were found to compare well with the field- and thermally-corrected experimental IEs; with both sets of data showing little to no change upon the sequential addition of oxygen atoms onto the Rh_2Ho_2 cluster. Overall, such good comparison between the experimental and theoretical data has indicated that *f*-electrons play no significant part in the valence active space of the neutral and cationic $Rh_2Ho_2O_m$ (m = 0-2) clusters, as was concluded for the $RhHo_2O_n$ (n = 0-2) clusters (in Chapter 6).

7.8. References

(1) This "arbitrary correction factor" is determined by shifting the simulated PIE spectrum by varying amounts of energy until the initial part of cluster signal onset visually aligns with that of the experimental PIE spectrum.

(2) Németh, G. I.; Ungar, H.; Yeretzian, C.; Selzle, H. L.; Schlag, E. W. *Chem. Phys. Lett.* **1994**, *228*, 1.

(3) Dryza, V.; Addicoat, M. A.; Gascooke, J. R.; Buntine, M. A.; Metha, G. F. *J. Phys. Chem. A* **2008**, *112*, 5582.

(4) Dryza, V.; Metha, G. F. *J. Chem. Phys.* **2009**, *130*, 1.

(5) Dryza, V.; Gascooke, J. R.; Buntine, M. A.; Metha, G. F. *Physical Chemistry Chemical Physics : PCCP* **2009**, *11*, 1060.

(6) Dryza, V.; Alvino, J. F.; Metha, G. F. *J. Phys. Chem. A* **2010**, *114*, 4080.

Chapter Eight

PIE Spectroscopy of Gas-Phase Gold-Praseodymium Clusters and Their Oxide Counterparts.

This chapter presents the experimentally determined adiabatic IEs of the gas-phase $AuPr_2O_x$ (x = 0-2), $Au_2Pr_2O_m$ (m = 0-1) and $Au_3Pr_2O_n$ (n = 0-2) clusters attained using PIE spectroscopy. Additionally, the experimentally determined adiabatic IEs of the gas-phase Au_2Pr and $Au_3Pr_2O_3H_2$ clusters are also presented. The generation of a variety of Pr and Au-Pr bare and oxide clusters produced in the laser ablation process is initially discussed, followed by presentation and discussion of the PIE spectra for each relevant cluster. For those clusters that have a different number of oxygen atoms (i.e. the same number of metal atoms), the observed IE trend as a function of sequential addition of oxygen atoms is discussed. Additionally, the IE trends as a function of: (i) substitution of gold atoms for praseodymium atoms for the Au_kPr_{3-k} (k = 0-3) clusters, and (ii) the sequential addition of gold atoms onto Pr_2 for the Au_yPr_2 (y = 0-3) clusters, are also discussed.

8.1. Mass Spectra and Photo-Ionisation Measurements

Figure 8.1 shows a TOF mass spectrum of praseodymium oxide (Pr-O) and gold-praseodymium bare (Au-Pr) and oxide clusters recorded at 218 nm (5.69 eV) measured under single-photon ionisation conditions (see Appendix A for linear √Mass vs. TOF conversion graph). It is observed that Pr-O clusters of the form Pr_2O, Pr_2O_2 and Pr_3O_a (a = 1-4) are generated in very low abundance. The Pr_2 dimer and Pr_3 trimer did not appear in the mass spectrum. The absence of these bare praseodymium clusters is surprising as threshold photoionisation experiments performed by Koretsky and Knickelbein have determined the experimental IEs of Pr_2 and Pr_3 to be 4.52 eV and 4.41 eV, respectively,[1] both of which are lower than the photon energy of 5.69 eV (218 nm). The lack of production of pure praseodymium clusters is potentially due to high binding affinity of praseodymium to gold and the high oxophilicity of praseodymium, which are both justified by the relatively large dissociation energies of the AuPr and PrO dimers (D^o = 3.223 ± 0.259 eV and 7.67 eV, respectively).[2] This particularly high binding affinity for gold, in addition to the high oxophilicity of praseodymium, could potentially preclude the formation of pure praseodymium clusters in an environment where there is a significant presence of gold atoms (due to ablation of gold rod) and oxygen atoms (from both the oxide layers on the gold and praseodymium metal rods in addition to any background oxygen present in the experiment), thus causing the lack of appearance of molecular praseodymium clusters under the experimental conditions used to collect the mass spectrum.

As also observed in Figure 8.1, the bimetallic clusters $AuPr_2O_x$ (x = 0-2), $AuPr_3O_y$ (y = 1-3), $AuPr_4O_b$ (b = 2-3), $Au_2Pr_3O_z$ (z = 1-3) and $Au_3Pr_2O_n$ (n = 0-2) are generated with intensities varying from weak to strong. The AuPr dimer is the most intense peak in the mass spectrum. In addition, the bimetallic clusters Au_2Pr, $AuPr_2O_3H_2$ and $Au_3Pr_2O_3H_2$ are also observed in the mass spectrum. The appearance of Au_2Pr is interesting as the experimental IE for Au_2 is 8.82 ± 0.18 eV,[3] and for Au_3 lies between 6.76-7.42 eV (from the experimental IE values determined by Bishea and

Morse (7.06 ± 0.3 eV)[4] and Cheeseman and Eyler (7.27 ± 0.15 eV)[5]).[6] These photon energies are higher than that used here (5.69 eV) and suggests that the substitution of one gold atom with a praseodymium atom in the Au_3 trimer substantially lowers the IE of the cluster. Additionally, the formation of $AuPr_2O_3H_2$ and $Au_3Pr_2O_3H_2$ is also surprising as hydrogen was not deliberately introduced into the experiment. Possible sources are most likely from background H_2O inside the source chamber of the experiment, and/or H_2O impurities present in the He gas-line. The latter was attributed to be the main source of hydrogen that lead to the formation of various H_2O adducts in numerous experiments performed by Bohme and co-workers involving the gas-phase reactivity of small molecules with atomic metal cations.[7-10]

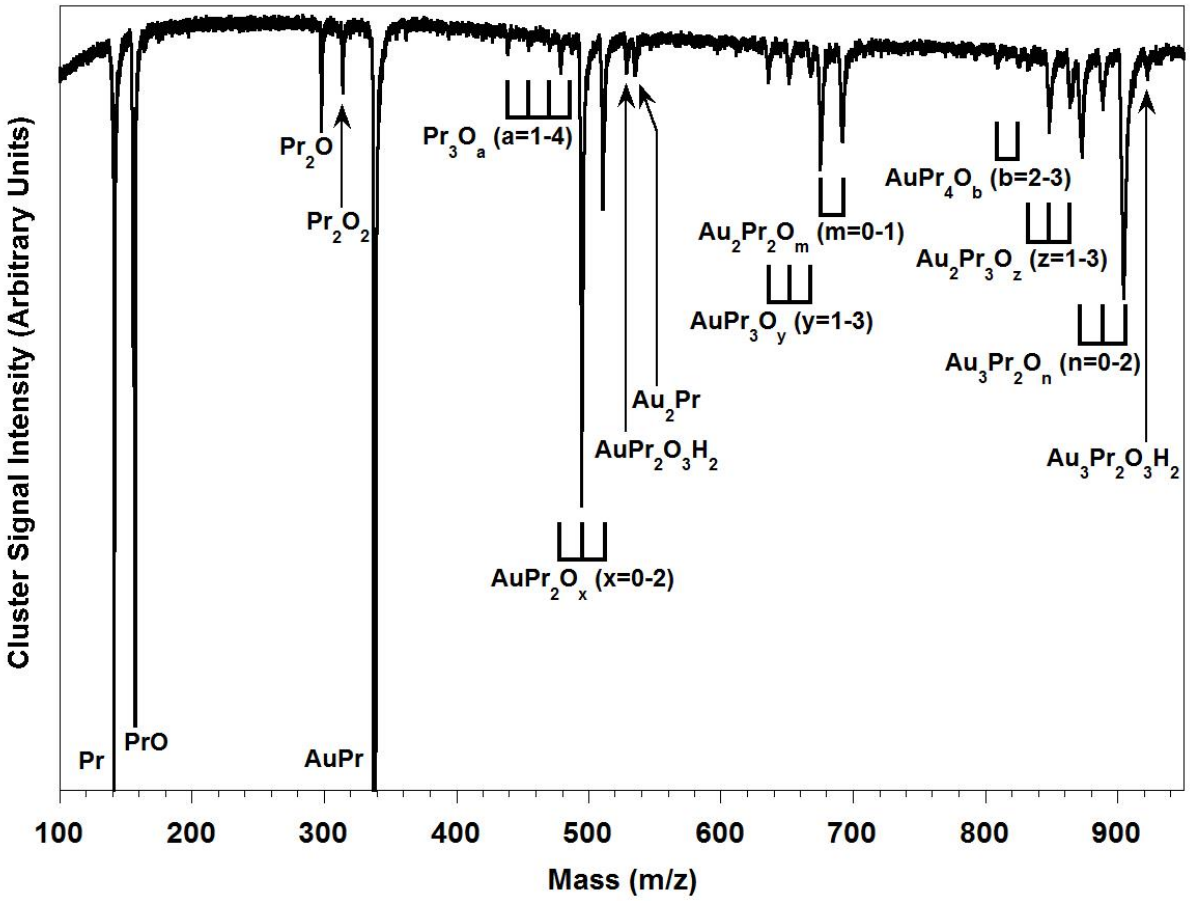

Figure 8.1. *Mass spectrum showing various praseodymium and gold-praseodymium clusters and their oxides recorded at 218 nm under single-photon ionisation conditions.*

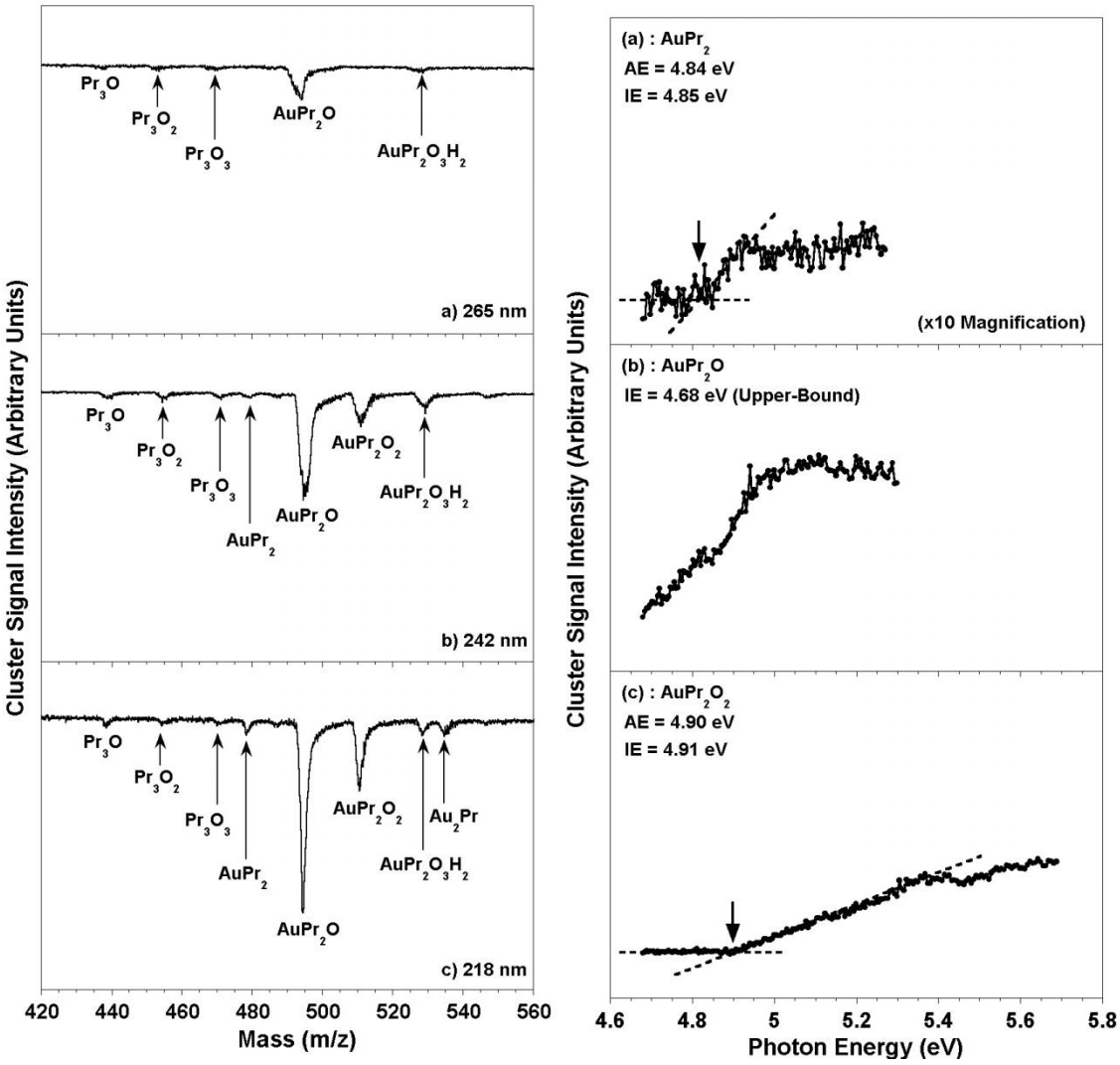

Figure 8.2. (Left) *Mass spectra of the $AuPr_2O_x$ (x=0-2) clusters recorded at three different ionisation wavelengths: (a) 265 nm, (b) 242 nm, and (c) 218 nm.*

Figure 8.3. (Right) *PIE spectra of the $AuPr_2O_x$ (x=0-2) clusters. The determined AEs and IEs are also displayed (estimated uncertainty in IEs = ±0.05 eV), with the black arrows indicating the values of the IEs.*

8.2. Mass and PIE Spectra of the $AuPr_2O_x$ (x = 0-2) Clusters

Figures 8.2(a)-(c) show the portion of the mass spectrum that contains the $AuPr_2O_x$ (x = 0-2) clusters recorded at three different ionising wavelengths; 265 nm, 242 nm and 218 nm. In the mass spectrum recorded at 218 nm (Figure 8.2(c)), it is clearly seen that these three clusters appear with different intensities; $AuPr_2O$ is the most intense, followed by $AuPr_2O_2$ then $AuPr_2$. Ionisation at 242 nm (Figure 8.2(b)) yields $AuPr_2O$ and $AuPr_2O_2$, both with a slight decrease in intensity. $AuPr_2$ also appeared at this wavelength, but with very weak intensity. At 265 nm (Figure 8.2(a)), only the Au_2PrO cluster appears at this wavelength, with signals due to $AuPr_2$ and $AuPr_2O_2$ having decreased to baseline, indicating that neither of these species are ionised at this wavelength.

The resultant PIE spectra for the $AuPr_2O_x$ (x = 0-2) clusters are displayed in Figures 8.3(a)-(c). The PIE spectrum for $AuPr_2$ has been magnified x10 relative to the other two clusters. As observed in Figures 8.3(a) and (b), the PIE spectra for $AuPr_2$ and $AuPr_2O$ both display gradual onsets of signal intensity upon ionisation. This indicates moderate FC overlap between the neutral and cationic structures of these two clusters and consequently, a significant amount of geometric change upon ionisation is expected. The PIE spectrum of $AuPr_2O$ is not considered to have reached baseline, indicating that the true experimental adiabatic IE of this cluster lies below the lowest photon energy used in the Au-Pr PIE experiments, which is consequently ascribed as the upper-bound IE for this cluster (< 4.68 eV). Relative to the PIE spectra of the $AuPr_2$ and $AuPr_2O$ clusters, the spectrum for $AuPr_2O_2$ (Figure 8.3(c)) shows a slower onset in signal intensity from baseline. This signifies less intense FC overlap between the neutral and cationic structures of this cluster and is indicative of major geometric change upon ionisation. Lastly, all PIE spectra are observed to level off at different photon energies, indicating that the highest energy FC-allowed transitions are attained for all three clusters.

In addition to the PIE Curves for the $AuPr_2O_x$ (x = 0-2) clusters, Figures 8.3(a)-(c) also show the experimentally determined appearance energies (AEs) and adiabatic IEs for the $AuPr_2O_x$ (x = 0-2) clusters (the latter indicated by the arrows in each figure). The experimental IE for $AuPr_2$ is determined to be 4.85 eV, which lies in between the experimental IEs of Pr_3 and Au_3 (4.41 ± 0.05 eV for Pr_3[1]; 7.06 ± 0.3 eV and 7.27 ± 0.15 eV for Au_3[4,5]). The addition of an oxygen atom to the $AuPr_2$ bare metal cluster to yield $AuPr_2O$ results in the IE changing by -0.17 eV relative to the upper-bound IE assigned to this cluster (4.68 eV). The addition of a second oxygen atom to form $AuPr_2O_2$ results in an IE increase of +0.23 eV relative to the upper-bound IE value of $AuPr_2O$. In comparing the IEs of $AuPr_2$ and $AuPr_2O_2$, it is observed that the addition of two oxygen atoms changes the IE by only +0.06 eV, which lies just outside the estimated experimental IE error (±0.05 eV).

8.3. Mass and PIE Spectra of the $Au_2Pr_2O_m$ (m = 0-1) Clusters

Figures 8.4(a)-(c) show the portion of the mass spectrum containing the $Au_2Pr_2O_m$ (m = 0-1) clusters recorded at three different ionising wavelengths; 265 nm, 242 nm and 218 nm. In the mass spectrum recorded at 218 nm (Figure 8.4(c)), it is clearly seen that both clusters appear with moderate signal intensities with the peak due to Au_2Pr_2 observed to be more intense than Au_2Pr_2O. Ionisation at 242 nm (Figure 8.4(b)) yields both Au_2Pr_2 and Au_2Pr_2O with reduced signal intensities, although the former is less intense. At 265 nm (Figure 8.4(a)), both signals due to Au_2Pr_2 and Au_2Pr_2O are observed to decrease to baseline, indicating that neither of these species are being ionised at this wavelength.

The PIE spectra for the $Au_2Pr_2O_m$ (m = 0-1) clusters are displayed in Figures 8.5(a) and (b). The PIE spectrum for Au_2Pr_2 displays a very slow onset of signal intensity upon ionisation, indicating weak FC overlap between the neutral and cationic structures of this cluster and consequently, a significant amount of geometric change upon ionisation. In contrast, the PIE spectrum for Au_2Pr_2O (Figure 8.5(b)) displays a rapid onset of signal intensity upon ionisation, indicating strong FC overlap between the neutral and cationic structures of this cluster and thus a minimal amount of geometric change upon ionisation. The PIE spectrum of Au_2Pr_2O is observed to level off at *ca.* 4.95 eV, indicating that the highest energy FC-allowed transitions was attained for this cluster.

In addition to the PIE Curves for the $Au_2Pr_2O_m$ (m = 0-1) clusters, Figures 8.5(a) and (b) also show the experimentally determined AEs and adiabatic IEs for the $Au_2Pr_2O_m$ (m = 0-1) clusters (the latter indicated by the arrows in each figure). The experimental IE for Au_2Pr_2 is determined to be 4.81 eV, which lies in between the experimental IEs of Pr_4 and Au_4 (4.47 ± 0.05 eV and 7.82 ± 0.18 eV, respectively[1,3]); slightly higher than the IE value for Pr_4. The addition of an oxygen atom to Au_2Pr_2 results in the IE changing by -0.03, which lies within the estimated experimental IE error (± 0.05 eV).

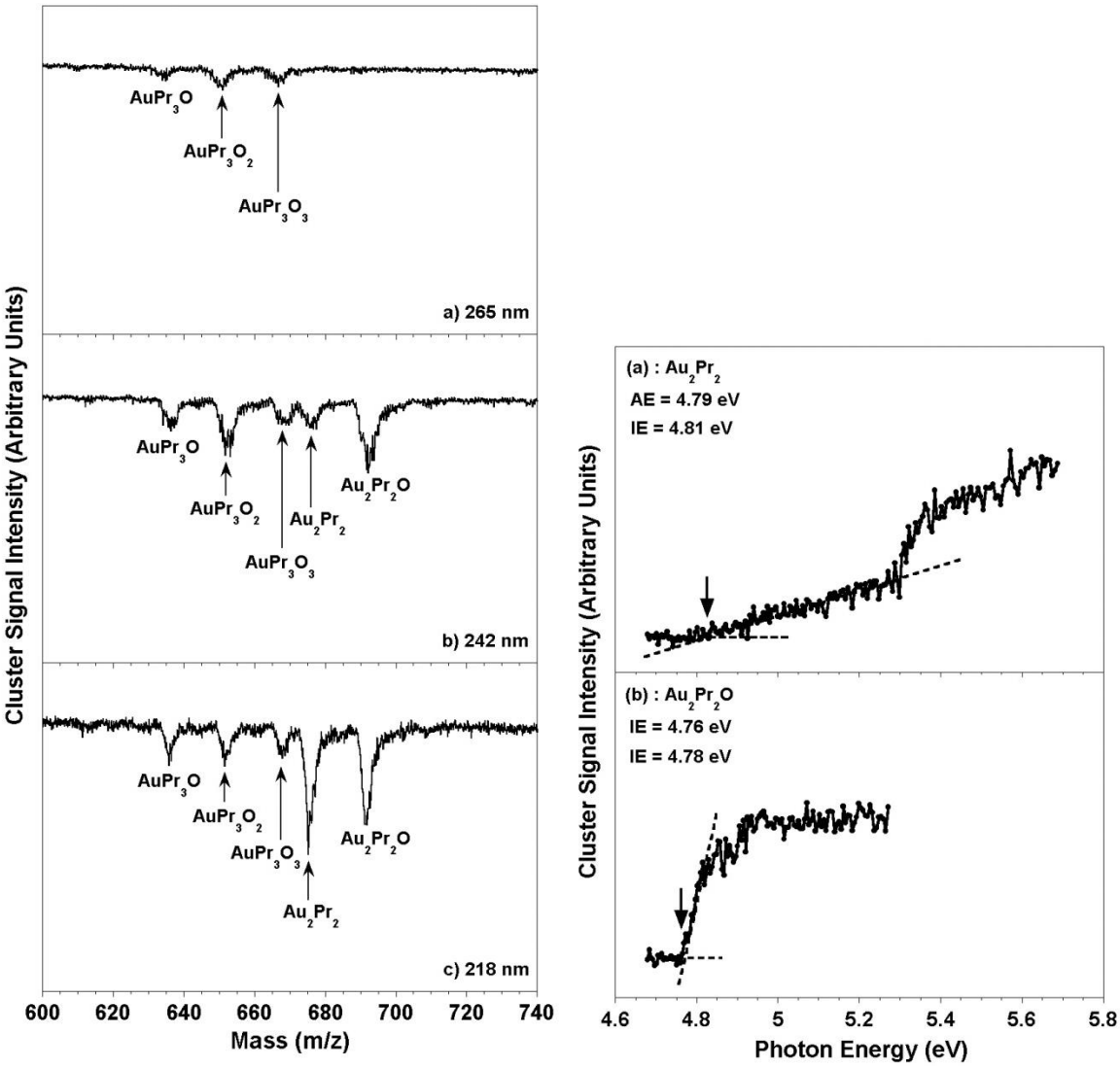

Figure 8.4. (Left) *Mass spectra of the $Au_2Pr_2O_m$ (m=0-1) clusters recorded at three different ionisation wavelengths: (a) 265 nm, (b) 242 nm, and (c) 218 nm.*
Figure 8.5. (Right) *PIE spectra of the $Au_2Pr_2O_m$ (m=0-1) clusters. The determined AEs and IEs are also displayed (estimated uncertainty in IEs = ±0.05 eV), with the black arrows indicating the values of the IEs.*

8.4. Mass and PIE Spectra of the $Au_3Pr_2O_n$ (n = 0-2) Clusters

Figures 8.6(a)-(c) show the portion of the mass spectrum containing the $Au_3Pr_2O_n$ (n = 0-2) clusters recorded at three different ionising wavelengths; 265 nm, 242 nm and 218 nm. In the mass spectrum recorded at 218 nm (Figure 8.6(c)), it is clearly seen that the three clusters appear with moderate to strong intensities; The $Au_3Pr_2O_2$ cluster is the most intense, followed by Au_3Pr_2 then Au_3Pr_2O. Ionisation at 242 nm (Figure 8.6(b)) yields only Au_3Pr_2 and Au_3Pr_2O, both with a large reduction in signal intensity. At 265 nm (Figure 8.6(a)), all signals due to the $Au_3Pr_2O_n$ (n = 0-2) clusters have decreased to baseline, indicating that all three clusters are not being ionised at this wavelength.

The PIE spectra for the $Au_3Pr_2O_n$ (n = 0-2) clusters are displayed in Figures 8.7(a)-(c), respectively. As observed in Figures 8.7(a) and (c), the PIE spectra for Au_3Pr_2 and $Au_3Pr_2O_2$ both display gradual onsets of signal intensity upon ionisation. This indicates moderate FC overlap between the neutral and cationic structures of these two clusters and consequently, a significant amount of experienced geometric change upon ionisation. Relative to the PIE spectra of the Au_3Pr_2 and $Au_3Pr_2O_2$ clusters, the PIE spectrum for Au_3Pr_2O (Figure 8.7(b)) shows a much slower onset in signal intensity from baseline. This signifies poor FC overlap between the neutral and cationic structures of this cluster and is indicative of major geometric change upon ionisation. Additionally, the PIE spectrum for Au_3Pr_2O is observed to level off at approximately 5.4 eV, indicating that the highest energy FC-allowed transitions are attained for this cluster.

In addition to the PIE spectra for the $Au_3Pr_2O_n$ (n = 0-2) clusters, Figures 8.7(a)-(c) also show the experimentally determined AEs and adiabatic IEs for the $Au_3Pr_2O_n$ (n = 0-2) clusters (the latter indicated by arrows in each figure). The experimental IE for Au_3Pr_2 is determined to be 5.28 eV, which is higher than the experimental IE of Pr_5 (4.45 ± 0.05 eV)[1]. The addition of an oxygen atom to the Au_3Pr_2 bare metal cluster to yield Au_3Pr_2O results in the IE changing by -0.26 eV.

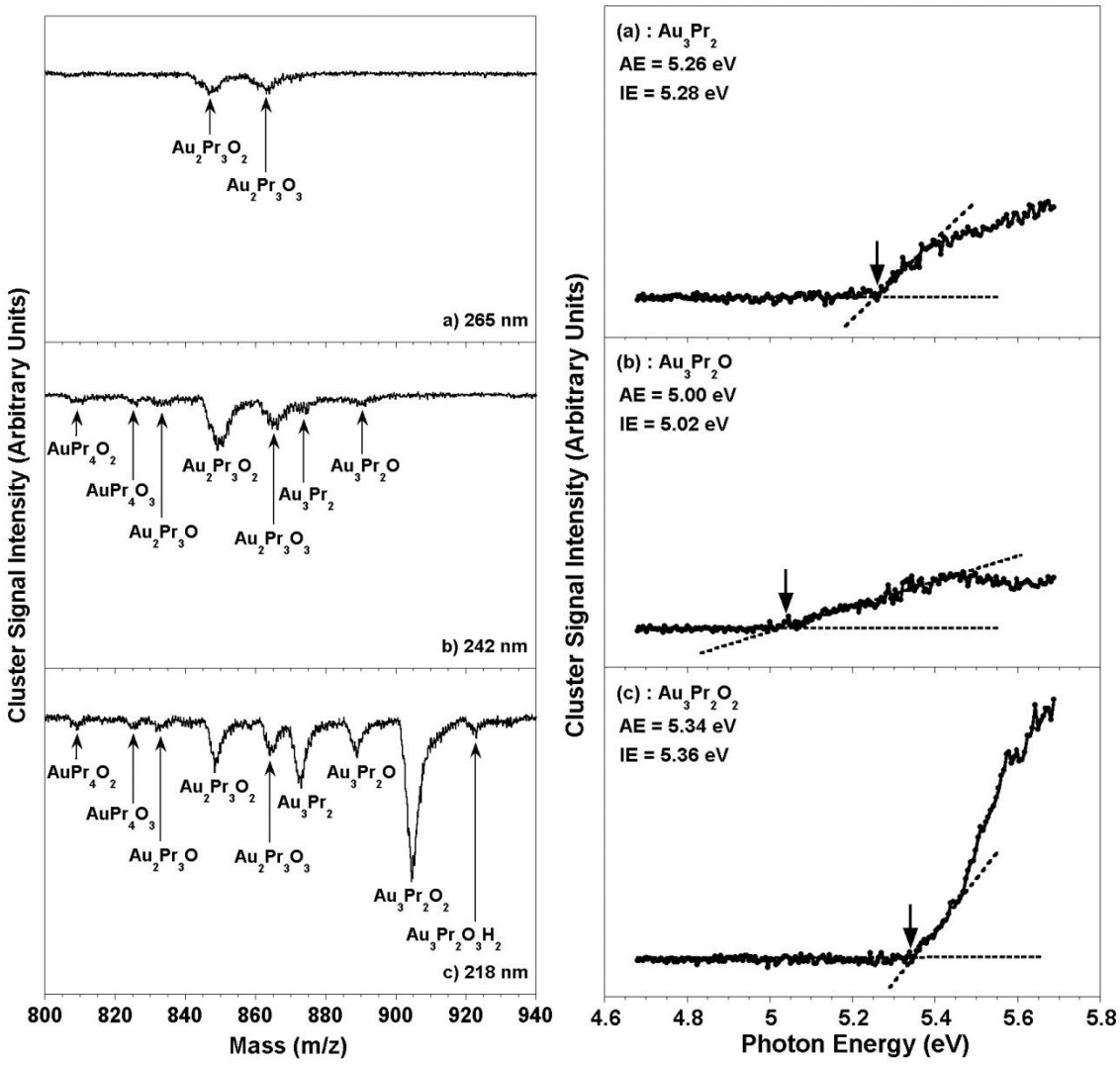

Figure 8.6. (Left) *Mass spectra of the $Au_3Pr_2O_n$ (n=0-2) clusters recorded at three different ionisation wavelengths: (a) 265 nm, (b) 242 nm, and (c) 218 nm.*

Figure 8.7. (Right) *PIE spectra of the $Au_3Pr_2O_n$ (n=0-2) clusters. The determined AEs and IEs are also displayed (estimated uncertainty in IEs = ±0.05 eV), with the black arrows indicating the values of the IEs.*

The addition of a second oxygen atom to form $Au_3Pr_2O_2$ results in an IE change of +0.34 eV relative to the IE of Au_3Pr_2O. In comparing the IEs of Au_3Pr_2 and $Au_3Pr_2O_2$, it is observed that the addition of two oxygen atoms changes the IE by only +0.08 eV, which lies just outside the estimated experimental IE error (±0.05 eV).

8.5. Mass and PIE Spectra of the Au_2Pr and $Au_3Pr_2O_3H_2$ Clusters

In addition to presenting the $AuPr_2O_x$ (x = 0-2) and $Au_3Pr_2O_n$ (n = 0-2) clusters, Figures 8.2(a)-(c) and 8.6(a)-(c) also show the portions of the mass spectrum that contain the Au_2Pr and $Au_3Pr_2O_3H_2$ clusters, respectively. In the mass spectra recorded at 218 nm in both Figures (Figure 8.2(c) and 8.6(c)), it is clearly seen that both clusters appear with weak intensities. At 242 nm and 265 nm (Figures 8.2(a)-(b) and Figure 8.6(a)-(b)), both signals have decreased to baseline, indicating that these clusters are not being ionised at photon wavelengths at and above 242 nm. The PIE spectra for the Au_2Pr and $Au_3Pr_2O_2H_2$ are displayed in Figures 8.8(a) and (b), respectively. As observed in both figures, the PIE spectrum for Au_2Pr displays a slightly more gradual onset than that of $Au_3Pr_2O_2H_2$. This indicates more extensive FC overlap between the neutral and cationic structures of Au_2Pr than of $Au_3Pr_2O_2H_2$ and consequently, a more significant amount of experienced geometric change upon ionisation for the former cluster.

In addition to the PIE spectra for the Au_2Pr and $Au_3Pr_2O_3H_2$, Figures 8.8(a) and (b) also show the experimentally determined adiabatic IEs for these clusters. The experimental IEs for Au_2Pr and $Au_3Pr_2O_3H_2$ are determined to be 5.52 eV and 5.65 eV, respectively. In regards to the former, the IE for Au_2Pr lies close to the mid-point between the experimental IEs of Pr_3 and Au_3 (4.41 ± 0.05 eV for Pr_3[1]; 7.06 ± 0.3 eV and 7.27 ± 0.05 eV for Au_3[4,5]). Regarding the latter, the presence of two hydrogen atoms in $Au_3Pr_2O_3H_2$ is found to shift the IE higher than those of all the $Au_3Pr_2O_n$ (n = 0-2) clusters. It is likely that this particular cluster possesses structural features involving bound OH groups rather than intact H_2O groups or associatively-bound H_2. This is supported by numerous investigations involving the formation, structures and/or reactivity of cerium hydroxide, gold hydroxide, vanadium-silver bimetallic oxide and tungsten oxide clusters; all of which have been found to involve the formation and/or presence of OH groups rather than intact H_2O or associatively-bound H_2 groups as more favourable structural aspects of these clusters.[11-14]

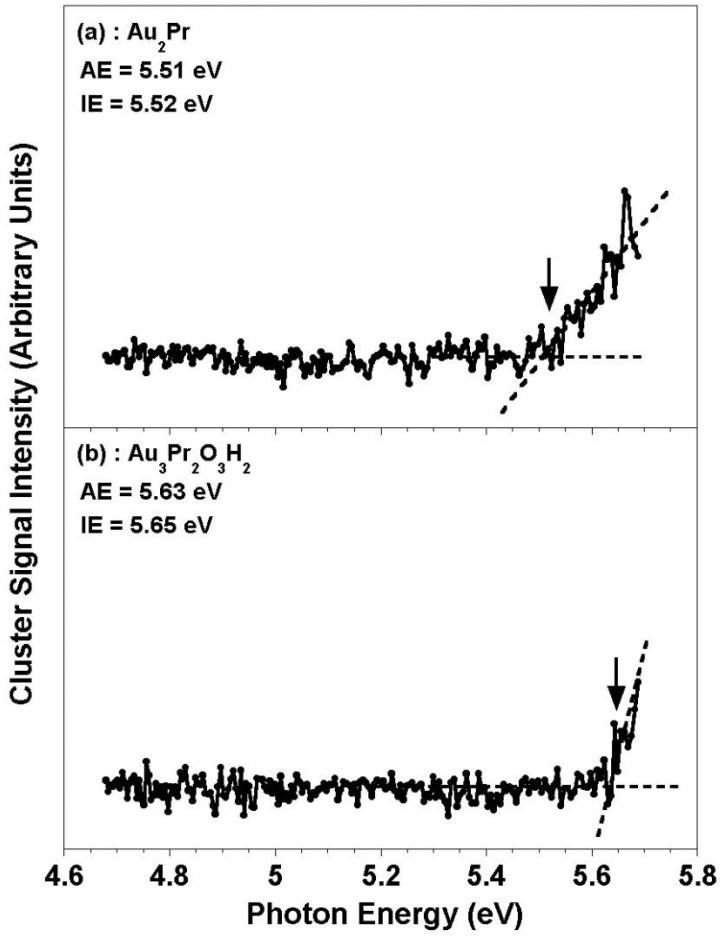

Figure 8.8. *PIE spectra of the (a) Au_2Pr, and (b) $Au_3Pr_2O_3H_2$ clusters. The determined AEs and IEs are also displayed (estimated uncertainty in IEs = ±0.05 eV), with the black arrows indicating the values of IEs.*

8.6. Experimental Adiabatic IEs for the $Au_{3-k}Pr_k$ (k = 0-3) Clusters: Substitution Effects

Figure 8.9 displays the experimentally determined adiabatic IEs for the Au_kPr_{3-k} (k = 3-0) clusters. The experimental adiabatic IEs of Au_3 shown in the figure were determined previously by Bishea and Morse (7.06 ± 0.30 eV) and Cheeseman and Eyler (7.27 ± 0.15 eV).[4,5] The experimental adiabatic IE of Pr_3 shown in the figure was determined previously by Koretsky and Knickelbein (4.41 ± 0.05 eV).[1] As observed, substitution of a gold atom for a praseodymium atom in Au_3 to yield Au_2Pr results in the IE changing by -1.54 eV and -1.75eV relative to the IE values of Au_3 determined by Bishea and Morse and Cheeseman and Eyler, respectively. Further substitution of a second gold atom to yield $AuPr_2$ results in a further reduction in IE by 0.67 eV relative to the IE value of Au_2Pr. Finally, substitution of the last gold atom to give Pr_3 results in a change of -0.44 eV relative the IE of $AuPr_2$. Clearly the initial substitution of a gold atom with a praseodymium atom in Au_3 results in a more significant decrease in IE than further subsequent substitution. Assuming that ionisation occurs mostly or solely from the HOMO of each cluster, this indicates that the substitution of the first gold atom causes a significant increase in the energy of HOMO; perhaps from significant involvement of the substituted praseodymium atom to this orbital, allowing for the easier removal of the electron from the Au_2Pr cluster. From here on, further substitution still increases the energy of the HOMO but to a more limited extent. Additionally, it is also possible that changes in the absolute energy of the cationic species of each cluster upon substitution of gold atoms may also have an effect on the IE trend observed. However, this will most likely have a more limited effect than the change in neutral HOMO energy upon gold atom substitution and thus, the energy of the HOMO is considered to be the dominant factor that affects the IE.

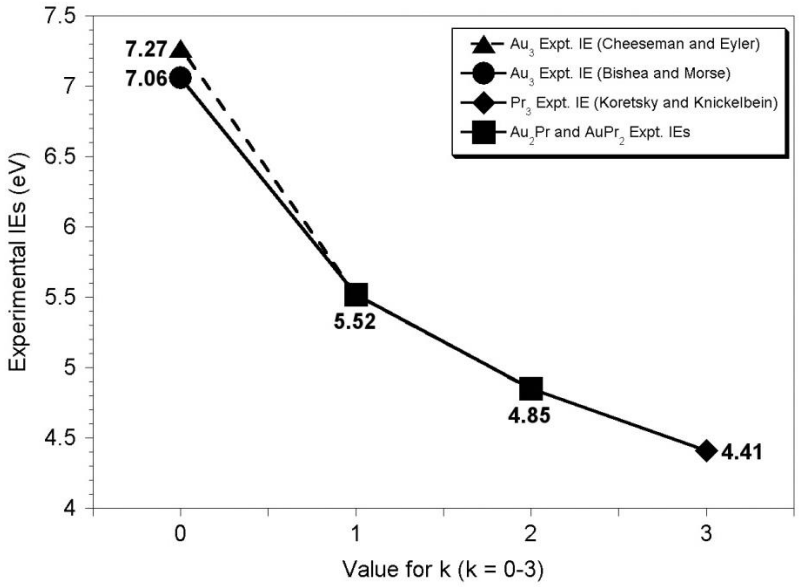

Figure 8.9. *Graph showing the change in IE as a function of substituting a gold atom for a praseodymium atom for the* $Au_{3-k}Pr_k$ *(k = 0-3) clusters. The experimentally determined adiabatic IE values for* Au_2Pr *and* $AuPr_2$ *are taken from Figures 8.8(a) and 8.3(b), respectively. The IE values for* Au_3 *and* Pr_3 *were experimentally determined in previous work by others.*[1,4,5]

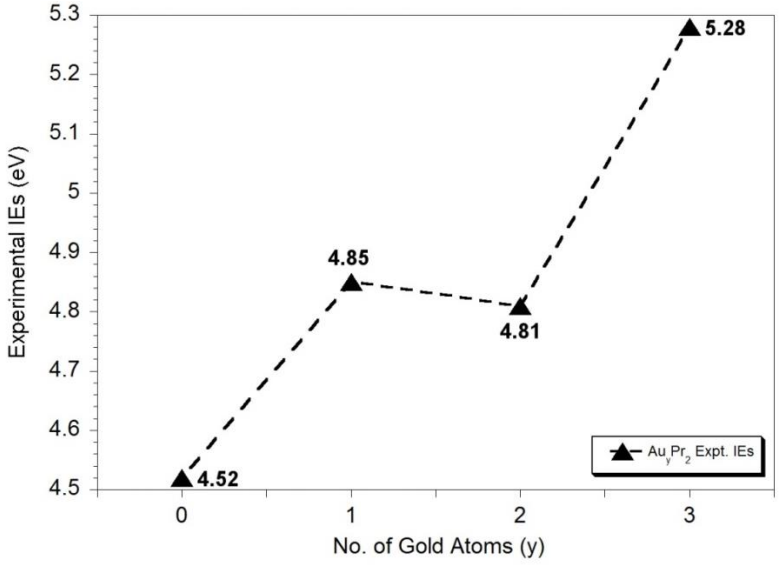

Figure 8.10. *Graph showing the change in IE as a function of sequential addition of gold atoms for the* Au_yPr_2 *(y = 0-3) clusters. The experimentally determined adiabatic IE values for* $AuPr_2$*,* Au_2Pr_2 *and* Au_3Pr_2 *are taken from Figures 8.3(a), 8.5(a) and 8.7(a), respectively. The IE value for* Pr_2 *was experimentally determined in previous work by Koretsky and Knickelbein.*[1]

8.7. Experimental Adiabatic IEs for the Au_yPr_2 (y = 0-3) Clusters: Effect of Gold Atoms

Figure 8.10 displays the experimentally determined adiabatic IEs for the Au_yPr_2 (y = 0-3) clusters. The experimental adiabatic IE of Pr_2 shown was determined previously by Korestky and Knickelbein (4.52 ± 0.05 eV) and is included for comparison.[1] As observed, addition of a gold atom onto Pr_2 to yield $AuPr_2$ results in an IE change of +0.33 eV. The addition of a second gold atom to give Au_2Pr_2 results in an IE change of -0.04 eV relative to the IE value of $AuPr_2$, which is within the estimated error of IE determination (± 0.05 eV). Lastly, the addition of a third gold atom to give Au_3Pr_2 results in an IE change of +0.47 eV relative to the IE value of Au_2Pr_2. In general, it appears that the sequential addition of gold atoms onto Pr_2 increases the IE; with the exception of the addition of a gold atom onto $AuPr_2$ to yield Au_2Pr_2, which results in no appreciable change. If it is assumed (as with the Au_kPr_{3-k} clusters) that ionisation occurs mostly or solely from the HOMO, then in general the sequential addition of gold atoms onto Pr_2 continually decreases the energy of HOMO and increases the IE of each cluster; perhaps due to significant involvement of each gold atom to this orbital, resulting in greater difficulty removing the electron. However, the addition of a gold atom onto $AuPr_2$ to give Au_2Pr_2 appears to have no effect on the energy of the HOMO, thus resulting in no appreciable change in IE.

8.8. Comparison between the $AuPr_2O_x$ (x = 0-2), $Au_2Pr_2O_m$ (m = 0-1) and $Au_3Pr_2O_n$ (n = 0-2) Clusters: Effect of Oxygen Atoms

Figure 8.11 displays the experimental adiabatic IEs determined for the $AuPr_2O_x$ (x = 0-2), $Au_2Pr_2O_m$ (m = 0-1) and $Au_3Pr_2O_n$ (n = 0-2) clusters. As observed, it appears that the addition of an oxygen atom onto $AuPr_2$ and Au_3Pr_2 results in a significant decrease in IE of each cluster. The addition of a second sequential oxygen atom to these clusters results in the IE increasing back to a value similar to that of the bare clusters. This is the same trend observed for the $RhHo_2O_n$ (n = 0-2) clusters in Chapter Five. These IE changes are contrary to the IE change observed for Au_2Pr_2, where the addition of an oxygen atom has little-to-no effect on the IE of this cluster; which is similarly observed for the $Rh_2Ho_2O_m$ (m = 0-2) clusters in Chapter Five. Hence, this experimental data implies that the addition of a gold atom onto $AuPr_2$ inhibits the significant change in electronic structure (i.e. the energy of the HOMO) that is accompanied by oxidation, whereas the addition of one and three gold atoms into Pr_2 does not.

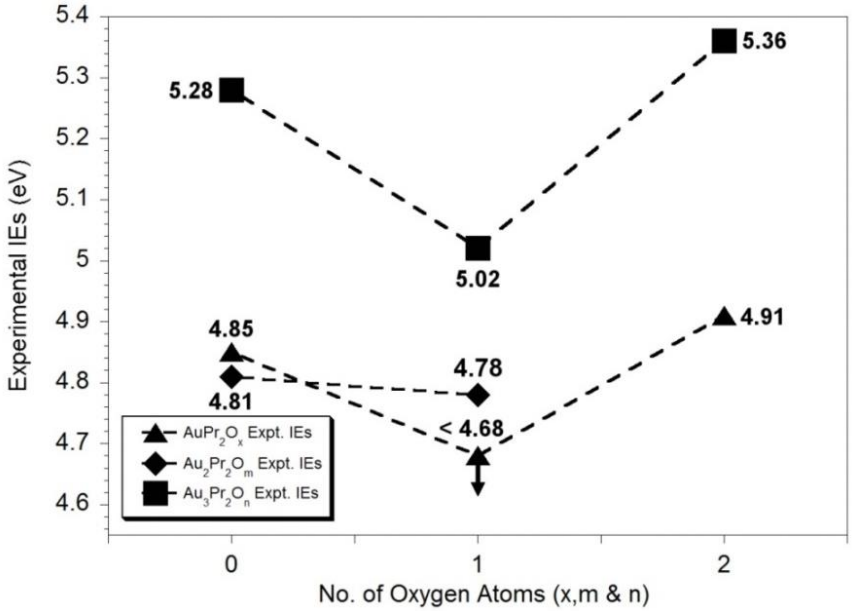

Figure 8.11. *Graph showing the change in IE as a function of substituting a gold atom for a praseodymium atom for the* $AuPr_2O_x$ (x = 0-2), $Au_2Pr_2O_m$ (m = 0-1) and $Au_3Pr_2O_n$ (n = 0-2) *clusters. The experimentally determined adiabatic IE values for* Au_2Pr *and* $AuPr_2$ *are taken from Figures 8.8(a) and 8.3(b), respectively. The IE values for* Au_3 *and* Pr_3 *were experimentally determined in previous work by others.*[1,4,5]

8.9. Conclusion

The gas-phase $AuPr_2O_x$ (x = 0-2), $Au_2Pr_2O_m$ (m = 0-1) and $Au_3Pr_2O_n$ (n = 0-2), Au_2Pr and $Au_3Pr_2O_3H_2$ clusters have been generated and detected experimentally using a dual laser ablation source coupled with a TOF-MS, and their experimental adiabatic IEs determined using PIE spectroscopy.

Firstly, the IE trend as a function of substitution of gold atoms for praseodymium atoms was discussed for the Au_kPr_{3-k} (k = 0-3) cluster series. In this trend, the initial substitution of a gold atom with a praseodymium atom in Au_3 is found to result in a more significant decrease in IE than further subsequent substitution. From here on, each sequential substitution was found to decrease the IE further but to a more limited extent. This indicated that the substitution of the first gold atom causes a significant increase in the energy of HOMO, whilst further substitution still increases the energy of the HOMO but to a more limited extent.

Secondly, the IE trend as sequential addition of gold atoms onto Pr_2 for the Au_yPr_2 (y = 0-3) clusters was also discussed. In this trend, it is generally observed that the sequential addition of gold atoms onto Pr_2 continually increases the IE of each cluster. However, contrary to this trend, the addition of a gold atom onto $AuPr_2$ to give Au_2Pr_2 appeared to have no effect on the IE. This indicated that sequential addition of gold atoms onto Pr_2 generally decreases the energy of HOMO and thus increases the IE of each cluster. However, the addition of a gold atom onto $AuPr_2$ to give Au_2Pr_2 appears to have no effect on the energy of the HOMO, thus resulting in no appreciable change in IE.

Lastly, the IE trend as function of sequential oxidation for the $AuPr_2O_x$ (x = 0-2), $Au_2Pr_2O_m$ (m = 0-1) and $Au_3Pr_2O_n$ (n = 0-2) cluster series was also discussed. Concerning the $AuPr_2O_x$ (x = 0-2) and $Au_3Pr_2O_n$ (n = 0-2) cluster series, the experimental IE of the monoxide species was found to be significantly red-shifted in comparison to the experimental IEs of the bare and dioxide species. This implies that there must be significant changes in the electronic properties (i.e. the energy of the

HOMO) of the $AuPr_2$ and Au_3Pr_2 clusters upon the sequential addition of oxygen atoms. Contrary to these IE trends, the experimental adiabatic IEs for the $Au_2Pr_2O_m$ (m = 0-1) clusters were found to remain effectively constant upon the sequential addition of an oxygen atom. This suggested that the addition of a gold atom onto the $AuPr_2$ cluster inhibits the significant change in electronic structure experienced by this cluster when it undergoes oxidation.

8.10. References

(1) Koretsky, G. M.; Knickelbein, M. B. *Eur. Phys. J. D* **1998**, *2*, 273.

(2) *CRC Handbook of Chemistry and Physics*; Lide, David R., Ed.; CRC Press, Taylor & Francis Group: Boca Raton, FL, 2008.

(3) Takahashi, L. K.; Zhou, J.; Wilson, K. R.; Leone, S. R.; Ahmed, M. *J. Phys. Chem. A* **2009**, *113*, 4035.

(4) Bishea, G. A.; Morse, M. D. *J. Chem. Phys.* **1991**, *95*, 8779.

(5) Cheeseman, M. A.; Eyler, J. R. *J. Phys. Chem.* **1992**, *96*, 1082.

(6) Both IEs for Au_3 determined by Bishea *et al.* and Cheeseman *et al.* have been included for comparison as the uncertainties in each of the IE values are relatively large.

(7) Koyanagi, G. K.; Bohme, D. K. *J. Phys. Chem. A* **2001**, *105*, 8964.

(8) Cheng, P.; Koyanagi, G. K.; Bohme, D. K. *J. Phys. Chem. A* **2006**, *110*, 12832.

(9) Shayesteh, A.; Lavrov, V. V.; Koyanagi, G. K.; Bohme, D. K. *J. Phys. Chem. A* **2009**, *113*, 5602.

(10) Jarvis, M. J. Y.; Blagojevic, V.; Koyanagi, G. K.; Bohme, D. K. *Phys. Chem. Chem. Phys.* **2010**, *12*, 4852.

(11) Aubriet, F.; Gaumet, J. J.; de Jong, W. A.; Groenewold, G. S.; Gianotto, A. K.; McIlwain, M. E.; Van Stipdonk, M. J.; Leavitt, C. M. *J. Phys. Chem. A* **2009**, *113*, 6239.

(12) Wallace, W. T.; Wyrwas, R. B.; Whetten, R. L.; Mitric, R.; Bonacic-Koutecky, V. *J. Am. Chem. Soc.* **2003**, *125*, 8408.

(13) Li, X. N.; Wu, X. N.; Ding, X. L.; Xu, B.; He, S. G. *Chem - Eur. J.* **2012**, *18*, 10998.

(14) Mann, J. E.; Mayhall, N. J.; Jarrold, C. C. *Chem. Phys. Lett.* **2012**, *525-26*, 1.

Chapter Nine

DFT Investigations, FCF Calculations and Spectral Simulations of the Gas-Phase $Au_{3-k}Pr_k$ (k = 0-3) Clusters.

This chapter presents the theoretical insight attained from DFT investigations and FCF calculations performed on the $Au_{3-k}Pr_k$ (k = 0-3) clusters. Various neutral and cationic structures calculated to lie within approximately 1 eV of the lowest energy structures of each charge state (including their intrinsic properties such as Hirshfeld charges, calculated vibrational modes etc.) are presented and discussed. Following this, ZEKE and PIE spectral simulations for Au_2Pr and $AuPr_2$ developed from FCF calculations performed for ionisation transitions of interest are presented, discussed and compared to the experimentally obtained PIE spectra shown in Chapter Eight. Overall, all theoretical data obtained from these investigations are used to: (i) assign the vibronic transitions that are most likely to occur upon ionisation for each cluster, (ii) apply slight corrections to the experimental IEs of Au_2Pr and $AuPr_2$ in order to account for thermal tailing that results from vibronic hot band transitions at 300 K, and (iii) determine the calculated IEs of the $Au_{3-k}Pr_k$ (k = 0-3) clusters and compare them to those obtained experimentally.

9.1. DFT Results for the Au_3 Cluster

9.1.1. Lowest Energy Neutral and Cationic Structures

For the neutral Au_3 species, the lowest energy structure is determined to be a C_{2v} obtuse-angled isosceles structure in a $^2B_2$ state with Au-Au' and Au'-Au' bond lengths of 2.603 Å and 4.772 Å, respectively and a Au'-Au-Au' bond angle of 132.9° (Structure **VIIA** – Figure 9.1). In addition to **VIIA**, there are two other low energy isomers calculated that are of particular interest. The lowest energy structure of these two isomers, calculated to lie +0.04 eV higher in energy, is a C_{2v} acute-angled isosceles structure in a $^2B_2$ state with Au-Au' and Au'-Au' bond lengths of 2.640 Å and 2.931 Å, respectively and a Au'-Au-Au' bond angle of 67.4° (Structure **VIIB**). The other isomer is calculated to lie +0.06 eV higher in energy than **VIIA** and is a C_{2v} acute-angled structure in a $^2A_1$ state with Au-Au' and Au'-Au' bond lengths of 2.777 Å and 2.600 Å, respectively and a Au'-Au-Au' bond angle of 55.8° (Structure **VIIC**). However, upon harmonic vibrational frequency analysis on **VIIC**, it is found to possess one imaginary frequency thus indicating that it is a transition state on the neutral potential energy surface of Au_3 rather than a true minimum. Additionally, a linear $D_{\infty h}$ structure in a $^2\Sigma_u$ state was also calculated to lie +0.05 eV higher in energy than **VIIA** but upon harmonic vibrational frequency analysis, was found to possess two imaginary frequencies. This indicates it is a higher-order saddle point on the neutral potential energy surface (i.e. not a minimum or a transition state) and as such, warrants no further discussion. Various other neutral minima were also calculated but only one additional structure was found to lie within 2 eV of **VIIA** (quartet D_{3h} structure – **VIID** – Figure 9.1). All other minima were found to lie much higher in energy (> 2 eV). In addition to the geometric data and Hirshfeld charges presented in Figure 9.1, Table 9.1 displays the calculated vibrational modes and symmetries of structures **VIIA** and **VIIB**. The Cartesian coordinates and electronic parameters of all the calculated neutral Au_3 structures presented in Figure 9.1 can be found in Appendix F.

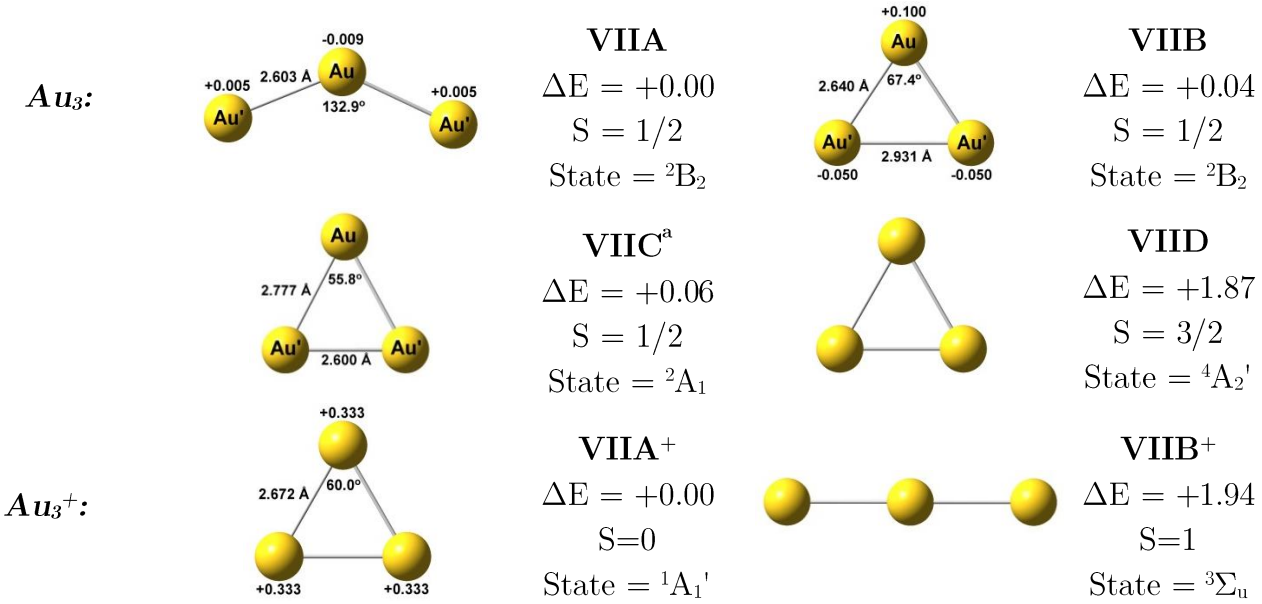

Figure 9.1. *Calculated structures for the neutral and cationic isomers of the Au_3 cluster. The relative energies (ΔE in eV) are calculated with respect to the lowest energy neutral and cationic isomers and are zero-point energy corrected. Hirshfeld charges and geometric data have also been provided for structures of relevance to the discussion.*

[a]*This is a transition state structure on the neutral potential energy surface.*

Mode	Symmetry[a]	Motion[b]	**VIIA** (cm^{-1})	**VIIB** (cm^{-1})	**VIIA⁺** (cm^{-1})
ν_1	a_1'/a_1	ν_s Au-Au/ν_s Au-Au'	124	162	170
ν_2	e'/a_1	δ_s Au-Au-Au/δ_s Au'-Au-Au'	19	56	109
ν_3	e'/b_2	ν_a Au-Au/ν_a Au-Au'	165	93	109

Table 9.1. *Calculated vibrational modes of the lowest energy neutral and cationic minima of Au_3.*

[a]*Structures **VIIA** and **VIIB** both has C_{2v} symmetry. Structure **VIIA⁺** has D_{3h} symmetry. Label format: D_{3h}/C_{2v}*

[b]ν_s: symmetric stretch; ν_a: asymmetric stretch; δ_s: symmetric bend.

For the cationic Au_3 species, the lowest energy structure is determined to be a D_{3h} equilateral triangle in the $^1A_1$ state with Au-Au bond lengths of 2.672 Å (Structure **VIIA**$^+$ – Figure 9.1). Table 9.1 shows the calculated vibrational modes and symmetry of this structure. Other cationic minima were also calculated, but only one additional structure is found to lie within 2 eV of **VIIA**$^+$ (triplet $D_{\infty h}$ structure – Structure **VIIB**$^+$). All others were found to lie much higher in energy (> 2 eV). The Cartesian coordinates and electronic parameters of all the calculated cationic Au_3 structures presented in Figure 9.1 can be found in Appendix F.

9.1.2. Geometric Changes and Hirshfeld Charges

For the two low-lying neutral minima (**VIIA** and **VIIB**) and the lowest energy cationic minimum (**VIIA**$^+$) discussed in Section 9.1.1, there are two ionisation transitions considered possible for Au_3: (i) a $^1A_1 \leftarrow {}^2B_2$ (**VIIA**$^+ \leftarrow$ **VIIA**) transition, and (ii) a different $^1A_1 \leftarrow {}^2B_2$ (**VIIA**$^+ \leftarrow$ **VIIB**) transition.

In analysing the change in atomic Hirshfeld charges (labelled in Figure 9.1) upon ionisation transition (i), the Au and Au' atoms gain a net charge of +0.342 and +0.328, respectively. This charge increase for both gold atoms is accompanied by the Au atom changing from a negatively charged state in the neutral structure, to a positively charged state in the cationic structure. Upon ionisation transition (ii), the Au and Au' atoms gain a net charge of +0.233 and +0.383, respectively, with both Au' atoms changing from a negatively charged state in the neutral structure to a positively charged state in the cationic structure. For both transitions, the largest bond length change observed is for the Au'-Au' bond, which is found to decrease by 2.000 Å and 0.259 Å for transitions (i) and (ii), respectively. This is despite the large gain in positive charge experienced by the two Au' atoms upon both ionisation transitions. Additionally, the Au-Au' bond length is found to increase by much smaller amounts of 0.070 Å and 0.032 Å for transitions (i) and (ii), respectively.

For both transitions, the Au'-Au' bond length change is significant and indicates that both involve significant motion along the appropriate FC co-ordinate. This should ultimately result in long vibronic progressions which will manifest as a gradual onset of cluster signal in the PIE spectrum. However, the 2.000 Å decrease experienced by the Au'-Au' bond length upon transition (i) is a much more significant geometric change than the 0.259 Å experienced by the same bond in transition (ii). This will ultimately result in extremely poor FC-overlap between **VIIA** and **VIIA**$^+$ and thus extremely small FCF values for transition (i). As there is significantly less geometric change experienced by the Au_3 cluster upon transition (ii), there should be much more favourable FC-overlap between **VIIB** and **VIIA**$^+$. These assertions are justified upon simulation of the ZEKE spectrum for each transition, where transition (ii) yields vibronic signals (see Appendix E for the corresponding ZEKE spectrum) that have vastly higher intensities than those simulated for transition (i); so much in fact that the latter ionisation transition failed to yield a ZEKE spectrum due to extremely low FCF values. Therefore, the transition (ii) is assigned to be more dominant ionisation transition.

9.1.3. Comparison to Previous Work

In previous work by Balasubramanian and Liao, Schwerdtfeger *et al.,* Metiu *et al.* and a review article by Willock *et al.*, it has been postulated that the doublet D_{3h} structure of the neutral Au_3 cluster has an unpaired electron occupying a doubly degenerate MO, yielding a $^2E'$ degenerate electronic ground state.[1-4] In order to remove this degeneracy, the neutral D_{3h} structure experiences Jahn-Teller distortion down to C_{2v} symmetry and splits the $^2E'$ state into two other electronic states, resulting in two structural candidates for neutral Au_3: one in a $^2A_1$ state and the other a $^2B_2$ state. Additionally, a linear $D_{\infty h}$ structure in a $^2\Sigma_u^+$ state has also been postulated as a structural candidate together with the two other aforementioned candidates.

Experimentally, Bishea and Morse recorded the resonant two-photon ionisation spectrum of jet-cooled Au_3 and assigned the ground state of neutral Au_3 to be in a $^2E'$

degenerate electronic state.[5] However, though it was mentioned that this structure undergoes Jahn-Teller distortion, a definitive C_{2v} electronic state was never assigned. Additionally, Howard *et al.* determined the neutral structure of Au_3 to be an obtuse-angled C_{2v} structure in a $^2B_2$ state through the use of electron spin resonance (ESR) spectroscopy.[6] However, as these experiments were performed on matrix-isolated Au_3, it has been suggested by Balasubramanian and Liao that the matrix may favour this particular geometry and thus a true gas-phase ground state structure is yet to be experimentally verified.[1] Hence, numerous computational studies have been performed at various levels of theory aimed (either directly or indirectly) at elucidating which of the structural candidates is the ground state structure of neutral Au_3 in the gas-phase.[1-3,7-19] Table 9.2 displays the results from the most comprehensive of these investigations. The structural and energetic properties of **VIIA**, **VIIB** and **VIIC** have also been included for comparison.

As observed in Table 9.2, the calculated structural and energetic properties of **VIIA** and **VIIC** compare best with those calculated at the CASSCF level of theory by Metiu *et al.*; both show that the lowest energy structure of neutral Au_3 is an obtuse-angled C_{2v} structure in a $^2B_2$ state and the corresponding $^2A_1$ structure is a transition state on the neutral potential energy surface of Au_3. Their lowest energy structure and **VIIA** are both consistent with the ESR structure for matrix-isolated Au_3. The CASSCF calculations failed to yield a structure comparable to **VIIB** in addition to yielding a linear $^2\Sigma_u^+$ structure with the same relative energy (to two decimal places) as the obtuse-angled C_{2v} structure. The latter observation is most likely due to the relatively small geometric differences between the linear $^2\Sigma_u^+$ and obtuse-angled C_{2v} structures (Δ(Au-Au) = 0.006 Å and $\Delta(\Theta) = 36.5^o$), which would be expected to result in a very small energy difference between the two structures. Interestingly, the results from the other Au_3 calculations performed at different levels of theory failed to yield an obtuse-angled $^2B_2$ structure; instead yielding acute-angled $^2B_2$ and $^2A_1$ structures and, in some instances, the linear $^2\Sigma_u^+$ geometry. However, the energy ordering of these neutral structures is found to be

extremely sensitive to the level of theory implemented, with the lowest energy structure predicted to be: (i) the acute-angled $^2A_1$ structure at the R-CCSD(T) level of theory, (ii) the acute-angled $^2B_2$ structure at the MRSDCI level of theory, and (iii) the linear $^2\Sigma_u^+$ structure at the UB3LYP level of theory. Regardless of this sensitivity in the energy ordering, the geometric properties of the acute-angled $^2B_2$ structure at all levels of theory compares well with those of **VIIB**.

In contrast to the neutral Au_3 cluster, there are significantly fewer computational investigations that have been performed on the cationic Au_3 cluster.[2,20,21] From those that have been performed, the work by Schwerdtfeger *et al.* has shown to be the most comprehensive. In their work, they calculated the lowest energy cationic structure to be a singlet D_{3h} structure in the $^1A_1$ state with Au-Au bond lengths of 2.631 Å at the CCSD(T) level of theory coupled with an all electron (10s7p5d3f)/[10s6p5d3f] relativistic basis set.[2] This is in excellent agreement with the calculated properties of **VIIA**$^+$.

	$^2B_2$			$^2A_1$			$^2\Sigma_u^+$	
	Au-Au'	Θ	ΔE	Au-Au'	Θ	ΔE	Au-Au	ΔE
This Work	2.603	132.9	0.00 (**VIIA**)	2.777	55.8	0.06[a] (**VIIC**)	-	-
	2.640	67.4	0.04 (**VIIB**)					
R-CCSD(T)[b]	2.607	65.4	0.007	2.723	56.2	0.00	-	-
CASSCF(3,3)[c]	2.749	143.5	0.00	3.031	52.2	0.08[a]	2.755	0.00
UB3LYP[c]	2.650	68.5	0.02	2.793	55.7	0.05	2.630	0.00
MRSDCI[d]	2.60	65.7	0.00	2.72	56.4	0.007	-	-

Table 9.2. *List of the structural and energetic properties of Au_3 calculated at various levels of theory. The Au-Au' and Au-Au bond lengths are in units of Å and the Au'-Au-Au' bond angle (Θ) is in units of degrees. The energy differences between competing structures (ΔE – in eV) are calculated relative to the lowest energy structure within each level of theory.*

[a]*Determined to be a transition state structure upon harmonic vibrational frequency analysis.*

[b]*Calculations performed with an all electron (10s7p5d3f)/[10s6p5d3f] relativistic basis set on all Au atoms – Reference 2.*

[c]*Calculations performed with the SBKJC(f)+sp basis set on all Au atoms. The SBKJC ECP was also used on each Au atom, retaining 19 electrons on each atom in the valence active space – Reference 3.*

[d]*Multi-reference single and double configuration interaction calculations were performed with a relativistic ECP used on each Au atom, retaining 11 electrons on each atom in the valence space – Reference 1.*

9.2. DFT Results for the Au_2Pr Cluster

9.2.1. Lowest Energy Neutral and Cationic Structures

For the neutral Au_2Pr species, the lowest energy structure is determined to be a C_{2v} isosceles triangle in a $^2A_1$ state with Au-Pr and Au-Au bond lengths of 2.745 Å and 4.759 Å, respectively (Structure **VIIIA** – Figure 9.2). The calculated vibrational modes and symmetries of **VIIIA** are listed in Table 9.3. Various other neutral minima were also calculated but no additional structures were found to lie within 1 eV of **VIIIA**; the closest being a quartet C_{2v} structure (Structure **VIIIB** – Figure 9.2) lying 1.85 eV higher in energy than **VIIIA**. All other minima are found to lie much higher in energy (> 1.85 eV). The Cartesian coordinates and electronic parameters of all the calculated neutral Au_2Pr structures presented in Figure 9.2 can be found in Appendix F.

For the cationic Au_2Pr species, the lowest energy structure is determined to be a C_{2v} isosceles triangle in a $^1A_1$ state with Au-Pr and Au-Au bond lengths of 2.638 Å and 4.348 Å, respectively (Structure **VIIIA**$^+$ – Figure 9.2). Table 9.3 shows the calculated vibrational modes and symmetry of this structure. Other cationic minima were also calculated but no additional structures were found to lie within 1 eV of **VIIIA**$^+$; the closest being a triplet C_{2v} structure (Structure **VIIIB**$^+$ – Figure 9.2) lying 1.52 eV higher in energy than **VIIIA**$^+$. All other minima are found to lie much higher in energy (> 1.52 eV). The Cartesian coordinates and electronic parameters of all the calculated cationic Au_2Pr structures presented in Figure 9.2 can be found in Appendix F.

9.2.2. Geometric Changes and Hirshfeld Charges

For Au_2Pr, there is only one possible ionisation transition to be considered: the $^1A_1 \leftarrow {}^2A_1$ (**VIIIA**$^+ \leftarrow$ **VIIIA**) transition. In analysing the change in Hirshfeld charges upon this transition (Figure 9.2), the Au and Pr atoms are found to gain a net charge of +0.197 and +0.606, respectively, with the charge increase for both Au atoms changing them from a negatively charged state in the neutral structure, to a positively charged state in the cationic structure. Despite the positively charged nature of both the Au and

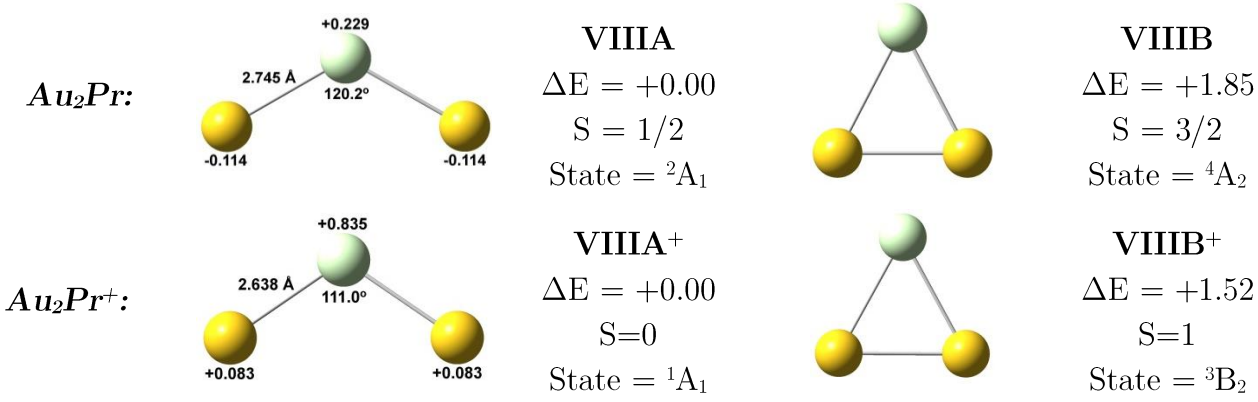

Figure 9.2. *Calculated structures for the neutral and cationic isomers of the Au_2Pr cluster. The relative energies (ΔE in eV) are calculated with respect to the lowest energy neutral and cationic isomers and are zero-point energy corrected. Hirshfeld charges and geometric data have also been provided for structures of relevance to the discussion.*

Mode	Symmetry[a]	Motion[b]	**VIIIA** (cm^{-1})	**VIIA$^+$** (cm^{-1})
ν_1	a_1	ν_s Au-Pr	132	164
ν_2	a_1	δ_s Au-Pr-Au	27	32
ν_3	b_2	ν_a Au-Pr	164	189

Table 9.3. *Calculated vibrational modes of the lowest energy neutral and cationic minima of Au_2Pr.*

[a]*Structures **VIIA** and **VIIA$^+$** both possess C_{2v} symmetry.*

[b]ν_s: symmetric stretch; ν_a:asymmetric stretch; δ_s: symmetric bend.

Pr atoms in the cation, the Au-Pr bond length is found to decrease by 0.107 Å upon ionisation

Additionally, the Au-Au bond length is observed to decrease by 0.411 Å which is consistent with the two Au atoms adopting a smaller overall magnitude of charge upon ionisation. Overall, these structural changes are considered relatively large and indicate that there is significant motion along the appropriate FC co-ordinate. This should ultimately result in long vibronic progressions which will manifest as a gradual onset of cluster signal in the PIE spectrum. This is consistent with the experimental PIE spectrum of Au_2Pr (Figure 8.8(a)) which exhibits gradual cluster signal onset following ionisation.

9.2.3. Comparison with Previous Work

Currently there are no previous computational studies on the neutral or cationic Au_2Pr clusters available for comparison with the results presented here. The only previous computational study involving Au_2-lanthanide trimers was performed by Zhao *et al.* on the DFT structures of neutral Au_nLa (n = 2-8) clusters calculated at the PW91PW91/CEP-121G level of theory.[22] In their work, the lowest energy neutral structure of the Au_2La trimer was determined to be doublet C_s structure with two slightly different Au-La bond lengths of 2.8302 Å and 2.8299 Å. However, as these two bond lengths are very close in value, it is more likely that this structure is a doublet C_{2v} isosceles triangle. Additionally in this work, the Au-Au bond length visually appeared to be much longer than the Au-La bond lengths but this value was not displayed nor was there enough structural data provided to calculate it. In comparison to the lowest energy neutral structure of Au_2Pr (**VIIIA**), both clusters were determined to possess C_{2v} symmetry with the gold-gold bond lengths calculated to be longer than the gold-lanthanide bond lengths.

9.3. DFT Results for the $AuPr_2$ Cluster

9.3.1. Lowest Energy Neutral and Cationic Structures

For the neutral $AuPr_2$ species, the lowest energy structure is determined to be a C_{2v} isosceles triangle in a $^6A_2$ state with Au-Pr and Pr-Pr bond lengths of 2.957 Å and 3.003 Å, respectively (Structure **IXA** – Figure 9.3). Within and around the experimental error of IE determination (±0.05 eV), there are two additional neutral structures that have been calculated (Structures **IXB** and **IXC** – Figure 9.3). Structure **IXB** is a C_{2v} isosceles triangle in a $^4A_2$ state which is found to lie +0.01 eV higher in energy than **IXA** and with Au-Pr and Pr-Pr bond lengths of 2.929 Å and 3.169 Å, respectively. Structure **IXC** is a C_{2v} isosceles triangle in a $^2A_1$ state which is found to lie +0.07 eV higher in energy than **IXA** and with Au-Pr and Pr-Pr bond lengths of 2.998 Å and 2.863 Å, respectively. This Pr-Pr bond length is considerably smaller than those in **IXA** and **IXB**. Other neutral minima (Structures **IXD-IXF)** were also calculated, but are found to lie higher in energy; especially the doublet and quartet linear structures which are calculated to lie +0.29 eV and +0.70 eV above **IXA**, respectively. In addition to the geometric data and Hirshfeld charges presented in Figure 9.3, Table 9.4 displays the calculated vibrational modes and symmetries of structures **IXA**, **IXB** and **IXC**. The Cartesian coordinates and electronic parameters of all the calculated neutral $AuPr_2$ structures presented in Figure 9.3 can be found in Appendix F.

For the cationic $AuPr_2$ species, the lowest energy structure is determined to be a C_{2v} isosceles triangle state in a $^5B_1$ with Au-Pr and Pr-Pr bond lengths of 2.953 Å and 2.930 Å, respectively (Structure $\mathbf{IXA^+}$ – Figure 9.3). Lying just outside the experimental error of IE determination (±0.05 eV), there is an additional cationic triplet structure possessing C_{2v} symmetry in a $^3B_1$ state which is +0.10 eV above $\mathbf{IXA^+}$ (Structure $\mathbf{IXB^+}$ – Figure 9.3) and with Au-Pr and Pr-Pr bond lengths of 2.941 Å and 3.034 Å, respectively. Other cationic minima (Structures $\mathbf{IXC^+}$-$\mathbf{IXD^+}$) were also calculated, but are found to lie higher in energy; especially the triplet linear structure which is calculated to lie +1.07 eV above $\mathbf{IXA^+}$. In addition to the geometric data and Hirshfeld charges presented in Figure

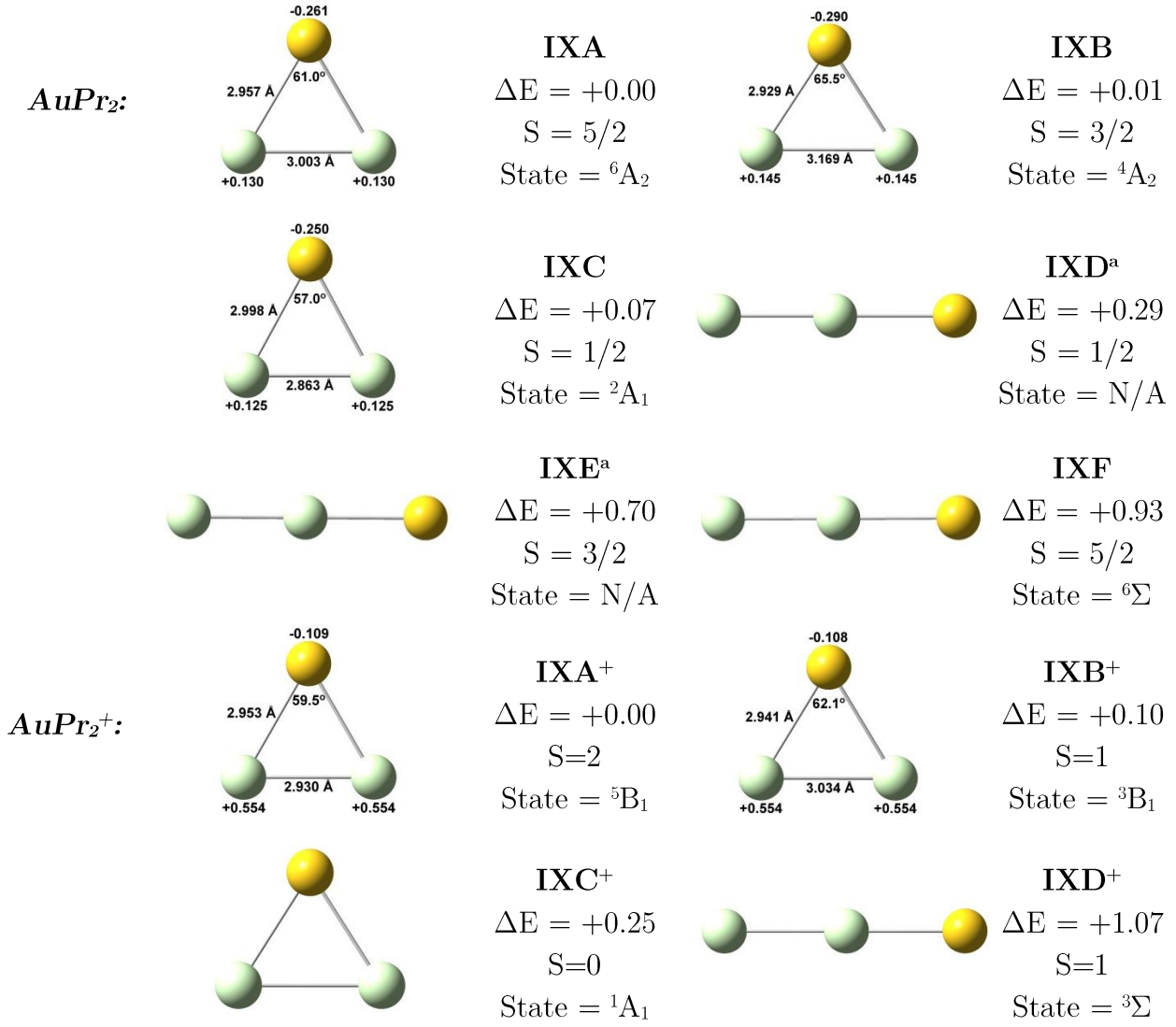

Figure 9.3. *Calculated structures for the neutral isomers of the $AuPr_2$ cluster. The relative energies (ΔE in eV) are calculated with respect to the lowest energy neutral isomers and are zero-point energy corrected. Hirshfeld charges and geometric data have also been provided for structures of relevance to the discussion.*

[a]The electronic states of these structures were unable to be determined due to some of the molecular orbitals of these structures having unidentified symmetry (even after constraining each structure to $C_{\infty V}$ symmetry).

Mode	Symmetry[a]	Motion[b]	**IXA** (cm^{-1})	**IXB** (cm^{-1})	**IXC** (cm^{-1})	**IXA$^+$** (cm^{-1})	**IXB$^+$** (cm^{-1})
ν_1	a_1	ν_s Au-Pr	150	146	165	166	154
ν_2	a_1	δ_s Au-Pr-Au	105	95	103	117	106
ν_3	b_2	ν_a Au-Pr	73	72	73	74	81

Table 9.4. *Calculated vibrational modes of the lowest energy neutral and cationic minima of $AuPr_2$.*
[a]All *structures possess C_{2v} symmetry.*
[b]ν_s: symmetric stretch; ν_a: asymmetric stretch; δ_s: symmetric bend.

9.3, Table 9.4 displays the calculated vibrational modes and symmetries of structures **IXA$^+$** and **IXB$^+$**. The Cartesian coordinates and electronic parameters of all the calculated cationic $AuPr_2$ structures presented in Figure 9.3 can be found in Appendix F.

9.3.2. Geometric Changes and Hirshfeld Charges

For the three low-lying neutral minima (**IXA, IXB** and **IXC**) and two low-lying cationic minima (**IXA$^+$** and **IXB$^+$**) discussed in Section 9.3.1, there are four possible ionisation transitions to consider for Au_2Pr: (i) the $^5B_1 \leftarrow {}^6A_2$ (**IXA** to **IXA$^+$**) transition, (ii) the $^5B_1 \leftarrow {}^4A_2$ (**IXB** to **IXA$^+$**) transition, (iii) the $^3B_1 \leftarrow {}^4A_2$ (**IXB** to **IXB$^+$**), and (iv) the $^3B_1 \leftarrow {}^2A_1$ (**IXC** to **IXB$^+$**) transition.

In analysing the change in atomic Hirshfeld charges upon ionisation (labelled in Figure 9.3), the Au and Pr atoms gain a net charge of +0.152 and +0.424, respectively upon transition (i). Upon ionisation transitions (ii) and (iii), the Au atom gains a net charge of +0.181 and +0.182, respectively; the Pr atoms gain the same net charge of +0.409 for both of these transitions. Lastly, upon ionisation transition (iv), the Au and Pr atoms gain a net charge of +0.141 and +0.429, respectively. Contrary to the observed Hirshfeld charge changes of the Au atoms in Au_2Pr, the Au atom in all of the ionisation transitions does not change in charge sign; it remains negatively charged before and after ionisation.

For all transitions, the largest bond length change observed is for the Pr-Pr bond, which is found to decrease by 0.073 Å for transition (i), decrease by 0.239 Å for transition (ii), decrease by 0.135 Å for transition (iii) and increase by 0.171 Å for transition (iv). For the first three transitions, the Pr-Pr bond length decreases despite the large gain in positive charge experienced by the two Pr atoms upon all three ionisation transitions. However, for the last transition, the increase in bond length is perhaps related to the Pr-Pr bond length in structure **IXC** being smaller than those of **IXA** and **IXB** before ionisation. Additionally, the Au-Pr bond length is found to decrease by 0.004 Å for transition (i), increase by 0.024 Å for transition (ii), increase by 0.012 Å for transition (iii) and decrease by 0.057 Å for transition (iv); all of which are much smaller bond length changes then the corresponding Pr-Pr bond length change for each transition.

Overall, the structural changes observed upon transitions (ii)-(iv) are considered relatively large and indicate that there is significant changes along the appropriate FC co-ordinates. This should ultimately result in long vibronic progressions which will manifest as a gradual onset of cluster signal in the PIE spectrum. However, the geometric changes observed for transition (i) are relatively small compared to the other three ionisation transitions. This indicates stronger FC-overlap between the neutral and cationic structures which will result in short vibronic progressions and thus a much sharper onset of cluster signal in the PIE spectrum then would be expected from the other three ionisation transitions. As it is difficult to discern the extent to which geometric change affects the observed rate of signal onset from the experimental PIE spectrum of $AuPr_2$ (Figure 8.8(a)), all ionisation transitions are considered potential candidates.

9.3.3. Comparison to Previous Work

Due to the scarcity of computational work on lanthanide-dominated bare transition-lanthanide metal trimers, the only comparison that can be made is with: (i) the $RhHo_2$ neutral and cationic structures from Chapter 6, and (ii) the DFT structures of bare lanthanum-nickel bimetallic clusters determined by Liu *et al.*[23] From Chapter 6, the neutral $RhHo_2$ structure was determined to be a doublet C_{2v} obtuse-angled isosceles triangle with Rh-Ho and Ho-Ho bond lengths of 2.386 Å and 3.498 Å, respectively and a Rh-Ho-Rh bond angle of 94.3°. From the work performed by Liu *et al.*, the neutral $NiLa_2$ trimer was found to be a singlet C_{2v} acute-angled isosceles triangle with bond lengths of La-Ni and La-La being 2.555 and 3.050 Å, respectively and a La-Ni-La bond angle of 73.3°. In comparison, structures **IXA**, **IXB** and **IXC** compare better with the lowest energy $LaNi_2$ neutral structure than with the lowest energy $RhHo_2$ structure, with all three structures being acute-angled in nature with relatively small differences between their transition-lanthanide and lanthanide-lanthanide bond lengths. This may be due to the fact that praseodymium and lanthanum are considered early lanthanide metals whereas holmium is a late lanthanide metal.

With respect to the cationic $AuPr_2$ structures, the only comparison that can be made is with the cationic $RhHo_2$ structure determined in Chapter 6. In this chapter, the cationic $RhHo_2$ structure was determined to be a triplet C_{2v} obtuse-angled isosceles triangle with Rh-Ho and Ho-Ho bond lengths of 2.380 Å and 3.391 Å, respectively and a Rh-Ho-Rh bond angle of 90.9°. In comparison, structures $\mathbf{IXA}^+$ and $\mathbf{IXB}^+$ do not compare well with this cationic $RhHo_2$ structure, with both being acute-angled in nature with relatively small differences between their transition-lanthanide and lanthanide dimer bond lengths. As mentioned above, this may be due to the fact that praseodymium is considered an early lanthanide metal whereas holmium is a late lanthanide metal, thus resulting in the differing geometric properties between structures $\mathbf{IXA}^+$ and $\mathbf{IXB}^+$ and the determined cationic structure of $RhHo_2$.

9.4. DFT Results for the Pr_3 Cluster

9.4.1. Lowest Energy Neutral and Cationic Structures

For the neutral Pr_3 species, the lowest energy structure is determined to be a C_{2v} isosceles triangle in a $^4A_2$ state (Structure **XA** – Figure 9.4) with Pr-Pr' and Pr'-Pr' bond lengths of 3.145 Å and 2.908 Å, respectively. An additional neutral structure lying just outside the experimental error of IE determination is also calculated and is found to lie +0.06 eV higher in energy than **XA**. This low-lying neutral isomer is determined to be a C_{2v} structure in a $^6B_1$ state (Structure **XB**) with Pr-Pr' and Pr'-Pr' bond lengths of 3.140 Å and 3.139 Å, respectively. As the Pr-Pr' and Pr'-Pr' bond lengths in this structure differ by only 0.001 Å, it would seem that **XB** may actually possess D_{3h} symmetry. However, re-optimisation of this structure within the constraints of D_{3h} symmetry failed to yield a genuine minimum, with an additional single point harmonic vibrational frequency analysis yielding an imaginary frequency, thus confirming that it is not a true minimum. This indicates that **XB** may give rise to a degenerate electronic state configuration when constrained to D_{3h} symmetry and thus, experiences marginal Jahn-Teller distortion down to C_{2v} symmetry in order to remove this degeneracy, resulting in the final structure described above. As such, the bond lengths and bond angles for **XB** have been reported to five and three decimal places, respectively in order to highlight that a very slight structural change means the difference between being either a true minimum or transition state on the neutral potential energy surface. Various other neutral minima at doublet and higher multiplicities are also calculated (Structures **XC**-**XH**), but are found to lie higher in energy; especially the doublet linear structure which is calculated to lie +0.81 eV above **XA**. In addition to the bond lengths and Hirshfeld charges presented in Figure 9.4, Table 9.5 shows the calculated vibrational modes and symmetries of structures **XA** and **XB**. The Cartesian coordinates and electronic parameters of all the calculated neutral Pr_3 structures presented in Figure 9.4 can be found in Appendix F.

Pr_3:

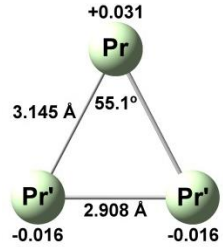

XA
$\Delta E = +0.00$
$S = 3/2$
State = $^4A_2$

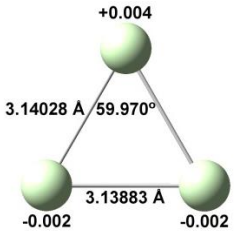

XB
$\Delta E = +0.06$
$S = 5/2$
State = $^6B_1$

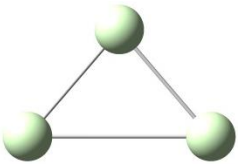

XC
$\Delta E = +0.17$
$S = 5/2$
State = $^6B_2$

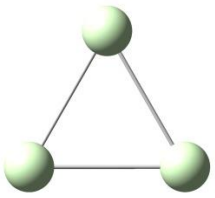

XD
$\Delta E = +0.20$
$S = 7/2$
State = $^8A_2''$

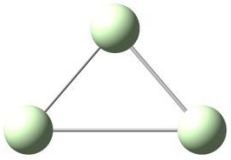

XE
$\Delta E = +0.42$
$S = 1/2$
State = $^2B_2$

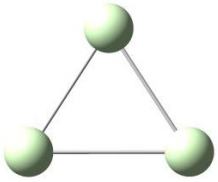

XF
$\Delta E = +0.62$
$S = 9/2$
State = $^{10}A_2$

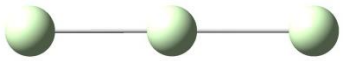

XG
$\Delta E = +0.81$
$S = 1/2$
State = $^2\Sigma_g$

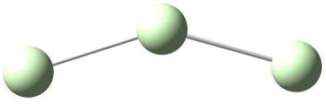

XH
$\Delta E = +0.98$
$S = 3/2$
State = $^4A_2$

Pr_3^+:

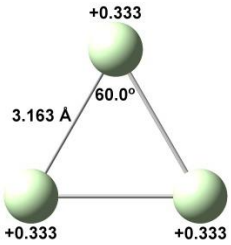

XA^+
$\Delta E = +0.00$
$S=1$
State = $^3A_1'$

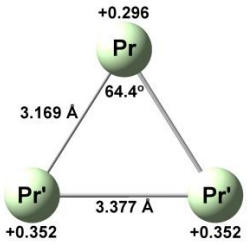

XB^+
$\Delta E = +0.04$
$S=2$
State = $^5B_1$

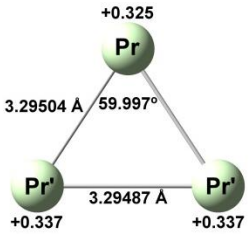

XC^+
$\Delta E = +0.04$
$S=3$
State = $^7B_1$

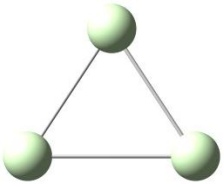

XD^+
$\Delta E = +0.20$
$S=3$
State = $^7A_1$

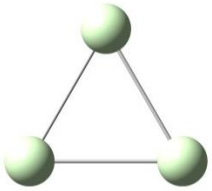

XE^+
$\Delta E = +0.40$
$S=3$
State = $^7A_2''$

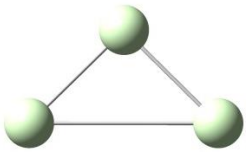

XF^+
$\Delta E = +0.79$
$S=1$
State = $^3A_2$

Figure 9.4. *Calculated structures for the neutral and cationic isomers of the Pr_3 cluster. The relative energies (ΔE in eV) are calculated with respect to the lowest energy neutral and cationic isomers and are zero-point energy corrected. Hirshfeld charges and geometric data have also been provided for structures of relevance to the discussion.*

Mode	Symmetry[a]	Motion[b]	**XA** (cm^{-1})	**XB**[c] (cm^{-1})	**XA**$^+$ (cm^{-1})	**XB**$^+$ (cm^{-1})	**XC**$^+$ (cm^{-1})
ν_1	a_1'/a_1	ν_s Pr-Pr/ν_s Pr-Pr'	146	142	148	145	139
ν_2	e'/a_1	δ_s Pr-Pr-Pr/δ_s Pr'-Pr-Pr'	109	76.3	75	103	95
ν_3	e'/b_2	ν_a Pr-Pr/ν_a Pr-Pr'	91	76.4	75	92	95

Table 9.5. *Calculated vibrational modes of the lowest energy neutral and cationic minima of Pr_3.*
[a]*Structures **XA**, **XB** and **XB**$^+$ both have C_{2v} symmetry. Structures **XA**$^+$ and **XC**$^+$ all possess D_{3h} symmetry. Label format: D_{3h}/C_{2v}*
[b]ν_s: symmetric stretch; ν_a: asymmetric stretch; δ_s: symmetric bend.
[C]*Vibrational modes ν_2 and ν_3 for structure **XB** have been expressed to 1 decimal place in order to indicate the non-degeneracy of them within the assigned C_{2v} symmetry of this structure.*

For the cationic Pr_3 species, there are low-lying three isomers calculated to lie within the estimated experimental IE error. The lowest energy structure is a D_{3h} equilateral triangle in the $^3A_1$ state (Structure **XA**$^+$ – Figure 9.4) with Pr-Pr bond lengths of 3.163 Å. The next two structures are both calculated to lie 0.04 eV higher in energy than **XA**$^+$ (Structures **XB**$^+$ and **XC**$^+$ - Figure 9.4). Structure **XB**$^+$ is a C_{2v} acute-angled isosceles triangle in a $^5B_1$ state with Pr-Pr' and Pr'-Pr' bond lengths of 3.169 Å and 3.377 Å, respectively and a Pr'-Pr-Pr' bond angle of 64.4°. Structure **XC**$^+$ appears to be a D_{3h} equilateral triangle with Pr-Pr bond lengths of 3.295 Å. However, upon closer inspection, **XC**$^+$ is actually a C_{2v} acute-angled isosceles triangle in a $^7B_1$ state with Pr-Pr' and Pr'-Pr' bond lengths of 3.29504 Å and 3.29487 Å, respectively (reported to five decimal places to show bond distance variation), and a Pr'-Pr-Pr' bond angle of 59.997° (reported to three decimal places to show bond angle variation). As with **XB**, optimisation of **XC**$^+$ within the constraints of D_{3h} symmetry failed to yield a genuine minimum, with the calculation consistently returning the very slight Jahn-Teller distorted C_{2v} structure. Additional single point harmonic vibrational frequency analysis of D_{3h}-constrained **XC**$^+$ also yielded an imaginary frequency, verifying that it is not a true minimum. Various other cationic

minima at triplet and higher multiplicities are also calculated to lie within 1 eV of $\mathbf{XA}^+$ (Structures $\mathbf{XD}^+$-$\mathbf{XF}^+$), but are found to lie higher in energy. In addition to the bond lengths and Hirshfeld charges presented in Figure 9.4, Table 9.5 shows the calculated vibrational modes and symmetries of structures $\mathbf{XA}^+$, $\mathbf{XB}^+$ and $\mathbf{XC}^+$. The Cartesian coordinates and electronic parameters of all the calculated cationic Pr_3 structures presented in Figure 9.4 can be found in Appendix F.

9.4.2. Geometric Changes and Hirshfeld Charges

For the two low-lying neutral minima (**XA** and **XB**) and three low-lying cationic minima ($\mathbf{XA}^+$-$\mathbf{XC}^+$) minima presented in Figure 9.4 and discussed in Section 9.4.1, there are four ionisation transitions considered possible for Pr_3: (i) the $^3A_1 \leftarrow {}^4A_2$ ($\mathbf{XA}^+ \leftarrow \mathbf{XA}$) transition, (ii) the $^5B_1 \leftarrow {}^4A_2$ ($\mathbf{XB}^+ \leftarrow \mathbf{XA}$) transition, (iii) the $^5B_1 \leftarrow {}^6B_1$ ($\mathbf{XB}^+ \leftarrow \mathbf{XB}$) transition, and (iv) the $^7B_1 \leftarrow {}^6B_1$ ($\mathbf{XC}^+ \leftarrow \mathbf{XB}$) transition. However, only geometric and atomic Hirshfeld charge changes for transition (d) will be discussed. This was chosen as the other transitions were found to yield ZEKE spectra with significantly reduced overall signal intensities than the ZEKE spectra produced from transition (d) (See Appendix E for the corresponding ZEKE spectra for all transitions).

In analysing the change in atomic Hirshfeld charges (labelled in Figure 9.4) transition (d), the Pr and Pr' atoms gain a net charge of +0.321 and +0.339, respectively. Interestingly, the charge increase for both sets of praseodymium atoms is accompanied by the Pr' atoms changing from a negatively charged state in the neutral structure (albeit very slightly negative), to a positively charged state in the cationic structure. In addition to these changes in Hirshfeld charges, the Pr-Pr' and Pr'-Pr' bond lengths increase by 0.155 Å and 0.156 Å, respectively ionisation. These geometric changes are considered significant and indicate significant motion along the appropriate FC coordinates, which should ultimately result in a gradual onset of cluster signal following ionisation. This is consistent with the experimental PIE spectrum for Pr_3 recorded by Koretsky and

Knickelbein, which was observed to exhibit gradual cluster signal onset for *ca.* 0.15 eV before eventually plateauing.[24]

9.4.3 Comparison to Previous Work

Tsipis *et al.* have recently performed DFT calculations on pure lanthanide trimers and their nitride counterparts using the B3LYP density functional coupled with the relativistic small-core SDD basis set (i.e. MWB28 ECP).[25] As part of this work, the neutral and cationic structures of Pr_3 were calculated. For the neutral cluster, the lowest energy structure was calculated to be a D_{3h} equilateral triangle in the $^{10}A_2$ state with a Pr-Pr bond length of 4.406 Å. For the cationic cluster, the lowest energy structure was calculated to be a D_{3h} equilateral triangle in the $^{7}A_1$ state with a Pr-Pr bond length of 3.976 Å. These long bond lengths suggest that the Pr_3 cluster, in both the neutral and cationic state, is very weakly bound; perhaps bordering on van der Waal-type interactions between all of the Pr atoms. In comparison with the Pr_3 structures calculated herein using the B3P86/SDD† level of theory, the Pr-Pr bond lengths determined for the neutral Pr_3 cluster by Tsipis *et al.* are 1.261 Å to 1.499 Å longer than those calculated for structures **XA** and **XB**, respectively. The Pr-Pr bond lengths calculated for the cationic Pr_3 cluster by Tsipis *et al.* are 0.681 Å-0.813 Å longer than those calculated for structures $\mathbf{XA}^+$, $\mathbf{XB}^+$ and $\mathbf{XC}^+$. This large discrepancy in bond lengths could perhaps be attributed to: (i) the use of different density functionals (B3LYP vs. B3P86), and (ii) the use of the small-core SDD basis set versus the large-core version of the same basis set.

9.5. Simulated ZEKE and PIE Spectra for the Au_2Pr and $AuPr_2$ Clusters

9.5.1. Simulated ZEKE Spectrum for the Au_2Pr cluster

As discussed in Section 9.2, there is only one transition to be considered for the $AuPr_2$ cluster (the $^1A_1 \leftarrow {}^2A_1$ (**VIIIA**$^+$ $\leftarrow$ **VIIIA**) transition). However, as with the $RhHo_2O_n$ (Chapter 6) and $Rh_2Ho_2O_m$ (Chapter 7) clusters, the vibrational temperature of the molecular beam at *ca.* 300 K could lead to an early onset of Au_2Pr cluster signal due to vibronic "hot band" transitions rather than the origin band.

Figure 9.5 shows the ZEKE spectrum simulated for the $^1A_1 \leftarrow {}^2A_1$ (**VIIIA**$^+$ $\leftarrow$ **VIIIA**) transition at 300 K. As observed, the simulation yields a dense array of vibronic signals comprised of various quanta of various modes from both structures. Due to the large number of ZEKE signals simulated, specific labelling has been omitted except for the band origin (0_0^0 – black arrow). It is unclear from the ZEKE spectrum which particular vibronic transition would be responsible for the thermal onset of the PIE spectrum. Hence, a range bar has been placed on the spectrum to indicate where the initial onset of experimental cluster signal would begin.

9.5.2. Comparison of Experimental and Simulated PIE Spectra for Au_2Pr

In simulating the ZEKE spectrum for the $^1A_1 \leftarrow {}^2A_1$ transition at 300 K, the theoretical 0_0^0 transition was set to the experimental appearance energy (denoted AE in Chapter 8) of Au_2Pr (5.51 eV). This was done based on the assumption that the initial onset of cluster signal in the experiment is due to the 0_0^0 transition and hence, any additional onset observed thereafter is due to various other vibronic transitions. However, the presence of the hot band features simulated to arise between *ca.* 5.465 – 5.479 eV (indicated by the blue range bar in Figure 9.5) indicates that the initial cluster signal onset is due to one of the vibronic transitions in this range and not the 0_0^0 transition. Hence, the initial experimental cluster signal onset observed at 5.51 eV is asserted to actually be due to a vibronic hot-band transition and the experimental AE (i.e. 0_0^0 transition) of Au_2Pr lies slightly higher in energy.

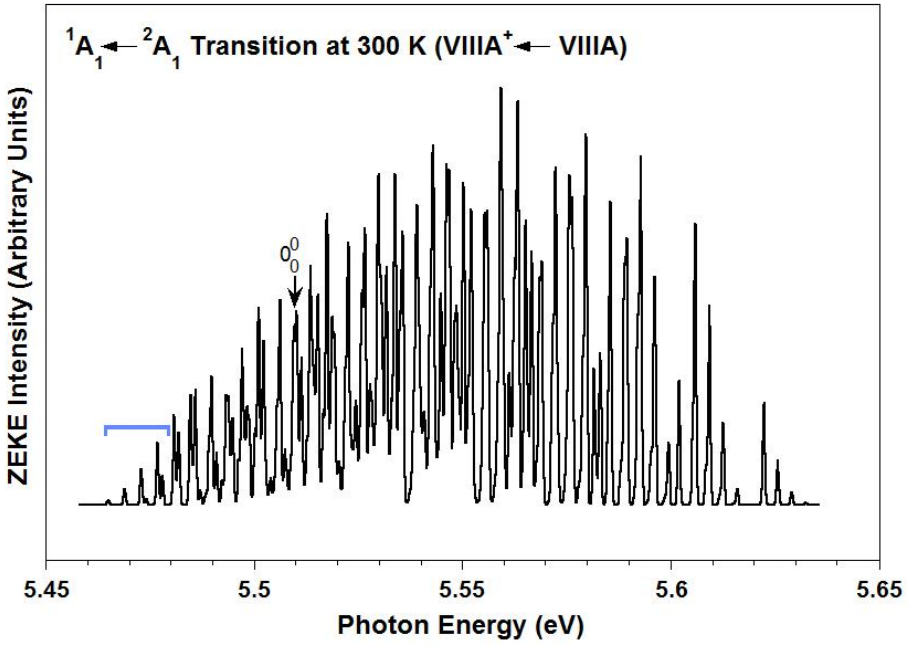

Figure 9.5. *ZEKE spectrum simulated at 300 K for the* $^1A_1 \leftarrow {}^2A_1$ (**VIIIA$^+$ ← VIIIA**) *transition for the* Au_2Pr *cluster. Due to the large number of ZEKE signals simulated, specific labelling has been omitted except for the theoretical band origin (black arrow) and possible range of the thermal onset starting position (blue range bar).*

For the ZEKE spectrum arising from the $^1A_1 \leftarrow {}^2A_1$ transition, an arbitrary correction factor of 0.041 eV is applied to all the transitions to account for the thermally-corrected experimental AE (denoted AE†) for Au_2Pr.[26] Figure 9.6 shows the comparison of the resulting corrected ZEKE and corresponding PIE spectra with the experimental PIE spectrum of Au_2Pr. In Figure 9.6(a), the addition of the 0.041 eV correction factor to all transition energies in the simulated ZEKE spectrum causes an initial cluster signal onset at 5.51 eV (blue arrow) and shifts the energy of the 0_0^0 transition to 5.551 eV in the simulated PIE spectrum (black arrow), the latter being the experimental AE† for Au_2Pr. In addition, the 0.041 eV correction factor shifts the highest energy FC-allowed vibronic transition with considerable intensity to *ca.* 5.670 eV, causing the simulated PIE spectrum to level off at around this point.

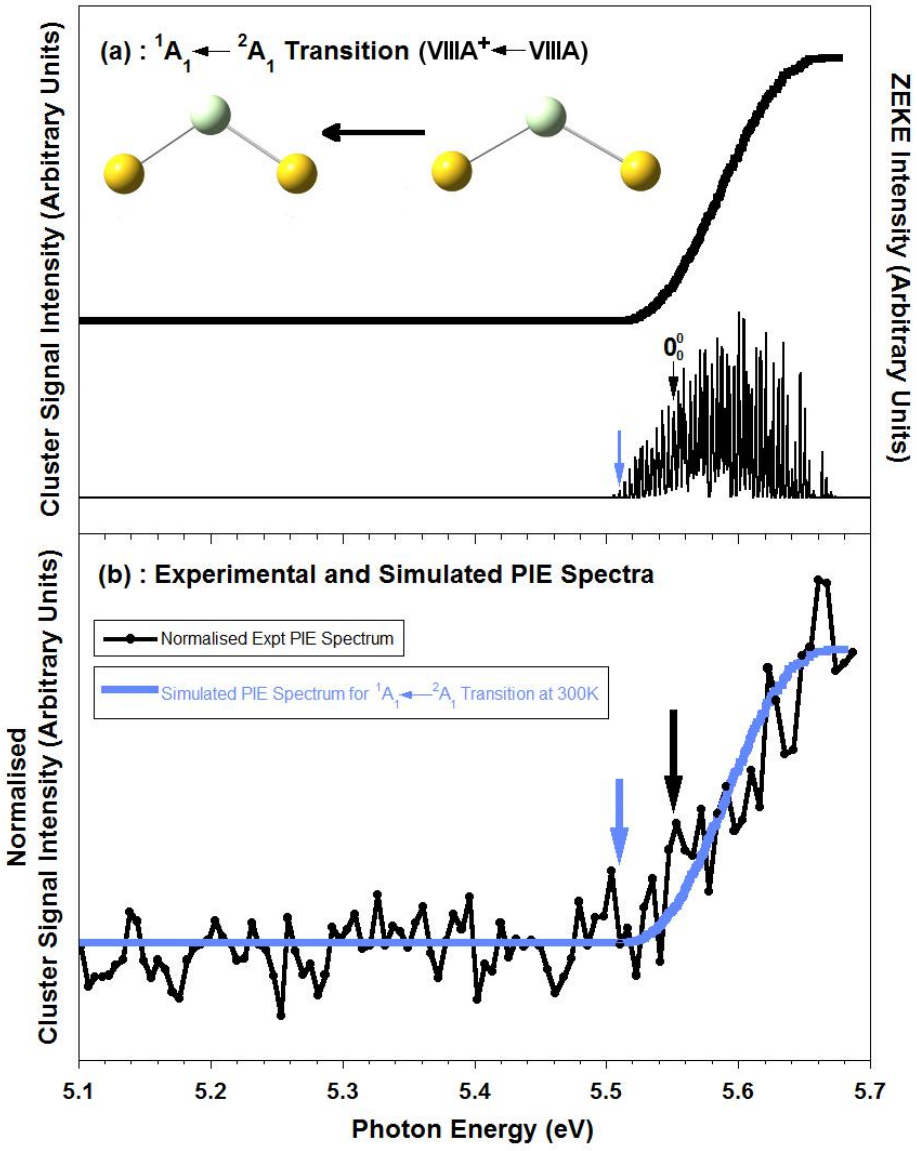

Figure 9.6. *(a) The corrected ZEKE and PIE spectra for the $^1A_1 \leftarrow {}^2A_1$ ($VIIIA^+ \leftarrow VIIIA$) transition of Au_2Pr simulated at 300 K, and (b) The normalised experimental and corrected PIE spectra for the $^1A_1 \leftarrow {}^2A_1$ ($VIIIA^+ \leftarrow VIIIA$) transition of Au_2Pr simulated at 300 K. The blue arrow indicates the energy position at which the thermal onset of the PIE spectrum is initiated. The black arrow indicates the energy of the band origin and the thermally-corrected experimental appearance energy (AE^t) of Au_2Pr.*

In Figure 9.6(b), the simulated and experimental PIE spectra have been independently normalised and compared. As observed, the shifting of the simulated ZEKE by 0.041 eV results in an excellent fit of the corresponding simulated PIE curve to the experimental PIE curve, with both displaying very similar levels of cluster signal onset upon ionisation and both appearing to level off at *ca.* 5.670 eV. Overall, such excellent comparison between the experimental and theoretical PIE spectra strongly indicates that structures **VIIIA** and **VIIIA**$^+$ are the structures for neutral and cationic Au_2Pr, respectively.

9.5.3. Simulated ZEKE Spectra for the $AuPr_2$ cluster

Due to the four possible ionisation transitions that are possible for $AuPr_2$ (*vide supra*), it is difficult to assign any of the transitions to the experimental data based solely on energetic and structural observation. In addition, as the vibrational temperature is *ca.* 300 K in the molecular beam, it is possible that the initial onset of experimental cluster signal is due to vibronic "hot band" transitions (as discussed in Chapters 6 and 7 for the $RhHo_2O_n$ and $Rh_2Ho_2O_m$ clusters, respectively and for the Au_2Pr cluster above).

Figure 9.7 shows the ZEKE spectra simulated at 300 K for: (a) the $^5B_1 \leftarrow {}^6A_2$ (**IXA**$^+ \leftarrow$ **IXA**) transition, (b) the $^3B_1 \leftarrow {}^4A_2$ (**IXB**$^+ \leftarrow$ **IXB**) transition, (c) the $^3B_1 \leftarrow {}^2A_1$ (**IXB**$^+ \leftarrow$ **IXC**) transition, and (d) the $^5B_1 \leftarrow {}^4A_2$ (**IXA**$^+ \leftarrow$ **IXB**) transition. The ZEKE spectra corresponding to transitions (b)-(d) have all been magnified so that they can be viewed on the scale as transition (a). Due to the small size of the each separate figure and the dense array of ZEKE signals arising from transitions (b)-(d), specific labelling has been omitted in all spectra except for the band origin (0_0^0 – black arrow) and the vibronic "hot band" transition potentially responsible for the initial onset of experimental cluster signal for transition (a) (1_1^0 vibronic transition – blue arrow)). Upon comparison of these ZEKE spectra, it is clear that the signals simulated for the $^5B_1 \leftarrow {}^6A_2$ transition (ZEKE spectrum (a)) possesses signals with greater overall intensities than those simulated for the other three transitions. In addition to this, the signals in the

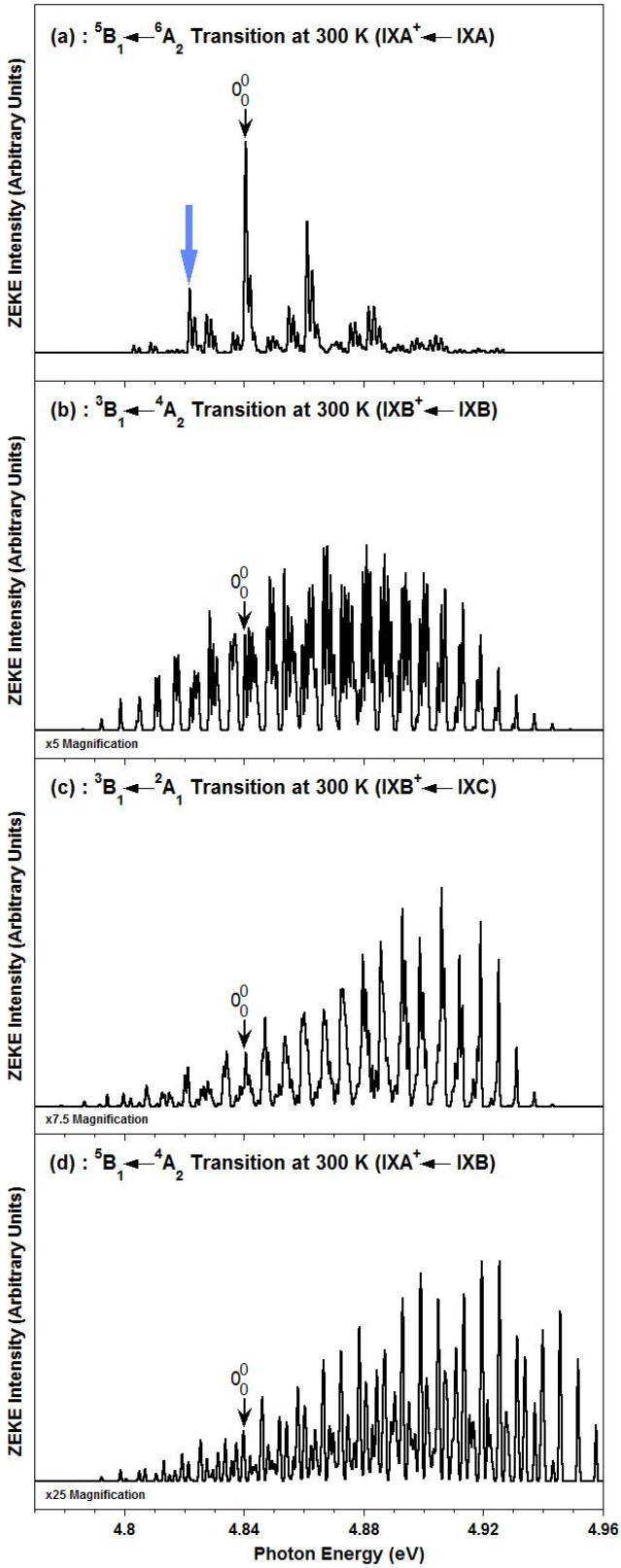

Figure 9.7. *ZEKE spectra simulated at 300 K for the various competing transition for the $AuPr_2$ cluster. The energies of the theoretical band origin (black arrow) and possible thermal onset starting position for the $^5B_1 \leftarrow {}^6A_2$ ($IXA^+ \leftarrow IXA$) transition (blue arrow) have been indicated. Due to the large number of ZEKE signals simulated, specific labelling has been omitted except for the band origin (0_0^0) for transitions (a)-(d).*

ZEKE spectra (b), (c) and (d) are also observed to cut-off abruptly in intensity towards the higher energy end in each spectrum (more so for ZEKE spectra (c) and (d) than for (b)). This indicates that the energy window considered for these ZEKE simulations, in addition to the maximum allowed vibrational quanta for the neutral and cationic structures are both not sufficient enough to cover all possible FC transitions for each of these ionisation transitions. Re-simulation of the ZEKE spectra due to transitions (b)-(d) at 300 K with an increase in vibrational quantum number of the neutral and cationic structures and expansion of the energy window yields spectra with complete FC profiles (located in Appendix E of this thesis). However, even these re-simulated ZEKE spectra were required to be magnified (x4 times for ZEKE spectra corresponding to transitions (b) and (c), x10 for ZEKE spectrum corresponding to transition (d)) in order to compare them on the same scale as the ZEKE spectrum in Figure 9.7(a). Therefore, transition (a) is most likely to be the dominant transition that occurs upon ionisation of the $AuPr_2$ cluster and will only be considered further.

Figure 9.8 shows the labelled ZEKE spectrum for the $^5B_1 \leftarrow {}^6A_2$ transition simulated at 300 K. As observed, the spectrum exhibits eleven progressions that appear with varying intensities, with the highest energy FC-allowed transition predicted to appear at *ca.* 4.925 eV (due to the 1_1^5 vibronic transition). Of these eleven progressions, seven of them possess a constant energy spacing of approximately 0.0206 eV (166 cm^{-1}), which corresponds to the energy of the symmetric stretching mode (mode ν_1 - ν_s Au-Pr) of $\mathbf{IXA}^+$. The other progressions possesses a constant energy spacing of approximately 0.0186 eV (150 cm^{-1}), which corresponds to the energy of the same symmetric stretching mode of **IXA**. Additionally, there are five other signals that appear with weak intensities due to the 2_3^2, 2_2^2, 2_1^1 $1_1^0 2_0^1$ and $1_0^1 2_1^0$ vibronic transitions. Overall, the most intense signal that arises in the ZEKE spectrum is due to the 0_0^0 transition. This indicates that the vertical and adiabatic IEs for $AuPr_2$ are equal and that there should be very little geometric change experienced by this cluster upon ionisation, which is substantiated by the minute structural difference between **IXA** and $\mathbf{IXA}^+$ as discussed in Section 9.3.2.

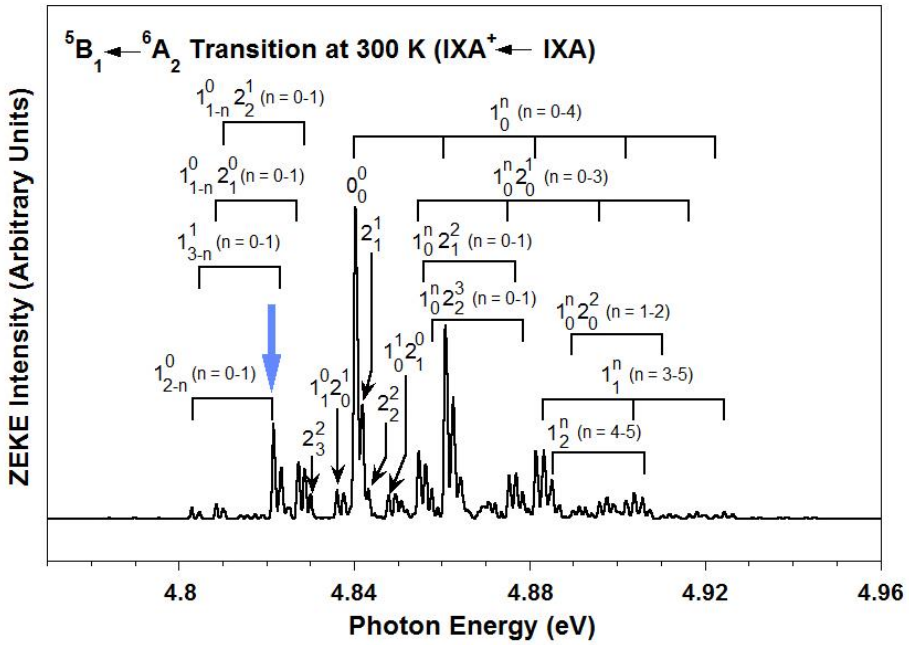

Figure 9.8. *ZEKE spectrum simulated at 300 K for the $^5B_1 \leftarrow {}^6A_2$ (**IXA$^+$ ← IXA**) transition for the $AuPr_2$ cluster. The energies of the theoretical band origin and possible thermal onset starting position (blue arrow) are indicated. The ZEKE signals whose origins are unambiguously known have been labelled accordingly with number of quanta of each vibrational mode from the neutral and cationic structures contributing to each of them.*

9.5.4. Comparison of Experimental and Simulated PIE Spectra for $AuPr_2$

In simulating the ZEKE spectrum for the $^5B_1 \leftarrow {}^6A_2$ transition at 300 K, the theoretical 0^0_0 transition was set to the experimental AE of $AuPr_2$ (4.84 eV). This was done based on the assumption that the initial onset of cluster signal in the experiment is due to the 0^0_0 transition and any additional onset observed thereafter is due to various other vibronic transitions. However, the presence of the strong hot band feature simulated to arise at *ca.* 4.821 eV (due to the 1^0_1 vibronic transition – indicated by the blue arrow in Figure 9.8) indicates that the initial cluster signal onset is most likely due to this vibronic transition and not the 0^0_0 transition. Hence, the initial experimental cluster signal onset observed at 4.84 eV is asserted to actually be due to the 1^0_1 vibronic transition and the experimental AE (i.e. 0^0_0 transition) of $AuPr_2$ lies slightly higher in energy.

For the ZEKE spectrum arising from the $^5B_1 \leftarrow {}^6A_2$ transition, a correction factor of 0.019 eV (the difference between the energy assigned to the theoretical 0_0^0 transition (4.84 eV) and the energy simulated for the 1_1^0 vibronic transition (*ca.* 4.821 eV)) is applied in order to attain the experimental $AE^{\dagger}$ for $AuPr_2$. Figure 9.9 shows the comparison of the resulting corrected ZEKE and corresponding PIE spectra simulated with the experimental PIE spectrum of the $AuPr_2$ cluster. As observed in Figure 9.9(a), the addition of the 0.019 eV correction factor to all transition energies in the simulated ZEKE spectrum causes an initial cluster signal onset at 4.84 eV due to the 1_1^0 vibronic transition (blue arrow) and shifts the energy of the 0_0^0 transition to 4.859 eV (black arrow), the latter being the experimental $AE^{\dagger}$ of $AuPr_2$. In addition, the 0.019 eV correction factor shifts the energy of 1_1^5 (the highest energy FC-allowed vibronic transition with considerable intensity) to *ca.* 4.944 eV, causing the simulated PIE spectrum to level off at around this point.

In Figure 9.9(b), the simulated and experimental PIE spectra have been independently normalised and compared. As observed, the shifting of the simulated ZEKE by 0.019 eV results in an excellent fit of the corresponding simulated PIE curve to the experimental PIE curve, with both displaying similar cluster signal curves and both appearing to level off at *ca.* 4.944 eV. Overall, such excellent comparison between the experimental and theoretical PIE spectra strongly indicates that structures **IXA** and IX$\mathbf{A}^+$ are the likely neutral and cationic $AuPr_2$ structures, respectively giving rise to the observed spectrum.

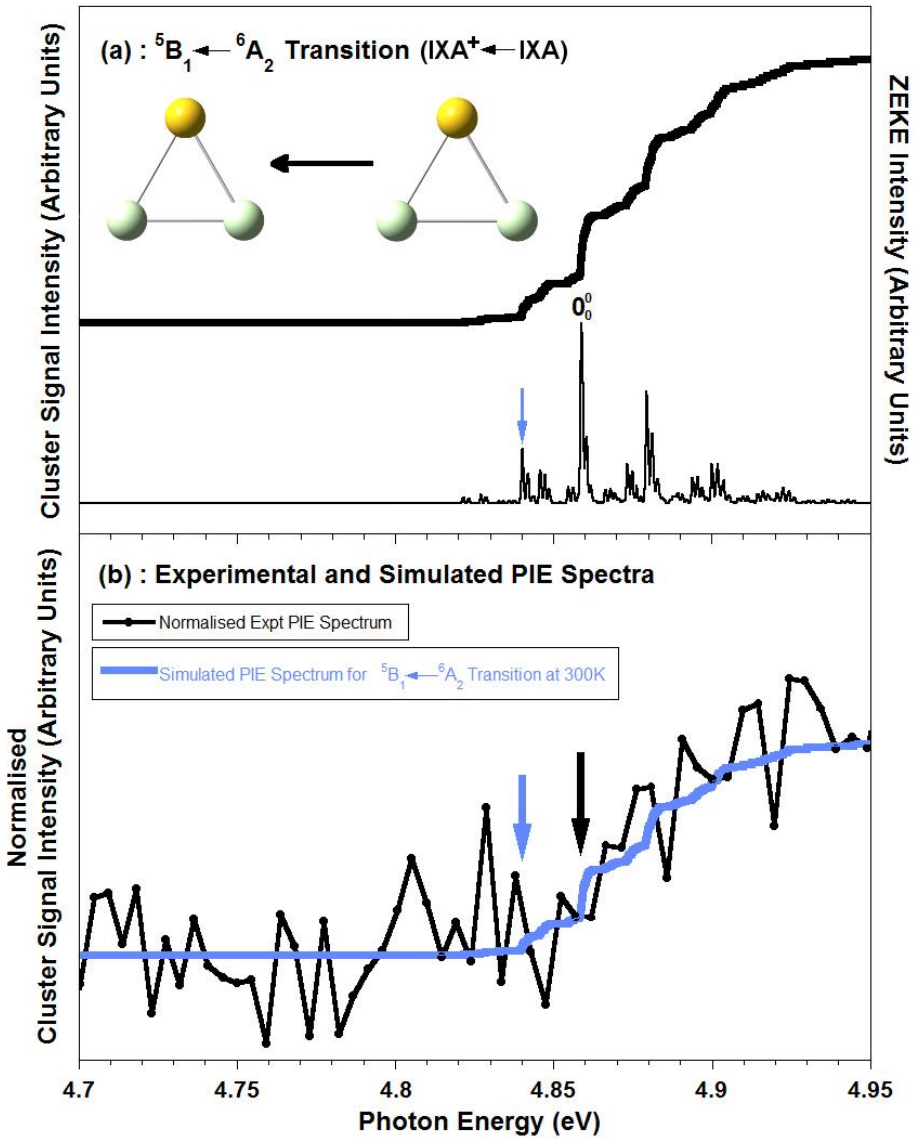

Figure 9.9. *(a) The corrected ZEKE and PIE spectra for the $^5B_1 \leftarrow {}^6A_2$ ($IXA^+ \leftarrow IXA$) transition of $AuPr_2$ simulated at 300 K, and (b) The normalised experimental and corrected PIE spectra for the $^5B_1 \leftarrow {}^6A_2$ ($IXA^+ \leftarrow IXA$) transition of $AuPr_2$ simulated at 300 K. The blue arrow indicates the energy at which the thermal onset of the PIE spectrum is initiated. The black arrow indicates the energy of the band origin and thermally-corrected experimental appearance energy (AE^t) of $AuPr_2$.*

9.6. Field-Correction to the Experimental IEs of Au_2Pr and $AuPr_2$

From the various ZEKE and PIE spectral simulations presented in the previous section, the thermally-corrected experimental AEs (denoted $AE^{\dagger}$) have been determined for the Au_2Pr and $AuPr_2$ clusters. By applying a field correction factor of 0.017 eV (derived from IE =AE+6.1$\sqrt{E}$; where E= 485 V/cm for the experimental setup)[27] to the determined $AE^{\dagger}$ values, the field- and thermally-corrected experimental IEs (rounded-off to two decimal places) become 5.57 eV and 4.88 eV for Au_2Pr and $AuPr_2$, respectively. These values for Au_2Pr and $AuPr_2$ are listed in Table 9.5 and denoted $IE^{\dagger}$ to differentiate them from the experimental IEs determined in Chapter 8 (denoted IE in that chapter).

9.7. Calculated IEs of the $Au_{3-k}Pr_k$ (k = 0-3) Clusters and Comparison to Experimental IEs

As done for the $RhHo_2O_n$ (n = 0-2) and $Rh_2Ho_2O_m$ (m = 0-2) clusters in Chapter 6 and 7, respectively, the calculated IEs of the Au_2Pr and $AuPr_2$ clusters are determined by taking the energy difference (in eV and including zero-point energy correction) between the assigned neutral and cationic structures determined by the ZEKE and PIE spectral simulations presented and discussed in Section 9.5 (and obeying the $\Delta S = \pm 1/2$ selection rule). The calculated IEs of Au_3 and Pr_3 are calculated in the same manner, with the exception of assignment of the neutral and cationic structures for Pr_3 being limited to which competing ionisation transition of the four listed in Section 9.4 produced the most viable ZEKE spectrum (see Appendix E for the ZEKE spectra corresponding to all potential ionisation transition candidates for Pr_3). Au_3 only had one ionisation transition that produced a viable ZEKE and hence, it was much easier to assign the neutral and cationic structures to this cluster. The calculated IE values for the $Au_{3-k}Pr_k$ (k = 0-3) clusters are listed in Table 9.5 (column 7). The calculated IE for Au_3 is determined to be 7.54 eV upon the $^1A_1 \leftarrow {}^2B_2$ transition. The substitution of a gold atom with a praseodymium atom decreases the IE by 1.37 eV, yielding a calculated IE of 6.17 eV for the $^1A_1 \leftarrow {}^2A_1$ transition of Au_2Pr. Substitution of second gold atom further decreases the

Cluster	Expt. AE†	Expt. IE/IE†	Structures	Calc. Transition	E of Neutral HOMO	Calc. IE (Incl. ZPE)	Offset IE
Au_3	-	7.06[a], 7.27[b]	$VIIA^+ \leftarrow VIIB$	$^1A_1 \leftarrow {}^2B_2$	-5.80	7.54	7.20
Au_2Pr	5.551	5.57	$VIIIA^+ \leftarrow VIIIA$	$^1A_1 \leftarrow {}^2A_1$	-4.66	6.17	5.83
$AuPr_2$	4.859	4.88	$IXA^+ \leftarrow IXA$	$^5B_1 \leftarrow {}^6A_2$	-3.82	5.10	4.76
Pr_3	-	4.41[c]	$XA^+ \leftarrow XB$	$^7B_1 \leftarrow {}^6B_1$	-3.61	4.75	4.41

Table 9.5. *List of the thermally-corrected experimental AEs (AE†) and field- and thermally-corrected experimental IEs (IE†) determined for the Au_2Pr and $AuPr_2$ clusters (uncertainty in IEs = ±0.05 eV). The experimental IE values of Au_3 and Pr_3 determined previously by other research groups have also been included for comparison. Additionally shown are the calculated transitions, energies of the neutral HOMOs and calculated IEs (offset and including ZPE) determined using the B3P86 density functional and the SDD basis set for each cluster. The offset IE was calculated by subtracting the difference between the calculated and corrected experimental IEs for the Pr_3 cluster (0.34 eV) from all the calculated IEs. All numerical values are in units of 'eV'.*

[a]*Experimental IE determined by Bishea and Morse – Reference 5.*

[b]*Experimental IE determined by Cheeseman and Eyler – Reference 28.*

[c]*Experimental IE determined by Korestky and Knickelbein – Reference 24.*

calculated IE by 1.07 eV relative to Au_2Pr, yielding an IE of 5.10 eV for the $^5B_1 \leftarrow {}^6A_2$ transition of $AuPr_2$. Substitution of the last gold atom decreases the calculated IE by 0.35 eV relative to $AuPr_2$, yielding an IE of 4.75 eV for the $^7B_1 \leftarrow {}^6B_1$ of Pr_3. Relative to the Au_3, complete substitution of all gold atoms with praseodymium atoms to form Pr_3 decreases the calculated IE by 2.79 eV.

As observed for the $RhHo_2O_n$ (n = 0-2) and $Rh_2Ho_2O_m$ (m = 0-2) clusters in Chapters 6 and 7, respectively and in previous studies on gas-phase metal carbide clusters by the Metha group, the calculated IEs listed in Table 9.5 are determined to be higher in energy than the experimental IE† values.[29-32] This is attributed to the nature of the B3P86 functional rather than that of the Stuttgart-Dresden ECP, which has been concluded

previously from the comparison of the experimental IEs of the Ta_4C_y (y = 0-4) clusters with those calculated using the B3P86/LANL2DZ and B3P86/SDD levels of theory.[30] Hence, in order to account for this over-estimation, the calculated IEs are corrected with respect to the experimental IE of Pr_3 as: (i) this IE value is more certain the IE value of Au_3 and, (ii) the main focus of this chapter is how the IE changes with respect to the substitution of gold atoms for praseodymium atoms, or vice-versa. Accordingly, the difference between the calculated and experimental IE of Pr_3 is determined to be +0.34 eV. This value is then subtracted from the calculated IE values for $AuPr_2$, Au_2Pr and Au_3 to give the offset IE values that are listed in the final column of Table 9.5.

Figure 9.10 shows the comparison of the experimental IE/IE† and calculated offset IE values, both plotted against the number of constituent praseodymium atoms for each cluster. The general trend in IE as a function of praseodymium atoms is the same in both sets of data; both show that the substitution of gold atoms with praseodymium atoms continually lowers the IE of each cluster with each individual substitution. Additionally, the difference between the experimental IE† and offset IE values is +0.26 eV for Au_2Pr and -0.12 for $AuPr_2$, indicating moderately good quantitative comparison between theory and experiment, especially since the experimental IE error is ±0.05 eV. Furthermore, the calculated offset IE of Au_3 (7.20 eV) lies in between the two previously determined experimental IEs of this cluster, further indicating good quantitative comparison between experiment and theory.

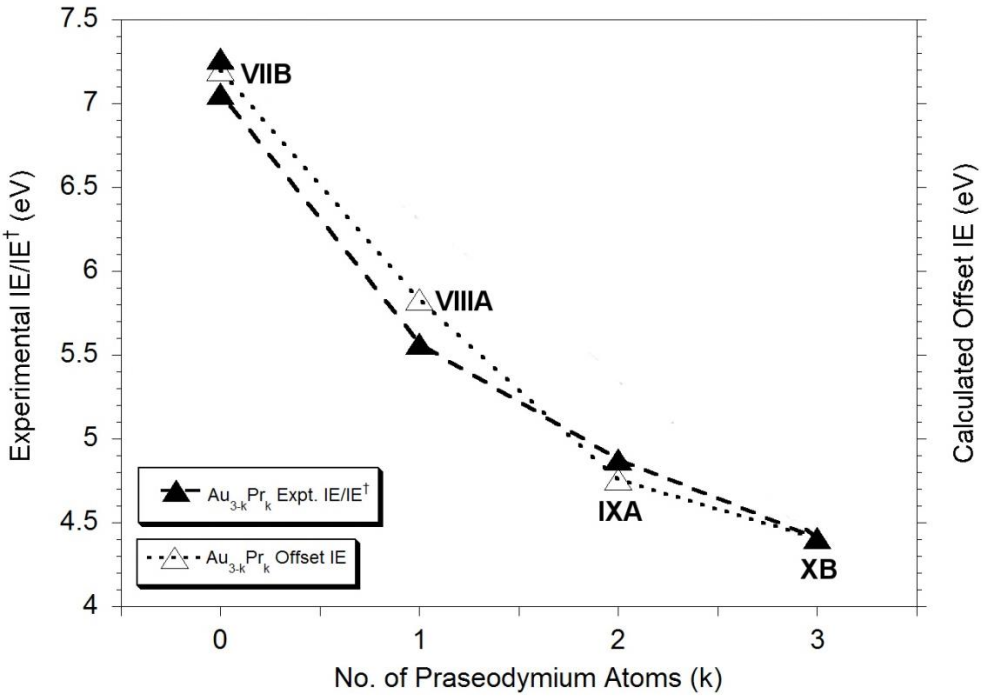

Figure 9.10. *Graph showing the field- and thermally-corrected experimental IE values (denoted IE†) for Au_2Pr and $AuPr_2$ and the previously determined experimental IE values of Au_3 and Pr_3 as a function of constituent praseodymium atoms. Also shown are the offset IE values calculated using DFT. Note that the "Calculate Offset" value for Pr_3 is arbitrarily set to the experimental IE and this difference is used as the offset correction for the other calculated IE values. The corresponding neutral isomer of each cluster from which ionisation is most likely to occur has also been labelled.*

Overall, observing a continual decrease in IE with increased praseodymium substitution indicates that there is a significant change in the electronic structure of each cluster upon sequential substitution. More specifically, any changes in the energies and bonding/non-bonding/anti-bonding characteristics of the HOMOs of each neutral cluster that occur upon substitution will have a direct effect on the IE, assuming that the electron is removed from the HOMO of the neutral cluster in the photoionisation process (as with the $RhHo_2O_n$ (n = 0-2) and $Rh_2Ho_2O_m$ (m = 0-2) clusters in Section 6.5 and 7.5). Hence, Figure 9.11 shows the comparison between the neutral HOMO energy of each cluster and the experimental IE/IE† values plotted against the number of constituent praseodymium atoms. The axes have been shifted but represent a linear relationship. The corresponding pictures of the neutral HOMO of each cluster have also been included in

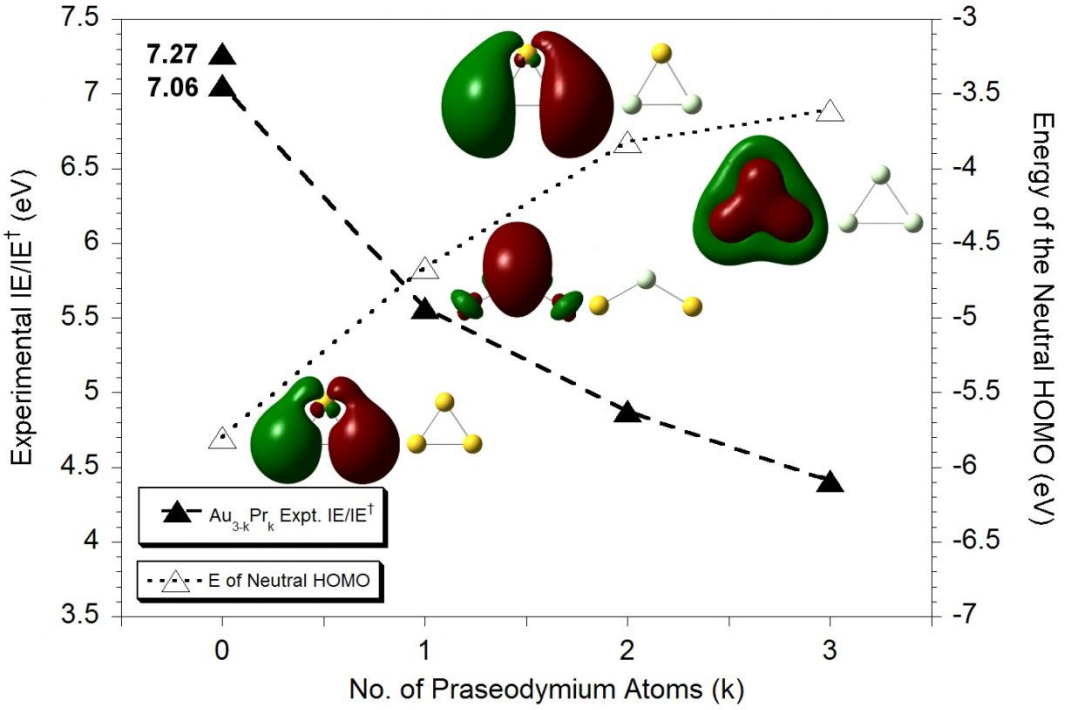

Figure 9.11. *Graph showing the comparison between the experimental IE/IE† values and the neutral HOMO energies of the assigned neutral structures for the $Au_{3-k}Pr_k$ (k = 0-3) clusters. Also displayed are pictures of each neutral HOMO and both previously determined experimental IEs of the Au_3 cluster.*

order to help explain any observed change in bonding/non-bonding/anti-bonding character upon substitution.

As seen in Figure 9.11, there is an anti-correlation observed between the energy of the neutral HOMO and the corresponding experimental IE/IE† of each cluster. This is expected as the IE of a neutral molecule should be low if the energy of its HOMO is high, keeping consistency with the assumption that electrons are removed from the neutral HOMO of each cluster in the photoionisation process. This is observed upon the first substitution of a gold atom for praseodymium atom, which results in the energy of the neutral HOMO increasing by 1.14 eV and the experimental IE decreasing by 1.49 eV. The next substitution to yield $AuPr_2$ further increases the neutral HOMO energy by 0.84 eV, which further decreases the experimental IE by 0.69 eV. Final substitution of the last gold atom to yield Pr_3 results in a smaller increase in the HOMO energy by 0.21 eV, which results in a smaller decrease of the experimental IE by 0.47 eV. Additionally, these trends

show that the first substitution has the most profound effect on the neutral HOMO energy and experimental IE, with the effect on these two values diminishing with each subsequent substitution.

Overall, the good comparison between the experimental and theoretical data in Figures 9.10 and 9.11 (in addition to Figures 9.6(b) and 9.9(b)) indicates that incorporating the *f*-electrons of the Pr atom into the ECP as part of the computational method is just as valid for the $Au_{3-k}Pr_k$ (k =0-3) clusters as incorporating the f-electrons of the Ho atom in the ECP for the $RhHo_2O_n$ (n = 0-2) and $Rh_2Ho_2O_m$ (m = 0-2) clusters. This infers that *f*-electrons seem to play no significant part in the valence active space of the neutral and cationic $Au_{3-k}Pr_k$ (k = 0-3) clusters.

9.8. Conclusion

In summary, this chapter has presented theoretical insight gained from DFT calculations, FCF calculations and ZEKE/PIE spectral simulations performed on the on the $Au_{3-k}Pr_k$ (k = 0-3) clusters. From these studies, it is concluded that: (i) the most likely neutral and cationic structures of Au_2Pr and $AuPr_2$ have been inferred from comparison between the experimental and simulated PIE spectra of each cluster, (ii) the experimental IEs of Au_2Pr and $AuPr_2$ have been corrected for thermal tailing that results from vibronic hot band transitions at 300 K, (iii) the calculated IEs of the $Au_{3-k}Pr_k$ (k = 0-3) clusters have been determined and after an applied offset, were found to compare well with the experimental IE/IE† values; with both sets of data showing that the substitution of gold atoms with praseodymium atoms continually lowers the IE of each cluster with each individual substitution, and (iv) the lowering of the IE upon praseodymium substitution is due to an increase in the energy of the neutral HOMO of each cluster with an anti-correlation observed between the energy of the neutral HOMO and the corresponding experimental IE/IE† values of each cluster. Overall, such good comparison between the experimental and theoretical data also indicates that *f*-electrons play no significant part in the valence active space of the neutral and cationic $Au_{3-k}Pr_k$ (k = 0-3) clusters (as was concluded for the $RhHo_2O_n$ (n = 0-2) and $Rh_2Ho_2O_m$ (m = 0-2) clusters in Chapters 6 and 7).

9.9. References

(1) Balasubramanian, K.; Liao., M. Z. *Chem. Phys.* **1988**, *127*, 313.
(2) Wesendrup, R.; Hunt, T.; Schwerdtfeger, P. *J. Chem. Phys.* **2000**, *112*, 9356.
(3) Varganov, S. A.; Olsen, R. M.; Gordon, M. S.; Metiu, H. *J. Chem. Phys.* **2003**, *119*, 2531.
(4) Coquet, R.; Howard, K. L.; Willock, D. J. *Chem. Soc. Rev.* **2008**, *37*, 2046.
(5) Bishea, G. A.; Morse, M. D. *J. Chem. Phys.* **1991**, *95*, 8779.
(6) Howard, J. A.; Sutcliffe., R.; Mile, B. *J. Chem. Soc. Chem. Comm.* **1983**, 1449.
(7) Bonacic-Koutecky, V.; Burda, J.; Mitric, R.; Ge, M. F.; Zampella, G.; Fantucci, P. *J. Chem. Phys.* **2002**, *117*, 3120.
(8) Xiao, L.; Tollberg, B.; Hu, X. K.; Wang, L. C. *J. Chem. Phys.* **2006**, *124*.
(9) Njegic, B.; Gordon, M. S. *J. Chem. Phys.* **2008**, *95*, 124705.
(10) Li, X. B.; Wang, H. Y.; Yang, X. D.; Zhu, Z. H.; Tang, Y. J. *J. Chem. Phys.* **2007**, *126*.
(11) Nijamudheen, A.; Datta, A. *J. Mol. Structure - Theochem* **2010**, *945*, 93.
(12) Deka, A.; Deka, R. C. *J. Mol. Structure - Theochem* **2008**, *870*, 83.
(13) Shi, Y. K.; Li, Z. H.; Fan, K. N. *J. Phys. Chem. A* **2010**, *114*, 10297.
(14) Lee, H. M.; Ge, M. F.; Sahu, B. R.; Tarakeshwar, P.; Kim, K. S. *J. Phys. Chem. B* **2003**, *107*, 9994.
(15) Lu, P.; Kuang, X. Y.; Mao, A. J.; Wang, Z. H.; Zhao, Y. R. *Mol. Phys.* **2011**, *109*, 2057.
(16) Assadollahzadeh, B.; Schwerdtfeger, P. *J. Chem. Phys.* **2009**, *131*.
(17) Joshi, A. M.; Delgass, W. N.; Thomson, K. T. *J. Phys. Chem. B* **2006**, *110*, 23373.
(18) Joshi, A. M.; Delgass, W. N.; Thomson, K. T. *J. Phys. Chem. B* **2006**, *110*, 2572.
(19) Chen, Y. K.; Tian, W. Q.; Wang, Y. A. *Int. J. Quantum Chem* **2012**, *112*, 65.
(20) Gilb, S.; Weis, P.; Furche, F.; Ahlrichs, R.; Kappes, M. M. *J. Chem. Phys.* **2002**, *116*, 4094.
(21) Weis, P. W., O.; Vollmer, E.; Kappes, M. M. *J. Chem. Phys.* **2004**, *120*, 677.
(22) Zhao L-.X.; Feng X-.J.; Zhang, M.; Luo, Y-.H. *J. Clust. Sci.* **2010**, *21*, 701.
(23) Liu, N.; Ma, Q. M.; Xie, Z.; Liu, Y.; Li, Y. C. *Chem. Phys. Lett.* **2007**, *436*, 184.
(24) Koretsky, G. M.; Knickelbein, M. B. *Eur. Phys. J. D* **1998**, *2*, 273.
(25) Tsipis, A. C.; Stalikas, A. V. *J. Comp. Chem.* **2011**, *32*, 620.
(26) This "arbitary correction factor" is determined by shifting the simulated PIE spectrum by varying amounts of energy until the initial part of cluster signal onset visually aligns with that of the experimental PIE spectrum..
(27) Németh, G. I.; Ungar, H.; Yeretzian, C.; Selzle, H. L.; Schlag, E. W. *Chem. Phys. Lett.* **1994**, *228*, 1.
(28) Cheeseman, M. A.; Eyler, J. R. *J. Phys. Chem.* **1992**, *96*, 1082.
(29) Dryza, V.; Addicoat, M. A.; Gascooke, J. R.; Buntine, M. A.; Metha, G. F. *J. Phys. Chem. A* **2008**, *112*, 5582.

(30) Dryza, V.; Metha, G. F. *J. Chem. Phys.* **2009**, *130*, 244301.
(31) Dryza, V.; Gascooke, J. R.; Buntine, M. A.; Metha, G. F. *Phys. Chem. Chem. Phys.* **2009**, *11*, 1060.
(32) Dryza, V.; Alvino, J. F.; Metha, G. F. *J. Phys. Chem. A* **2010**, *114*, 4080.

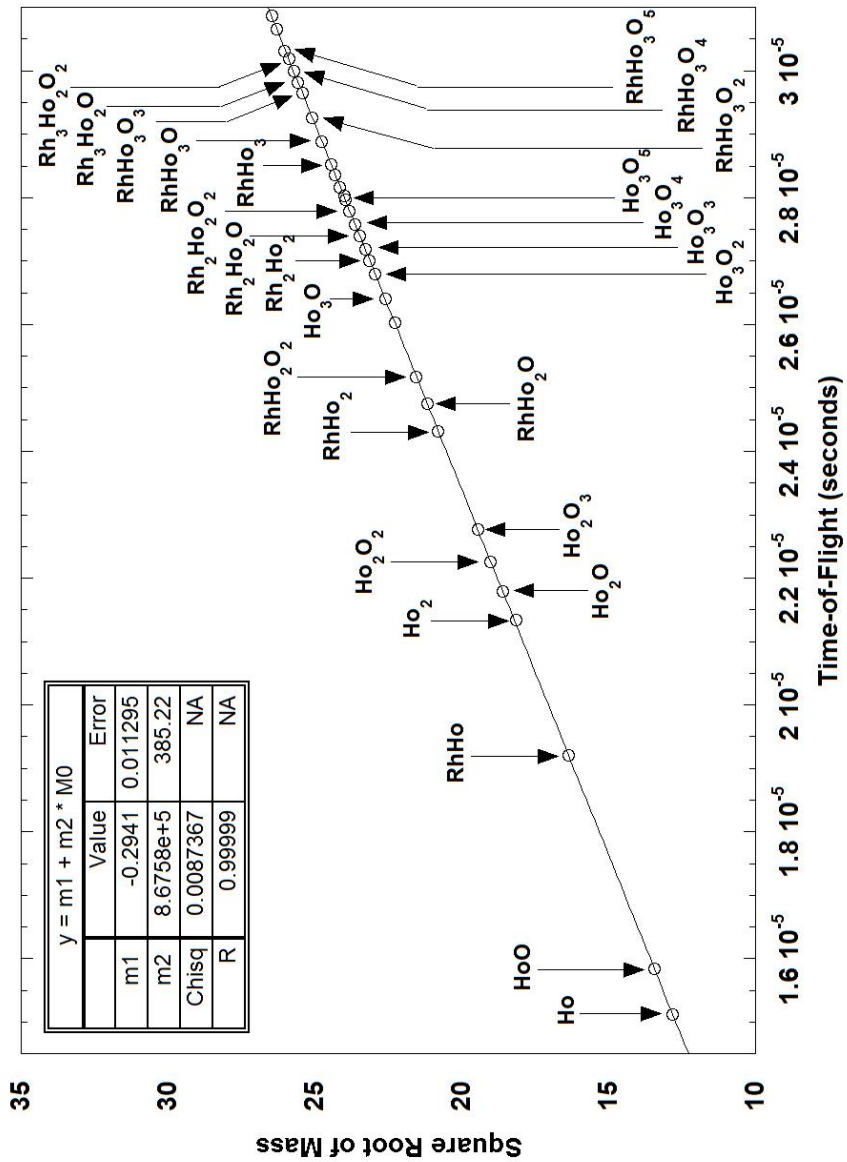

Appendix A1. *$\sqrt{(m/q)}$ versus time-of-flight graph used to transform the time-of-flight spectrum of the Ho and Rh-Ho clusters and their oxide counterparts into the mass spectrum presented in Chapter Five (Figure 5.1). Also displayed is the linear equation used to perform the transformation.*

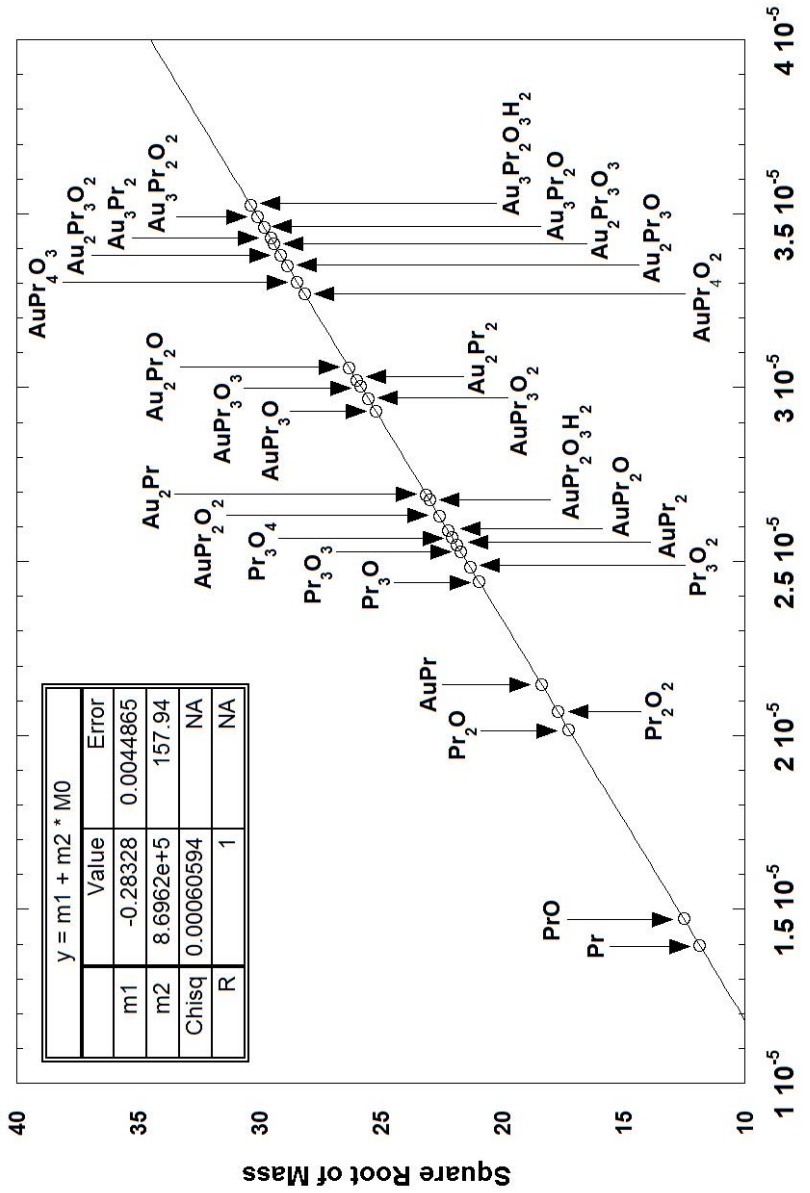

Appendix A2. *√(m/q) versus time-of-flight graph used to transform the time-of-flight spectrum of the Pr and Au-Pr clusters and their oxide counterparts into the mass spectrum presented in Chapter Eight (Figure 8.1). Also displayed is the linear equation used to perform the transformation.*

$RhHo_2$ - Neutrals

Structure IA

E= -186.727818 a.u.

E+V= -186.726725 a.u.

Ho	0.000000	1.749343	-0.407968
Ho	0.000000	-1.749343	-0.407968
Rh	0.000000	0.000000	1.214838

Structure IB

E= -186.713030 a.u.

E+V= -186.711836 a.u.

Rh	0.000000	0.000000	1.351661
Ho	0.000000	1.586791	-0.453916
Ho	0.000000	-1.586791	-0.453916

Structure IC

E= -186.702691 a.u.

E+V= -186.701607 a.u.

Ho	0.000000	1.557270	-0.459395
Ho	0.000000	-1.557270	-0.459395
Rh	0.000000	0.000000	1.367975

Structure ID

E= -186.653731 a.u.

E+V= -186.652843 a.u.

Rh	0.000000	0.000000	-2.970919
Ho	0.000000	0.000000	2.833290
Ho	0.000000	0.000000	-0.837897

$RhHo_2$ - Cations

Structure IA^+

E= -186.514549 a.u.

E+V= -186.513439 a.u.

Ho	0.000000	1.961115	-0.339060
Ho	0.000000	-1.961115	-0.339060
Rh	0.000000	0.000000	1.009646

Structure IB^+

E= -186.514005 a.u.

E+V= -186.512856 a.u.

Ho	0.000000	1.695770	-0.419844
Ho	0.000000	-1.695770	-0.419844
Rh	0.000000	0.000000	1.250203

Structure IC^+

E= -186.501994 a.u.

E+V= -186.500777 a.u.

Ho	0.000000	1.533212	-0.465798
Ho	0.000000	-1.533212	-0.465798
Rh	0.000000	0.000000	1.387043

Structure ID^+

E= -186.494714 a.u.

E+V= -186.493565 a.u.

Rh	0.000000	0.000000	1.408998
Ho	0.000000	1.501325	-0.473171
Ho	0.000000	-1.501325	-0.473171

$RhHo_2O$ - Neutrals

Structure IIA

E= -262.267649 a.u.

E+V= -262.263530 a.u.

Ho	0.000000	1.553153	-0.394934
Ho	0.000000	-1.553153	-0.394934
Rh	0.000000	0.000000	1.474635
O	0.000000	0.000000	-1.679687

Structure IIB

E= -262.216922 a.u.

E+V= -262.213125 a.u.

Ho	0.000000	1.612106	-0.458896
Ho	0.000000	-1.612106	-0.458896
Rh	0.000000	0.000000	1.658485
O	0.000000	0.000000	-1.642476

$RhHo_2O$ - Cations

Structure IIA^+

E= -262.070316 a.u.

E+V= -262.065936 a.u.

Ho	0.000000	1.535074	-0.397158
Ho	0.000000	-1.535074	-0.397158
Rh	0.000000	0.000000	1.480136
O	0.000000	0.000000	-1.673376

Structure IIB^+

E= -262.015846 a.u.

E+V= -262.012156 a.u.

Ho	0.000000	1.630082	-0.440817
Ho	0.000000	-1.630082	-0.440817
Rh	0.000000	0.000000	1.594248
O	0.000000	0.000000	-1.583956

$RhHo_2O_2$ - Neutrals

Structure IIIA

E= -337.717857 a.u.

E+V= -337.711110 a.u.

O	0.000000	1.331650	-1.039336
Ho	-1.431616	0.000000	-0.483048
Ho	1.431616	0.000000	-0.483048
Rh	0.000000	0.000000	1.807951
O	0.000000	-1.331650	-1.039336

Structure IIIB

E= -337.716275 a.u.

E+V= -337.709674 a.u.

O	0.459570	1.417042	0.000000
O	1.393752	-1.097017	0.000000
Rh	-1.697978	0.060401	0.000000
Ho	0.459570	-0.039390	1.454020
Ho	0.459570	-0.039390	-1.454020

Structure IIIC

E= -337.682570 a.u.

E+V= -337.676089 a.u.

O	1.315442	0.980385	1.193037
O	-0.009186	-1.697943	0.155094
Rh	-0.247578	1.504479	-0.135182
Ho	-1.591826	-0.493420	0.030452
Ho	1.602139	-0.431372	-0.100629

Structure IIID

E= -337.682540 a.u.

E+V= -337.676051 a.u.

O	0.298151	-1.362659	-0.963606
Ho	1.662417	-0.236964	0.011515
Ho	-1.362615	-0.760206	0.027280
Rh	-0.512822	1.723420	-0.117822
O	0.075624	0.019719	1.301439

Structure IIIE

E= -337.676748 a.u.

E+V= -337.670103 a.u.

O	-1.017158	-1.416377	0.000000
Rh	1.713796	0.644473	0.000000
Ho	-0.485800	-0.203822	1.519815
Ho	-0.485800	-0.203822	-1.519815
O	-0.485800	1.205244	0.000000

Structure IIIF

E= -337.570604 a.u.

E+V= -337.563815 a.u.

O	0.000000	0.771102	-1.678987
Ho	1.557665	0.000000	-0.317000
Ho	-1.557665	0.000000	-0.317000
Rh	0.000000	0.000000	1.540930
O	0.000000	-0.771102	-1.678987

$RhHo_2O_2$ - Cations

Structure $IIIA^+$

E= -337.509791 a.u.

E+V= -337.502334 a.u.

O	0.418994	1.276078	0.000000
O	1.176371	-1.288973	0.000000
Rh	-1.531293	0.590206	0.000000
Ho	0.418994	-0.197434	1.499993
Ho	0.418994	-0.197434	-1.499993

Structure $IIIB^+$

E= -337.492486 a.u.

E+V= -337.485542 a.u.

O	-0.000684	-0.122706	1.328905
O	-0.000657	-1.361694	-0.983320
Ho	1.512929	-0.508630	0.014740
Ho	-1.513749	-0.507126	0.014643
Rh	0.001460	1.776241	-0.105185

Structure $IIIC^+$

E= -337.372310 a.u.

E+V= -337.365105 a.u.

O	0.000000	0.774208	-1.658692
Ho	1.538402	0.000000	-0.322355
Ho	-1.538402	0.000000	-0.322355
Rh	0.000000	0.000000	1.549660
O	0.000000	-0.774208	-1.658692

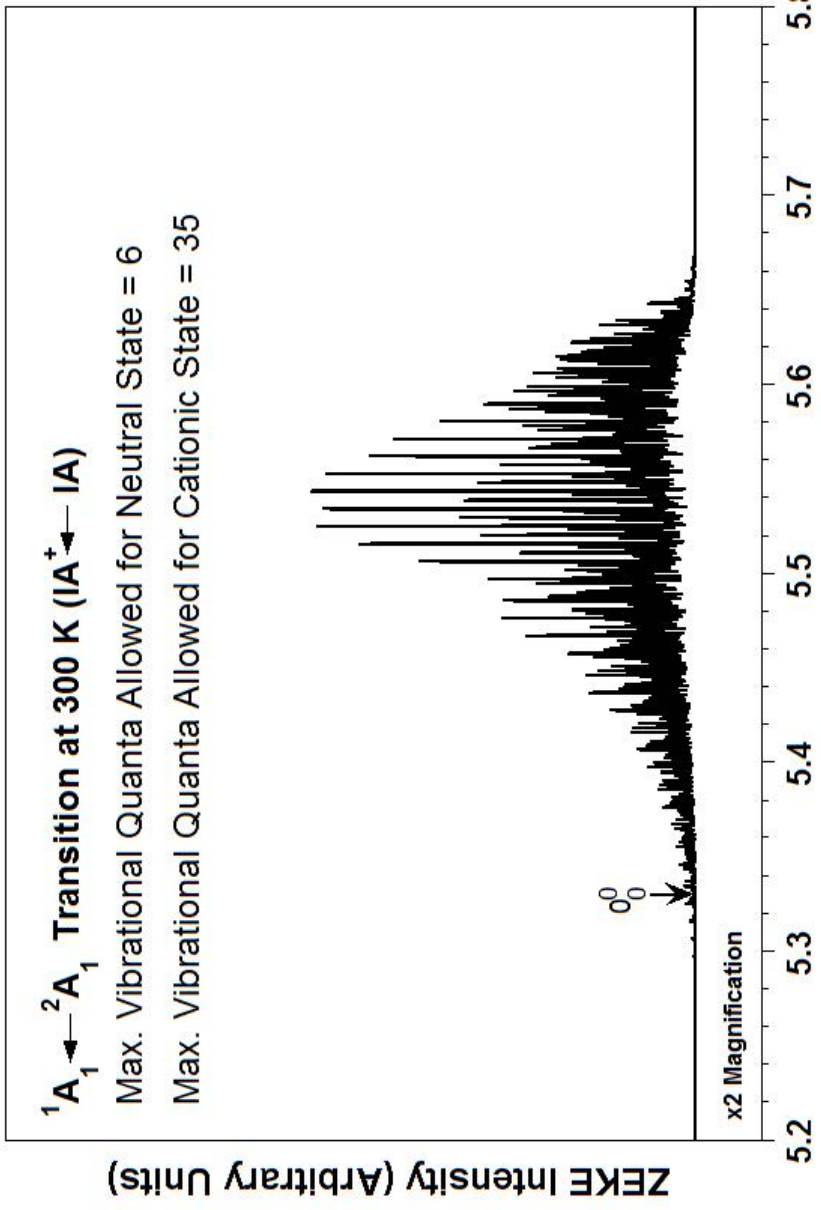

Appendix C. *Re-simulated ZEKE spectrum for the $^1A_1 \leftarrow ^2A_1$ ($IA^+ \leftarrow IA$) transition of the $RhHo_2$ cluster at 300 K with an increase in vibrational quantum number of the neutral and cationic structures (number of max quanta allowed for each state labelled on Figure), and expansion of the energy window. Specific labelling has been omitted except for the theoretical band origin (black arrow). Please note that the* x*2 magnification is relative to the ZEKE spectrum of the $^3B_2 \leftarrow ^2A_1$ ($IB^+ \leftarrow IA$) transition displayed in Figure 6.4(b).*

Rh_2Ho_2 - Neutrals

Structure IVA
E= -297.779498 a.u.
E+V= -297.777459 a.u.

Rh	0.000000	1.377989	0.446966
Rh	0.000000	-1.377989	0.446966
Ho	1.882159	0.000000	-0.300201
Ho	-1.882159	0.000000	-0.300201

Structure IVB
E= -297.774341 a.u.
E+V= -297.772231 a.u.

Rh	0.000000	0.000000	1.916189
Rh	0.000000	0.000000	-1.916189
Ho	0.000000	1.527030	0.000000
Ho	0.000000	-1.527030	0.000000

Structure IVC
E= -297.771340 a.u.
E+V= -297.769414 a.u.

Rh	0.000000	1.867877	0.000000
Rh	0.000000	-1.867877	0.000000
Ho	0.000000	0.000000	1.579490
Ho	0.000000	0.000000	-1.579490

Structure IVD
E= -297.768928 a.u.
E+V= -297.767006 a.u.

Rh	0.000000	1.579750	0.428249
Rh	0.000000	-1.579750	0.428249
Ho	1.706846	0.000000	-0.287630
Ho	-1.706846	0.000000	-0.287630

Structure IVE
E= -297.757960 a.u.
E+V= -297.755951 a.u.

Rh	0.000000	1.328113	0.804573
Rh	0.000000	-1.328113	0.804573
Ho	1.630596	0.000000	-0.540385
Ho	-1.630596	0.000000	-0.540385

Structure IVF
E= -297.753301 a.u.
E+V= -297.751263 a.u.

Rh	-2.390150	-0.348824	0.000000
Ho	2.211050	1.173544	0.000000
Ho	-0.605725	-1.623556	0.000000
Rh	0.000000	1.018842	0.000000

Rh_2Ho_2 - Cations

Structure IVA$^+$
E= -297.568059 a.u.
E+V= -297.565983 a.u.

Rh	0.000000	1.383859	0.529265
Ho	1.810612	0.000000	-0.355477
Rh	0.000000	-1.383859	0.529265
Ho	-1.810612	0.000000	-0.355477

Structure IVB$^+$
E= -297.565334 a.u.
E+V= -297.563328 a.u.

Rh	0.000000	1.889709	0.000000
Rh	0.000000	-1.889709	0.000000
Ho	0.000000	0.000000	1.556992
Ho	0.000000	0.000000	-1.556992

Structure IVC$^+$
E= -297.551672 a.u.
E+V= -297.549618 a.u.

Rh	0.000000	1.336760	0.855581
Ho	-1.555855	0.000000	-0.574644
Rh	0.000000	-1.336760	0.855581
Ho	1.555855	0.000000	-0.574644

Structure IVD$^+$
E= -297.531757 a.u.
E+V= -297.529737 a.u.

Rh	-2.351987	-0.333725	0.000000
Rh	0.000000	1.047627	0.000000
Ho	-0.596429	-1.636371	0.000000
Ho	2.176122	1.156885	0.000000

Rh_2Ho_2O - Neutrals

Structure VA
E= -373.275125 a.u.
E+V= -373.270148 a.u.

Rh	0.000000	1.313294	-1.047319
Rh	0.000000	-1.313294	-1.047319
Ho	1.487627	0.000000	0.586119
Ho	-1.487627	0.000000	0.586119
O	0.000000	0.000000	1.964844

Structure VB
E= -373.251810 a.u.
E+V= -373.247273 a.u.

Rh	-0.003693	1.138113	1.233491
Rh	-0.003674	1.140743	-1.231933
Ho	-1.541851	-0.652127	-0.000413
Ho	1.546170	-0.645867	-0.000399
O	0.005265	-1.947865	-0.001967

Rh_2Ho_2O - Cations

Structure VA^+
E= -373.061068 a.u.
E+V= -373.056076 a.u.

Rh	0.000000	1.234799	-1.147760
Rh	0.000000	-1.234799	-1.147760
Ho	1.526034	0.000000	0.654885
Ho	-1.526034	0.000000	0.654885
O	0.000000	0.000000	1.942980

Structure VB^+
E= -373.031022 a.u.
E+V= -373.026029 a.u.

Ho	0.000000	1.555448	0.683053
Ho	0.000000	-1.555448	0.683053
Rh	1.220301	0.000000	-1.188609
Rh	-1.220301	0.000000	-1.188609
O	0.000000	0.000000	1.930712

$Rh_2Ho_2O_2$ - Neutrals

Structure VIA
E= -448.702760 a.u.
E+V= -448.694645 a.u.

Rh	-1.278906	1.407119	0.000000
Rh	-1.265983	-1.077372	0.000000
Ho	0.700941	-0.139115	1.454914
Ho	0.700941	-0.139115	-1.454914
O	1.873303	-0.953891	0.000000
O	0.700941	1.429244	0.000000

Structure VIB
E= -448.701519 a.u.
E+V= -448.694020 a.u.

Rh	0.000000	1.332650	1.127641
Rh	0.000000	-1.332650	1.127641
Ho	1.494413	0.000000	-0.618432
Ho	-1.494413	0.000000	-0.618432
O	0.000000	-1.347561	-1.163618
O	0.000000	1.347561	-1.163618

Structure VIC
E= -448.701048 a.u.
E+V= -448.693383 a.u.

Rh	-1.404027	1.295904	0.000000
Rh	-1.272367	-1.164976	0.000000
Ho	0.742860	-0.073424	1.447550
Ho	0.742860	-0.073424	-1.447550
O	1.868958	-0.954017	0.000000
O	0.742860	1.447404	0.000000

Structure VID
E= -448.694495 a.u.
E+V= -448.686623 a.u.

Rh	-0.232369	1.566966	-0.770836
Rh	-0.388702	0.558054	1.537778
Ho	1.636230	-0.528089	0.047395
Ho	-1.428811	-0.793769	-0.322732
O	0.238158	-1.833146	-0.696905
O	1.518226	0.950474	-1.311188

Structure VIE
E= -448.687139 a.u.
E+V= -448.679811 a.u.

Rh	-0.049933	1.654708	-0.698541
Rh	0.534079	0.500372	1.511770
Ho	1.496275	-0.674007	-0.430503
Ho	-1.585486	-0.667912	0.111616
O	-0.120697	-1.787469	-0.803178
O	-1.855484	0.903718	-1.100557

Structure VIF
E= -448.673678 a.u.
E+V= -448.666302 a.u.

Rh	-1.500028	-0.811604	-0.919475
Rh	-0.430044	-1.306141	1.139739
Ho	1.719309	-0.297787	-0.320909
Ho	-0.604004	1.497343	0.245869
O	1.339888	1.311291	0.834247
O	0.176088	0.554740	-1.444773

Structure VIG
E= -448.661707 a.u.
E+V= -448.654241 a.u.

Rh	0.307801	1.317614	-1.056700
Rh	0.182351	1.109424	1.336949
Ho	-1.692927	-0.597942	0.071009
Ho	1.555400	-0.866953	-0.063958
O	-1.497069	0.542520	-1.527278
O	-0.108244	-1.926114	-0.108178

Structure VIH
E= -448.570264 a.u.
E+V= -448.563063 a.u.

Rh	0.000000	1.293452	-1.132005
Rh	0.000000	-1.293452	-1.132005
Ho	-1.488707	0.000000	0.524140
Ho	1.488707	0.000000	0.524140
O	0.000000	-0.779844	1.977855
O	0.000000	0.779844	1.977855

$Rh_2Ho_2O_2$ - Cations

Structure VIA$^+$
E= -448.494180 a.u.
E+V= -448.486402 a.u.

Rh	0.000000	1.258525	1.255235
Rh	0.000000	-1.258525	1.255235
Ho	1.522497	0.000000	-0.715460
Ho	-1.522497	0.000000	-0.715460
O	0.000000	-1.332868	-1.068719
O	0.000000	1.332868	-1.068719

Structure VIB$^+$
E= -448.491074 a.u.
E+V= -448.482697 a.u.

Rh	1.473356	-0.878277	0.000000
Rh	1.221597	1.497621	0.000000
Ho	-0.756479	-0.216482	1.482597
Ho	-0.756479	-0.216482	-1.482597
O	-0.756479	1.294684	0.000000
O	-1.731614	-1.152429	0.000000

Structure VIC$^+$
E= -448.489070 a.u.
E+V= -448.481195 a.u.

Rh	-1.368309	1.296506	0.000000
Rh	-1.447846	-1.080523	0.000000
Ho	0.799799	-0.086343	1.492600
Ho	0.799799	-0.086343	-1.492600
O	0.799799	1.361075	0.000000
O	1.644441	-1.129727	0.000000

Structure VID$^+$
E= -448.467204 a.u.
E+V= -448.459244 a.u.

Rh	0.371894	0.885117	1.412680
Rh	0.421846	1.473864	-0.929183
Ho	-1.744168	-0.454764	0.052769
Ho	1.401576	-0.994368	-0.164693
O	-0.333661	-1.884400	-0.318283
O	-1.261918	0.751612	-1.464021

Structure VIE$^+$
E= -448.462174 a.u.
E+V= -448.454401 a.u.

Rh	0.283640	1.361635	-1.042362
Rh	0.550366	1.082431	1.305015
Ho	1.426784	-1.018337	-0.167445
Ho	-1.773130	-0.463173	0.174177
O	-0.308588	-1.891341	-0.053523
O	-1.482041	0.551114	-1.480280

Structure VIF$^+$
E= -448.456198 a.u.
E+V= -448.448366 a.u.

Rh	1.532476	-1.018760	-0.901771
Rh	-0.134431	-1.027621	1.267896
Ho	-1.897601	0.141832	-0.356932
Ho	1.096590	1.181657	0.258124
O	-0.693575	1.710937	-0.517952
O	-0.461959	-1.284257	-0.713989

Structure VIG$^+$
E= -448.355642 a.u.
E+V= -448.348198 a.u.

Rh	0.000000	1.224725	1.227075
Rh	0.000000	-1.224725	1.227075
Ho	1.524339	0.000000	-0.591168
Ho	-1.524339	0.000000	-0.591168
O	0.000000	0.778140	-1.951267
O	0.000000	-0.778140	-1.951267

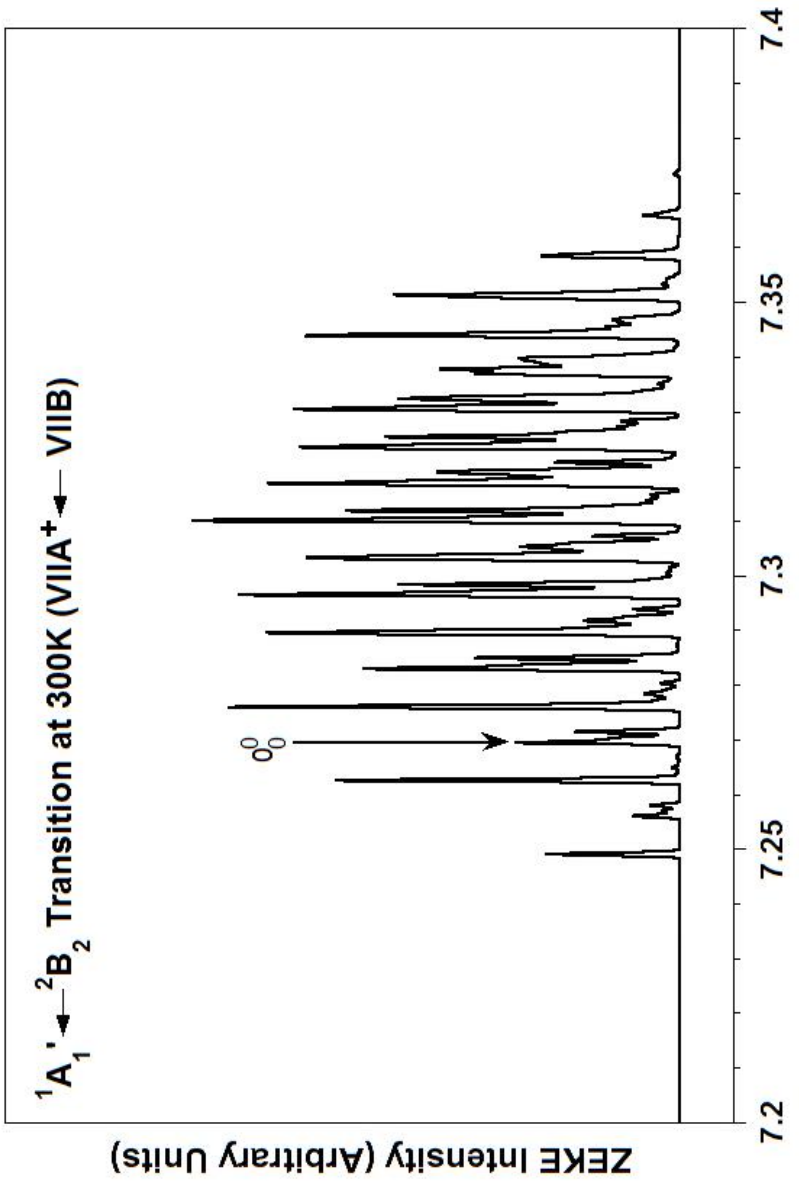

Appendix E1. *ZEKE spectrum simulated at 300 K for the $^1A_1 \leftarrow {}^2B_2$ ($VIIA^+ \leftarrow VIIB$) transition for the Au_3 cluster. Specific labelling has been omitted except for the theoretical band origin (black arrow). Please note that the spectrum was simulated with the energy of the band origin transition set to the experimental IE value postulated by Bishea and Morse (IE = 7.27 eV – See reference 5 in Chapter Nine).*

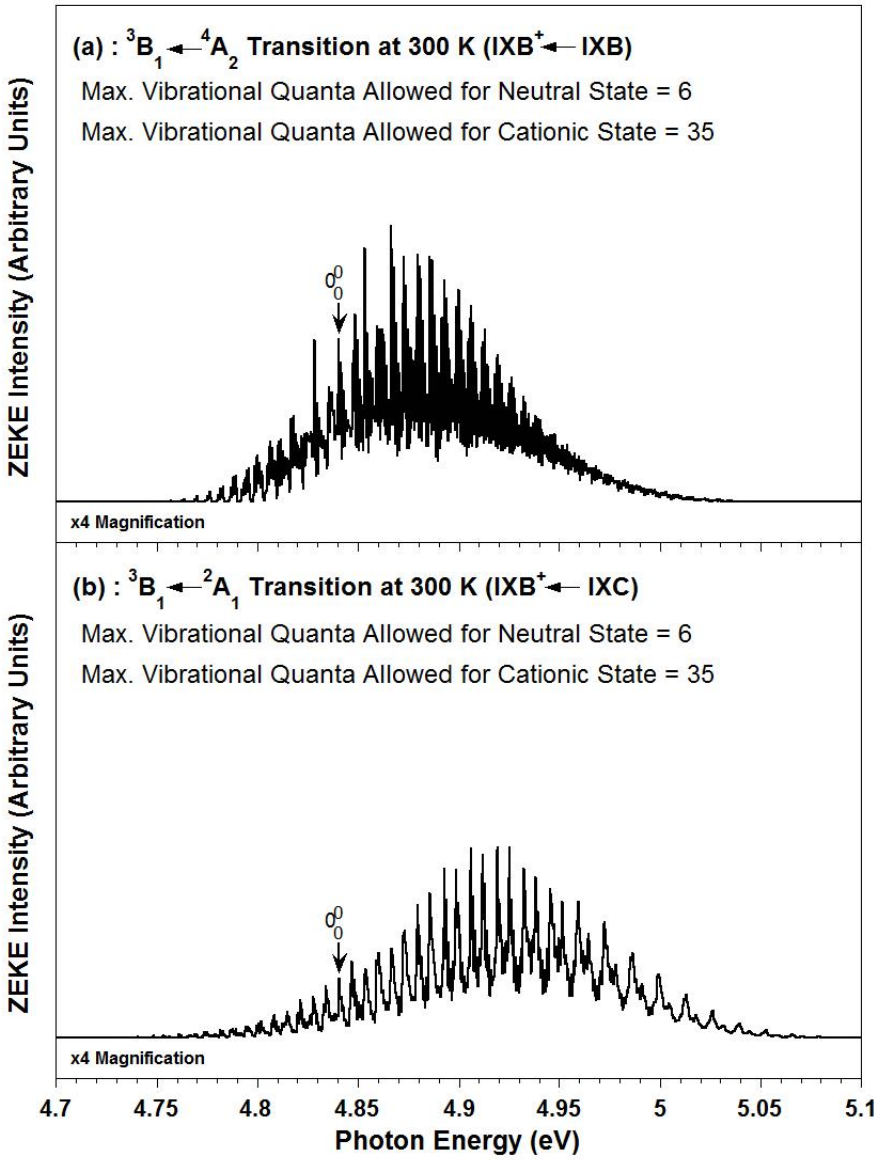

AppendixE2. *Re-simulated ZEKE spectra for the: (a) $^3B_1 \leftarrow {}^4A_2$ ($IXB^+ \leftarrow IXB$) transition, and (b) $^3B_1 \leftarrow {}^2A_1$ ($IXB^+ \leftarrow IXC$) transition of the $AuPr_2$ cluster at 300 K with an increase in vibrational quantum number of the neutral and cationic structures (number of max quanta allowed for each state labelled on Figure), and expansion of the energy window. Specific labelling has been omitted in both spectra except for the band origin transition (0_0^0 – black arrow). Please note that the x4 magnification is relative to the ZEKE spectrum of the $^5B_1 \leftarrow {}^6A_2$ ($IXA^+ \leftarrow IXA$) transition displayed in Figure 9.7(a).*

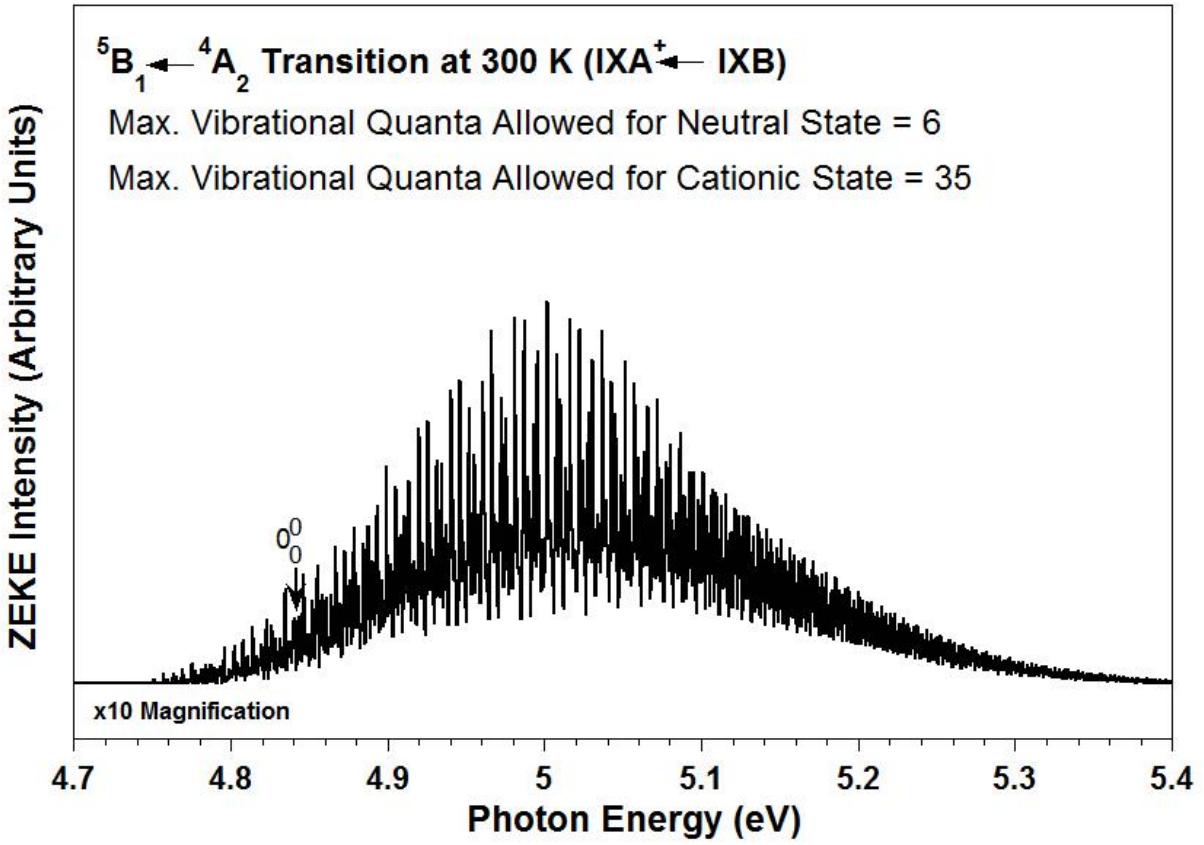

Appendix E3. *Re-simulated ZEKE spectrum for the $^5B_1 \leftarrow {}^4A_2$ ($IXA^+ \leftarrow IXB$) transition of the $AuPr_2$ cluster at 300 K with an increase in vibrational quantum number of the neutral and cationic structures (number of max quanta allowed for each state labelled on Figure), and expansion of the energy window. Specific labelling has been omitted except for the theoretical band origin (black arrow). Please note that the* x10 *magnification is relative to the ZEKE spectrum of the $^5B_1 \leftarrow {}^6A_2$ ($IXA^+ \leftarrow IXA$) transition displayed in Figure 9.7(a).*

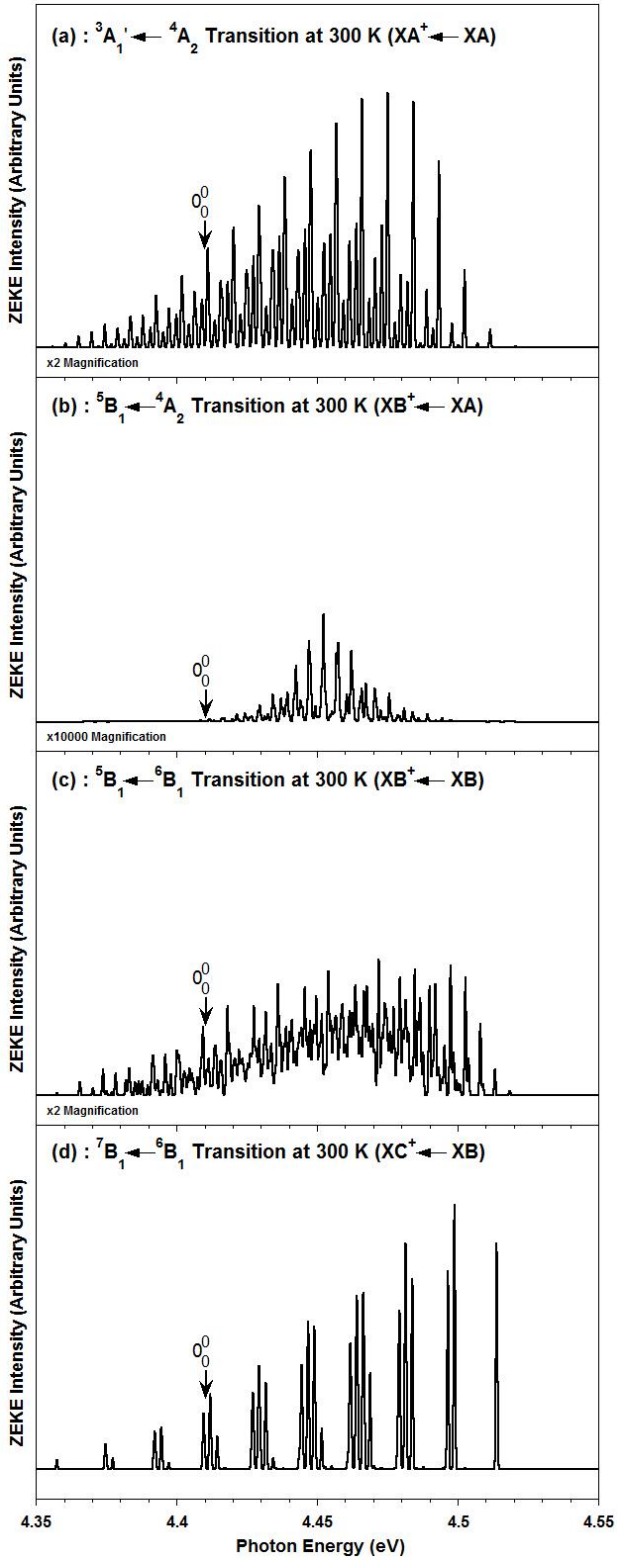

AppendixE4. *ZEKE spectra simulated at 300 K for the various competing transitions for the Pr_3 cluster. Specific labelling has been omitted for all spectra except for the band origin transition (0_0^0 – black arrow). Please note that all spectra were simulated with the energy of the band origin transition set to the experimental IE value determined for Pr_3 by Koretsky and Knickelbein (IE = 4.41 eV – See Reference 24 in Chapter Nine).*

Au_3 - Neutrals

Structure VIIA
E= -408.677475 a.u.
E+V= -408.676775 a.u.

Au	0.000000	2.385743	-0.346760
Au	0.000000	-2.385743	-0.346760
Au	0.000000	0.000000	0.693521

Structure VIIB
E= -408.676147 a.u.
E+V= -408.675438 a.u.

Au	0.000000	1.465735	-0.731982
Au	0.000000	-1.465735	-0.731982
Au	0.000000	0.000000	1.463963

Structure VIIC
E= -408.675249 a.u.
E+V= -408.674634 a.u.

Au	0.000000	1.299868	-0.818007
Au	0.000000	-1.299868	-0.818007
Au	0.000000	0.000000	1.636015

Structure VIID
E= -408.608773 a.u.
E+V= -408.607916 a.u.

Au	0.000000	1.542170	0.000000
Au	1.335559	-0.771085	0.000000
Au	-1.335559	-0.771085	0.000000

Au_3 - Cations

Structure VIIA$^+$
E= -408.399234 a.u.
E+V= -408.398353 a.u.

Au	0.000000	1.542875	0.000000
Au	1.336169	-0.771438	0.000000
Au	-1.336169	-0.771438	0.000000

Structure VIIB$^+$
E= -408.327671 a.u.
E+V= -408.326996 a.u.

Au	0.000000	0.000000	2.694954
Au	0.000000	0.000000	-2.694954
Au	0.000000	0.000000	0.000000

Au_2Pr - Neutrals

Structure VIIIA
E= -305.608594 a.u.
E+V= -305.607859 a.u.

Pr	0.000000	0.000000	0.996693
Au	0.000000	2.379224	-0.372183
Au	0.000000	-2.379224	-0.372183

Structure VIIIB
E= -305.540724 a.u.
E+V= -305.539955 a.u.

Pr	0.000000	0.000000	1.876858
Au	0.000000	1.337194	-0.700852
Au	0.000000	-1.337194	-0.700852

Au_2Pr - Cations

Structure VIIIA$^+$
E= -305.381987 a.u.
E+V= -305.381110 a.u.

Au	0.000000	2.173868	-0.406340
Au	0.000000	-2.173868	-0.406340
Pr	0.000000	0.000000	1.088164

Structure VIIIB$^+$
E= -305.326176 a.u.
E+V= -305.325360 a.u.

Pr	0.000000	0.000000	1.811742
Au	0.000000	1.362170	-0.676537
Au	0.000000	-1.362170	-0.676537

$AuPr_2$ - Neutrals

Structure IXA
E= -202.376394 a.u.
E+V= -202.375649 a.u.

Pr	0.000000	1.501568	-1.021500
Pr	0.000000	-1.501568	-1.021500
Au	0.000000	0.000000	1.525785

Structure IXB
E= -202.375932 a.u.
E+V= -202.375220 a.u.

Pr	0.000000	1.584362	-0.988094
Pr	0.000000	-1.584362	-0.988094
Au	0.000000	0.000000	1.475888

Structure IXC
E= -202.373956 a.u.
E+V= -202.373180 a.u.

Au	0.000000	0.000000	1.577924
Pr	0.000000	1.431380	-1.056406
Pr	0.000000	-1.431380	-1.056406

Structure IXD
E= -202.365761 a.u.
E+V= -202.364925 a.u.

Au	0.000000	0.000000	2.479043
Pr	0.000000	0.000000	-3.012110
Pr	0.000000	0.000000	-0.307287

Structure IXE
E= -202.350622 a.u.
E+V= -202.349811 a.u.

Au	0.000000	0.000000	2.471119
Pr	0.000000	0.000000	-3.002529
Pr	0.000000	0.000000	-0.306257

Structure IXF
E= -202.342274 a.u.
E+V= -202.341426 a.u.

Au	0.000000	0.000000	2.481412
Pr	0.000000	0.000000	-3.006867
Pr	0.000000	0.000000	-0.315702

$AuPr_2$ - Cations

Structure IXA^+
E= -202.189076 a.u.
E+V= -202.188262 a.u.

Au	0.000000	0.000000	1.535962
Pr	0.000000	1.465005	-1.028313
Pr	0.000000	-1.465005	-1.028313

Structure IXB^+
E= -202.185319 a.u.
E+V= -202.184541 a.u.

Au	0.000000	0.000000	1.509403
Pr	0.000000	1.517155	-1.010532
Pr	0.000000	-1.517155	-1.010532

Structure IXC^+
E= -202.179893 a.u.
E+V= -202.179063 a.u.

Pr	0.000000	1.551492	-0.975682
Pr	0.000000	-1.551492	-0.975682
Au	0.000000	0.000000	1.457348

Structure IXD^+
E= -202.149861 a.u.
E+V= -202.149000 a.u.

Au	0.000000	0.000000	2.453666
Pr	0.000000	0.000000	-3.035424
Pr	0.000000	0.000000	-0.249994

Pr_3 - Neutrals

Structure XA
E= -99.145275 a.u.
E+V= -99.144486 a.u.

Pr	0.000000	1.453742	-0.929581
Pr	0.000000	-1.453742	-0.929581
Pr	0.000000	0.000000	1.859161

Structure XB
E= -99.143061 a.u.
E+V= -99.142389 a.u.

Pr	0.000000	0.000000	1.813317
Pr	0.000000	1.569415	-0.906659
Pr	0.000000	-1.569415	-0.906659

Structure XC
E= -99.139053 a.u.
E+V= -99.138395 a.u.

Pr	0.000000	1.891388	-0.737788
Pr	0.000000	-1.891388	-0.737788
Pr	0.000000	0.000000	1.475576

Structure XD
E= -99.137700 a.u.
E+V= -99.137097 a.u.

Pr	0.000000	1.833555	0.000000
Pr	1.587905	-0.916777	0.000000
Pr	-1.587905	-0.916777	0.000000

Structure XE
E= -99.129932 a.u.
E+V= -99.129084 a.u.

Pr	0.000000	1.797434	-0.701688
Pr	0.000000	-1.797434	-0.701688
Pr	0.000000	0.000000	1.403377

Structure XF
E= -99.122236 a.u.
E+V= -99.121623 a.u.

Pr	0.000000	1.658480	-0.849559
Pr	0.000000	-1.658480	-0.849559
Pr	0.000000	0.000000	1.699117

Structure XG
E= -99.117572 a.u.
E+V= -99.117055 a.u.

Pr	2.885629	0.000290	0.000000
Pr	-2.885629	-0.001855	0.000000
Pr	0.000000	0.001565	0.000000

Structure XH
E= -99.108946 a.u.
E+V= -99.108351 a.u.

Pr	0.000000	2.685203	-0.276503
Pr	0.000000	-2.685203	-0.276503
Pr	0.000000	0.000000	0.553007

Pr_3 - Cations

Structure XA^+
E= -98.970587 a.u.
E+V= -98.969908 a.u.

Pr	0.000000	1.826118	0.000000
Pr	1.581465	-0.913059	0.000000
Pr	-1.581465	-0.913059	0.000000

Structure XB^+
E= -98.969205 a.u.
E+V= -98.968429 a.u.

Pr	0.000000	1.688345	-0.893816
Pr	0.000000	-1.688345	-0.893816
Pr	0.000000	0.000000	1.787632

Structure XC^+
E= -98.969296 a.u.
E+V= -98.968548 a.u.

Pr	0.000000	1.647434	-0.951212
Pr	0.000000	-1.647434	-0.951212
Pr	0.000000	0.000000	1.902424

Structure XD^+
E= -98.963355 a.u.
E+V= -98.962679 a.u.

Pr	0.000000	0.000000	1.763330
Pr	0.000000	1.743505	-0.881665
Pr	0.000000	-1.743505	-0.881665

Structure XE^+
E= -98.956030 a.u.
E+V= -98.955267 a.u.

Pr	0.000000	1.790067	0.000000
Pr	1.550243	-0.895033	0.000000
Pr	-1.550243	-0.895033	0.000000

Structure XF^+
E= -98.941601 a.u.
E+V= -98.940783 a.u.

Pr	0.000000	1.929755	-0.634806
Pr	0.000000	-1.929755	-0.634806
Pr	0.000000	0.000000	1.269611